Energy harvesting for microsystems

Xu, Ruichao

Publication date:
2012

Document Version
Publisher's PDF, also known as Version of record

TECHNICAL UNIVERSITY OF DENMARK

Energy harvesting for microsystems

by

Ruichao Xu

A thesis submitted in partial fulfillment for the
degree of Doctor of Philosophy

in the

Silicon microtechnology group
Department of micro- and nanotechnology

May 2012

The most exciting phrase to hear in science, the one that heralds the most discoveries, is not "Eureka" but "That's funny ..."

- Isaac Asimov

TECHNICAL UNIVERSITY OF DENMARK

Abstract

Silicon microtechnology group
Department of micro- and nanotechnology

Doctor of Philosophy

by Ruichao Xu

The purpose of this project is to design and fabricate piezoelectric energy harvesters based on integration of $Pb(Zr_xTi_{1-x})O_3$ (PZT) thick film technology and silicon microtechnology. The fabrication processes are carried out in close collaboration with Meggitt Sensing Systems (MSS) who has the unique expertise to screen print piezoelectric thick film layers, thus all screen printing steps are done by MSS while the silicon micromachining is carried out at Danchip facility at DTU. The presented energy harvesters are all based on using piezoelectric thick film operating in the 31-mode to generate power when strained. Three archetypes of the numerous fabricated energy harvesters will be presented in detail, they represent three major milestones in this project. The first energy harvester archetype has an unimorph cantilever beam, which consists of a 20 μm silicon layer and 10-30 μm screen printed PZT layer, anchored on a silicon frame at one end and attached to a silicon proof mass at the other. Electrodes will cover both side of the PZT layer, so the harvested energy can be collected electrically. The second archetype has a bimorph cantilever beam, which consists of two 15-35 μm PZT layers, anchored on a silicon frame at the one end and attached to a silicon proof mass at the other. Electrodes are deposited below, between and above the two PZT layers. The root mean square (RMS) power output measured on this type of harvesters is as high as 37.1μW at 1 g. The third archetype is similar to the first one, the screen printed PZT layer is replaced by a lead free piezoelectric material, $(K_xNa_{1-x})NbO_3$ (KNN). Some of the major challenges encountered during the development processes are bad adhesion, fragile structures and short circuiting through the PZT layer. All which have being fully or partially solved in this project. The final energy harvesters are designed to be used in an energy harvester powered wireless sensing system.

Resumé

Formålet med projektet er at designe, fremstille og karakterisere energihøstere baseret på integration af $Pb(Zr_xTi_{1-x})O_3$ (PZT) tykfilm med silicium mikroteknologi. Fabrikationen er foregået i tæt samarbejde med Meggitt Sensing Systems (MSS) der er eksperter i silketrykning af piezoelektriske tykfilm, og alle tykfilm i projektet er blevet trykt hos MSS, mens al mikrofremstilling er udført i rentrums faciliteterne på DTU Danchip. Alle energihøstere, der er blevet fremstillet i projektet, er baseret på piezoelektriske tykfilm benyttet i 31-mode til at konvertere tidsvarierende tøjning til elektrisk energi. Tre arketypiske energihøstere er blevet fremstillet i et stort antal eksemplarer, og hver type repræsenterer en milesten i projektet. Den første energihøstertype består af en bjælke af 20 μm silicium med et 10-30 μm tykfilm PZT lag forankret på en silicium ramme i den ene ende og forsynet med en silicium masse i den anden. PZT filmen er forsynet med elektroder hvorfra elektrisk energi høstes. Den anden type består af en bjælke af to 15-35 μm tykke PZT tykfilm igen på en silicium ramme og med en silicium masse. Denne type energihøster har tre elektroder, hvoraf den ene er placeret mellem de to PZT lag. Den energihøstertype leverer 37,1 μW ved en acceleration på 1 g. Den tredje energihøstertype ligner den første, men PZT laget er blevet erstattet af det blyfri piezoelektriske materiale $(K_xNa_{1-x})NbO_3$ (KNN). I projektet er der blevet udviklet en robust fremstillingsteknologi og under projektet er betydelige fremstillingsrelaterede udfordringer blevet løst. De færdige energihøstere tænkes anvendt til energiforsyning af trådløse sensorsystemer.

Preface

This thesis is submitted as a partial fulfillment of the requirements to obtain the Ph.D. degree at the Technical University of Denmark (DTU). The work has been carried out at the Department of Micro- and Nanotechnology (DTU Nanotech) at DTU from the 1st of March 2009 to the 31th of May 2012. The main supervisor has been professor Ole Hansen and professor Erik Vilain Thomsen as co-supervisor. This Ph.D. project is financed by DTU and DTU Nanotech, the idea was that this project will be a forerunner for the Eliminating batteries (Elba) project. Thus much of the work had been done in close collaboration with the Elba project which had been financed by The Danish National Advanced Technology Foundation (Danish: Højteknologifonden). The Elba project is a three year collaboration project between DTU Nanotech and two companies Vestas wind systems and Meggitt sensing systems (MSS). The vision of the Elba project is to eliminate batteries by introducing energy harvesters enabling a new generation of distributed wireless sensing and control systems. To achieve this the Elba project is to develop smart, integrated and miniaturized energy harvesters, which can replace batteries in wireless sensors and help replace wired sensors by wireless ones [1]. The objective of this Ph.D. project is to make the best possible piezoelectric energy harvesting device for the use in the Elba wireless sensing system.

Acknowledgements

First, I would like to thank my main supervisor professor Ole Hansen for his tutelage and tremendous support throughout the project and beyond. My thanks also goes to my co-supervisor professor Erik V. Thomsen, who took me into his group and made me an integral part of it. I would also like to thank the people from Meggitt Sensing Systems for being very flexible and easy to work with. In particular I would like to thank Karsten Hansen, Lise Nielsen, Michele Guizzetti, Konstantin Astafiev and later Louise Borregaard for the screen printing of the wafers and their valuable opinions and suggestions. I would like to thank Erling Ringgaard and Tomasz Zawada for the discussions regarding the works and goals of the Elba project, and Tomasz Zawada in particular for the equipments he made available.

I would also like to thank the enthusiastic students who worked on the numerous projects sparked by this project and the Elba project. The master students like Johan Nagstrup and Christoffer Mølleskov Pedersen, and bachelor students like Christian Dahl-Petersen, Adnan Silajdzic, Ivan Fuglø, Mikkel Wennemoes Hvitfeld Ley, Anders Thyssen, Adam Carsten Stoot and Thomas Lehrmann Christiansen have all contribute to the work presented in this thesis.

I would also like to thank the employees at DTU Danchip, who are maintaining the equipments needed for the fabrication processes and have provided valuable inputs for the process optimization.

Finally, I would like to thank two of my closest colleagues Anders Lei and Karen Birkelund, who worked on the Elba project at DTU Nanotch. Their valuable discussions and cooperations have being vital for the completion of this project.

Ruichao Xu
May 29th 2012, Copenhagen

Contents

List of Figures

List of Tables

Abbreviations

Elba	**El**iminating **ba**tteries
RIE	**R**eactive **I**on **E**tch
DRIE	**D**eep **R**eactive **I**on **E**tch
KOH	Potassium hydroxide
bHF	**b**uffered **H**ydro**f**loric acid
SOI	**S**ilicon **O**n **I**nsulator
LPCVD	**L**ow **P**ressure **C**hemical **V**apour **D**eposition
SEM	**S**canning **E**lectron **M**icroscopy
EDX	**E**nergy **D**ispersive **X**-ray spectroscopy
PZT	Lead zirconate titanate
KNN	Sodium potassium niobate

Physical Constants

Vacuum permittivity $\epsilon_0 = 8.85 \times 10^{-12}$ F m^{-1}

Symbols

a	RMS acceleration	m s^{-2}
P	RMS power	W
V	voltage	V
V_{oc}	open circuit voltage	V
I	current	A
f	frequency	Hz
f_{res}	resonant frequency	Hz
ω	angular frequency	$s^{-}1$
ω_0	natural angular frequency	$s^{-}1$
Q	charge	C
T	stress	N m^{-2}
S	strain	-
E	electric field	V/m
D	displacement field	C m^{-2}
d	piezoelectric coefficient	m/V
e	piezoelectric constant	C m^{-2}
ϵ_r	dielectric constant	F/m
s	elastic compliance	m^2/N
c	stiffness	N m^{-2}
α	proof mass length to total cantilever length ratio	-
L_m	proof mass length	m
L	cantilever beam length	m
W	cantilever width	m
h	cantilever beam height	m
F	force	N

Dedicated to my friends and family.

Chapter 1

Introduction

In the first chapter of this thesis a brief introduction of energy harvesting will be given. This includes the motivations to research in the field of energy harvesting, the advantages of microelectromechanical system (MEMS) based energy harvesters, MEMS based vibration energy harvesters in particular and a brief review of the current generation of vibration MEMS energy harvesters.

1.1 Motivation

One of the most severe challenges man is facing today is to fulfill the need for energy without harmful environmental consequences. This complicated and huge challenge must be met by a wide range of solutions; among these are more efficient use of resources and replacement of fossil fuels by renewable energy sources. More efficient use of resources will require more widespread use of sensing microsystems to control and optimize processes.

The increased usage of microsystems can be seen in its increased market revenue, which increased from 12 billion $ in 2004 to 25 billion $ in 2009 [2]. Figure 1.1 shows the market breakdown for 1st level package microelectromechanical systems. Some of these systems will be placed in remote areas where it would be desirable if the system was self supported also with power, a feature that would be equally desirable for the increasing number of portable complex electronic systems that are being used. Here, the MEMS energy harvester becomes a viable solution of choice. By making a sensor systems self sufficient with power, there will be no need for replacing batteries or refueling, the service lifetime will be determined by material decay or fatigue. Thus the frequency of periodic maintenance may be reduced from months to years, and maybe even decades.

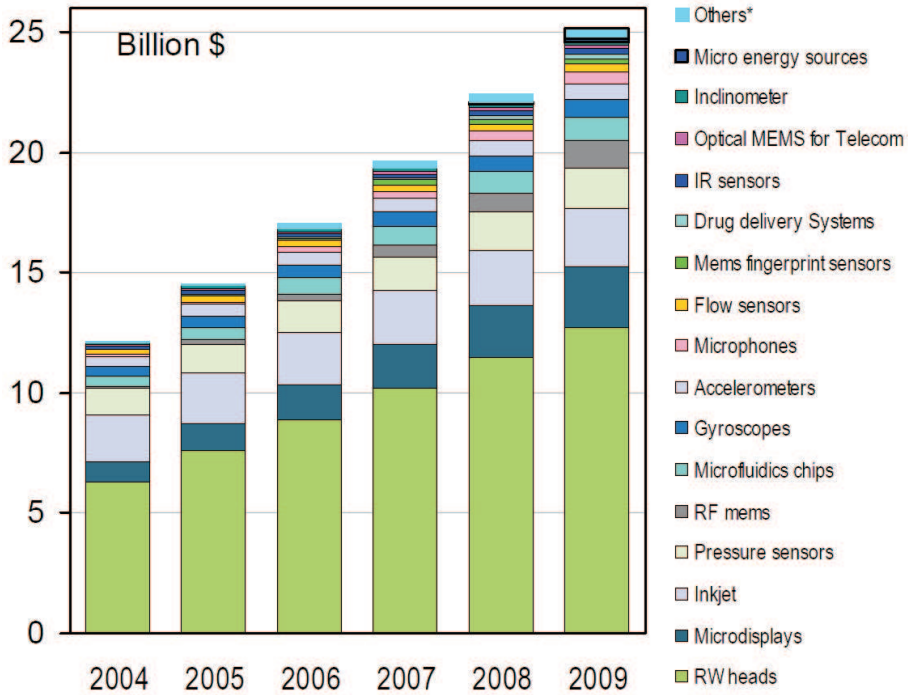

FIGURE 1.1: The diagram shows the market breakdown for 1st level package MEMS, taken from [2].

Furthermore, the inherent small size of a MEMS energy harvester insures its compatibility with the microsystems it powers and the comparability to the battery it replaces.

1.2 Vibration energy harvesting

In the environment a lot of energy, such as ambient light, mechanical vibrations, sound or thermal gradients, is available to be harvested for free. With the advances in microtechnology many useful systems have low enough power requirements to make completely self supported systems realistic [3]. This is supported by the fact that harvesting of energy from mechanical vibrations is not a new idea; fully mechanical systems relying on energy harvesting have been available for many years in the form of wrist watches. Vibration energy harvesters or inertial generators are devices that when subjected to vibration have a proof mass which will move, part of the kinetic energy in this movement can then be converted to electrical energy using electromagnetic induction, electrostatic principles or piezoelectric materials [4]. Though the harvesting source is the same the three methods differ in detail.

1.2.1 Electromagnetic energy harvesters

The principle used in the electromagnetic transduction is the generation of current in a conductor in a magnetic field. The conductor typically takes form of a coil, and electricity is generated by the relative motion of the conductor and a permanent magnet. The amount of electricity generated depends on the strength of the magnet, the velocity of the movement and the number of coil windings. The requirement of a large number of windings with low resistance gives a huge limitation for making a MEMS energy harvester with electromagnetic transduction. The planar processes used in silicon microtechnology limits the amount of windings one can achieve, unless a complicated stacking configuration is developed. The wires can be made using thin film deposition techniques. However this will lead to a very high resistance, since it will be difficult and costly to deposit a metal film of more than 1 μm in thickness. Another major problem is that the magnetic field might interfere with the device one wish to power. Electromagnetic energy harvesters are often characterized by high current, low voltage and low optimal resistive load.

1.2.2 Electrostatic energy harvesters

The electrostatic transduction exploits the relative motion of electrodes acting as capacitor plates. Some of the electrodes can be electrets, which is a charged dielectric material. The work done against the electrostatic force between the electrodes provides the energy for harvesting. Figure 1.2 shows a concept of a simplified electrostatic energy harvesting device, with an electret at the top, which is negatively charged and is moving along with a proof mass relative to electrodes 1 and 2 at the bottom. A resistive load R, *e.g.* a sensor which the energy harvester is delivering power to, is connected between electrode 1 and 2. Since the electret is negatively charged, it will induce positive charges on the two electrodes. When the electret is moving towards right, the right electrode needs to be more positively charged. This results in a current through the load. Similar argument holds for the left electrode. As the charged electret is oscillating back and forth, an alternating current will be generated. This method is often very suited for MEMS applications, since it is cleanroom compatible, and a small and precise gap between the electrodes can be achieve with silicon microtechnology. However the need for pre-charging and extremely low power density are some of its issues.

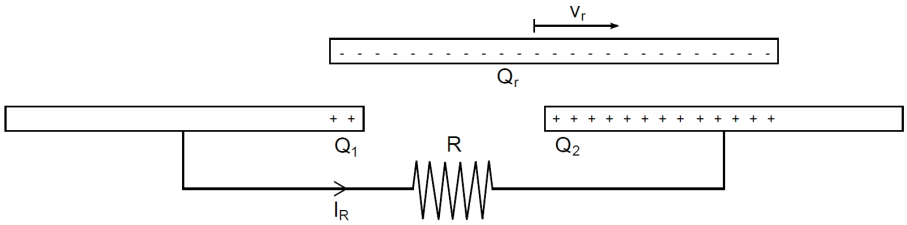

FIGURE 1.2: This figure illustrates the main working principle of a three electrode configuration electrostatic energy harvester.

1.2.3 Piezoelectric energy harvesters

The word, piezo, derived from the Greek piezo or piezein, which means to squeeze or press. A piezoelectric material can generate a displacement field in response to applied mechanical stress, the displacement field will give rise to a electrical potential. The creation of an electric potential when stress is applied is called the direct piezoelectric effect. In the reverse piezoelectric effect a material gets strained due to an applied electric field. A typical piezoelectric energy harvester is based on a cantilever with a heavy proof mass attached. The cantilever beam becomes stressed when the mass is displaced. The cantilever consists of at least one layer of piezoelectric material. When the mass is accelerated the cantilever will be bend, hereby a stress is induced. The stress in the piezoelectric material will give rise to a displacement field which will induce a current. Piezoelectric energy harvesting is chosen in this project due to their higher power density, comparable to the popular battery technologies, and much broader output voltage range as seen in Fig. 1.3.

1.3 Scope of this thesis

One of the main advantages for energy harvesters, compared to batteries, is its *in-situ* power generation. For vibration energy harvesters it is the ambient mechanical noise that provides the source of power. Mechanical noise for most systems consists of a wide spectrum with peaks at different frequencies. Some of these frequency peaks from various sources are given in Table 1.1. Table 1.1 introduce two important parameters, acceleration level and excitation frequency. The accelerations varies from 0.02-1.22 g, harvesting energy from these low levels of acceleration requires a very sensitive structure, which often is fragile. To harvest as much energy as possible the resonant frequency of the harvester must also match the source excitation frequency. The excitation frequencies shown in Table 1.1 varies from 1-200 Hz, which is low compared to the size of MEMS devices, *e.g.* if linear dimensions are reduced the resonant frequency of a given topology will increase. Based on the aforementioned data and the harvester size requirements in

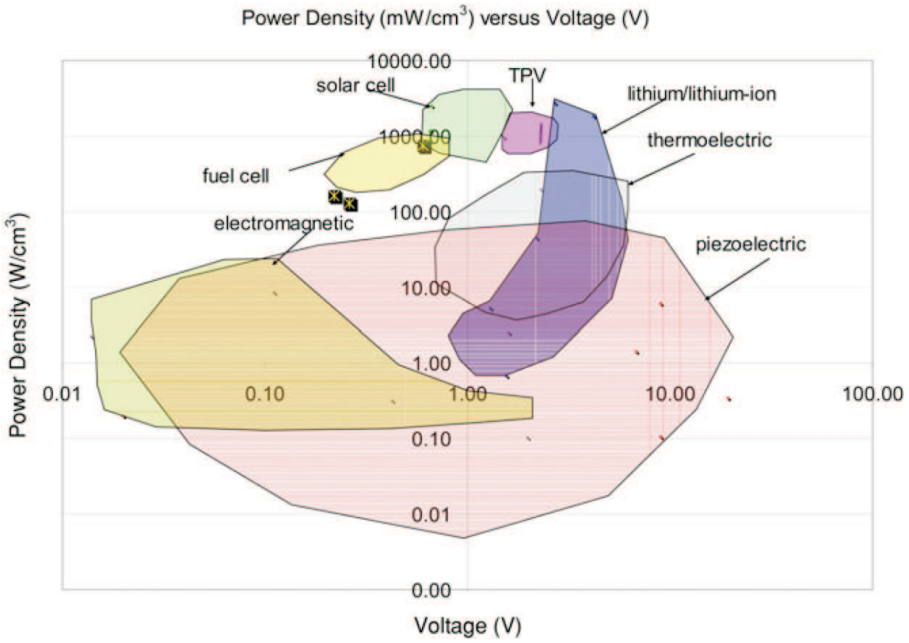

FIGURE 1.3: Plot of power density versus voltage for common regenerative and lithium/lithium-ion power supply strategies. Taken from [5].

the Elba project, the final piezoelectric MEMS energy harvester must be able to harvest energy up to at least 1.5 g ($a > 1.5g$) and have a resonant frequency f_{res} below 500 Hz. The harvester size must be limited to 10 mm $\times$ 10 mm in its lateral dimension. The final device is to be implemented in a complete energy harvester powered wireless sensing system, shown in Fig. 1.4. The complete system will consist of the piezoelectric energy harvester; energy transformation and storage module; energy management and control module; sensor module and wireless communication module.

TABLE 1.1: Acceleration [m/s^2] magnitude and frequency of fundamental vibration mode for various sources. Taken from [6].

Vibration source	a [m/s^2]	f_{peak} [Hz]
Car engine compartment	12	200
Base of 3-axis machine tool	10	70
Blender casing	6.4	121
Clothes dryer	3.5	121
Person nervously tapping their heel	3	1
Car instrument panel	3	13
Door frame just after door closes	3	125
Small microwave oven	2.5	121
HVAC vents in office building	0.21.5	60
Windows next to a busy road	0.7	100
CD on notebook computer	0.6	75
Second story floor of busy office	0.2	100

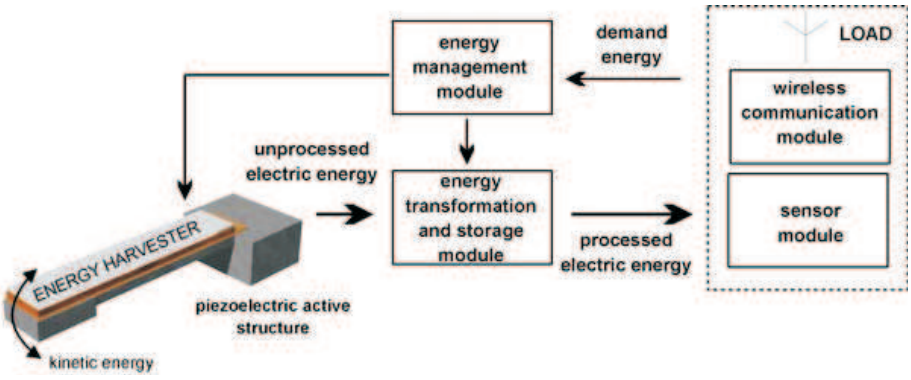

FIGURE 1.4: A concept art of the final self powered wireless sensing system for the Elba project, taken from [1].

1.4 Review of MEMS vibration energy harvester

Several reviews were published between 2006-2008 where many energy harvesters were discussed [3, 5, 7]. In [3] a general overview of various available ambient energy sources, the energy harvesting methods and fabricated devices are discussed. Where in [7] the focus is on the piezoelectric energy harvesters published between years 2003-2006. This brief review will only focus on piezoelectric MEMS energy harvesters developed in recent years.

In 2009 Elfrink *et al.* published a device [8] where the piezoelectric material aluminum nitride (AlN) was used to fabricate MEMS unimorph vibration energy harvesters. AlN has low piezoelectric constant $d_{31} = -1.1$ Cm^{-2}, however the low dielectric constant ($\epsilon_r = 10.5$) keeps its power generation figure of merit high. The low dielectric constant will normally lead to a high optimal resistive load, however with AlN thickness of only 400 nm, the load will be in the range of 0.1-1.0 MΩ. Figure 1.5 shows a cross sectional view of the harvester, the fabrication processes are done using conventional silicon microtechnology. Potassium hydroxide (KOH) was used to define the proof mass and the frame. The AlN film is deposited by using reactive sputtering from an aluminum (Al) target. The devices were packaged using top and bottom glass substrates with cavities, allowing the proof mass to move up to 800 μm. Figure 1.6 is a photograph showing the packaged energy harvester mounted on a printed circuit board (PCB). A maximum power output of 60 μW was measured at 2 g input acceleration at the excitation frequency of 572 Hz for an unpackaged harvester. The high power output was mainly due to the high quality factor, which is around 500. The packaging solutions used in [8] causes the high quality factor to decrease drastically to below 100 and reduces the power output more than an order of magnitude. This is due to air damping caused by the air inside the package unable to flow freely. In 2010 Elfrink *et al.* published [9] a solution to this problem by introducing vacuum packaging of the energy harvester. Top

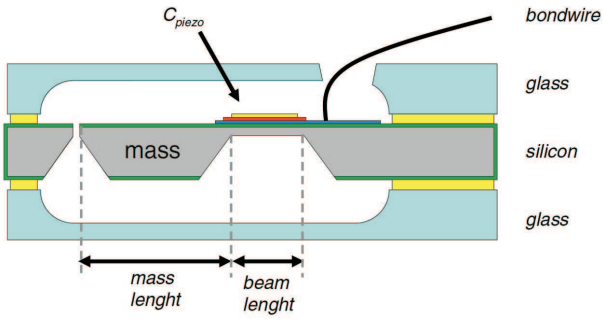

FIGURE 1.5: Cross sectional view of the aluminum nitride based energy harvester by Elfrink *et al.* taken from [8].

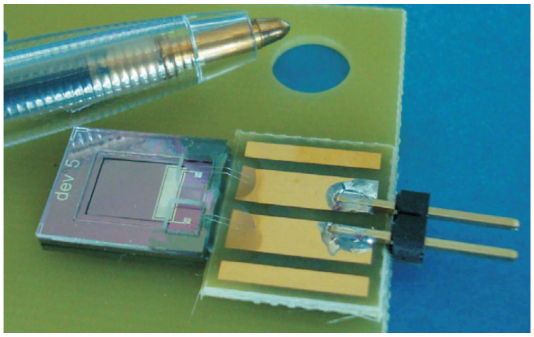

FIGURE 1.6: Photograph of the aluminum nitride based energy harvester by Elfrink *et al.* taken from [8].

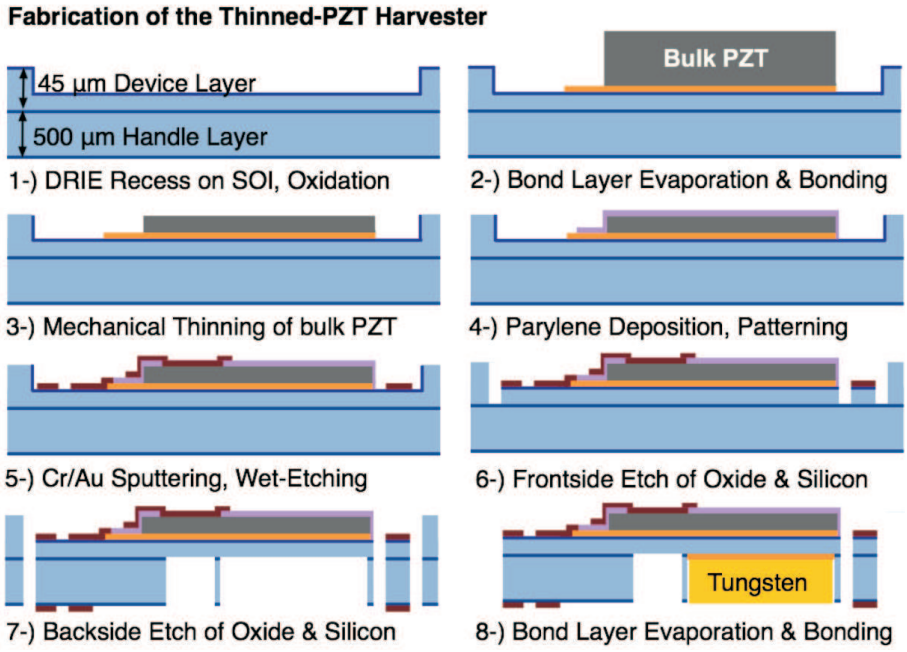

FIGURE 1.7: Cross sectional view of the thinned-PZT based energy harvester process sheme by Aktakka *et al.* taken from [10].

and bottom glass wafers and the silicon wafer are vacuum bonded in two consecutive bonding steps using SU-8 as bonding layers.

In 2011 Aktakka *et al.* published a device [10] where standard bulk PZT-5A was used to fabricate MEMS energy harvesters. The fabrication process is shown in Fig. 1.7. Bulk PZT is bonded to the device layer of the silicon on insulator (SOI) wafer by gold indium (AuIn) transient liquid phase bonding. The silicon surface is used as a stop layer for the mechanical thinning of the PZT, the hardness of silicon and high wafer-level uniformity provide excellent control. Parylene is used as an insulation layer between the top and bottom electrodes. The silicon proof mass is then hollowed out and the cavity is filled with tungsten in an attempt to decrease resonant frequency and increase power output.

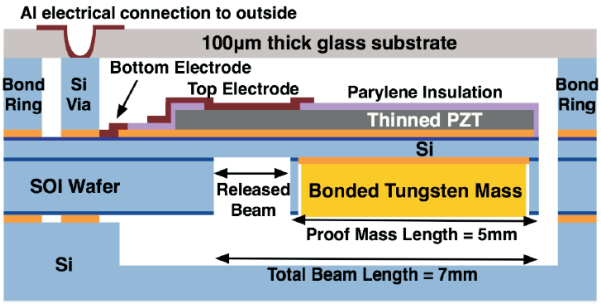

FIGURE 1.8: Cross sectional view of the packaged thinned-PZT based energy harvester by Aktakka *et al.* taken from [10].

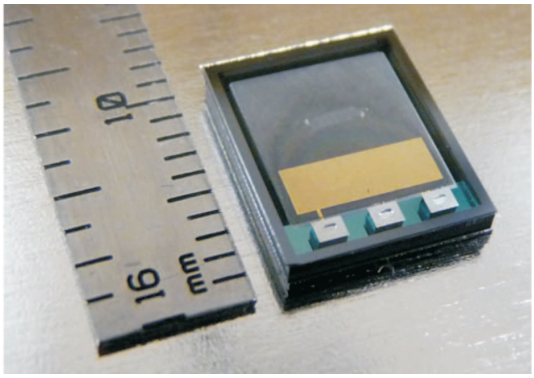

FIGURE 1.9: Photograph of the thinned-PZT based energy harvester by Aktakka *et al.* taken from [10].

A maximum power output of 205 μW was measured at 1.5 g input acceleration at the excitation frequency of 154 Hz for these kind of thinned-PZT based energy harvesters with tungsten mass.

1.5 Thesis overview

Here is a short overview of this thesis.

1.5.1 Chapter 2: Piezoelectric harvesting theory

The theory of piezoelectric materials and how it can be utilized to harvest energy will be explained. The concepts of piezoelectric unimorph and bimorph energy harvester will be discussed.

1.5.2 Chapter 3: Design and modeling

The important design considerations throughout the project will be given. The final design was achieved by extensive modeling and practical experience gained during fabrication processes.

1.5.3 Chapter 4: Process development

The current fabrication process will be given. Major improvements made during this project will be explained in detail. The serious issues encountered are bad adhesion,

fragile structures and short circuiting through the PZT layer, these issues and their solutions will be addressed.

1.5.4 Chapter 5: Characterization of the harvesters

The setup used to characterize the fabricated energy harvesters is explained. The results from the fabricated harvesters are presented and discussed.

1.5.5 Chapter 6: Packaging

Two packaging solutions are investigated, though both are deemed useful, more experimental research is need for their implementation.

1.5.6 Chapter 7: Additional topics

The non-resonant usage of the fabricated energy harvesters is investigated. Two ideas were investigated. The first idea is an impact solution, where a ball is encapsulated in a tube and will be moving due to external vibration. Each time the ball hits the end of the tube the impact energy will excite the harvester on the other side, and harvest energy. The second idea is to create a bistable system using permanent magnets. Each change in the force direction from the external vibration will move the cantilever from one stable position to another, this will cause the cantilever to be excited, and harvest energy.

1.5.7 Chapter 8: Conclusion and outlook

In the final chapter of this thesis the most important results obtained are summarized and concluded upon. An outlook for suggested future work both regarding energy harvesters and the overall system is given.

Chapter 2

Piezoelectric harvesting theory

2.1 Piezoelectric effect

Piezoelectric effect was first discovered in tourmaline crystals by brothers Pierre and Jacques Curie. They found that a mechanical deformation of the crystal will cause an electrical surface charge build up. Gabriel Lippmann later predicted the inverse piezoelectric effect through thermodynamic considerations, which was confirmed by the Curie brothers. Later, the same effect was observed in quartz, topaz and other crystals. It was found that in order for a material to be piezoelectric a polar axes must exist within the crystal structure [11]. Deformations along the polar axis will give rise to an electrical dipole caused by the displacements of the electrical charge in the chemical bond. The deformations along the polar axis can be caused by force parallel to the the axis, which is called the longitudinal effect as it is shown in Fig. 2.1a). Figure 2.1b) shows the transversal effect where the force is perpendicular to the axis.

2.1.1 Piezoelectric ceramics

Polycrystalline ceramics such as PZT can also exhibit piezoelectric property, even though such behavior should only exist on microscopic level. By applying an external electric field to the material the polarizations can be reorientated thus creating the macroscopic piezoelectric behavior. In modern days piezoelectric ceramics are most commonly used in the industry. Especially PZT due to its flexibility, low manufacturing cost and good piezoelectric and dielectric properties. PZT has the Perovskite structure, as it is shown in Fig. 2.2. When the temperature is above the curie temperature the Perovskite crystal structure has a cubic lattice structure and is not piezoelectric. If the temperature falls below the curie temperature the cubic lattice structure changes to the tetragonal

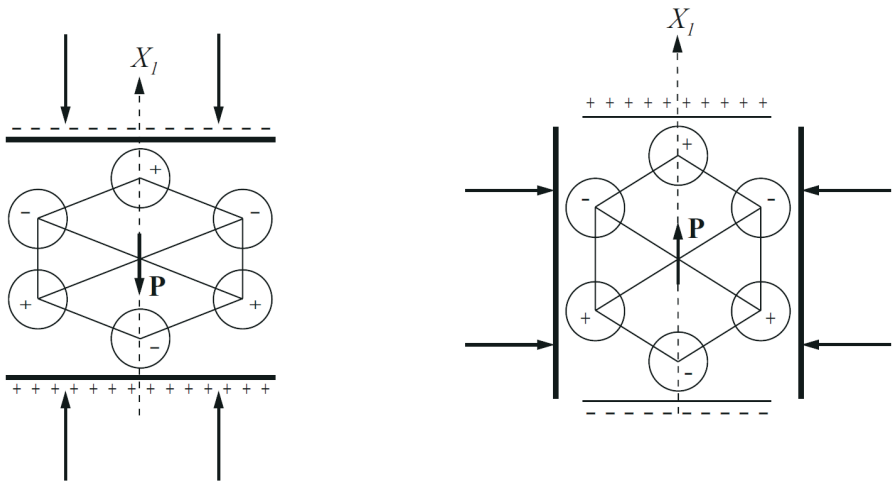

FIGURE 2.1: A sketch of how quartz crystal structure exhibits direct piezoelectric effect. a) Longitudinal piezoelectric effect. b) Transversal piezoelectric effect. Drawing is taken from [11].

lattice structure, causing a spontaneous polarization where a dipole moment is created. The dipole moment in the crystal lattice effects other lattices thus generates a region of same dipole orientation, these regions are called domains. In each grain there will be several domains separated by domain walls as it is shown in Fig. 2.3. The tetragonal lattice structure materials have two kinds of domains, the 90° domain and the 180° domain. The 90° domains have polarization directions perpendicular with respect to their neighboring domains, whereas 180° domains have the opposite polarization direction as its neighboring domains. By apply a sufficient external electric field the domains will reoriented to the direction of the electric field, as it is shown in Fig. 2.3. The reorientation process differs dependent on which domain type. The reorientation process in 180° domains happens gradually until all domains are aligned with the electric field. The reorientation process in 90° domains happens in two steps, first the antiparallel polarized domains reorientates and become perpendicular to the electric field, thereafter a 90° domain is recreated, this time the professed direction is along the electric field. Notice the polarization directions are partially determined by the crystal axis and due to the anisotropic nature of polycrystalline materials a 100% alignement of the polarization to the electric field will not be possible. The polarization process can be seen in Fig. 2.4, where the ceramic starts at position A with zero electric field and no macroscopic polarization. Next, an electric field is applied and the ceramic gains a polarization along the electric field, thus moved to position B. Finally, the eletric field is removed and the polarization is partially kept, see position C.

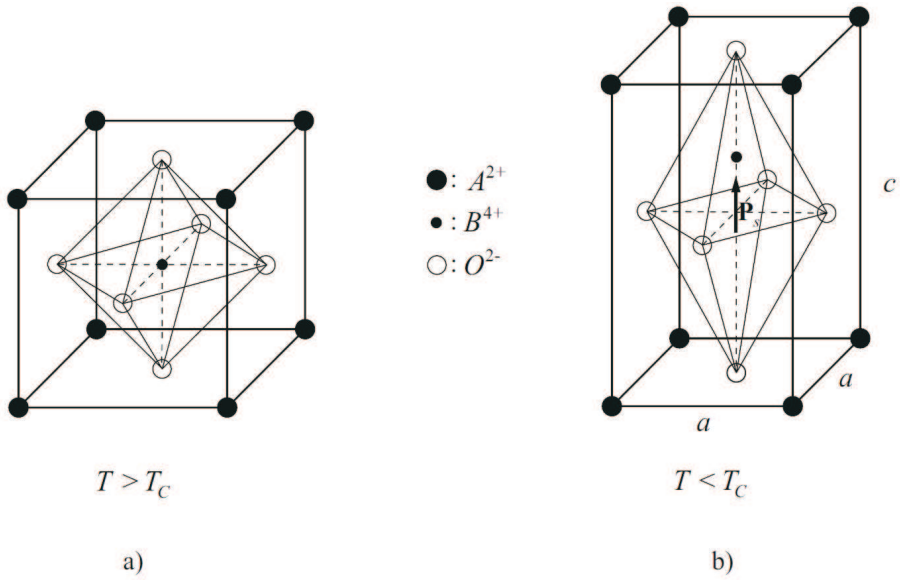

FIGURE 2.2: The Perovskite structure, where a) is when the temperature is above the curie temperature b) is when the temperature is below. For PZT in particular, A represents the positive charged lead ion, B represents the charged titanium or zirconium ion and O represent the negatively charged oxygen ion. Drawing is taken from [11].

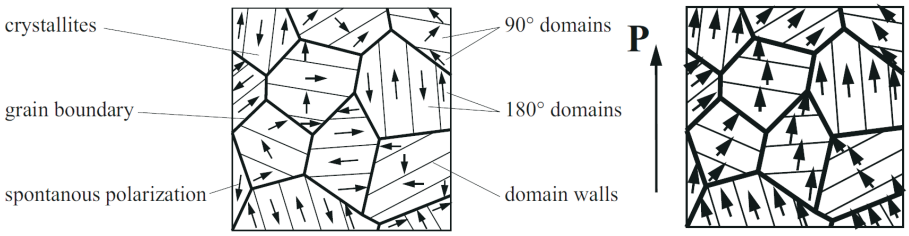

FIGURE 2.3: A sketch shows the crystallites, domains and grains of PZT. To the left the material is a unpolarized, to the right the material is polarized along P. The drawing is modified from [11].

2.2 Piezoelectric constitutive equations

By using the theory of energy density of elastic deformation and the thermodynamics of deformation the linear constitutive equations can be derived in tensor index notation as

$$dD_i = \left(\frac{\partial D_i}{\partial E_k}\right)_T dE_k + \left(\frac{\partial D_i}{\partial T_{kl}}\right)_E dT_{kl} \tag{2.1}$$

$$dS_{ij} = \left(\frac{\partial S_{ij}}{\partial E_k}\right)_T dE_k + \left(\frac{\partial S_{ij}}{\partial T_{kl}}\right)_E dT_{kl}, \tag{2.2}$$

where E is the electric field, D is the electric displacement field, T is stress and S is strain. Notice here that the electric field and electric displacement field are first order tensors and the stress and strain are matrices, and thus second order tensors. The subscript T means that the derivative is taken at zero or constant stress, similarly the subscript E means zero or constant electric field. The constitutive equations in their

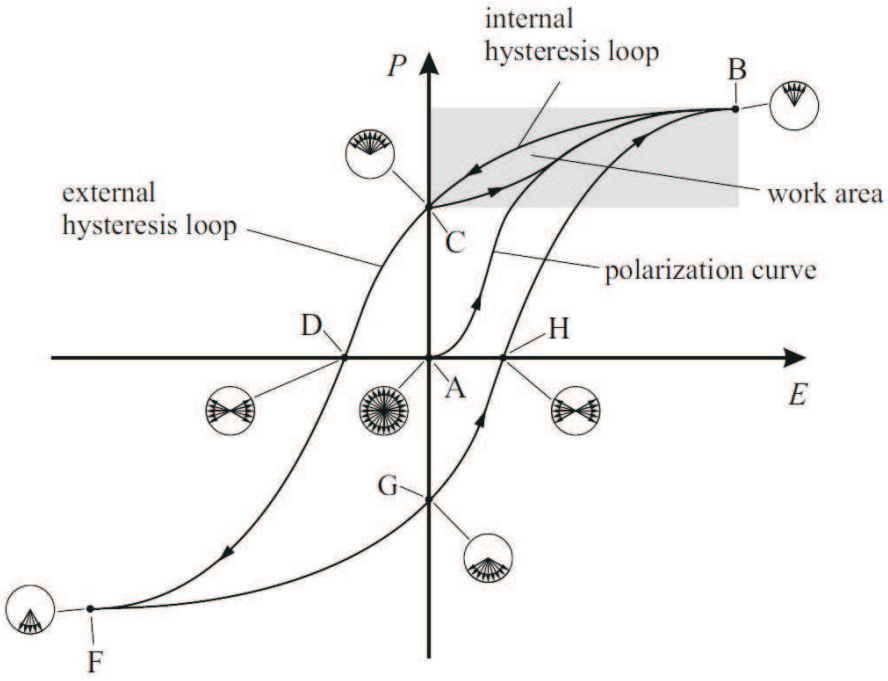

FIGURE 2.4: A hysteresis curve of the polarization P and the applied electric field E. Drawing is taken from [11].

closed form yields

$$D_i = \varepsilon_{ik}^T E_k + d_{ikl} T_{kl} \tag{2.3}$$

$$S_{ij} = d_{ijk} E_k + s_{ijkl}^E T_{kl}, \tag{2.4}$$

where the aforementioned subscripts are now changed to superscript and parameters in tensor notation shown in Table 2.1 is used. Notice that permittivity is a second order tensor, the piezoelectric coefficient and the piezoelectric constant are third order tensors and the elastic compliance and stiffness coefficient are fourth order tensors.

TABLE 2.1: Tensor notation of piezoelectric material parameters.

Material parameter	notation	unit
permittivity	$\varepsilon_{ik} = \frac{\partial D_i}{\partial E_k}$	F/m
piezoelectric coefficient	$d_{ikl} = \frac{\partial D_i}{\partial T_{kl}} = \frac{\partial S_{ij}}{\partial E_k}$	m/V
elastic compliance	$s_{ijkl} = \frac{\partial S_{ij}}{\partial T_{kl}}$	m^2/N

2.2.1 PZT

The material parameters in tensor notations can be rewritten in matrix form, as it is done in [12] for silicon. Since the polarized PZT ceramic exhibits a hexagonal crystal

symmetry, the elastic compliance matrix for PZT can be given as

$$s = \begin{pmatrix} s_{11} & s_{12} & s_{13} & 0 & 0 & 0 \\ s_{12} & s_{11} & s_{13} & 0 & 0 & 0 \\ s_{13} & s_{13} & s_{33} & 0 & 0 & 0 \\ 0 & 0 & 0 & s_{44} & 0 & 0 \\ 0 & 0 & 0 & 0 & s_{44} & 0 \\ 0 & 0 & 0 & 0 & 0 & 2(s_{11} - s_{12}) \end{pmatrix} \tag{2.5}$$

Similarly, the piezoelectric coefficient for PZT is can be described as

$$d = \begin{pmatrix} 0 & 0 & 0 & 0 & d_{15} & 0 \\ 0 & 0 & 0 & d_{15} & 0 & 0 \\ d_{31} & d_{31} & d_{33} & 0 & 0 & 0 \end{pmatrix} \tag{2.6}$$

Finally, the permittivity matrix for PZT is

$$\varepsilon = \begin{pmatrix} \varepsilon_{11} & 0 & 0 \\ 0 & \varepsilon_{22} & 0 \\ 0 & 0 & \varepsilon_{33} \end{pmatrix}. \tag{2.7}$$

Of course not all of the coefficients in the matrices are important for later modeling, the measured material parameters for PZT which will be used in later chapters are s_{11}, d_{31}, ε_{33} and density ϱ.

TABLE 2.2: The relevant material parameters of untreated as well as high pressure treated TF2100 thick film [13] are shown. For comparison material parameters for Pz26 [14], which is the bulk counterpart of TF2100, are also shown.

	d_{31} [pC/N]	$\frac{\varepsilon_{33}}{\varepsilon_0}$	s_{11} [10^{-12} m^2/N]	ϱ [10^3 kg/m^3]
TF2100	-60	600	16	6
TF2100 (pressure treated)	-89	825	14.1	7.2
Pz26 Bulk	-130	1300	14	7.7

2.3 Piezoelectric cantilever beams

It is not hard to see from the piezoelectric constitutive equations 2.3 that a high stress/strain will give rise to high current/voltage. In an attempt to maximize the power output a high stress in the piezoelectric ceramic at minimum acceleration must be achieved. Therefore the energy harvesting device should have a large proof mass and a thin cantilever beam. The optimal mass dimension will be discussed in the next chapter.

The cantilever beam can essentially be strained in two ways, pure bending or stretching. The stretching basically means that the cantilever is pulled by the external force like a simple spring. The stretching mechanism is characterized by a large force and small deflection. As it was mentioned in chapter 1, section 1.3, the available acceleration a will not likely be more that 1 g. Using rough dimensions corresponding to the current device: proof mass $m = 25$ mg, the cantilever width $W = 5.5$ mm and the cantilever thickness $h = 40$ μm yields

$$\sigma = \frac{ma}{Wh} = \frac{S}{s_{11}} \Leftrightarrow S = \frac{mas_{11}}{Wh}, \tag{2.8}$$

where s_{11} the elastic compliance of PZT. By inserting the known values a strain S less then 10^{-7} is found. Such a low strain means that an efficient harvesting mechanism based on stretching will be difficult to implement.

Pure bending means the cantilever is bended and strained in such way that the overall normal force in the x-plane is zero, *e.g.* the upper part of the cantilever beam experiences a tensile stress and the lower part experiences a compressive stress as it is shown in Fig. 2.5. The axis where the strain is zero is called neutral axis or neutral plane. The internal moment of the cantilever beam can be written as

$$M_0 = FL = W\int_{-\frac{h}{2}}^{\frac{h}{2}} \sigma z dz = W\int_{-\frac{h}{2}}^{\frac{h}{2}} \sigma_{\max}\frac{z^2}{\frac{h}{2}} dz, \tag{2.9}$$

where L is the length of the cantilever. By solving Eq. 2.9 the surface stress $\sigma_{\max}$ is found to be

$$\sigma_{\max} = 6\frac{L}{h}\frac{ma}{Wh}. \tag{2.10}$$

Using the fact that the stress is proportional to z, the average stress magnitude becomes

$$\overline{|\sigma|} = \frac{\sigma_{\max}}{2} = 3\frac{L}{h}\frac{ma}{Wh}, \tag{2.11}$$

comparing this result with Eq. 2.8 yields a geometric stress amplification of $3\frac{L}{h}$. So bending will be the favorable mechanism as long as the length is larger than the beam thickness. In the following chapters only pure bending will be considered since it will be the dominant mechanism.

2.3.1 Unimorph cantilever beams

A unimorph cantilever beam consists of an active piezoelectric layer, such as PZT, and a passive layer, like silicon, as it is shown in Fig. 2.6. The reason it is call "unimorph",

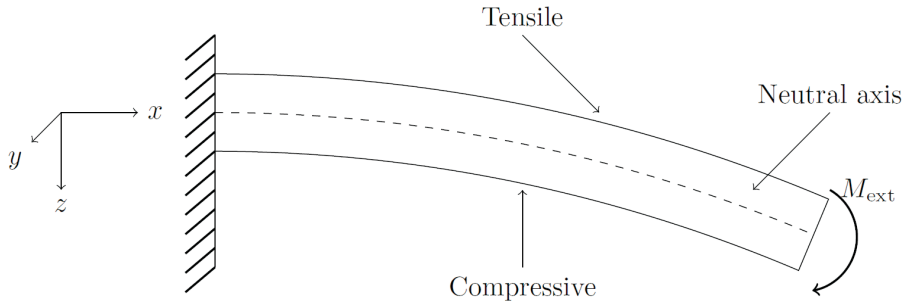

FIGURE 2.5: A sketch of a cantilever beam, which experiences an bending moment M_{ext}.

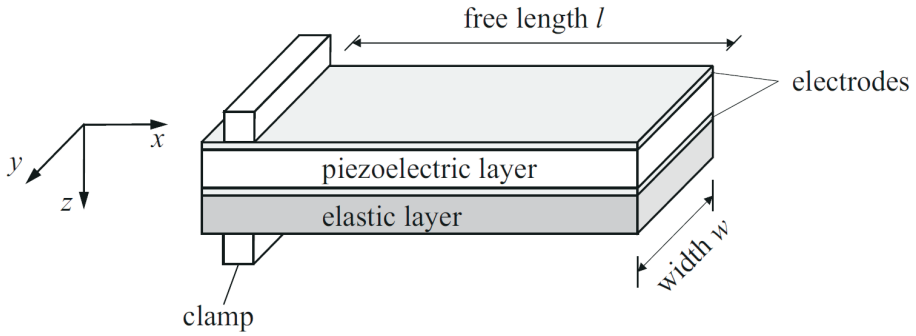

FIGURE 2.6: A sketch of unimorph cantilever beam structure [11], where the cantilever is considered double clamped. The cantilever consists of a elastic support layer, a bottom electrode layer, the piezoelectric layer and a top electrode layer.

even though there are clearly two different layers, is because only the active piezoelectric layer is counted. For an unimorph energy harvester a periodic external acceleration will cause the proof mass to move up and down. The upper active part of the cantilever will be in tensile mode when the beam is bended downward as it is shown in Fig. 2.5, and be in compressive mode when the beam is bended upward. The strain energy then collected by the electrodes creating an AC current. There are several reasons for the need of the passive layer. The passive layer can function as a mechanical support, because the active piezoelectric layer might be too soft. Of course even if the active piezoelectric layer is stiff enough the passive layer is still needed. Imagine if the cantilever beam only consist of the active piezoelectric layer with electrodes on both sides, so the polarization is perpendicular to the electrodes across the whole cantilever. Due to the nature of pure bending with compressive strain on one side and tensile strain on the other voltage generated on the electrodes will cancel each other thus no energy will be harvested. For the same reason, when optimizing the output power, it is often an advantage to have the neutral plane in the passive layer or at least be at the material junction.

2.3.2 Bimorph cantilever beams

If the active piezoelectric material is stiff enough, which is the case for PZT, it is possible to harvest energy without the passive layer. To do this an extra electrode (middle electrode) must be introduced at the position where the neutral plane is. So the piezoelectric layer is basically divided into two layers, thus the name: "Bimorph". To harvest energy one can polarize the layer in the same directions or in opposite directions. If they are polarized in the same direction, the two layers can be considers as two separate energy harvesters with the same ground which is the middle electrode. This is often called parallel bimorph. The parallel bimorph configuration is characterized by having high current, low voltage and low optimal resistive load. If the two layers are polarized in opposite directions using the middle electrode, the external load can just be connected between the bottom and top electrode. This is often called series bimorph. The series bimorph configuration is characterized by having low current, high voltage and high optimal resistive load. Due to advantage offered by higher voltage for the later rectifier circuit, which will convert the AC current to DC current, mainly the series bimorph configuration will be used.

Chapter 3

Design and modeling

In this chapter a model for the bimorph energy harvester model is derived using the piezoelectric constitutive equations, Euler's beam equation and lumped element model. From the model the power output of the harvesters can be estimated. The model for the bimorph harvester is considered a more generalized model to the unimorph harvester, therefore the model for the unimorph harvester is not presented. The optimal electrode size, cantilever shape and proof mass size are also discussed in this chapter, which the final design solution is partially based upon.

3.1 Model for the bimorph energy harvester

In this section a model for the bimorph energy harvester will be derived. A cross sectional sketch of the model is shown in 3.1. The PZT bimorph beam of length L is attached to a rigid frame in the one end and a proof mass in the other. The bimorph beam is fitted with three electrodes, a top electrode with the potential V_t, a bottom electrode with the potential V_b and a middle electrode that is considered grounded. The beam height h between the top and middle electrode is the same as the beam height between the middle and bottom electrode. The conventional Cartesian coordinate system is introduced here and the $z-$ axis is pointing downwards and has its origin in the middle electrode in agreement with the conventions used in most literature [12]. The proof mass has its center of gravity ℓ from the end of the bimorph beam. Assuming the mass is symmetric and isotropic in density the length of the proof mass $L_\mathrm{m} = 2\ell$. Notice that in this model the center of gravity for the proof mass in $z-$ axis considered zero, this will not be the case for the fabricated harvesters, since the effect is considered of limited importance. The resulting force from the input acceleration acting on the proof mass is F.

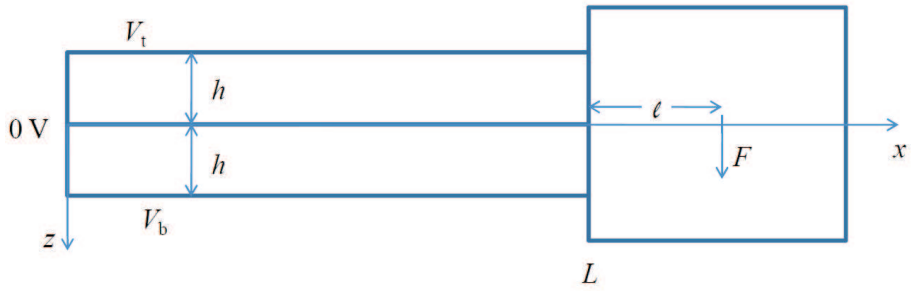

FIGURE 3.1: A cross sectional sketch of the bimorph energy harvester model is shown. The bimorph PZT beam consists of two PZT layers which both are assumed to have the thickness h. At $x = 0$ the beam is rigidly clamped to a frame, and at $x = L$ a proof mass (of mass m) is Fixed to the beam. The center of gravity for the proof mass is at $x = L + \ell$, where $\ell = L_m/2$ is half of the length of the proof mass.

In order to derive a transducer model for the harvester the relation between the macroscopic electrical quantities to the mechanical quantities need to to be found as well as the coupling of these to the proof mass.

3.1.1 Piezoelectric bimorph transducer model

Since the beam is rigidly clamped at $x = 0$, the boundary condition for the bending displacement w becomes

$$w(x = 0) = 0 \tag{3.1}$$

$$w'_x(x = 0) = 0, \tag{3.2}$$

and for the elongation u

$$u(x = 0) = 0. \tag{3.3}$$

Due to symmetry the neutral plane during bending is at the middle electrode, since both PZT layers have the same thickness h. The electrodes in the model are considered to be infinitely thin and thus they by themselves do not contribute to the mechanical part of the model. Since the length dimensions of the electrodes are considered to be significantly larger than the PZT thickness only the electric field normal to electrodes E_z is non-zero, and since the electric displacement is divergence free ($\nabla \cdot \mathbf{D} = 0$) because there are no free space charges in the PZT film, it can be assumed that $\partial_z D_z = 0$. The stress in the beam is assumed to be unidirectional so only T_1 (σ_{xx} in some literature) is non-zero, since the small shear stress T_5 (or τ_{xz}) can be neglected. The two PZT layers are assumed to be poled in opposite directions.

Since the electric field and the stress both are unidirectional the simplest materials relations are obtained if electric displacement and strain are expressed as functions of the electric field and the stress, as it is expressed in the piezoelectric constitutive equations 2.3

$$D_3 = \varepsilon_{33} E_3 + d_{31} T_1 \tag{3.4}$$

$$S_1 = d_{31} E_3 + s_{11} T_1, \tag{3.5}$$

where only the three material parameters s_{11}, d_{31} and ε_{33} are needed. Note that the superscripts in Eq. 3.4 are omitted. Using that fact that the strain can be induced by either bending and elongation

$$S_1 = u'_x - z w''_{xx}, \tag{3.6}$$

the Eqs. 3.4 can be rewritten as

$$T_1 = \frac{1}{s_{11}} S_1 - \frac{d_{31}}{s_{31}} E_3 \tag{3.7}$$

$$D_3 = \frac{d_{31}}{s_{11}} S_1 + \varepsilon_{33} \left(1 - \frac{d_{31}^2}{s_{11}\varepsilon_{33}}\right) E_3 = \frac{d_{31}}{s_{11}} S_1 + \varepsilon_{33} \left(1 - k_{31}^2\right) E_3, \tag{3.8}$$

where $k_{31} = \sqrt{d_{31}^2/(s_{11}\varepsilon_{33})}$ is the piezoelectric coupling coefficient.

3.1.1.1 Charge and current

In order to find the charge on the electrodes, the D_3 value should first be calculated for the beam system. This is done by integrating Eq. 3.8 across the top PZT beam

$$\int_{-h}^{0} D_3 \mathrm{d}z = \frac{d_{31}}{s_{11}} \int_{-h}^{0} S_1 \,\mathrm{d}z + \varepsilon_{33} \left(1 - k_{31}^2\right) \int_{-h}^{0} E_3 \,\mathrm{d}z \Rightarrow \tag{3.9}$$

$$h D_3 = \frac{d_{31}}{s_{11}} h u'_x + \frac{d_{31}}{s_{11}} \frac{h^2}{2} w''_{xx} + \varepsilon_{33} \left(1 - k_{31}^2\right) V_\mathrm{t}, \tag{3.10}$$

where Eq. 3.4 and the definition of the electric potential and the divergence free electric displacement was used. Using this the charge on the top electrode Q_t can be calculated

using Gauss' law

$$Q_\mathrm{t} = \int\int D_3 \mathrm{d}y\mathrm{d}x = W\int D_3 \mathrm{d}x \Leftrightarrow \tag{3.11}$$

$$Q_\mathrm{t} = W\int_0^L \left(\frac{d_{31}}{s_{11}}u'_x + \frac{d_{31}}{s_{11}}\frac{h}{2}w''_{xx} + \varepsilon_{33}\left(1-k_{31}^2\right)\frac{V_\mathrm{t}}{h}\right)\mathrm{d}x \Leftrightarrow \tag{3.12}$$

$$Q_\mathrm{t} = W\frac{d_{31}}{s_{11}}u(L) + \frac{d_{31}}{s_{11}}\frac{Wh}{2}w'_x(L) + \frac{\varepsilon_{33}\left(1-k_{31}^2\right)WL}{h}V_\mathrm{t} \Leftrightarrow \tag{3.13}$$

$$Q_\mathrm{t} = \gamma_\mathrm{t}u(L) + \Gamma_\mathrm{t}w'_x(L) + C_\mathrm{t}V_\mathrm{t}, \tag{3.14}$$

where $C_\mathrm{t} = \varepsilon_{33}\left(1-k_{31}^2\right)WL/h$ is the capacitance of the top layer at constant strain, $\Gamma_\mathrm{t} = \left(d_{31}/s_{11}\right)_\mathrm{t} Wh/2$ is is the coupling coefficient from cantilever end slope to charge, while $\gamma_\mathrm{t} = W\left(d_{31}/s_{11}\right)_\mathrm{t}$ is the coupling coefficient from cantilever end elongation to charge. Note, the subscript t for top layer has been added to indicate that the sign of $\left(d_{31}/s_{11}\right)_\mathrm{t}$ is dependent on poling direction of the top layer.

The charge on the bottom electrode $Q_\mathrm{b} = W\int_0^L(-D_3)\,\mathrm{d}x$ is similarly calculated

$$Q_\mathrm{b} = \gamma_\mathrm{b}u(L) + \Gamma_\mathrm{b}w'_x(L) + C_\mathrm{b}V_\mathrm{b}, \tag{3.15}$$

where $C_\mathrm{b} = \varepsilon_{33}\left(1-k_{31}^2\right)WL/h$ is the capacitance of the bottom layer at constant strain, $\Gamma_\mathrm{b} = \left(d_{31}/s_{11}\right)_\mathrm{b} Wh/2$ is the coupling coefficient from cantilever end slope to charge, while $\gamma_\mathrm{b} = -W\left(d_{31}/s_{11}\right)_\mathrm{b}$ is the coupling coefficient from cantilever end elongation to charge. Note the sign change compared to the similar expression for the top beam. As above the subscript b for bottom layer has been added to indicate that the sign of $\left(d_{31}/s_{11}\right)_\mathrm{b}$ is dependent on poling direction of the bottom layer.

If both PZT films are poled in the same direction $\Gamma_\mathrm{b} = \Gamma_\mathrm{t}$ while $\gamma_\mathrm{b} = -\gamma_\mathrm{t}$. If the PZT films are poled in opposite directions $\Gamma_\mathrm{b} = -\Gamma_\mathrm{t}$ while $\gamma_\mathrm{b} = \gamma_\mathrm{t}$.

From Eqs. 3.14 and 3.15 the currents to the top and bottom electrodes are

$$I_\mathrm{t} = \dot{Q}_\mathrm{t} = \gamma_\mathrm{t}\dot{u}(L) + \Gamma_\mathrm{t}\dot{w}'_x(L) + C_\mathrm{t}\dot{V}_\mathrm{t} \tag{3.16}$$

$$I_\mathrm{b} = \dot{Q}_\mathrm{b} = \gamma_\mathrm{b}\dot{u}(L) + \Gamma_\mathrm{b}\dot{w}'_x(L) + C_\mathrm{b}\dot{V}_\mathrm{b}, \tag{3.17}$$

where $\dot{X}$ is a shorthand for $\partial X/\partial t$.

3.1.1.2 Force and moment

The total normal force in the $x-$direction F_x on the cantilever cross section is obtained from

$$F_x = W\int_{-h}^{h} T_1\,\mathrm{d}z = W\int_{-h}^{h}\left(\frac{1}{s_{11}}S_1 - \frac{d_{31}}{s_{11}}E_3\right)\mathrm{d}z \tag{3.18}$$

$$F_x = \frac{2hW}{s_{11}}u_x' - W\left[\int_0^h \frac{d_{31}}{s_{11}}E_3\,\mathrm{d}z + \int_{-h}^{0}\frac{d_{31}}{s_{11}}E_3\,\mathrm{d}z\right] \tag{3.19}$$

$$F_x = \frac{2hW}{s_{11}}u_x' + W\left(\frac{d_{31}}{s_{11}}\right)_{\mathrm{b}}V_{\mathrm{b}} - W\left(\frac{d_{31}}{s_{11}}\right)_{\mathrm{t}}V_{\mathrm{t}} \tag{3.20}$$

$$F_x = \frac{2hW}{s_{11}}u_x' - \gamma_{\mathrm{b}}V_{\mathrm{b}} - \gamma_{\mathrm{t}}V_{\mathrm{t}},, \tag{3.21}$$

where the coefficients γ_{b} and γ_{t} also serve as coupling coefficients from applied voltages to normal force.

The bending moment M (moment around the $y-$axis) is obtained from

$$M = W\int_{-h}^{h} zT_1\,\mathrm{d}z = W\int_{-h}^{h}\left(\frac{1}{s_{11}}zS_1 - \frac{d_{31}}{s_{11}}zE_3\right)\mathrm{d}z \tag{3.22}$$

$$M = -\frac{W}{s_{11}}w_{xx}''\int_{-h}^{h} z^2\,\mathrm{d}z - W\left(\frac{d_{31}}{s_{11}}\right)_{\mathrm{b}}\int_0^h zE_3\,\mathrm{d}z - W\left(\frac{d_{31}}{s_{11}}\right)_{\mathrm{t}}\int_{-h}^{0} zE_3\,\mathrm{d}z \tag{3.23}$$

$$M = -\frac{2Wh^3}{3s_{11}}w_{xx}'' + \left(\frac{d_{31}}{s_{11}}\right)_{\mathrm{b}}\frac{Wh}{2}V_{\mathrm{b}} + \left(\frac{d_{31}}{s_{11}}\right)_{\mathrm{t}}\frac{Wh}{2}V_{\mathrm{t}} \tag{3.24}$$

$$M = -YIw_{xx}'' + \Gamma_{\mathrm{b}}V_{\mathrm{b}} + \Gamma_{\mathrm{t}}V_{\mathrm{t}} \tag{3.25}$$

where $YI = 2Wh^3/(3s_{11})$ is the product of Young's modulus and area moment of inertia, that usually appear in Euler's beam equation. Note, in the two integrals of the electric field a contribution to the electric field that may vary linearly with z has been ignored.

If external forces are absent the total moment will be zero and the deflection of the beam and its slope becomes

$$w(x) = \frac{1}{2}x^2\frac{\Gamma_{\mathrm{b}}V_{\mathrm{b}} + \Gamma_{\mathrm{t}}V_{\mathrm{t}}}{YI},\ \text{and}\ w_x'(x) = x\frac{\Gamma_{\mathrm{b}}V_{\mathrm{b}} + \Gamma_{\mathrm{t}}V_{\mathrm{t}}}{YI}, \tag{3.26}$$

and at the cantilever end L

$$w(L) = \frac{1}{2}L^2\frac{\Gamma_{\mathrm{b}}V_{\mathrm{b}} + \Gamma_{\mathrm{t}}V_{\mathrm{t}}}{YI},\ \text{and}\ w_x'(L) = L\frac{\Gamma_{\mathrm{b}}V_{\mathrm{b}} + \Gamma_{\mathrm{t}}V_{\mathrm{t}}}{YI}. \tag{3.27}$$

Similarly, the normal force F_x in Eq. 3.21 is also zero, solving that for the the longitudinal displacement yields

$$u(x) = x\frac{s_{11}}{2hW}\left(\gamma_\mathrm{b}V_\mathrm{b} + \gamma_\mathrm{t}V_\mathrm{t}\right) \tag{3.28}$$

$$u(L) = L\frac{s_{11}}{2hW}\left(\gamma_\mathrm{b}V_\mathrm{b} + \gamma_\mathrm{t}V_\mathrm{t}\right). \tag{3.29}$$

3.1.2 Beam dynamics

From Newtons Second Law and the longitudinal force balance the longitudinal wave equation can be derived as

$$2hW\varrho\ddot{u} = \frac{\partial F_x}{\partial x} = \frac{\partial}{\partial x}\left(\frac{2hW}{s_{11}}u'_x - \gamma_\mathrm{b}V_\mathrm{b} - \gamma_\mathrm{t}V_\mathrm{t}\right) = \frac{2hW}{s_{11}}u''_{xx} \tag{3.30}$$

$$\ddot{u} = \frac{1}{\varrho s_{11}}u''_{xx}, \tag{3.31}$$

which can be solved using boundary conditions imposed by the applied load at $x = L$ and the zero displacement condition $u(x = 0) = 0$.

In the same manner the partial differential equation that govern vertical displacement is obtained from a vertical force balance

$$2hW\varrho\ddot{w} - \frac{\partial^2 M}{\partial x^2} = 2hW\varrho\ddot{w} - \frac{\partial^2}{\partial x^2}\left(-YIw''_{xx} + \Gamma_\mathrm{b}V_\mathrm{b} + \Gamma_\mathrm{t}V_\mathrm{t}\right) = q \tag{3.32}$$

$$2hW\varrho\ddot{w} + YIw''''_{xxxx} = q, \tag{3.33}$$

where ϱ is the mass density, while q is the distributed force load per unit length. This equation may be solved with the zero slope and zero deflection boundary conditions at $x = 0$ combined with boundary conditions imposed at $x = L$.

Due to the large magnitude of the proof mass attached to the beam end compared to the cantilever mass, it is sufficiently accurate to use static deflection profiles for the cantilever beam, and thus ignore the mass of the cantilever.

3.1.2.1 Static deflection

The static deflection with a force load F at the centre of gravity of the proof mass as shown in Fig. 3.1, i.e. at $x = L + \ell$ is obtained from $YIw''''_{xxxx} = 0$, with $w(0) = 0$, $w'(0) = 0$, $M'_x(L) = F$ and $M(L) = -\ell F$. With Eq. 3.25 ($M = -YIw''_{xx} + \Gamma_\mathrm{b}V_\mathrm{b} + \Gamma_\mathrm{t}V_\mathrm{t}$) the boundary conditions at the cantilever end become $w'''_{xxx}(L) = -F/(YI)$ and

$w''_{xx}(L) = \ell F/(YI) + (\Gamma_\mathrm{b} V_\mathrm{b} + \Gamma_\mathrm{t} V_\mathrm{t})/(YI)$. The solution is

$$w(x) = \frac{\Gamma_\mathrm{b} V_\mathrm{b} + \Gamma_\mathrm{t} V_\mathrm{t}}{2YI} x^2 + \frac{F}{2YI} x^2 \left(L + \ell - \frac{1}{3} x \right) \tag{3.34}$$

$$w'_x(x) = \frac{\Gamma_\mathrm{b} V_\mathrm{b} + \Gamma_\mathrm{t} V_\mathrm{t}}{YI} x + \frac{F}{YI} x \left(L + \ell - \frac{1}{2} x \right), \tag{3.35}$$

and at the end of the beam the deflection and slope become

$$w(L) = \frac{\Gamma_\mathrm{b} V_\mathrm{b} + \Gamma_\mathrm{t} V_\mathrm{t}}{2YI} L^2 + \frac{F}{2YI} L^2 \left(\frac{2}{3} L + \ell \right) \tag{3.36}$$

$$w'_x(L) = \frac{\Gamma_\mathrm{b} V_\mathrm{b} + \Gamma_\mathrm{t} V_\mathrm{t}}{YI} L + \frac{F}{YI} L \left(\frac{1}{2} L + \ell \right). \tag{3.37}$$

Since the proof mass may be considered perfectly rigid, the deflection w_c at the center of the proof mass becomes $w_c = w(L) + \ell w'_x(L)$

$$w_c = \frac{\Gamma_\mathrm{b} V_\mathrm{b} + \Gamma_\mathrm{t} V_\mathrm{t}}{2YI} L \left(L + 2\ell \right) + \frac{F}{3YI} L \left(L^2 + 3L\ell + 3\ell^2 \right). \tag{3.38}$$

If a characteristic length Λ is defined, where

$$\Lambda = \frac{2\left(L^2 + 3L\ell + 3\ell^2 \right)}{3\left(L + 2\ell \right)}, \tag{3.39}$$

then the center of mass deflection may be write as

$$w_c = \frac{L\left(L^2 + 3L\ell + 3\ell^2 \right)}{3YI} \left(F + \frac{\Gamma_\mathrm{b} V_\mathrm{b} + \Gamma_\mathrm{t} V_\mathrm{t}}{\Lambda} \right) = \frac{1}{k} \left(F + \frac{\Gamma_\mathrm{b} V_\mathrm{b} + \Gamma_\mathrm{t} V_\mathrm{t}}{\Lambda} \right) \tag{3.40}$$

where k is the effective spring constant of the beam seen from the center of mass for the proof mass

$$k = \frac{3YI}{L\left(L^2 + 3L\ell + 3\ell^2 \right)}. \tag{3.41}$$

From the static deflection profile at zero voltage a relation between the end slope and the center of mass deflection

$$w_c = w(L) + \ell w'_x(L) = \left(\ell + \frac{w(L)}{w'_x(L)} \right) w'_x(L) = \Lambda w'_x(L), \tag{3.42}$$

and thus the electrode short circuit charges ΔQ_t and ΔQ_b (and thus currents) due to end slope obtained from Eqs. 3.14 and 3.15 may be expressed as

$$\Delta Q_\mathrm{t} = \Gamma_\mathrm{t} w'_x(L) = \frac{\Gamma_\mathrm{t}}{\Lambda} w_c, \text{ and } \Delta Q_\mathrm{b} = \Gamma_\mathrm{b} w'_x(L) = \frac{\Gamma_\mathrm{b}}{\Lambda} w_c \tag{3.43}$$

$$\Delta I_\mathrm{t} = \Gamma_\mathrm{t} \dot{w}'_x(L) = \frac{\Gamma_\mathrm{t}}{\Lambda} \dot{w}_c, \text{ and } \Delta I_\mathrm{b} = \Gamma_\mathrm{b} \dot{w}'_x(L) = \frac{\Gamma_\mathrm{b}}{\Lambda} \dot{w}_c \tag{3.44}$$

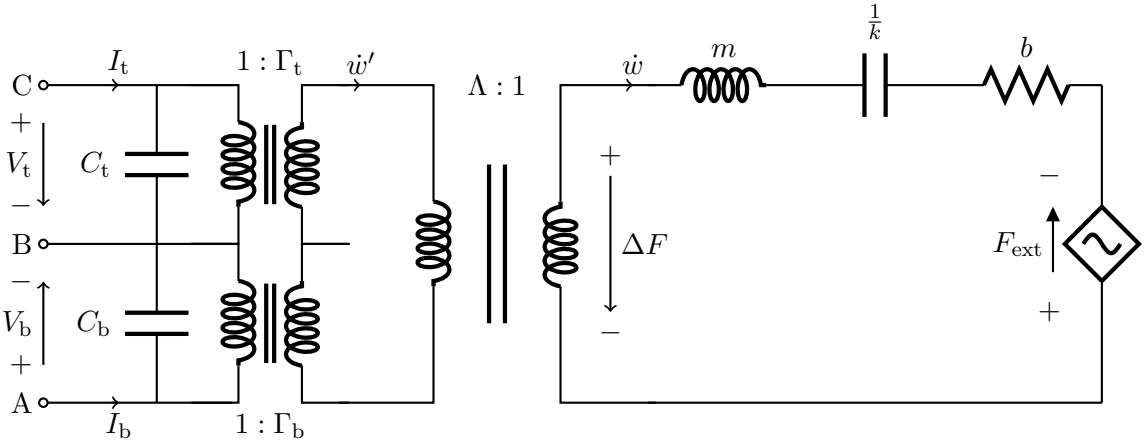

FIGURE 3.2: Equivalent circuit model of the energy harvester. The piezoelectric bimorph transducer is represented by two capacitors C_t and C_b and two transformers that relate bending moments to voltages and slope rates to currents. The mechanical side is represented by the proof mass m, the equivalent spring constant k, a mechanical loss resistor b, and the external force F_{ext}. Recalculation from center of mass velocity to slope rate and bending moment to force is done by a transformer with the transformation ratio $\Lambda : 1$.

3.1.3 Equivalent circuit model

The set of equations derived above may be represented graphically in the equivalent circuit model shown in Fig. 3.2. The piezoelectric bimorph transducer is represented by two capacitors C_t and C_b and two transformers that relate bending moments to voltages and slope rates to currents. The mechanical side is represented by the proof mass m, the equivalent spring constant k, a mechanical loss resistor b, and the external force F_{ext}. Recalculation from center of mass velocity to slope rate and bending moment to force is done by a transformer with the transformation ratio $\Lambda : 1$. A summary of the device equations that this circuit represents is

$$I_t = \dot{Q}_t = \Gamma_t \dot{w}'_x(L) + C_t \dot{V}_t, \text{ and } I_b = \dot{Q}_b = \Gamma_b \dot{w}'_x(L) + C_b \dot{V}_b, \tag{3.45}$$

$$\Delta M = \Gamma_b V_b + \Gamma_t V_t \tag{3.46}$$

$$\dot{w}_c = \Lambda \dot{w}'_x(L), \text{ and } \Delta M = \Lambda \Delta F \tag{3.47}$$

$$F_{ext} + \Delta F = m\ddot{w}_c + b\dot{w}_c + kw_c. \tag{3.48}$$

The circuit model may be simplified by concatenation of transformers as shown in Fig. 3.3, so the device equations becomes

$$I_t = \frac{\Gamma_t}{\Lambda}\dot{w}_c + C_t \dot{V}_t, \text{ and } I_b = \frac{\Gamma_b}{\Lambda}\dot{w}_c + C_b \dot{V}_b, \tag{3.49}$$

$$F_{ext} + \frac{\Gamma_t}{\Lambda}V_t + \frac{\Gamma_b}{\Lambda}V_b = m\ddot{w}_c + b\dot{w}_c + kw_c. \tag{3.50}$$

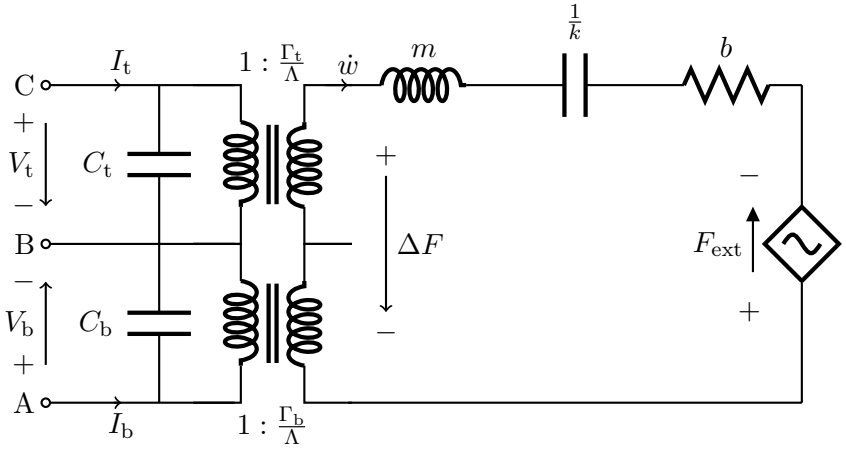

FIGURE 3.3: Simplified equivalent circuit model.

For analysis of the network it is useful to use Laplace (and Fourier) transformed quantities and a generalized impedance concept, where electrical impedance Z_e is the ratio of Laplace transformed voltage to current and mechanical impedance Z_m the ratio of Laplace transformed force to velocity. It follows that the mechanical impedance of the mass spring damper network is

$$Z_\mathrm{m} = sm + b + k/s \tag{3.51}$$

where s is the complex frequency ($s = j\omega$). At the mechanical resonance frequency $\omega_0 = \sqrt{k/m}$ the mechanical impedance assumes its minimum value b.

With resistive loads R_Lt and R_Lb on the electrical side the electrical impedances are

$$Z_\mathrm{et} = R_\mathrm{Lt}/(1 + sC_\mathrm{t}R_\mathrm{Lt}) \tag{3.52}$$

$$Z_\mathrm{eb} = R_\mathrm{Lb}/(1 + sC_\mathrm{b}R_\mathrm{Lb}). \tag{3.53}$$

The electrical impedances may be transformed to the mechanical side, where the equivalent mechanical impedances are

$$Z_\mathrm{mt} = Z_\mathrm{et}\left(\frac{\Gamma_\mathrm{t}}{\Lambda}\right)^2 = \left(\frac{\Gamma_\mathrm{t}}{\Lambda}\right)^2 \frac{R_\mathrm{Lt}}{(1 + sC_\mathrm{t}R_\mathrm{Lt})} \tag{3.54}$$

$$Z_\mathrm{mb} = Z_\mathrm{eb}\left(\frac{\Gamma_\mathrm{b}}{\Lambda}\right)^2 = \left(\frac{\Gamma_\mathrm{b}}{\Lambda}\right)^2 \frac{R_\mathrm{Lb}}{(1 + sC_\mathrm{b}R_\mathrm{Lb})}. \tag{3.55}$$

The output voltages may now easily be calculated

$$V_{\mathrm{t}} = \left(\frac{\Lambda}{\Gamma_{\mathrm{t}}}\right) F_{\mathrm{ext}} \frac{Z_{\mathrm{mt}}}{Z_{\mathrm{mt}} + Z_{\mathrm{mb}} + Z_{\mathrm{m}}} = \left(\frac{\Lambda}{\Gamma_{\mathrm{t}}}\right) \frac{F_{\mathrm{ext}}}{1 + Z_{\mathrm{mb}}/Z_{\mathrm{mt}} + Z_{\mathrm{m}}/Z_{\mathrm{mt}}} \tag{3.56}$$

$$V_{\mathrm{b}} = \left(\frac{\Lambda}{\Gamma_{\mathrm{b}}}\right) F_{\mathrm{ext}} \frac{Z_{\mathrm{mb}}}{Z_{\mathrm{mt}} + Z_{\mathrm{mb}} + Z_{\mathrm{m}}} = \left(\frac{\Lambda}{\Gamma_{\mathrm{b}}}\right) \frac{F_{\mathrm{ext}}}{1 + Z_{\mathrm{mt}}/Z_{\mathrm{mb}} + Z_{\mathrm{m}}/Z_{\mathrm{mb}}} \tag{3.57}$$

3.1.3.1 Identical PZT layers

If the two PZT layers are equal, *i.e.* ($C_{\mathrm{t}} = C_{\mathrm{b}} = C_0$), but oppositely poled ($\Gamma_{\mathrm{t}} = -\Gamma_{\mathrm{b}} = \Gamma$) as the series bimorph configuration, and the two load resistors are also equal in size or even just a single resistor $R_{\mathrm{L}} = R_{\mathrm{Lt}} + R_{\mathrm{Lb}}$ then the total electrical impedance is

$$Z_{\mathrm{e}} = Z_{\mathrm{et}} + Z_{\mathrm{eb}} = R_{\mathrm{L}}/(1 + sC_0R_{\mathrm{L}}/2), \tag{3.58}$$

$$Z_{\mathrm{em}} = Z_{\mathrm{e}} \left(\frac{\Gamma}{\Lambda}\right)^2 = \left(\frac{\Gamma}{\Lambda}\right)^2 \frac{R_{\mathrm{L}}}{1 + sC_0R_{\mathrm{L}}/2} \tag{3.59}$$

and the total output voltage $V_{\mathrm{out}} = V_{\mathrm{t}} - V_{\mathrm{b}}$ becomes

$$V_{\mathrm{out}} = \left(\frac{\Lambda}{\Gamma}\right) F_{\mathrm{ext}} \frac{Z_{\mathrm{em}}}{Z_{\mathrm{em}} + Z_{\mathrm{m}}} = \left(\frac{\Lambda}{\Gamma}\right) F_{\mathrm{ext}} \frac{1}{1 + Z_{\mathrm{m}}/Z_{\mathrm{em}}} \tag{3.60}$$

$$= \left(\frac{\Lambda}{\Gamma}\right) F_{\mathrm{ext}} \frac{R_{\mathrm{L}} \left(\frac{\Gamma}{\Lambda}\right)^2}{R_{\mathrm{L}} \left(\frac{\Gamma}{\Lambda}\right)^2 + (sm + b + k/s)\,(1 + sC_0R_{\mathrm{L}}/2)}. \tag{3.61}$$

The output power is $P = |V_{\mathrm{out}}|^2_{\mathrm{RMS}} / R_{\mathrm{L}}$

$$P = |F_{\mathrm{ext}}|^2_{\mathrm{RMS}} \frac{R_{\mathrm{L}} \left(\frac{\Gamma}{\Lambda}\right)^2}{\left| R_{\mathrm{L}} \left(\frac{\Gamma}{\Lambda}\right)^2 + (sm + b + k/s)\,(1 + sC_0R_{\mathrm{L}}/2) \right|^2} \tag{3.62}$$

The power is maximized at frequencies between the mechanical resonant frequency $\omega_0 = \sqrt{k/m}$ and the anti-resonant frequency $\omega_a = \omega_0 \sqrt{1 + \frac{2}{kC_0} \left(\frac{\Gamma}{\Lambda}\right)^2}$. At ω_0 the maximum power is obtained for quite low load resistances (the device is operated close to short-circuit conditions) while at ω_a the maximum power is obtained for rather high load resistances (the device is operated close to open-circuit conditions).

At the mechanical resonance frequency ($\omega_0 = \sqrt{k/m}$), where the mechanical impedance reduces to b, the power becomes

$$P = |F_{\text{ext}}|^2_{\text{RMS}} \frac{R_{\text{L}} \left(\frac{\Gamma}{\Lambda}\right)^2}{\left| R_{\text{L}} \left(\frac{\Gamma}{\Lambda}\right)^2 + b(1 + j\omega_0 C_0 R_{\text{L}}/2) \right|^2} \tag{3.63}$$

$$= |F_{\text{ext}}|^2_{\text{RMS}} \frac{R_{\text{L}} \left(\frac{\Gamma}{\Lambda}\right)^2}{\left(R_{\text{L}} \left(\frac{\Gamma}{\Lambda}\right)^2 + b \right)^2 + (b\omega_0 C_0 R_{\text{L}}/2)^2} \tag{3.64}$$

The optimum load resistance R_{Lopt} that maximizes the output power at the mechanical resonant frequency may be obtained from differentiation of Eq. 3.64, and the result is

$$R_{\text{Lopt}}(\omega_0) = b \left(\frac{\Lambda}{\Gamma}\right)^2 \frac{1}{\sqrt{1 + \left(\frac{\Lambda}{\Gamma}\right)^4 b^2 \omega_0^2 C_0^2/4}} \simeq b \left(\frac{\Lambda}{\Gamma}\right)^2 \tag{3.65}$$

The optimum power at the mechanical resonant frequency is then obtained as

$$P_{\text{opt}}(\omega_0) = \frac{|F_{\text{ext}}|^2_{\text{RMS}}}{4b} \frac{4}{2 + \sqrt{4 + \left(\frac{\Lambda}{\Gamma}\right)^4 b^2 \omega_0^2 C_0^2}} \simeq \frac{|F_{\text{ext}}|^2_{\text{RMS}}}{4b}, \tag{3.66}$$

where the first factor $|F_{\text{ext}}|^2_{\text{RMS}} / (4b)$ is the maximum available power from the vibrational mechanical source. Due to the capacitance of the PZT layers the harvester output power is slightly less than the maximum available power.

The input impedance is

$$Z_{in} = \frac{2}{sC_0} \frac{(sm + b + k/s) \left(\frac{\Lambda}{\Gamma}\right)^2}{\frac{2}{sC_0} + (sm + b + k/s) \left(\frac{\Lambda}{\Gamma}\right)^2} =$$

$$Z_{in} = \frac{2}{sC_0} \frac{sm + b + k/s}{\frac{2}{sC_0} \left(\frac{\Gamma}{\Lambda}\right)^2 + sm + b + k/s} \tag{3.67}$$

which is seen to be almost entirely capacitive except in a marrow frequency range near the mechanical resonance frequency. The denominator of Eq. 3.67 becomes minimum at the antiresonance frequency

$$\omega_a = \sqrt{\left(k + \frac{2}{C_0} \left(\frac{\Gamma}{\Lambda}\right)^2\right) \frac{1}{m}} = \omega_0 \sqrt{1 + \frac{2}{kC_0} \left(\frac{\Gamma}{\Lambda}\right)^2} \tag{3.68}$$

where the input impedance then becomes

$$Z_{\text{in}}(\omega_a) = \frac{2}{j\omega_a C_0} \frac{b - \frac{2}{j\omega_a C_0} \left(\frac{\Gamma}{\Lambda}\right)^2}{b} = \frac{2}{j\omega_a C_0} + \frac{2}{b\omega_a^2 C_0^2} \left(\frac{\Gamma}{\Lambda}\right)^2. \tag{3.69}$$

where the magnitude of the real part is significantly larger that the imaginary part, therefore the optimum load resistance becomes

$$R_{\mathrm{Lopt}}(\omega_a) \simeq \frac{2}{b\omega_a^2 C_0^2}\left(\frac{\Gamma}{\Lambda}\right)^2. \tag{3.70}$$

The open circuit voltage at the anti-resonance frequency is thus

$$V_{\mathrm{out_{oc}}}(\omega_a) = \left(\frac{\Lambda}{\Gamma}\right) F_{\mathrm{ext}} \frac{\frac{2}{C_0}\left(\frac{\Gamma}{\Lambda}\right)^2}{j\omega_a b} = \left(\frac{\Gamma}{\Lambda}\right) F_{\mathrm{ext}} \frac{2}{j\omega_a C_0 b}, \tag{3.71}$$

and an output power approximately equal to the available power

$$P_{\mathrm{opt}}(\omega_a) \simeq \frac{|F_{\mathrm{ext}}|^2_{\mathrm{RMS}}}{4b}. \tag{3.72}$$

3.1.3.2 Numerical values

The maximum available power $P_{\mathrm{ava}} = |F_{\mathrm{ext}}|^2_{\mathrm{RMS}} / (4b)$ may be recast in terms of the quality factor and the external RMS accelaration a, since $|F_{\mathrm{ext}}|_{\mathrm{RMS}} = ma$, and thus

$$P_{\mathrm{ava}} = \frac{(ma)^2}{4b} = \frac{ma^2 Q}{4\omega_0} \tag{3.73}$$

For 1 g acceleration at 250 Hz and a proof mass of 25 mg the available power becomes $P_{\mathrm{ava}} \simeq Q \times 0.38\ \mu\mathrm{W}$, and thus at $Q = 100$ the available power is $P_{\mathrm{ava}} \simeq 38\ \mu\mathrm{W}$.

3.2 Optimal mass length

Since the energy harvester is limited in size, the proof mass size becomes a interesting optimization topic. There is obviously an optimal length for the mass compared to the total available length of the total cantilever length including the mass length, *i.e.* $L+L_{\mathrm{m}}$. The ratio of the mass length to the total cantilever length is defined as α. If $\alpha = 0\%$ then there is no proof mass and if $\alpha = 100\%$ there is no cantilever, either of the two will result in good harvester design. The best design will therefore be somewhere in between. But first one must define what is the best design, the two critiria are high power and low resonant frequency. The angular resonant frequency is defined as $\omega_0 = \sqrt{\frac{k}{m}}$ where the spring constant k is given in Eq. 3.41. Recast k and m in the appropriate geometric and material parameters and using the fact that the mass length L_{m} is proprotional to

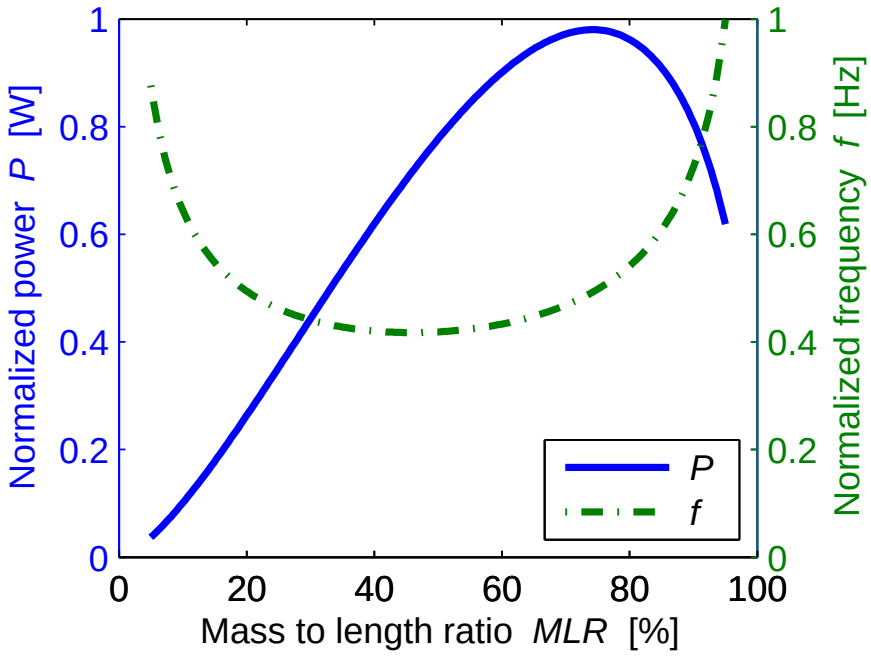

FIGURE 3.4: The normalized power output and normalized resonant frequency as a function of the mass to total length ratio α.

α and the beam length L is proprotional to $1-\alpha$ yields

$$f_0 \propto \frac{1}{\sqrt{\alpha(1-\alpha)((1-\alpha)^2+\frac{3}{2}\alpha(1-\alpha)+\frac{3}{4}\alpha^2)}}. \tag{3.74}$$

The minimum for Eq. 3.74, *i.e.* the resonant frequency is found for $\alpha = 46\%$. Similarly, the same can be done for the power output derived in Eq. 3.73 where

$$P_{\text{ava}} \propto \sqrt{\alpha^3(1-\alpha)((1-\alpha)^2+\frac{3}{2}\alpha(1-\alpha)+\frac{3}{4}\alpha^2)}. \tag{3.75}$$

The maximum output power is achieved at $\alpha = 74\%$. The normalized resonant frequency and power output is calculated as a function of α and is shown in Fig. 3.4.

Comsol Multiphysics is used to compute the resonant frequency for a cantilever beam with a mass attached where α is near 46%, the resulting resonant frequency is shown in Table 3.1. Note that in the Comsol calculation the lowest resonant frequency is observed at $\alpha = 50\%$. This is believed to be caused by the rotation of the proof mass along with beam bending.

TABLE 3.1: The calculated resonant frequencies using Comsol Multiphysics on an cantilever beam anchored at one end and a mass attached at the other for different α values.

α [%]	Resonant frequency
45	333.70
46	333.24
47	332.91
48	332.68
49	332.55
50	332.54
51	332.63
52	332.82
53	333.13
54	333.55
55	334.08

3.2.1 Rotation of the proof mass

The deflection w_c of the proof mass is accompanied by a rotation of the mass through the angle $\theta \simeq w_x'(L)$ around the center of mass. As a result the total kinetic energy $\mathcal{T}$ is

$$\mathcal{T} = \frac{1}{2} m \left(\dot{w}_c\right)^2 + \frac{1}{2} \mathcal{J} \left(\dot{w}_x'(L)\right)^2 = \frac{1}{2} m \left(\dot{w}_c\right)^2 \left[1 + \frac{\mathcal{J}}{m} \left(\frac{\dot{w}_x'(L)}{\dot{w}_c}\right)^2\right], \tag{3.76}$$

where $\mathcal{J}$ is the moment of inertia of the mass around the $y-$axis through the center of mass. The added kinetic energy from the rotation will lower the resonant frequency of the energy harvester.

As a first approximation the relation $w_c = \Lambda w_x'(L)$ can be used to estimate the effect of rotation. Thus, the kinetic energy becomes

$$\mathcal{T} \simeq \frac{1}{2} m \left(\dot{w}_c\right)^2 \left[1 + \frac{\mathcal{J}}{m\Lambda^2}\right]. \tag{3.77}$$

If the proof mass is assumed to be long and slender $\mathcal{J}/m \simeq L_m^2/12 = \ell^2/3$, and thus

$$\frac{\mathcal{J}}{m\Lambda^2} \simeq \frac{1}{3}\frac{\ell^2}{\Lambda^2} = \frac{3}{4}\frac{\ell^2 \left(L + 2\ell\right)^2}{\left(L^2 + 3L\ell + 3\ell^2\right)^2}. \tag{3.78}$$

An effective mass can be written as

$$m_{\text{eff}} = m\left(1 + \frac{\mathcal{J}}{m\Lambda^2}\right) \simeq m\left(1 + \frac{3}{4}\frac{\ell^2 \left(L + 2\ell\right)^2}{\left(L^2 + 3L\ell + 3\ell^2\right)^2}\right), \tag{3.79}$$

as a first order correction for the effect of rotation. In the case of $\alpha = 50\%$ the effective mass is 7% higher than the real mass. Taking the effective mass into account the resonant

frequency

$$f_0 = \frac{1}{\sqrt{\alpha(1-\alpha)((1-\alpha)^2 + \frac{3}{2}\alpha(1-\alpha) + \frac{3}{4}\alpha^2)}} \cdot \frac{1}{\sqrt{(1 + \frac{3}{4}\frac{(1+\frac{1}{2}\alpha)^2}{((1-\alpha)^2+\frac{3}{2}\alpha(1-\alpha)+\frac{3}{4}\alpha)^2})}}, \tag{3.80}$$

the lowest resonant frequency in that case is achieved at $\alpha = 58\%$, however several rough assumptions were made so the result need to be taken with a grain of salt. Nevertheless this might explained the discrepency between the analytical and the Comsol solution. In the light of these results the α values of 50% and 70% were implemented in the later design and fabricated, one is aimed to achieved a low resonant frequency and the other is aimed for higher power output.

3.3 Trapezoidal shaped beams

The trapezoidal shaped beams instead of the a rectangular beam was suggested by various sources [15], therefore they were investigated and later fabricated. The idea of using a trapezoidal shaped cantilever beam is to ensure an uniform distribution of the stress in the cantilever beam, as it is shown in Fig. 3.5 and 3.6, where a Comsol simulation of two different shaped cantilever beams, which were anchored at the one end and attached to a proof mass at the other. The stress T_1 is induced by an external body load, and the surface stress can be seen. These simulations clearly shows that the trapezoidal beam has less stress variation across the beam. This is important since cantilever breakage happens at the point with the highest stress. To achieve high average stress in the material, thus high power density and still keeping the point with the highest stress below the yield strength of the material, a uniform stress distribution is most desirable. Therefore several trapezoidal cantilever designs were implemented and fabricated.

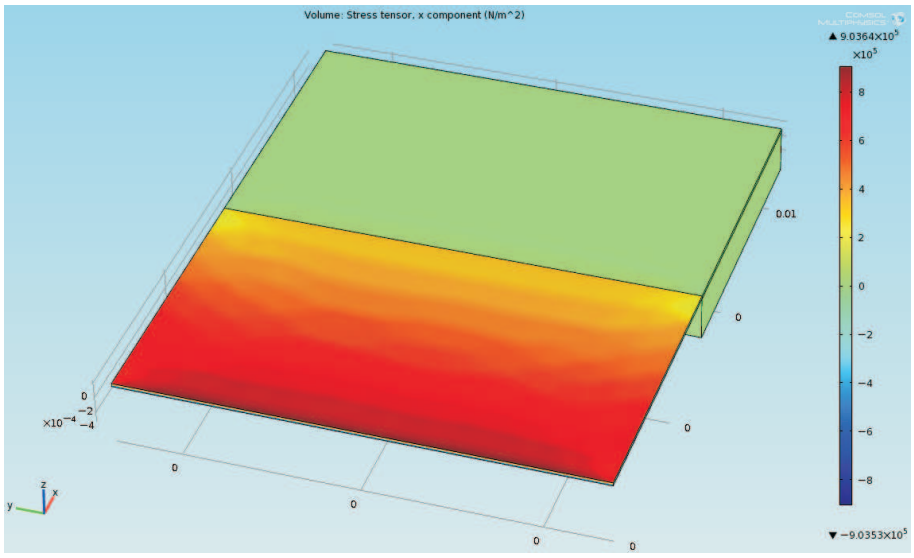

FIGURE 3.5: a Comsol simulation of a rectangular shaped cantilever beam, which anchored at the one end and attached to a proof mass at the other. The stress T_1 on the surface induced by an external body load is shown on the beam.

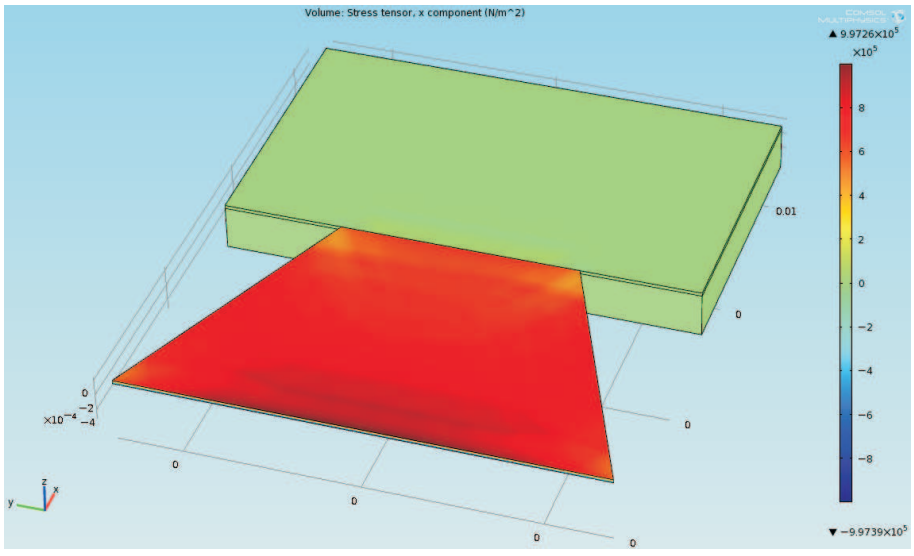

FIGURE 3.6: a Comsol simulation of a trapezoidal shaped cantilever beam, which anchored at the one end and attached to a proof mass at the other. The stress T_1 on the surface induced by an external body load is shown on the beam.

Chapter 4

Process development

In this chapter the fabrication process development will be presented. The overarching theme of the energy harvester fabrication process is yield. It is a story of how the first batch with 4 wafers has one surviving chip to wafers with full yield, see Fig. 4.1.

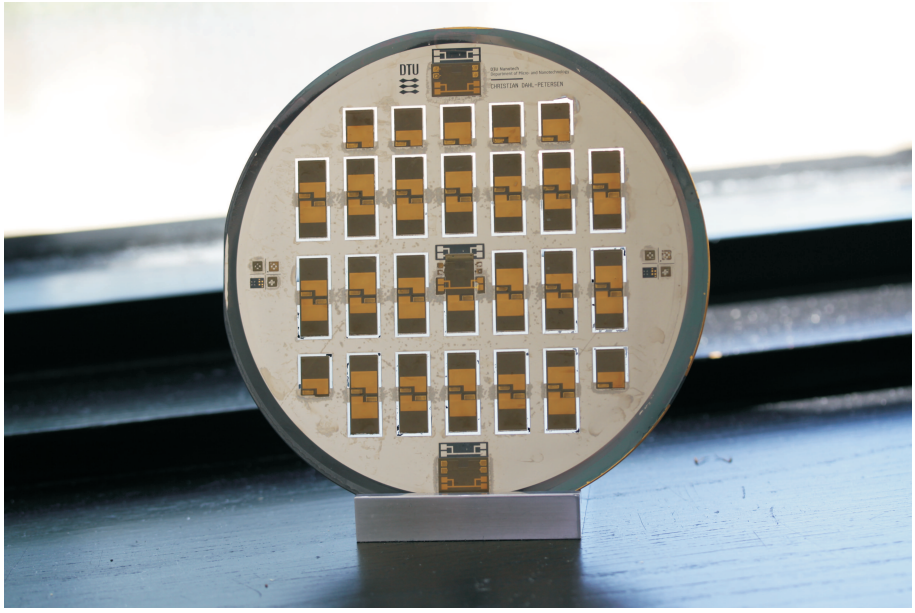

FIGURE 4.1: A photograph of a fabricated bimorph energy harvester wafer with screen printed middle electrode taken just before dicing.

4.1 Design improvements

Due to the fragile nature of the energy harvesters, the chip design is not only determined by the theory discussed in the previous chapters but also evolves with the fabrication development.

One of the original ideas was to have 2-3 narrow cantilever beams on one harvester chip. This was found to be a bad idea,

- the narrow cantilever is more prone to fracture,
- the cantilevers even with the same design can have different resonant frequency (a few hertz difference),
- the narrower cantilever does not have a higher energy density (the ratio between harvested power and PZT volume).

Therefore these designs were phased out in later fabrication iterations.

The trapezoidal shaped cantilever was also phased out due to its fragility. Furthermore with the usage of a large proof mass, *i.e.* proof mass length to the total cantilever length (including proof mass length) ratio α is more than 50%, the uniform stress argument for the trapezoidal shaped cantilever is no longer a major factor. In the final design the aforementioned mass length ratio α was set to be 50% and 70%. $\alpha = 50\%$ is an attempt to have a low resonant frequency whereas $\alpha = 70\%$ should harvest more power. The actual dimensions for the harvesters are shown in Tabel 4.1.

TABLE 4.1: Energy harvester dimensions.

General dimensions	
Frame dimensions	10×10 mm^2
Medial dimensions	< 1 mm
Cantilever width	5.5 mm
Harvesters where $\alpha = 70\%$	
Cantilever length	1.95 mm
Mass length	4.55 mm
Proof mass	ca. 36 mg
Harvesters where $\alpha = 50\%$	
Cantilever length	3.25 mm
Mass length	3.25 mm
Proof mass	ca. 25 mg
Unimorph harvesters	
Silicon thickness	20 μm
PZT thickness	15 - 30 μm
Bimorph harvesters	
Total cantilever thickness (2 $\times$ PZT thickness)	30 - 60 μm

4.2 Fabrication process

Both unimorph and bimorph energy harvesters were fabricated and their current fabrication processes will be presented. A yield of above 97% has been achieved with the

fabrication processes for both the bimorph and unimorph harvesters. 4 inch (100 mm) Silicon on insulator (SOI) wafers were used in fabrication of the harvesters. The SOI wafers have a 20 μm device layer, a 1 μm buried oxide layer and a 500 - 525 μm handle layer.

4.2.1 Overview of the unimorph energy harvester fabrication process

First, an overview of the fabrication of the unimorph energy harvester will be given, then the detail of etch steps will be presented. The general fabrication scheme of the unimorph energy harvester is to use the device layer of the SOI wafer as the passive layer of the cantilever beam. Part of the handle layer should be etched to form proof mass and chip frame.

A cross sectional view of the currently used fabrication scheme of the unimorph energy harvester is shown in Fig. 4.2. The starting point is the aforementioned SOI wafer, see Fig. 4.2(a). First, a 1 μm thick silicon dioxide is thermally grown on the SOI wafer Fig. 4.2(a), and then a 170 nm thick silicon nitride is deposited using low pressure chemical vapor deposited (LPCVD), see Fig. 4.2(b). The nitride is removed on the front side and patterned on the back side using conventional UV lithography processes, see Fig. 4.2(c). A Pt bottom electrode is deposited on the front side of the wafer and patterned, see Fig. 4.2(d), followed by screen printing and sintering of the PZT thick film layer, see Fig. 4.2(e), the Au top electrode is deposited through a prefabricated shadow mask, see Fig. 4.2(f). The oxide on the backside is etched in bHF, while the front side of the SOI wafer is protected. The backside of the SOI wafer is then etched in KOH until the buried oxide layer is reached and then the buried oxide layer is removed in bHF, see Fig. 4.2(g). Finally, the trench is etched in reactive ion etch (RIE), releasing the cantilevers, see Fig. 4.2(h). Last, the wafer is diced and the PZT thick film is polarized by applying an electric field between the bottom and top electrodes at an elevated temperature.

One of the most significant fabrication improvements for the energy harvesters is the change from etching the membrane using the deep reactive ion etch (DRIE) tool to using a KOH etch process, which is discussed in [16, 17].

One of the earlier versions of the unimorph energy harvester fabrication process will be quickly sketched. The starting point is the same, an SOI wafer with a 20 μm device layer, a 1 μm thick buried oxide layer and a 525 μm thick handle layer. The thickness of the device layer defines the thickness of the silicon part of the cantilever. The frame and the proof mass are defined with a DRIE process from the back side of the wafer. The DRIE tool used is the STS Pegasus with the same etch parameters used for the aforementioned

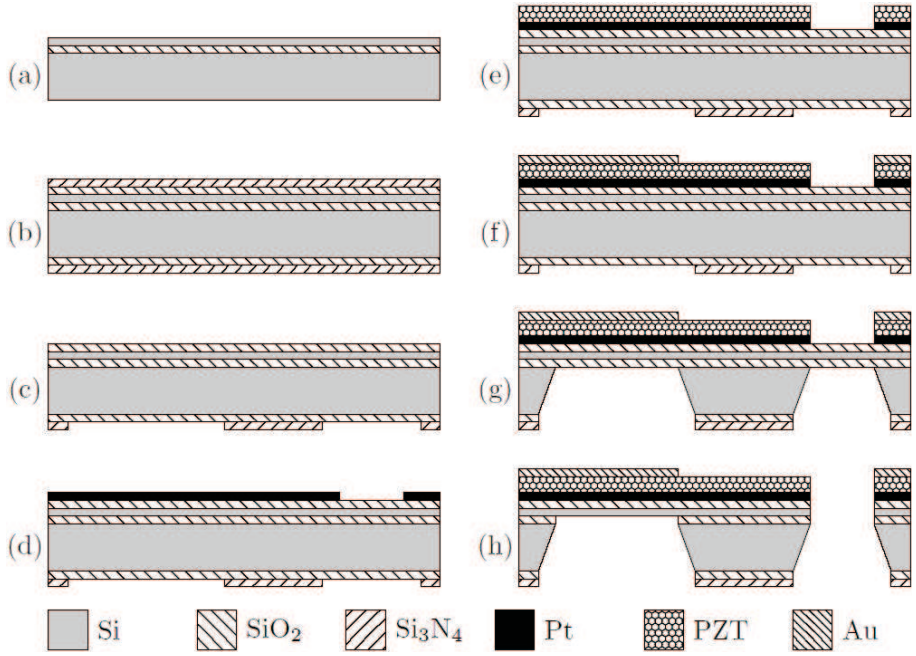

FIGURE 4.2: A cross sectional sketch of the process flow for the unimorph energy harvester. First, a 1 μm thick silicon dioxide is thermally grown on a SOI wafer (a), and then a 170 nm thick silicon nitride is deposited using LPCVD (b). The nitride is removed on the front side and patterned on the back side using conventional UV lithography processes (c). A Pt bottom electrode is deposited on the front side of the wafer and patterned (d), followed by screen printing and sintering of the PZT thick film layer (e), the Au top electrode is deposited through a prefabricated shadow mask (f). The oxide on the backside is etched in bHF, while the front side of the SOI wafer is protected. The backside of the SOI wafer is then etched in KOH until the buried oxide layer is reached and then the buried oxide layer is removed in bHF (g). Finally, the trench is etched in RIE, releasing the cantilevers (h).

shadow mask etch, shown in Table 4.7. The buried oxide layer is used as an etch stop layer and thus the etched depth is 525 μm. An RCA clean [18] is performed and a 1 μm silicon oxide layer is thermally grown. The 50 nm Ti and 500 nm Pt bottom electrode is deposited by e-beam evaporation. The bottom electrode layer is patterned by etching in a solution of H_2O:HCl:HNO_3 (8:7:1) at 85°C with a 10 μm thick AZ4562 photoresist layer as masking material. Next, a PZT thick film is screen printed on the wafer by MMS. Notice that since the membrane etch is already done at this stage, the screen printing process is made difficult. When the paste is pressed onto the membrane the membrane has a tendency to curve, causing a non uniform distribution of the paste. This will result in less uniform film thickness. Furthermore the high pressure treatment to condense the film will often result in the breakage of the membrane as it was discussed in [13]. Many attempts have been made to circumvent this issue, one example is the use of silicone to support the membrane during the screen printing and the later high pressure treatment. The used silicone molds are shown in Fig. 4.3. However this method was not ideal, when separating the silicone from the wafer there is a tendency for the membrane to stick to the silicone, as it can be seen from one of the molds in Fig. 4.3. Furthermore

there are silicone residuals left on the wafers that are very difficult to remove, as it can be seen in Fig. 4.4.

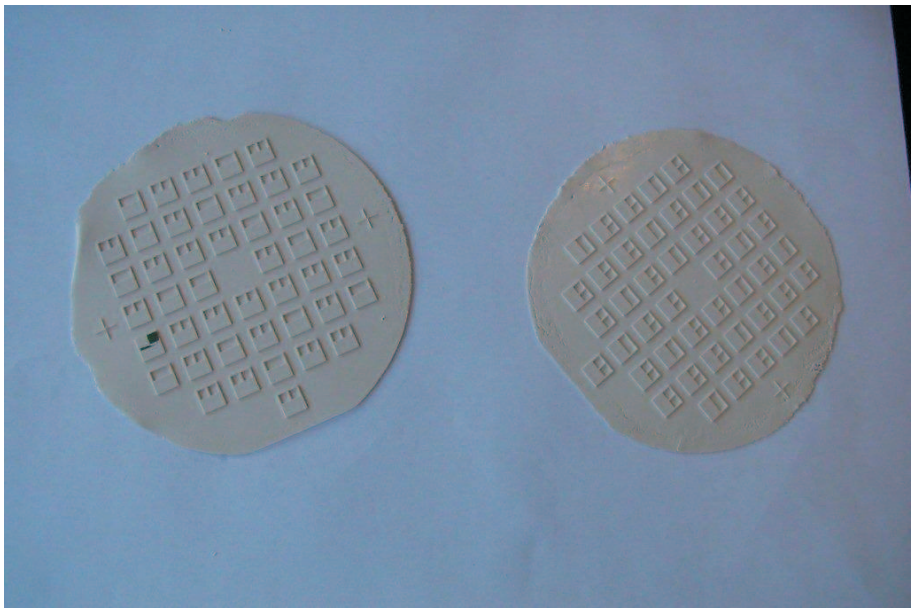

FIGURE 4.3: A photograph of two silicone molds used to protect the silicon membrane during screen printing and high pressure treatment.

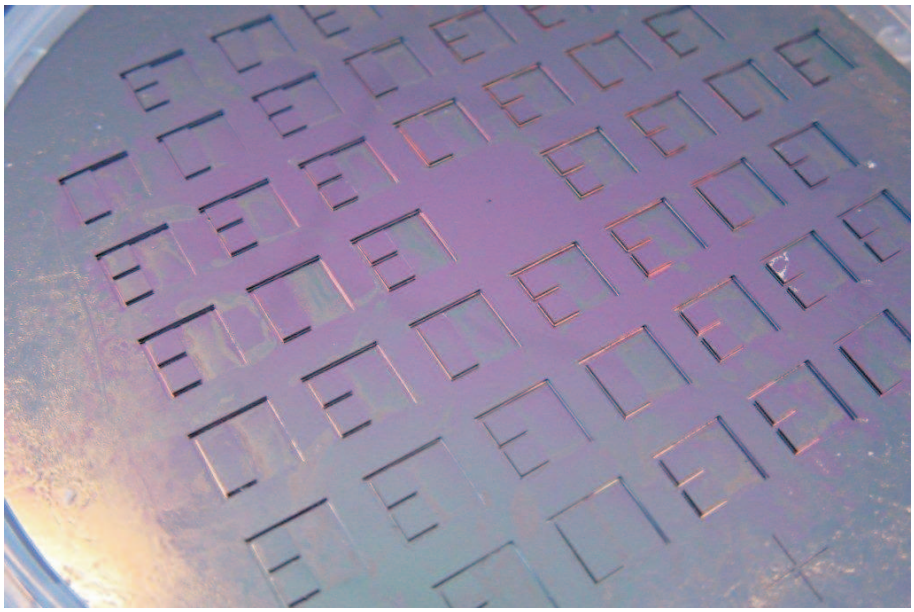

FIGURE 4.4: A photograph showing the silicone residuals left on the wafer after screen printing and high pressure treatment.

So, at this stage if the high pressure is used high chip loss would be expected, if the high pressure treatment is not used the piezoelectric property of the thick film would be less desirable, as it is discussed in [19]. After thick film is sintered, a 500 nm Au top electrode is deposited by e-beam evaporation and defined by a lift-off process. However,

the use of ultrasound in the acetone bath, which is necessary for a clean lift-off, often causes the membranes to break, thus reducing the yield. Next, the wafers are patterned on the front and etched in bHF, so that the buried oxide under the membrane and the aforementioned contaminated oxide in the trench can be removed. Finally, the wafer is etched in the RIE tool with parameters shown in Table 4.2, so the silicon trenches are etched to release the cantilevers.

TABLE 4.2: The silicon etching parameters used in the RIE tool.

RIE	Silicon
SF_6 gas flow [sccm]	32
O_2 gas flow [sccm]	8
Pressure [mTorr]	80
RF power [W]	30

The major issue with the old process is that the DRIE process happens at a very early stage, before screen printing and metal deposition. It would be ideal if the process could be moved to a later stage, *e.g.* after the top electrode deposition. However, PZT is not an allowed material in the STS Pegasus DRIE tool, due to fear of contamination. Furthermore, the non flat surface of the wafer after PZT is screen printed will cause leakage of the cooling gas in the STS tool.

Introduction of the KOH etching process made it possible to move the membrane etch process to a much later stage of the fabrication process. This eliminates the aforementioned problems related to screen printing and high pressure treatment of the thick film. Since the KOH etch process is a wet process, the front side of the wafer must be protected, this is done using the AMMT wet etch holder.

4.2.2 Detailed description of the current unimorph energy harvester fabrication process

In the following a detailed description the fabrication process is presented.

4.2.2.1 Oxidation

First, a 1 μm silicon oxide is thermally grown in a furnace, see Fig. 4.2(b). The oxidation parameters used in the furnace are shown in Table 4.3. This layer has two purposes. First, it is a sacrificial layer protecting the silicon beneath from small amount of PZT contamination. All areas where PZT is intended are protected by a Pt diffusion barrier, but unintended contamination of other surface areas, *e.g.* the trench are which is to be etch later, is possible. The mechanism behind the contamination here is possibly caused

TABLE 4.3: The furnace parameters used in the silicon oxidation process.

Thermal oxidation	
Type	Wet
Temperature [°C]	1150
Oxidation time [min]	160
Annealing time [min]	20

by surface diffusion or evaporation of Pb during sintering, an effect also observed in [20]. Before RIE of the trench, releasing the cantilevers, this 1 μm sacrificial layer will be removed in buffered hydrofluoric acid along with the most of the contaminants. If the sacrificial layer is not grown the RIE of the trench will take long time and contaminate the RIE tool. Second, the LPCVD nitride is prone to have pinholes. Pinholes are of course a issue when doing potassium hydroxide (KOH) etch, a thick oxide beneath the nitride ensures a good buffer layer and added protection against KOH.

4.2.2.2 LPCVD nitride

A LPCVD nitride of around 170 nm is deposited on both side of the wafer in a furnace. The process parameters used are shown in Table 4.4. This layer is used as masking

TABLE 4.4: The parameters used in the LPCVD furnace for silicon nitride deposition.

LPCVD nitride	
Temperature [°C]	780-790
Pressure [mTorr]	200
SiH_2C_l2 gas flow [sccm]	33
NH_3 gas flow [sccm]	100
Deposition time [min]	60
Deposition rate [nm/min]	2.6-2.7

layer for the later KOH etch. The back side of the wafer is patterned using conventional photolithography. A 1.5 μm AZ5214E photoresist is spun on the wafer and soft baked on a hotplate for 90 seconds. The wafer is then exposed in an aligner through a 5 inch UV mask (**KOH etch mask**) with patterned chromium. Notice that in this step it is particular important that the mask patterns are parallel or orthogonal to the major flat of the wafer. If they are not, a larger area will be etched during the KOH process, due to the anisotropic nature of the KOH etch process. This will reduce the proof mass size and the chip frame. The EVG620 mask aligner is used, since its ruler system is particularly suited for the this kind of alignment. The exposure time should be around 3.5 seconds. Next, the photoresist is developed in AZ 351 Developer, where the photoresist on the exposed areas of the wafer should be dissolved.

4.2.2.3 RIE etch

The back side of the wafer is then etched in RIE using the parameters shown in Table 4.5. where the 170 nm nitride layer should be removed in the unprotected areas. Then the

TABLE 4.5: The RIE parameters used to etch the LPCVD nitride.

RIE	Nitride
CHF_3 gas flow [sccm]	8
N_2 gas flow [sccm]	43
Pressure [mTorr]	80
Power [W]	50
Time [min]	6

front side of the wafer is also etched in the same process, to completely remove the nitride layer. The residual photoresist is then removed in a ultrasonic bath with acetone, see Fig. 4.2(c).

4.2.2.4 Bottom electrode

A 50 nm titanium (Ti) adhesion layer and layer of 500 nm platinum (Pt) are deposited on the front side of the wafer using e-beam evaporation. The Pt layer serves both as the bottom electrode of the final harvester and as a diffusion barrier for the thick film high temperature sintering process. To pattern the metal layer a wet etch solution is used and 10 μm AZ4562 photoresist serves as masking material. The photoresist is spun on the wafer followed by a 5 min soft bake on a hotplate at 100°C. Then, the wafer is exposed through a second mask (**Bottom electrode mask**) aligned to the back side, *i.e.* patterns from the **KOH etch mask**. The photoresist is then developed. The wet etch solution $HCl:HNO_3:H_2O$ (7:1:8) is heated to 85°C and the wafers are submerged into the solution for about 8 min for the metal layers to be removed. The residual photoresist is removed in a plasma ashing tool with parameters shown in Fig. 4.6. The resulting structure is shown in Fig. 4.2(d). Fig. 4.5 is a microscope picture showing the etched areas at the alignment mark, it shows a resolution of a few micro meters which is acceptable.

TABLE 4.6: Parameters used in the plasma ashing tool for resist stripping.

Plasma ashing	
O_2 gas flow [sccm]	350
N_2 gas flow [sccm]	50
Power [W]	1000
Time [min]	30

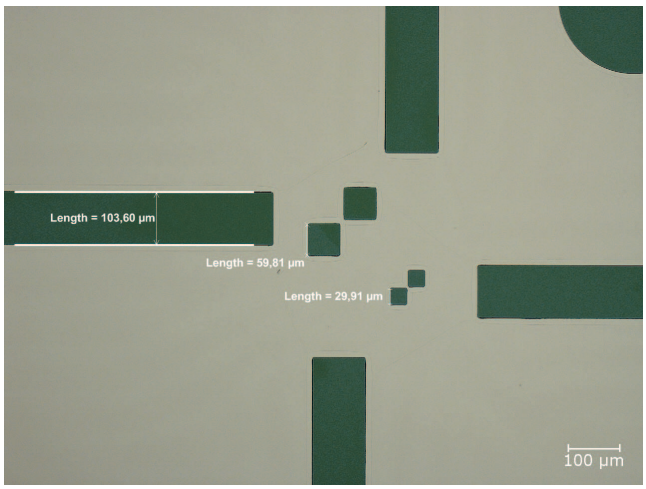

FIGURE 4.5: An optical microscope picture of the bottom electrode metal layer at the alignment mark area.

An alternative process to pattern the Pt bottom electrode is to use a lift-off process instead of the wet etch process. However, it was discovered that due to the thick layer of Pt, adhesion between silicon and Pt is insufficient even with the use of adhesion promoting Ti. The bad adhesion will cause all of the Pt to be lifted during the lift-off process, and this renders the process useless. This is also why plasma ashing was used in favor of acetone stripping.

4.2.2.5 Screen printing

The screen printing process is done at MMS with TF2100 thick film PZT paste developed by MMS. The screen printer is shown in Fig. 4.6. The basic idea of the screen printing process is shown in Fig. 4.7. The thick film paste is placed on the metal thread mask (**PZT1 mask**), the paste can be squeezed through the thin threads but not the thick ones. The wafer is placed under the mask with its front side up. The metal thread mask is of course patterned in such way that the areas where the PZT is to be placed have thin threads. After each print the wafer is heat treated, and then another layer is printed until the target thickness is achieved. Thereafter the wafer is high pressure treated [13] condensing the thick film. Finally, the thick film is sintered around 850°C baking out all of the organic solvents and further consolidating the thick film [13], see Fig. 4.2(e).

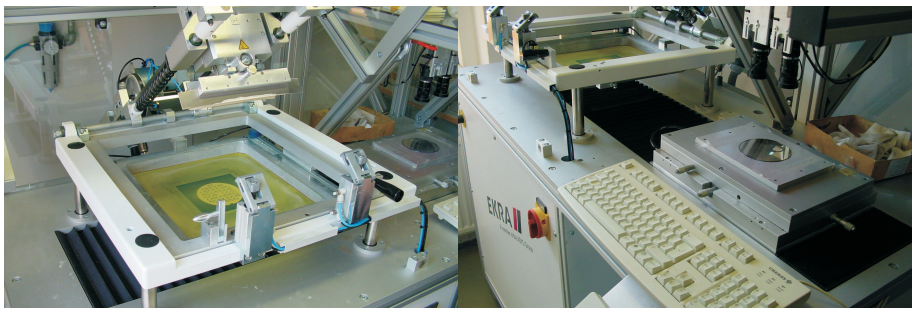

FIGURE 4.6: Photographs of the screen printer at MMS.

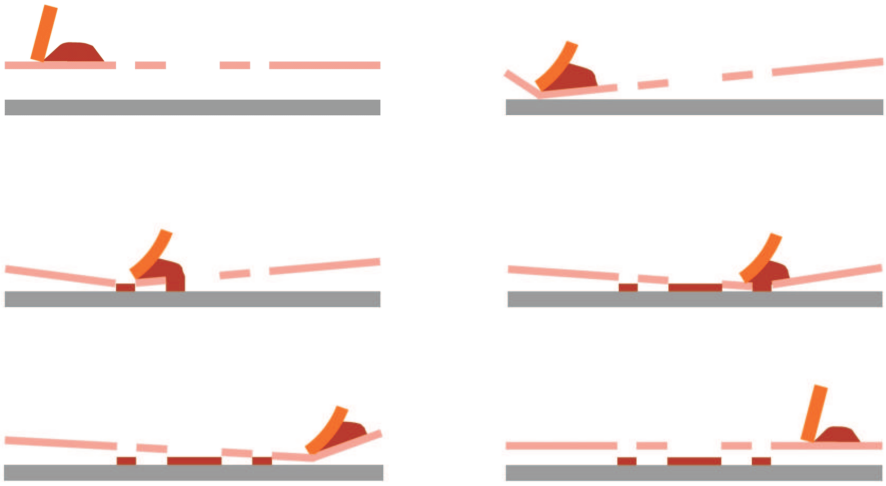

FIGURE 4.7: A sketch of the screen printing process at MMS.

4.2.2.6 Top electrode

A 10 nm chromium adhesion layer and 500 nm gold (Au) are deposited on the front side of the wafer through a prefabricated shadow mask using e-beam evaporation, see Fig. 4.2(f). The relatively thick Au layer is used due to the large PZT roughness. The roughness of the high pressure treated TF2100 PZT layer is measured using profilometry and was found to be around 1 μm, where the standard TF2100 PZT layer has a roughness of 2-3 μm.

The shadow mask was fabricated using a 350 μm thick 4 inch (10 mm) silicon wafer. A 6.2 μm AZ4562 photoresist layer soft baked for 100 seconds at 100°C is sufficient for the later etch process. The aligning and development process are same as before, the mask used in the aligner is **Top electrode mask**. Before the DRIE process of the shadow mask wafer, the shadow mask wafers must be bonded to a carrier wafer. The fast etch rate achieved in the DRIE process is due to the introduction of the inductive coil, which significantly increased the plasma density. Because of this, there is an effective cooling system on the wafer chuck in DRIE tool, which incorporates the wafers itself as a lid

for the cooling system. When large areas of the wafer are etched completely through, the cooling gas will leak in the the main chamber of the DRIE tool, and interrupt the etching process. Therefore a carrier wafer is bonded to the shadow mask wafer using Crystalbond™ 555. Crystalbond™ 555 is a good choice since it has a low flow point (54 °C) and is solvable in water. Due to the use of the carrier wafer and the low thermal conductivity of Crystalbond™ compared to silicon, the wafer chuck temperature in the DRIE tool should be reduced to 0 °C from the standard 20 °C to keep the shadow mask wafer cooled. The parameters used in the DRIE tool are shown in Table 4.7, the Bosch process is used here where the process alternates between a SF_6 etch step and a passivation step, where a chemically inert (CF_2) layer is deposited from C_4F_8. The alternation between etch and passivation ensures a vertical sidewall [21]. The etch process will take 100 cycles, which is about 20 min in total. This gives an etch rate of about 17.5 μm/min After the etch process the wafers are separated by heating the wafers to 60 °C (above the flow point of Crystalbond™ 555). Then the shadow mask wafer is ashed in the plasma asher, so both the residual photoresist and Crystalbond™ are removed. The resulting shadow mask wafer is shown in Fig. 4.8.

TABLE 4.7: The parameters used in the STS Pegasus DRIE tool for the shadow mask etch.

Parameter	Etch	Passivation
SF_6 gas flow [sccm]	550	-
C_4F_8 gas flow [sccm]	-	200
Cycle time [s]	7	4
Pressure [mTorr]	150	25
Coil power [W]	2800	2000
Platen power [W]	45	0

The use of a shadow mask will of course limits the precision of the alignment. However, it is possible to achieve a precision of $\pm 20\mu$m as it is shown in Fig. 4.9. Another issue which may rase some concern is the shadowing effect from the thickness of the shadow mask. To estimate its effect the deposition equipement is investigated. The e-beam evaporation tool used is the Wordentec QCL 800, where the wafer will be placed about 500 mm above the metal crucible. Assuming the evaporation is a point source, *i.e.* the point where the e-beam hits the crucible, the shadowing effect is found to be

$$\frac{\text{wafer radius}}{\text{Wafer to crucible distance}} = \frac{\text{Shadowing distance}}{\text{Shadow mask thickness}} \Leftrightarrow \text{Shadowing distance} = 3.5\mu\text{m}. \tag{4.1}$$

So the worst case scenario with the current equipment is a loss of 3.5 μm resolution, which is well below the level of tolerance.

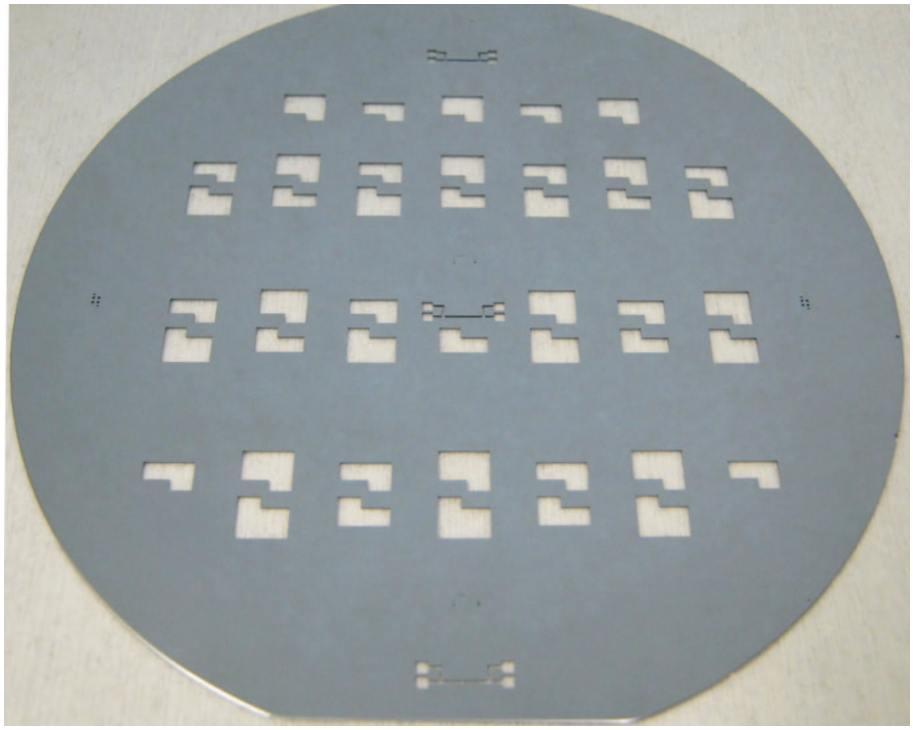

FIGURE 4.8: A photograph of the prefabricated shadow mask.

4.2.2.7 Membrane etch

To protect the front side of the wafer from the subsequent etch a 4 inch tandem series wet etch holder from Advanced Micromachining Tool (AMMT) used. A photographic image is shown in Fig. 4.10, where the AMMT wet etch holder is placed on A4 paper with a dummy wafer mounted in it. Two wafers can be etched simultanously as it is shown in Fig. 4.11. Three o-rings on each side ensures a tight seal of the cover lids and at the same time keeping the stress on the wafers to a minimum. Water can be injected through the equilibration tube to eliminate the pressure difference across the wafer.

The wafer is mounted in the wet etch holder with the front side pointing inwards and the back side exposed through the cover lid. With the front side of the wafer protected, the holder is dipped for 15-20 min in a bHF solution to remove the 1 μm thermal oxide on the back side. Next, the holder is submerged into the prepared 28wt% KOH solution. If the temperature of the solution is kept around 85°C the total etch process will take around 7 hours. The buried oxide of the SOI wafer will serve both as an etch stop and an end point indicator for the process. As an etch stop, the etch rate of thermal oxide is ~140 times slower than that for the (100) plane in silicon [22]. Even though the oxide is a good etch stop the etch process should still be stopped in reasonable time after completion of the silicon etch, since the four convex corners of the proof mass are still being etched. Here, the buried oxide is a good indicator of whether or not the process is finished. The plane silicon etch is a very active process with a large amount

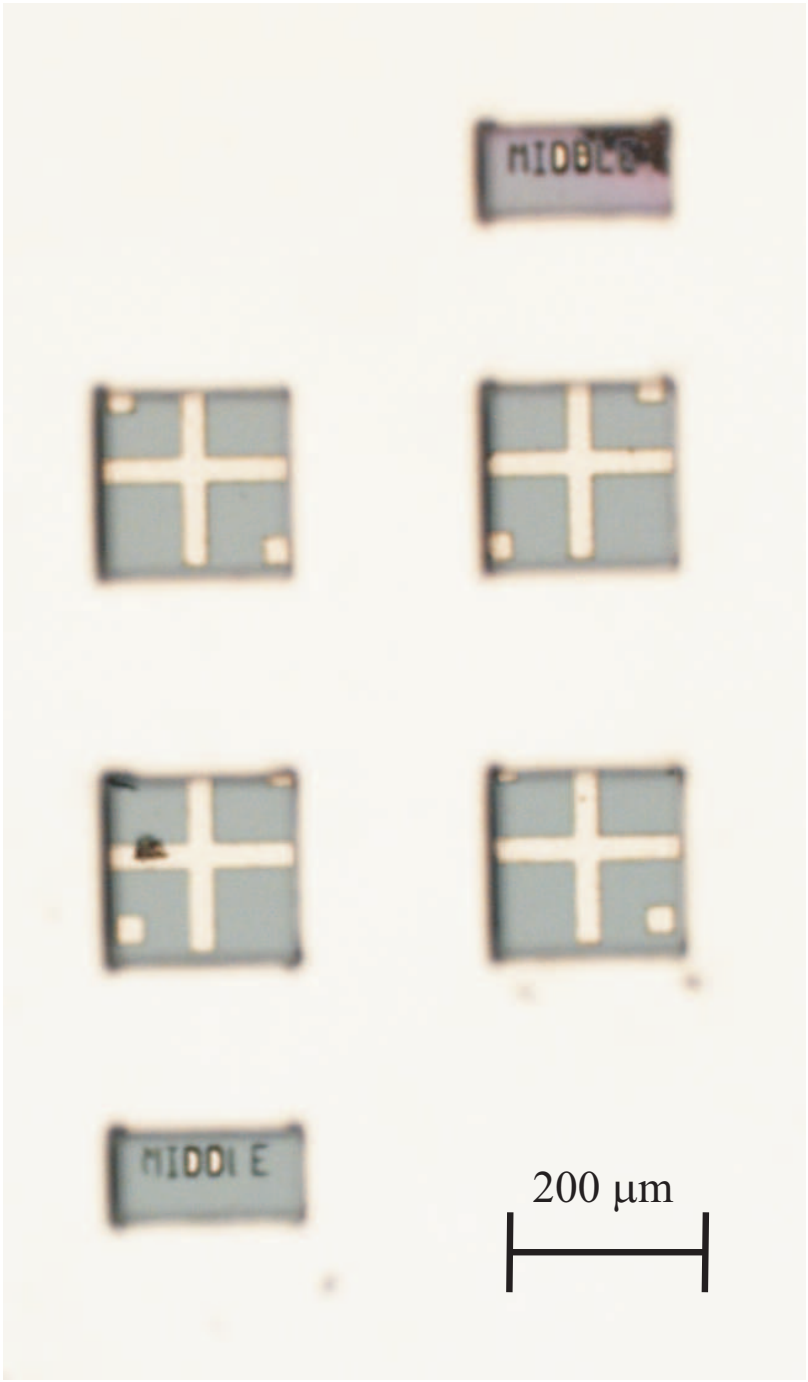

FIGURE 4.9: An optical microscope image of the alignment of the shadow mask.

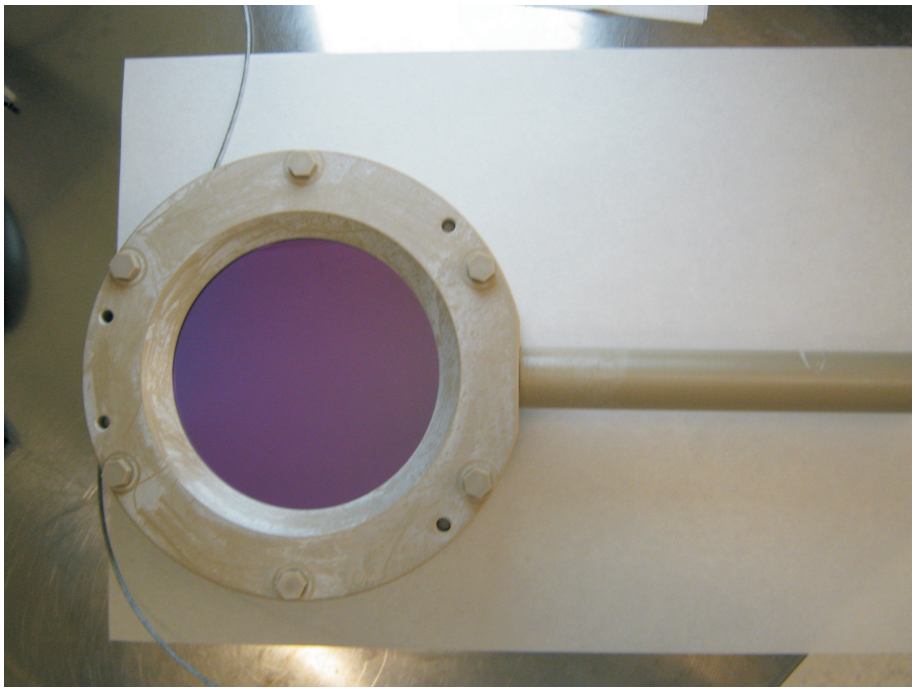

FIGURE 4.10: A photograph of the 4 inch tandem series wet etch holder used in the etching process. A dummy wafer is mount in the holder, which is placed on A4 paper.

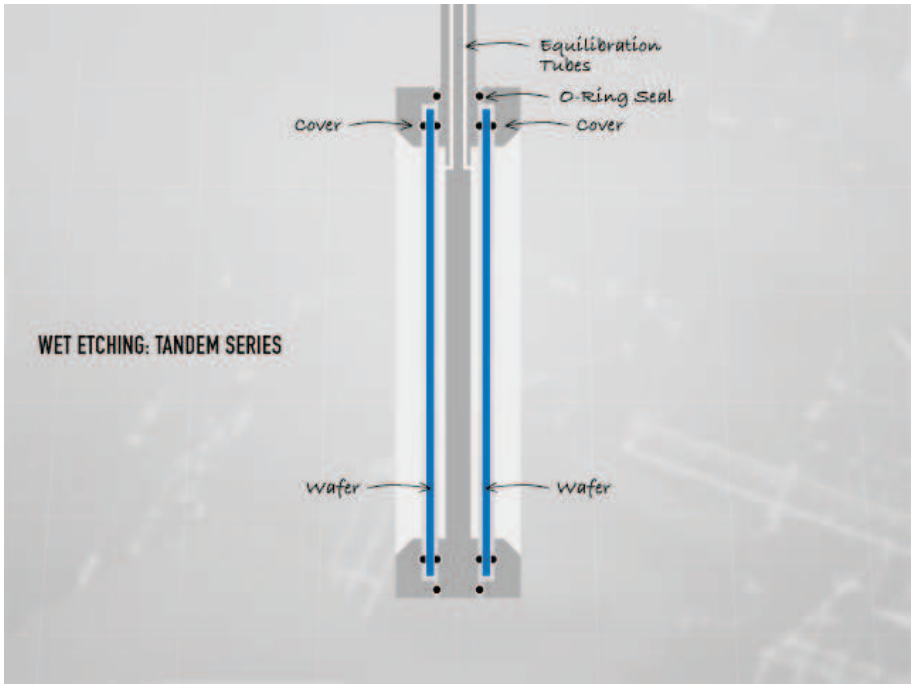

FIGURE 4.11: A cross sectional view of the tandem series wet etch holder from Advanced Micromachining Tool (AMMT). The sketch is taken from http://www.ammt.com/content/products/wetetching/wetetching_tandemseries.html.

of bubble generation, whereas bubble generation will only occur at the aforementioned convex corners if the buried oxide layer is reached. Then the wafer is dismounted and rinsed, the etch result is shown in Fig. 4.12. Notice that there are several pinholes and some areas where the nitride mask has failed. This is believed to be caused by the small a mount of contamination related to the PZT sintering process. This is supported by the fact that test wafers that were etched along with the wafer do not exhibit any severe problems with pin holes and masking failures. This is further supported by the fact that during the KNN unimorph energy harvester fabriation process the KOH etch result is much more better, as it is shown in Fig. 4.21.

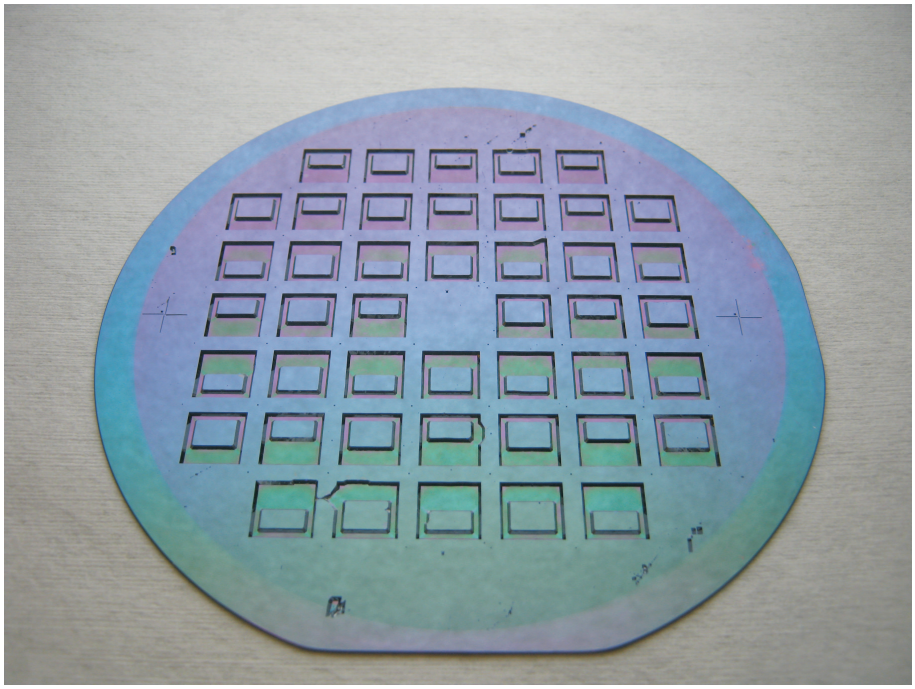

FIGURE 4.12: A photograph of the back side of the PZT screen printed wafer after the KOH etch process.

The KOH wet etch is an anisotropic etch, which means the etch rate differs dependent on the silicon crystal plane [23]. The (SOI) wafers used in the process are (100) wafers, which means that sloped sidewall of 54.7° instead of 90° will be formed during etching, as it is shown in Fig. 4.13(a). This means the defined proof mass will be smaller than if the proof masses are etched vertically as it is the case in DRIE process. However, the advantages of using KOH etch far out weights the loss of a small amount of proof mass.

Furthermore, the convex corners of the proof mass will also be etched faster. To prevent further loss of the proof mass size, corner compensation shown in Fig. 4.14 is implemented in the mask design for **KOH etch mask**. The idea of this corner compensation is to introduce pointed blocks at each of the convex corners in proof mass. These point

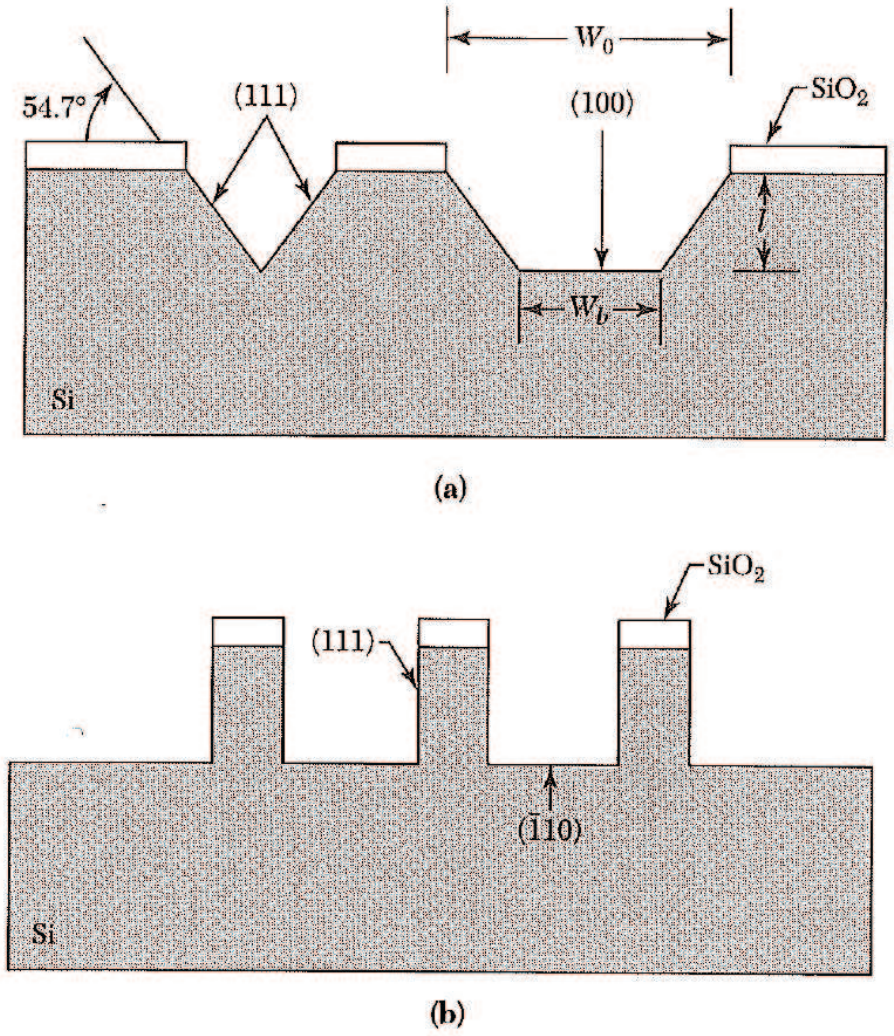

FIGURE 4.13: A sketch of the resulting KOH etch on silicon taken from [24], (a) with mask opening in (100)-plane (b) with mask opening in (110)-plane.

blocks should prevent the etch of the corners immediately by extended the corner with length L, which is set to be as long as the structure permits. At the same time, the extended corners have a width $W = 1050\mu$m, which is twice the etch depth. This will ensure the point blocks will be gone by the time the etching process finishes.

4.2.2.8 Release etch

Before the final releasing etch, the thermal oxide on the front side and the buried oxide must be removed in bHF. Patterned photoresist is used to protect the PZT on the front side, however it was discovered that 10 μm photoresist is insufficient to cover the wafer reasonably as it is shown in Fig. 4.15. By spinning a second layer of photoresist the coverage becomes significantly better as it is shown in Fig. 4.16. The PZT film thickness shown in Fig. 4.15 and Fig. 4.16 is about 30 μm, experience shown that with the 2 times

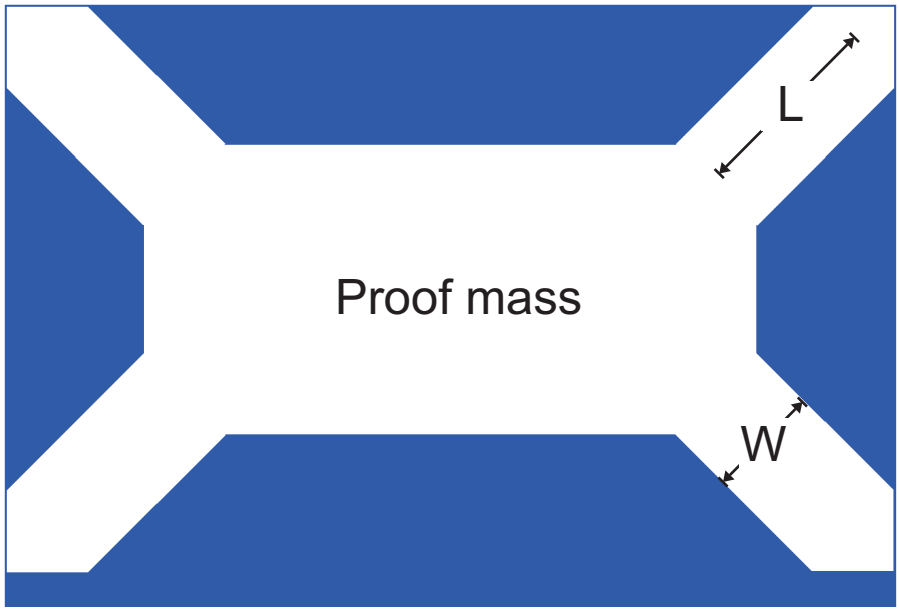

FIGURE 4.14: The corner compensations designed for the four convex corners of the proof mass is shown.

spinning step the photoresist coverage will be sufficient even with a PZT film of 60 μm. During the spinning process a mechanical chuck holder should be used instead of the normal vacuum chuck. This will prevent any membrane fracture due to the pressure. After each spinning process the wafer is placed in an oven for soft bake at 90°C for 30 min The use of an oven instead of a hot plate will yield a better temperature distribution and reduce temperature induced stress in the wafer. After the two spinning and baking steps the wafer is aligned to the last mask (**Trench mask**), and exposed for 4 $\times$ 50 seconds, with a 30 seconds break after each exposure. This is to prevent the popping of the photoresist [25]. After the wafers are developed, they are submerged in bHF removing the oxide. Due to the aforementioned lead in the thermal oxide an extended etch time in bHF is needed. After around 45 min the lead contaminated oxide is removed along with most of the contaminants, as it can be seen in Fig. 4.17 and 4.18. Energy dispersive X-ray spectroscopy (EDX) measurements were done in [26] both before the bHF etch Fig. 4.17 and after the etch Fig. 4.18. The area of spectrum 1 in Fig. 4.17 contains silicon, oxide and a modest amount of lead, the area of spectrum 2 contains a large amount of lead. After the etch only trace amounts of lead is left at areas 2 and 3, shown in Fig. 4.18.

With most of the contaminants removed along with the oxide the wafer is ready to be etched in the RIE tool, so the trench can be removed thus the cantilever can be formed. The parameters used in the RIE tool are shown in Table 4.2. It takes about 45-50 min to etch through the trench of 20 μm, which give an etch rate of 0.40-0.45 μm/min Thereafter, the wafer is carefully rinsed in acetone, removing the residual photoresist.

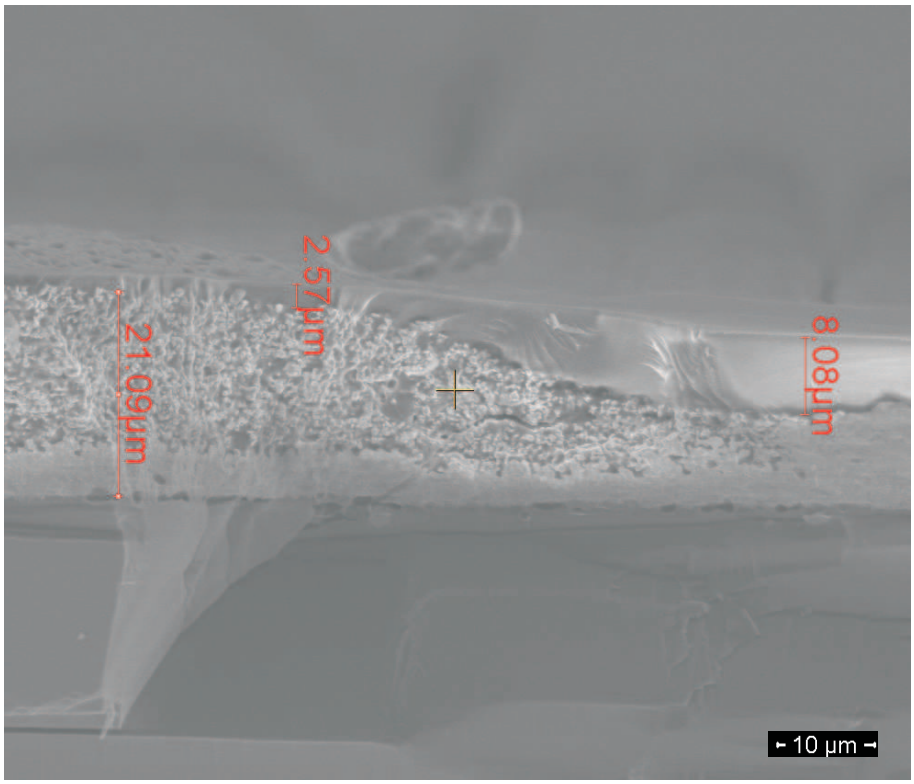

FIGURE 4.15: A SEM image showing the coverage of 10 μm AZ4562 photoresist on a wafer with 30 μm screen printed PZT.

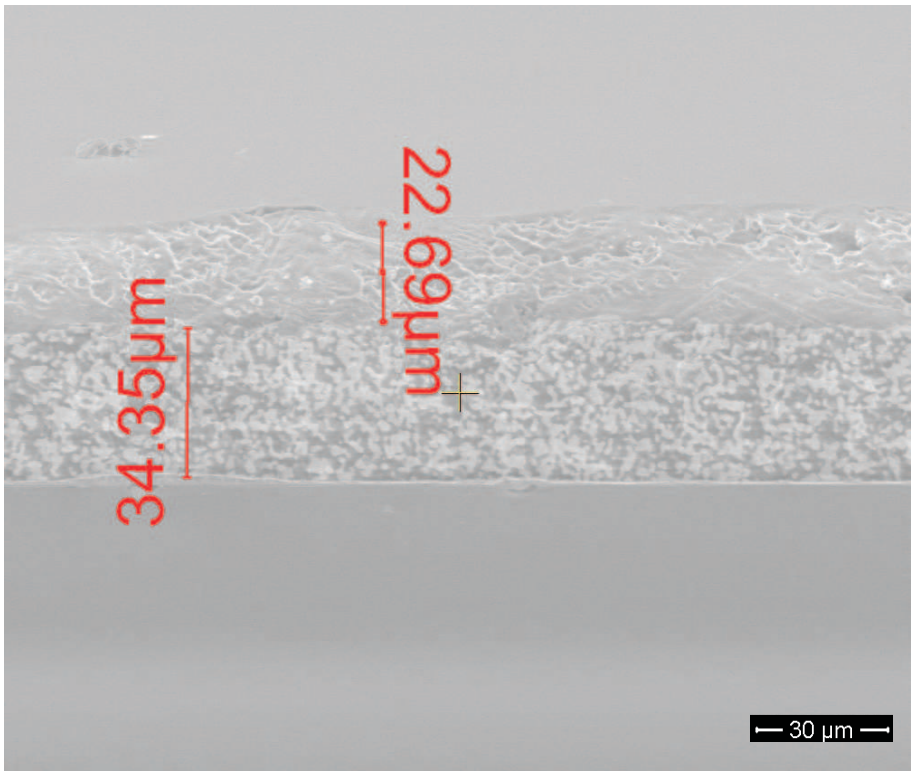

FIGURE 4.16: A SEM image showing the coverage of 2 $\times$ 10 μm AZ4562 photoresist on a wafer with 30 μm screen printed PZT.

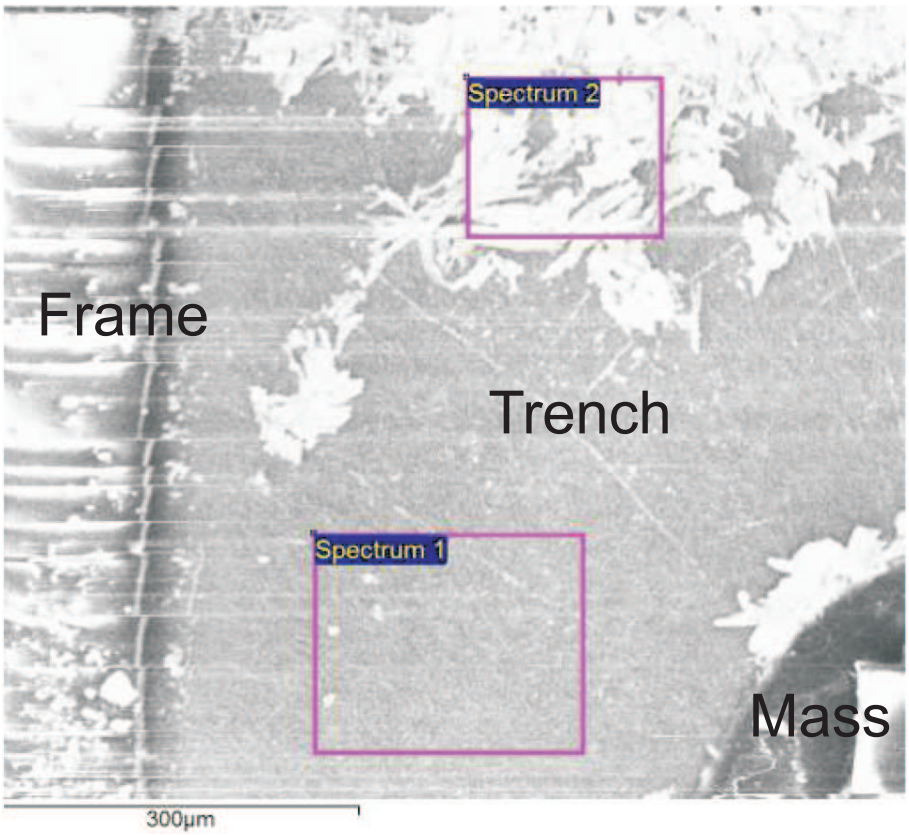

FIGURE 4.17: SEM images of the trench area of the energy harvester before the bHF etch of the 1 μm oxide. This is a modified figure from [26].

The final result is illustrated in Fig. 4.2(h). Last, the wafer is diced and the chips polarized by applying a voltage between the electrodes and heating the chips. Two of the diced energy harvester chips are shown in Fig. 4.19.

4.2.3 The KNN unimorph energy harvesters

The fabrication process presented in Fig. 4.2 is not only suited for PZT thick film, but also other thick films such as KNN. The problem with PZT is that it contains more than 60% lead, which is a heavy metal and very toxic. Lead poisoning is known to cause headaches, nausea, constipation, anaemia and reduced fertility. Prolonged exposure could cause severe nerve, brain and kidney damage [27]. Furthermore many of the alternatives also contain heavy metals, such as bismuth (Bi) or barium (Ba). Therefore a search for an alternative lead free piezoelectric ceramic leads to the KNN thick films. Basically, the PZT thick film is replaced by screen printed KNN thick film as it is shown in Fig. 4.20. An interesting phenomenon is the reduced numbers of pinholes and nitride failure during the KOH etch in all of the fabricated KNN wafers compared to its PZT conterpart. A typical KNN wafer after the KOH etch process is shown in Fig. 4.21. The successful fabrication of KNN energy harvesters is a proof that the developed fabrication

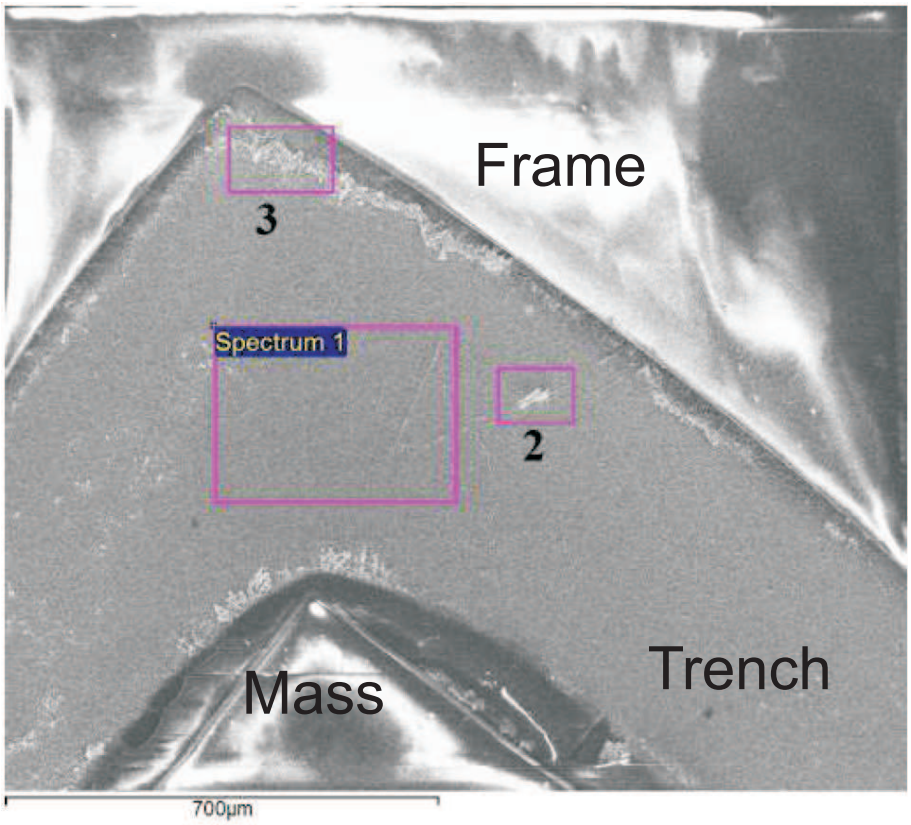

FIGURE 4.18: SEM images of the trench area of the energy harvester after the bHF etch of the 1 μm oxide. This is a modified figure from [26].

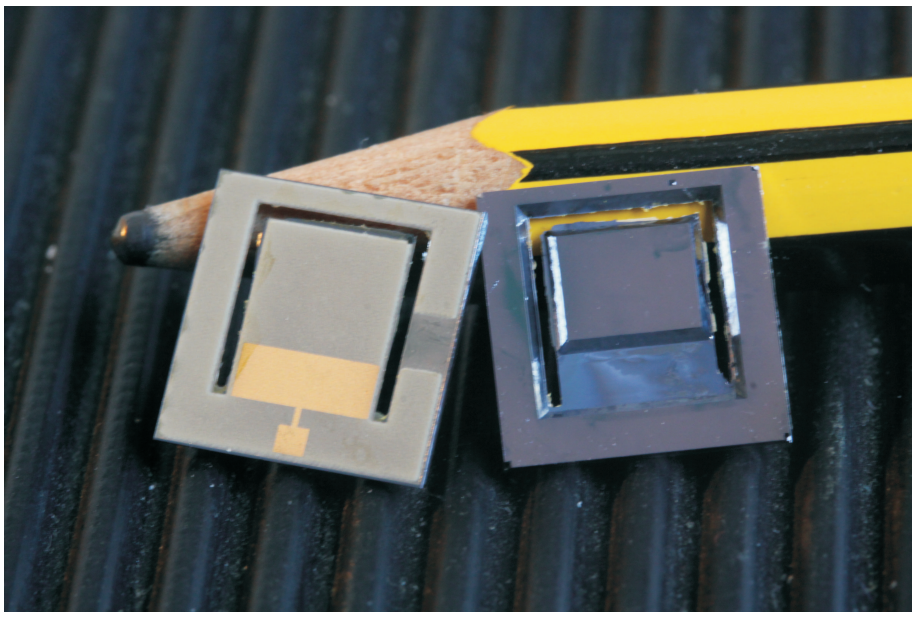

FIGURE 4.19: A photograph of two fabricated unimorph energy harvester chips next to an ordinary pencil. One of the chips is viewed from the front side and the other is viewed from the back side.

process can be considered a platform for various piezoelectric thick film based energy harvesters.

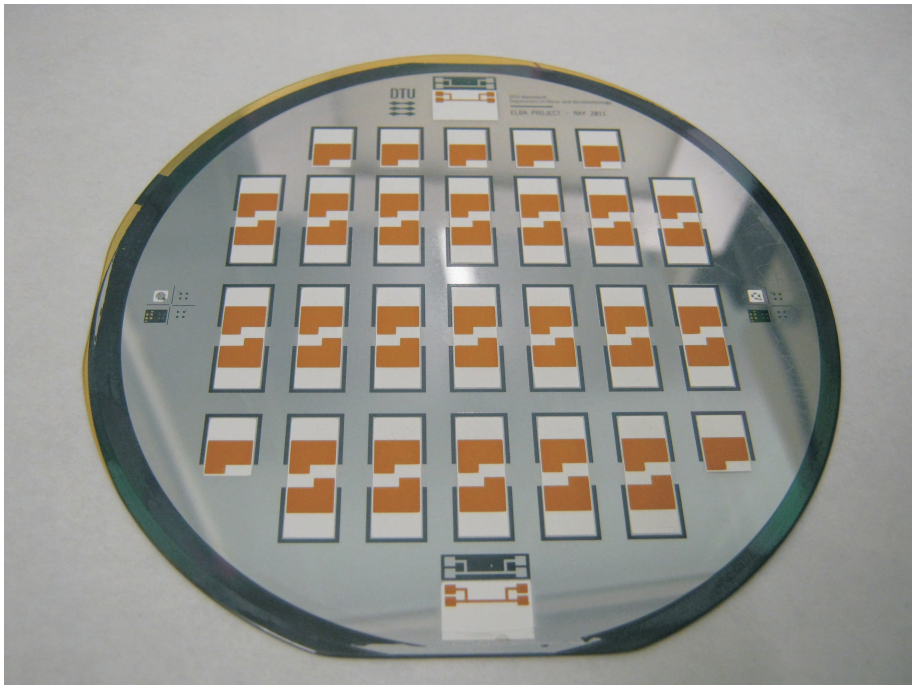

FIGURE 4.20: A photograph of the front side of the KNN screen printed wafer.

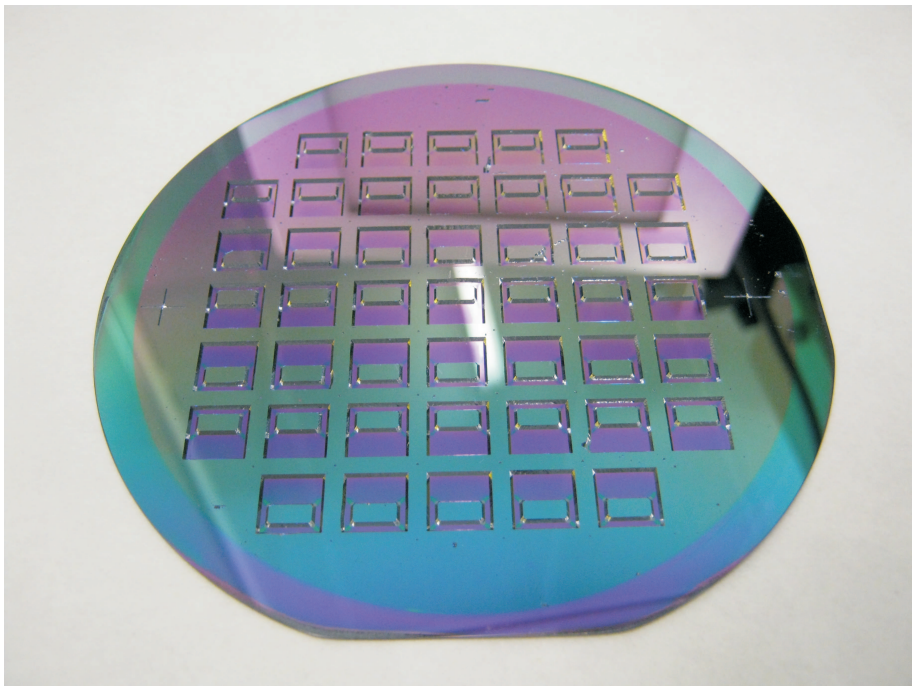

FIGURE 4.21: A photograph of the back side of the KNN screen printed wafer after the KOH etch process.

4.2.4 The fabrication of the bimorph energy harvester

The earlier version of the bimorph energy harvester fabrication scheme is similar to the old unimorph version, and is presented in [28], where DRIE is used for the membrane etch. The same advantages are achieved by a change to KOH etch for the bimorph energy harvester as seen for the unimorph energy harvester. The accessibility to high pressure treatment of the PZT thick film is even more crucial for the bimorph beam, since it gives the opportunity to have thiner beams.

The current fabrication scheme for the bimorph energy harvester is mostly based on the presented unimorph energy harvester fabrication process, as it is shown in Fig. 4.22. First, a 1 μm thick silicon dioxide is thermally grown on a SOI wafer, see Fig. 4.22(a), and then a 170 nm thick silicon nitride is deposited using LPCVD, see Fig. 4.22(b). The nitride is removed on the front side and patterned on the back side using conventional lithography processes, see Fig. 4.22(c). A Pt bottom electrode is deposited on the front side of the wafer and patterned, see Fig. 4.22(d), followed by deposition of the first PZT thick film layer, the Pt middle electrode, see Fig. 4.22(e), the second PZT thick film layer and the Au top electrode, see Fig. 4.22(f). The oxide on the backside is etched in bHF, while the front side of the SOI wafer is protected. The backside of the SOI wafer is then etched in KOH until the buried oxide layer is reached and then the buried oxide layer is removed in bHF, see Fig. 4.22(g). Finally, the sacrificial device layer is etched in RIE, releasing the cantilevers, see Fig. 4.22(h). The chips on the wafer are then diced and polarized.

4.2.4.1 Similar steps

As it is explained in the previous section, the change between the bimorph and the unimorph fabrication scheme begins at Fig. 4.22(e), after the first PZT screen printing a 500 nm Pt middle electrode deposited through a prefabricated shadow mask. The shadow mask fabrication steps are discussed in 4.2.2.6, this time the UV mask **Middle electrode** is used for photoresist patterning.

The second PZT layer is screen printed on top of the first PZT and the middle electrodes, as it is seen in Fig. 4.22(f). The result is shown in Fig. 4.23, where the top PZT layer is distinguishable from the bottom PZT layer and the contact pad for the middle electrode is clearly visible.

The top electrode consist of a 10 nm Cr adhesion promoter and 500 nm Au layer, which is deposited through another shadow mask. The shadow mask is patterned using UV mask **Top electrode**. The membrane etch, which defines the proof mass and the frame,

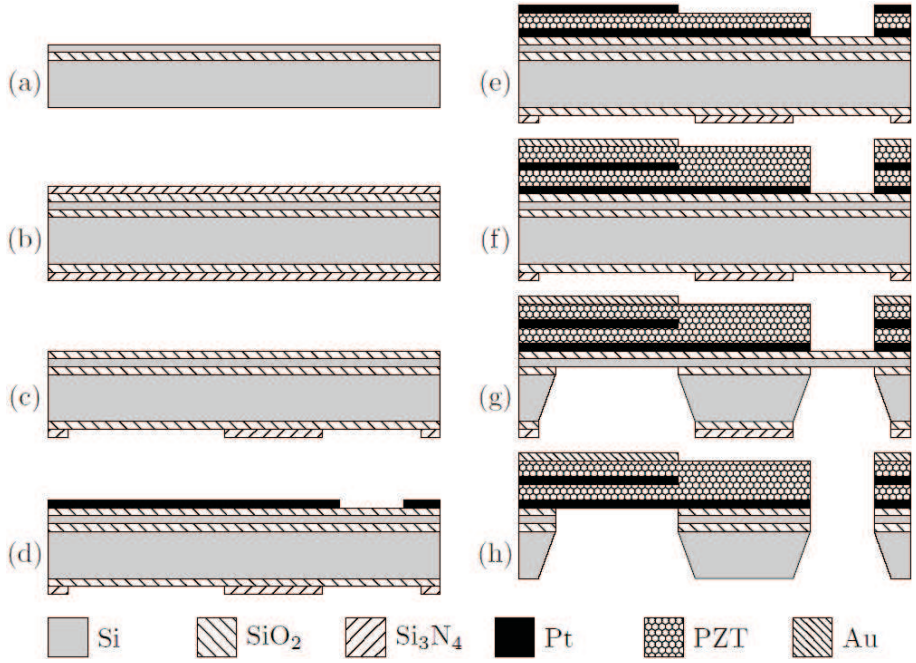

FIGURE 4.22: A cross sectional sketch of the process flow for the bimorph energy harvester. First, a 1 μm thick silicon dioxide is thermally grown on a SOI wafer (a), and then a 170 nm thick silicon nitride is deposited using LPCVD (b). The nitride is removed on the front side and patterned on the back side using conventional lithography processes (c). A Pt bottom electrode is deposited on the front side of the wafer and patterned (d), followed by deposition of the first PZT thick film layer, the Pt middle electrode (e), the second PZT thick film layer and the Au top electrode (f). The oxide on the backside is etched in bHF, while the front side of the SOI wafer is protected. The backside of the SOI wafer is then etched in KOH until the buried oxide layer is reached and then the buried oxide layer is removed in bHF (g). Finally, the sacrificial device layer is etched in RIE, releasing the cantilevers (h).

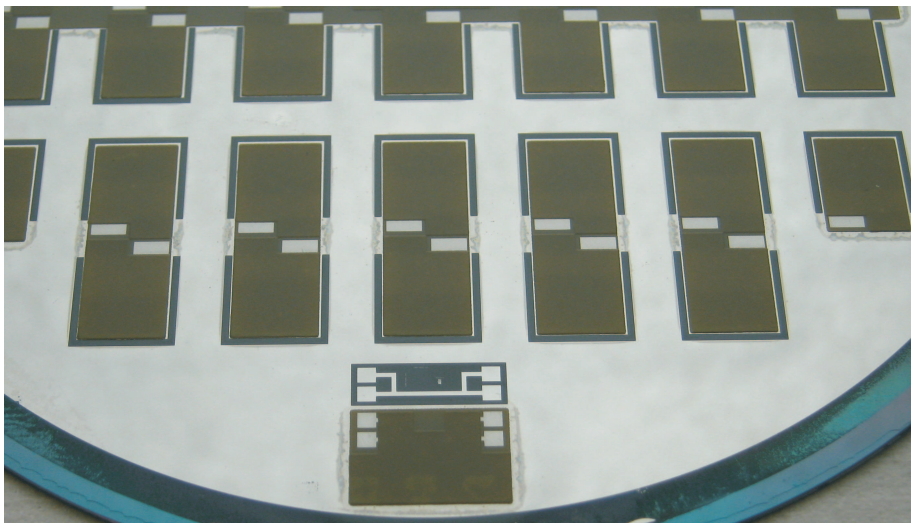

FIGURE 4.23: A photograph of the bimorph energy harvester wafer after the second PZT layer is screen printed.

is the same as before. The AMMT wet etch holder is used to protect the front side of the wafer, where PZT stacks were screen printed. The back side of the wafer is exposed to the KOH solution. The etch procedure is the same as described in 4.2.2.7.

4.2.4.2 Release etch

After the KOH etch, two layers of 10 μm AZ 4562 photoresist are spun on the front side of the wafer. This layer is used to protect the PZT and electrodes from the later etching processes. The first etching process is the removal of the residual buried oxide (KOH etch stop layer), which is done in a bHF solution, as it is seen in Fig. 4.22(g). The second etching process is the RIE release etch, notice here that the RIE etch is done from the back side of the wafer and not the front side, as it was in the case with the unimorph energy harvester. The parameters used in the RIE tool are shown in Table 4.2. The process takes 60 min which is longer than the releasing etch for the unimorph energy harvester. The reduced etch rate is due to the increased etch load, caused by the etch from the back side. After the RIE process, the wafers are rinsed in acetone to remove the residual photoresist, see Fig. 4.22(h). The back side of the wafer after the RIE process is shown in Fig. 4.24. Last, the wafer is diced and the chips polarized. The polarization directions of the two layers are aligned opposite to each other, *i.e.* during polarization the top and bottom electrodes are grounded and a polarization voltage is applied to the middle electrode. This structure is the aforementioned serial bimorph configuration, where the structure can be considered as two energy harvesters connected in series. Two of the diced bimorph energy harvester chips are shown in Fig. 4.25.

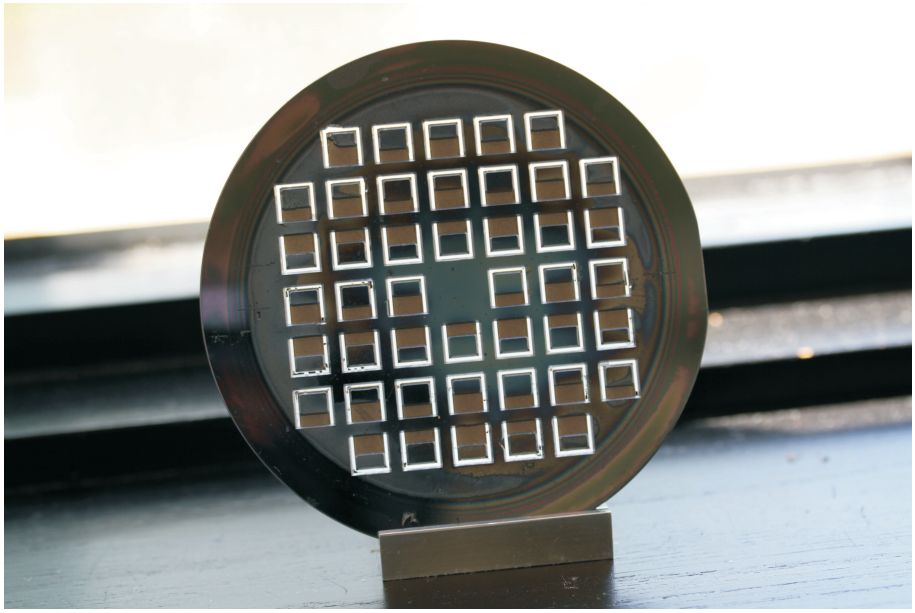

FIGURE 4.24: A photograph of the back side of the KNN screen printed wafer after the KOH etch process and release etch.

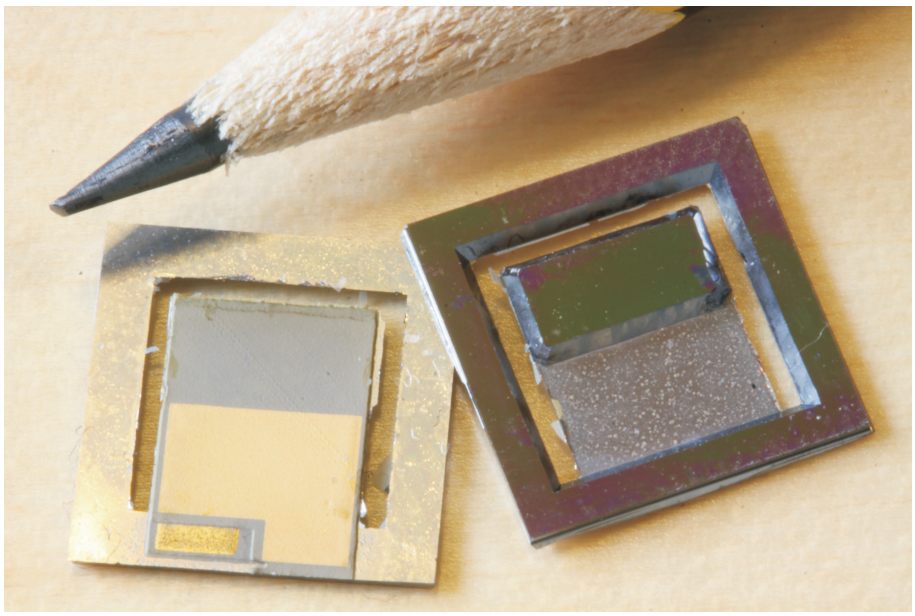

FIGURE 4.25: A photograph of two fabricated bimorph energy harvester chips next to an ordinary pencil. One of the chips is viewed from the front side and the other is viewed from the back side.

4.2.5 Ongoing improvements on the bimorph energy harvesters

Due to the uniqueness of the bimorph energy harvester, such as its three electrode configuration, the release etch is done from the back side of the wafer and the device layer of the SIO wafer is only used as a sacrificial layer, several alternative versions of the bimorph energy harvesters have been made, and some ideas are to be implemented. In this section some of these alternative versions and ideas will be presented and discussed.

4.2.5.1 Screen printed middle electrode

Screen printing electrodes would normally be a bad idea. The thinnest screen printed film are often around 4-5 μm, that is much thicker than the films deposited by e-beam evaporation. If that is used as top electrode, not only it will increase the resonant frequency of the energy harvester, it will also waste significant amount of the strain energy. The strain S from pure bending is determined by

$$S = -\frac{z}{\rho}, \tag{4.2}$$

where ρ is the radius of curvature and z is the position along the thickness of the cantilever. Equation 4.2 clearly shows that the surface is most strained. The same argument holds for the bottom electrode. For the middle electrode it might be a different

story. Equation 4.2 shows that the strain is low for small z, even zero at the neutral axis ($z = 0$). Furthermore, having a thicker middle electrode also ensures that the neutral axis will always be in the middle electrode. So the screen printed middle electrode will be more forgiving if the two PZT layers differ in thickness and property. So it is even possible to see a power increase by introduce a thicker middle electrode. Of course the resonant frequency will increase, but the cantilever will also be more robust.

This type bimorph energy harvester was successfully fabricated. The Pt thin film middle electrode is replaced by a Au screen printed middle electrode, with at thickness around 5 μm. The fabricated chips are shown in Fig. 4.25. Of the two wafers that were fabricated, no chips were lost. This demonstrated the predicted robustness of the design.

4.2.5.2 Screen printed mass

The increased thickness of the screen printed middle electrode will increase the resonant frequency, which already is a parameter that should be to reduced. A direct way to decrease the resonant frequency is to increase the proof mass. Furthermore, increasing the proof mass will also increase the induced stress in the cantilever beam. So the idea of this version is that before the KOH membrane etch, a tungsten thick film of around 230 μm thickness is screen printed on the proof mass area. This was successfully accomplished, as it is shown in Fig. 4.26. However, it was discovered that the chosen thick film degenerates during the later RIE process, due to the high process temperature that might be above 100°C. The degeneration is hardly noticeable at first, but the thick film dissolves in acetone. A replacement thick film is currently under development.

4.2.5.3 Standard wafer in the bimorph process

The use of a standard wafer instead of using SOI for the bimorph process a possibility. standard wafers are about 1/10 the price of the SOI wafers, so there is an economical incentive to use standard wafers. To be able to use standard wafers a well controlled KOH etch is required, where the temperature is constant both in time and across the wafer and the process is reproducible. The constant temperature in time and reproducibility are needed since no end point detection is available, so the process need to be exactly timed. Constant temperature across the entire wafer is needed since severe non uniformity will cause issues with the later releasing RIE process. The 1 μm thermal oxide is intended to be an etch stop layer for the releasing RIE etch. The RIE etch process has an etch rate of around 0.02 μm/min for oxide and 0.4 μm/min for silicon. This means a difference between the thickest and the thinnest silicon part should be no more than 20 μm, *i.e.* if the target membrane thickness after the KOH etch is 30 μm the real thickness across

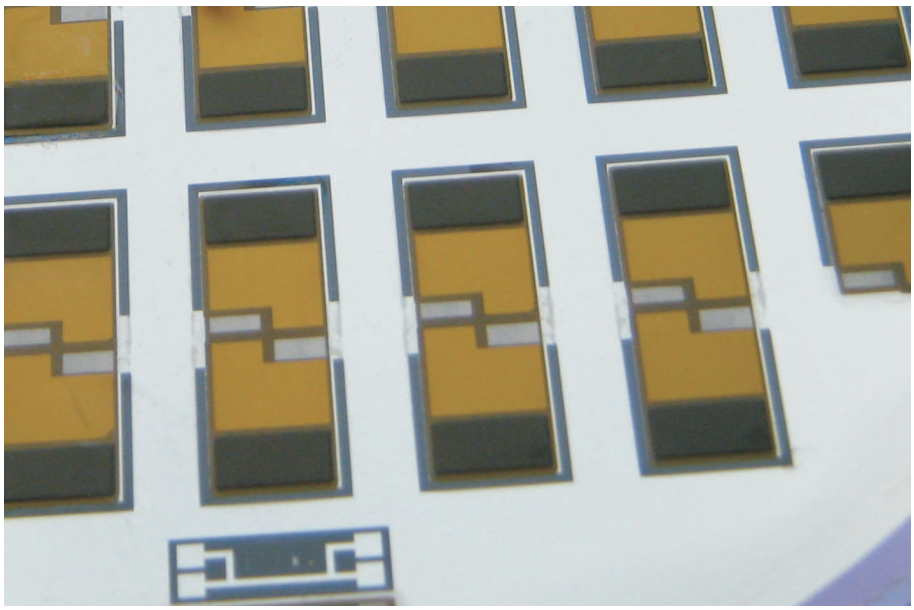

FIGURE 4.26: A photograph of the bimorph energy harvester wafer with screen printed tungsten mass.

the wafer can be between 20 μm to 40 μm. The requirement will be more strict if the 5% non uniformity of the RIE etch is also taken in to account. At the current point in time the requirement of between 20 μm to 40 μm remaining silicon, can not be achieved. The is concluded from the fact that when using the SOI wafers the time between the buried oxide is partially visible and the end of the process is between 20 - 40 min With an average etch rate of 1.25 μm/min the thickness difference between the thinnest and the thickest part will be between 25 - 50 μm. The huge non uniformity is believe to be caused by two things:

- The use of the AMMT wet etch holder.
- The use of beaker and hot plate, not using a wet bench for the etch.

The argument for the AMMT wet etch holder as a cause for non uniformity is based on the fact that the dummy wafers, placed in the same solution usually have better uniformities. A wet bench will of course have better temperature distribution than a beaker on hot plate. The reason for why wet bench is not used is the risk of lead contamination.

4.3 Issues and solutions

Some of the problems and issues encountered in this project will be discussed in this section.

4.3.1 Diffusion barrier

Like bulk PZT ceramic processing the thick film fabrication requires a high temperature sintering to consolidating the ceramic, as it was used in section 4.2.2.5. In a thick film fabrication process it is unavoidable to have the ceramic in contact with other materials, *e.g.* the substrate. Therefore it is necessary to screen print the thick film onto a chemically and thermally stable material to avoid inter diffusions and interfacial reactions. The silicon substrate is not such a material, which is confirmed in [20, 29]. The existence of an oxide or nitride layer does not seem to have any positive effect either [30]. Besides the diffusion of silicon into the PZT layer, which will degrade the piezoelectric properties of PZT [30], it was also found that Pb will diffuse into the silicon layer, leading to the formation of lead silica and causing delaminations, as it is shown in Fig. 4.27.

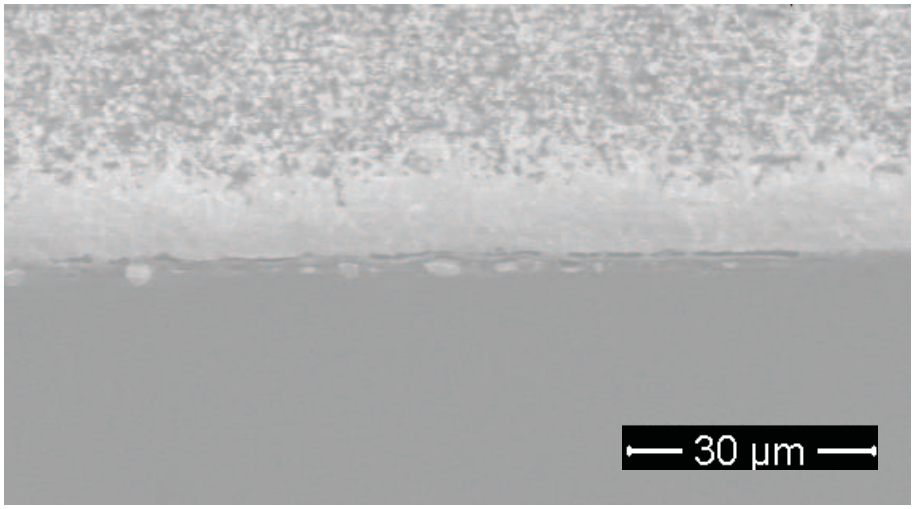

FIGURE 4.27: A SEM image showing the effect of directly screen printing PZT onto a silicon surface (with 1 μm thermal oxide).

Due to the fabrication advantages offered by silicon, the change to other substrate material is of course out of the question. Therefore a good diffusion barrier is needed. A diffusion barrier is basically a film deposited onto the substrate, which will prevent inter diffusion of atomic species between the substrate and the film. Various diffusion barriers were discussed in [31], both conducting and electrical isolating. Remember that between the PZT layer and the silicon substrate there is already a layer: the bottom electrode. The requirement for the bottom electrode is somewhat similar to the requirement for the diffusion barrier, it must be able to withstand the high temperature sintering process and remain electrically conducting. Metals that meet this requirements are noble metals, such as Pt and Au, which are not easily oxidized. However, problems involved the formation of Si-Au eutectic reported in [32] means Au is a poor choice. Therefore

Pt was used as the bottom electrode, the advantage of Pt is that it not only serves at an electrode but can also work as a diffusion barrier [20]. However due to the inert nature of Pt and the thermal mismatch between silicon and Pt an adhesion promoting layer of 50 nm Ti is introduced. In order for the Pt layer to serve as a diffusion barrier the oxide must be sufficiently thick, an in depth investigation of the needed Pt thickness is done in [33]. One of the most convincing result is shown in Fig. 4.28 where the dielectric constant of the PZT layers is plotted as a function of the Pt diffusion barrier thickness. The dielectric constant is a good quantitative benchmark for the quality of the PZT and can be easily found from a capacitance measurement. The idea is that significant inter diffusion between the layers and delamination will change the dielectric constant. TF2100 PZT thick film is used, which has an expected dielectric constant around 600. Result from Fig. 4.28 shows that at least 400 nm Pt is needed, taken the large standard deviation of measured dielectric constant in to account it is concluded 500 nm Pt should be used.

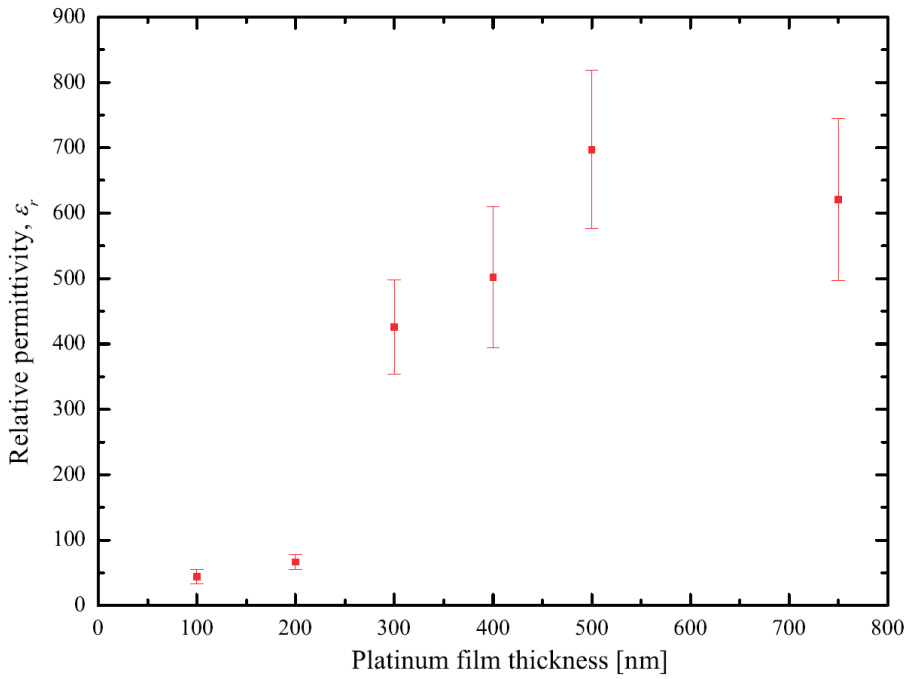

FIGURE 4.28: A plot showing the calculated dielectric constants from the measured capacitance of the TF2100 film as a function of the Pt diffusion barrier thickness. Taken from [33].

The result of using a 500 nm thick Pt diffusion barrier is shown in Fig. 4.29, where a SEM cross sectional image of the silicon/PZT interface is shown. This image clearly shows the separation of the PZT layer and the silicon layer, by the 1 μm oxide layer, the Ti adhesion layer and the Pt diffusion barrier layer. Notice the PZT grains and the pores between the grains are clearly visible. Comparing this PZT with the PZT damaged by inter diffusion, shown in Fig. 4.30, the difference is clear. Fig. 4.30 shows

the PZT layer from a wafer with insufficient Pt thickness. This part of the PZT layer is delaminated and is no longer in contact with the silicon layer, and the pores between the PZT grains are filled with silicon.

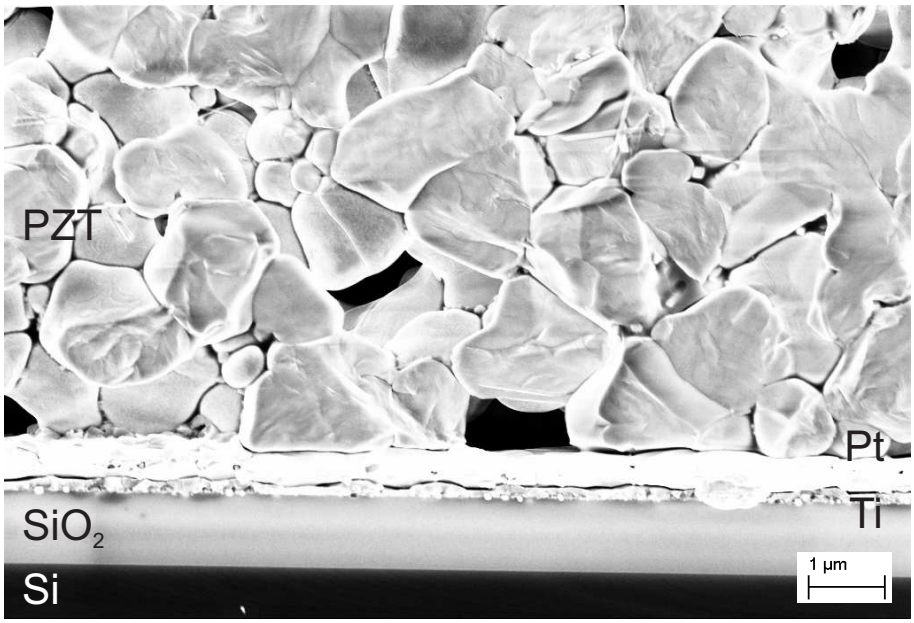

FIGURE 4.29: A cross sectional SEM image showing the effect of a good diffusion barrier. This image shows the separation of the PZT layer and the silicon layer. The PZT grains are clearly visible.

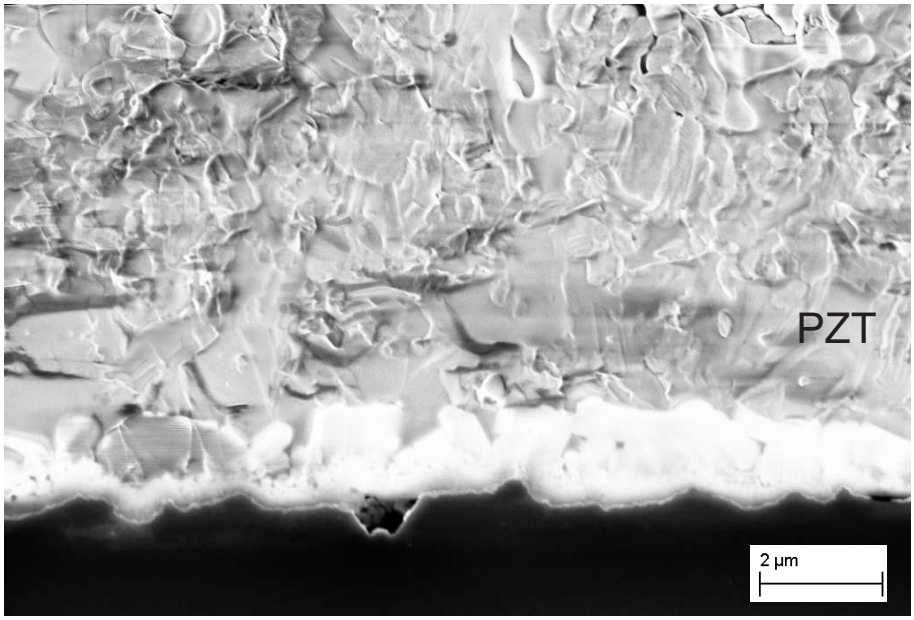

FIGURE 4.30: A cross sectional SEM image showing the effect of inter diffusion on PZT. This image shows the delaminated PZT layer. The pores between the PZT grains are filled with silicon.

4.3.1.1 Further investigation

To further understand the inter diffusion process the PZT thick film is screen printed on purposely constructed openings in the diffusion barrier and then sintered. The effect of the inter diffusion is clearly shown in Fig. 4.31 and Fig. 4.32, the difference between the two figures is the opening width. In both cases a depletion of the silicon is observed, causing cavities to form in the silicon layer. With a barrier opening width of 5 μm in Fig. 4.31 the part of the PZT layer right above the opening is completely contaiminated by silicon, no pores are visible. The contaiminated region has the form of a trapezoid as it is marked in Fig. 4.31. With a barrier opening width of 50 μm two cavities are formed. The depletion of silicon seems to be stopped in the middle of the opening, pores in PZT are observed a few microns above this interface. This suggests that the silicon saturation point is reached at the area.

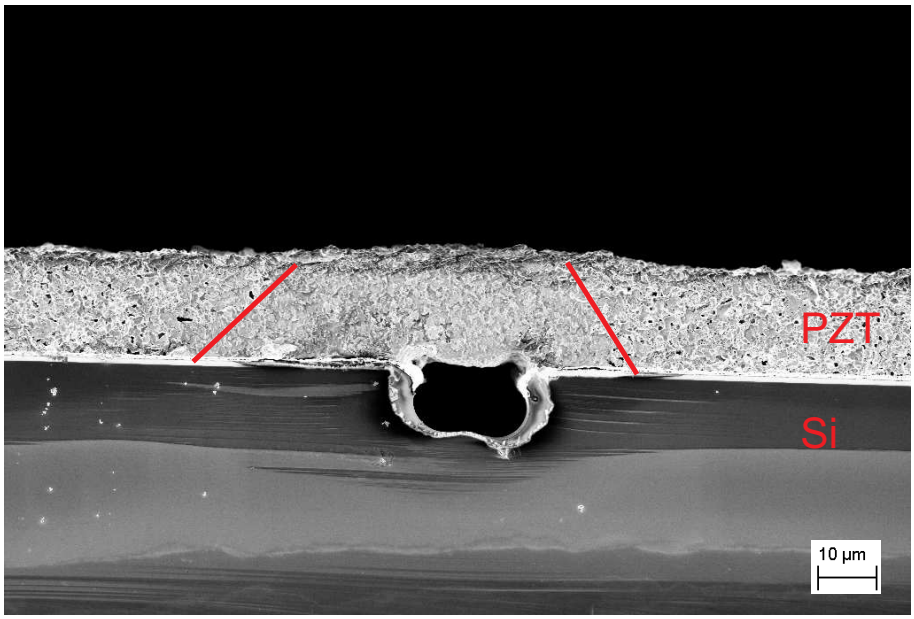

FIGURE 4.31: A cross sectional SEM image showing the inter diffusion between the PZT thick film and the silicon substrate through a purposely constructed opening of 5 μm in width.

4.3.1.2 Other diffusion barriers

Two other diffusion barriers were investigated titanium oxide (TiO_2) and alumina (Al_2O_3), but was found to be unsuitable as diffusion barrier.

The titanium oxide diffusion barrier is fabricated using thermal oxidation. So first, a 500 nm Ti layer is deposited on a silicon wafer with 1 μm thermal oxide using e-beam evaporation. The wafer is then placed in an oxygen rich atmosphere furnace at 600°C

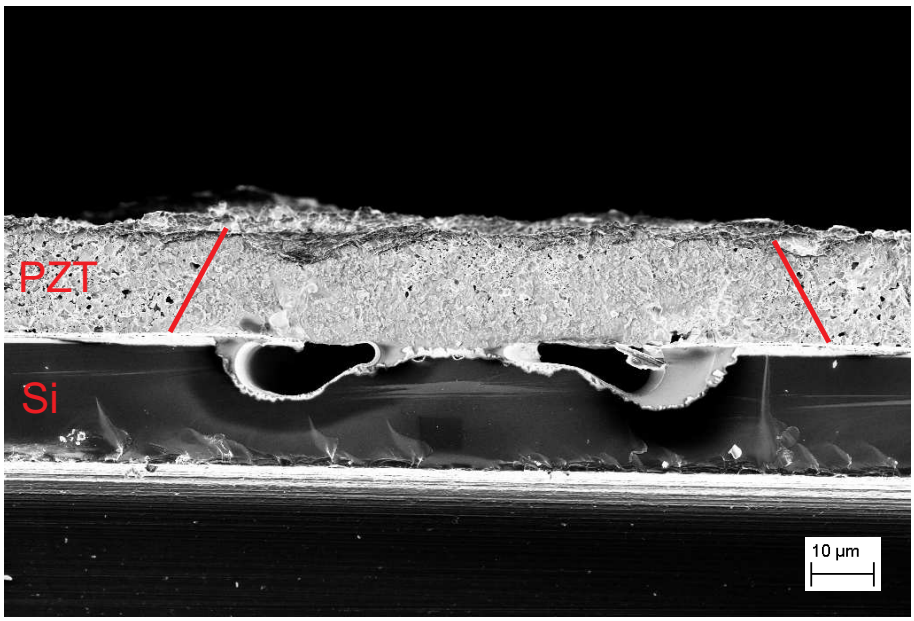

FIGURE 4.32: A cross sectional SEM image showing the inter diffusion between the PZT thick film and the silicon substrate through a purposely constructed opening of 50 μm in width.

for an hour. The relatively low temperature and the thick thermal oxide keep the silicon oxidation to a minimum. The expected thickness t_{final} can be calculated from the density of the Ti (ρ_{Ti}) and TiO_2 (ρ_{TiO_2}), and the molar mass of the Ti (m_{Ti}) and oxygen (m_{O}).

$$t_{\text{final}} = t_{\text{initial}} \frac{\rho_{\text{Ti}}}{\rho_{TiO_2}} \frac{m_{\text{Ti}} + 2m_{\text{O}}}{m_{\text{Ti}}} \tag{4.3}$$

$$t_{\text{final}} = 1.78 t_{\text{initial}} \approx 890\text{nm} \tag{4.4}$$

The actual TiO_2 thickness is measured using profilometry and was found to be a few nanometers above the calculated value. The consistency of multiple measurements on several wafers hints that it is not caused by measurement error but truly a larger thickness. This might caused by the fact that the grown TiO_2 film is not completely stoichiometric, an thus less dense than the ideal density. Attempts to achieve a completely stoichiometric TiO_2 film were made, such as increase of the growth temperature from 600°C to 1000°C, increase of the oxygen flow and an thinner initial Ti layer, but non seems to help. Nevertheless, this almost 900 nm thick TiO_2 was used as a diffusion barrier for the PZT sintering process. The result is disappointing, severe inter diffusion was observed throughout the wafer.

Alumina is widely considered as a good diffusion barrier. Therefore attempt has be made to deposit alumina layer onto the silicon wafer. Due to the low growth rate of alumina [34], sputtering was used to deposit the alumina diffusion barrier. The parameters used in the sputtering process is shown in Tabel 4.8, the deposition rate was found to be

20 nm/hour. Thicknesses between 80-240 nm were deposited to be used at a diffusion barrier. The result is shown in Fig. 4.33, where the screen printed PZT thick film does not adhere to the alumina at all. This may be caused by the low roughness of the alumina thin film.

TABLE 4.8: The sputter parameters used in the alumina deposition process.

Target	Al_2O_3
Bias power [W]	150
RF power [W]	10
Temperature	room temperature
Pressure [mTorr]	5
Flow gas	Ar

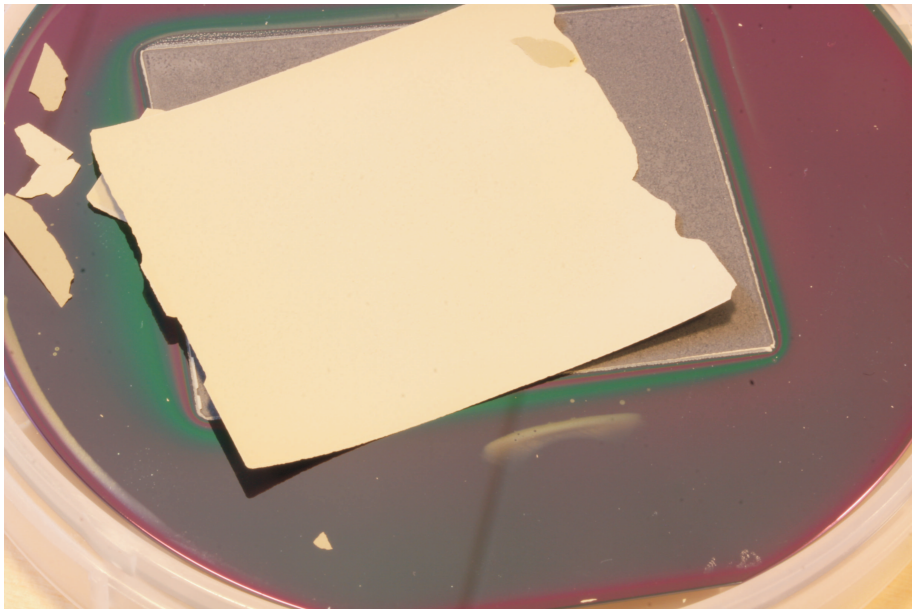

FIGURE 4.33: A photograph showing the result where PZT thick film is screen printed a silicon wafer with alumina diffusion barrier.

Some other candidates for the diffusion barrier are investigated but similarly without any good results.

4.3.2 Adhesion

Adhesion problems are observed from time to time and the consequence of a wafer with bad adhesion is quite severe, which often ends up with discarding of the wafer. The first adhesion problem arises after the PZT sintering process (1st layer of the bimorph structure), where the corners of the PZT thick film layer curves up as it is shown in Fig. 4.34. In order to improve the adhesion an annealing step has being introduced before screen printing. The annealing of the wafer is done in a belt furnace that are

running at 400°C. The idea is that by annealing the Pt bottom electrode larger grains will be formed in the metal and increase its surface roughness thus increase its adhesion to the PZT layer. After the introduction of the annealing step, the adhesion of the PZT have indeed been significantly improved, and is no longer an issue.

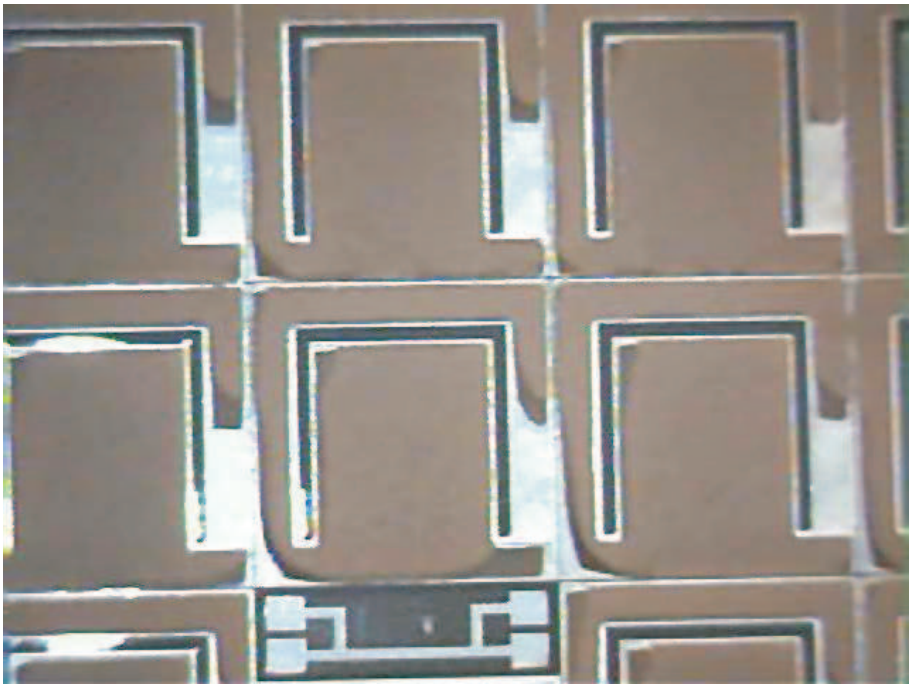

FIGURE 4.34: A photograph showing the corner curvature of the PZT thick film due to bad adhesion of PZT to the bottom electrode.

The second adhesion problem is the bad adhesion between the Pt bottom electrode to silicon, even with the Ti adhesion promoter. This problem rarely occurs, and if it does it is unfortunately first noticeable near the end of the process. As it is shown in Fig. 4.35 the loss of adhesion happens just before the release etch. Various alternative adhesion layers have been tested, such as Cr and titanium tungsten (TiW) alloy. Cr and TiW yield inconclusive results due to the random occurring nature of the problem.

4.3.3 Short circuit through the PZT layer

An initial problem with the some of the fabricated energy harvesters is short circuits through the PZT layer. The short circuiting issue is measurable already after the top electrode is deposited for an unimorph energy harvester and the middle electrode is deposited for a bimorph energy harvester. The resistance between the two electrode can be as low as 0.1 Ω.

The reason for the short circuit was later discovered to be caused by the mask design of **Bottom electrode mask**. The original bottom electrode design is shown in Fig. 4.36,

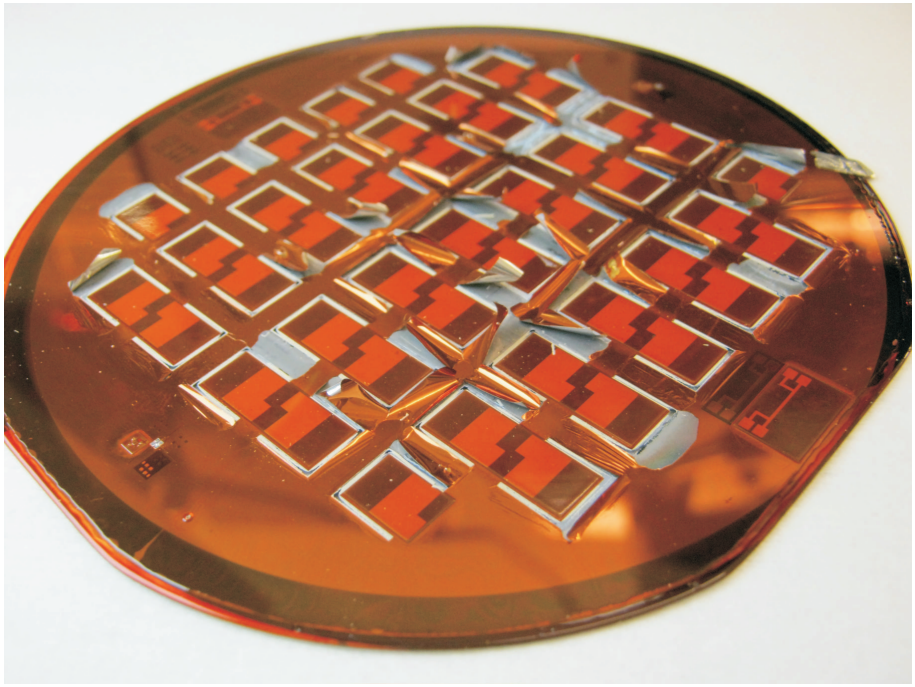

FIGURE 4.35: A photograph showing the bad adhesion of the bottom electrode on the silicon layer.

notice that the Pt layer is removed on rest of the wafer outside the chips. The large open area with silicon causes the silicon to diffused into the PZT thus short circuiting the layer. By leave the Pt layer be on the wafer periphery, as it is shown in Fig. 4.1 the problem was solved.

4.4 Bulk fabrication

One of the strengths of the silicon microtechnology is the advantages of batch processes. Considerations have being made regarding which of the current fabrication processes can be changed to fit better a mass production situation.

The first process that comes to mind is the nitride patterning/removing process. This process takes 6 min on each side, however with wafer loading and gas purging steps, it could take up to 1 hour per wafer. Therefore, the removal of nitride in phosphoric acid H_3PO_4 (85 wt%) at 180°C should be considered. The reported etch rate of nitride in phosphoric acid H_3PO_4 (85 wt%) at 180°C is around 8.4 nm/min, which means the needed etch time is only 20 min Of course photoresist can not be used as masking material, LPCVD TEOS oxide would be an obvious candidate for this purpose.

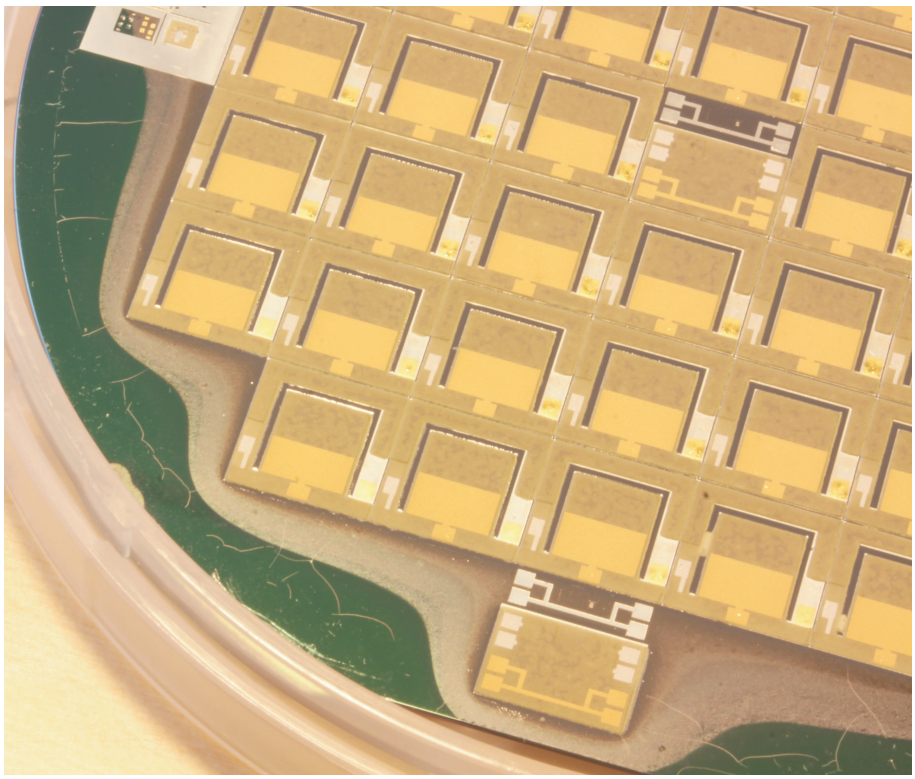

FIGURE 4.36: A photograph of part of the original bimorph energy harvester wafer, where the Pt bottom electrode is removed on the wafer periphery.

The use of a shadow mask is a practical solution, but it is not a good method in bulk fabrication. A spray coater might be a good solution to overcome the need of having good step coverage.

Wafer level polarization was implemented in the original mask design. However, due to the low fabrication yield it was not used and the design was phased out. With the high fabrication yield achieved with the current fabrication process wafer level polarization should be reimplemented.

Chapter 5

Characterization of the harvesters

In this chapter different types of unpackaged energy harvesters are characterized. Two primary methods of characterization are presented. The first one uses the Agilent 4294A impedance analyzer, where the electrical response of the energy harvesters is measured. In this measurement an external AC RMS voltage of 500 mV is applied to the electrodes using probes, the frequency is swept near the resonant frequency of the device and the corresponding impedance magnitude and phase are recorded. In the case of the bimorph energy harvester the response of each individual layer can also be measured. To measure the top layer the probes are connected to the top and middle electrodes, while the bottom electrode is kept in open circuit. Similarly, when measuring the bottom layer the probes are connected to the middle and bottom electrodes, while the top electrode is kept in open circuit. The impedance measurement gives information regarding the resonant frequency, the thick film capacitance, coupling coefficient and the device impedance.

The second characterization method is the shaker measurement, where the transducer property of the energy harvester is measured through the direct piezoelectric effect. In this measurement a shaker is used to simulate an external vibration, the energy harvester transforms some of this mechanical energy to electrical energy, which is dissipated in an external electric load. The applied vibration is a harmonic oscillation with a frequency and an acceleration. During measurements the frequency is swept near the resonant frequency with a resolution of 0.1 Hz at different accelerations. Furthermore, the effect of the spring softening in the harvester will be presented and its effect on the measurements is discussed.

5.1 The shaker measurement setup

The components in the shaker measurement setup are shown in Fig. 5.1, where all the vital components are marked and explained. The Brüel & Kjær type 4810 mini-shaker (Fig. 5.1(c)) is used to simulate the ambient vibration from the harvesting environment. The vibration waveform is generated by the Agilent 33220A 20kHz Arbitrary Function Generator (Fig. 5.1(a)), which is connected directly to the measurement computer through an USB port. The vibration waveform is then amplified by the Pioneer VSX-405RDS Mk II audio amplifier, see Fig. 5.1(b). The energy harvester (Fig. 5.1(g)) and a Brüel & Kjær standard piezoelectric reference accelerometer type 8305 (Fig. 5.1(d)) are mounted on the mini-Shaker. The accelerometer is used to measure the acceleration generated by the mini-shaker. The reference accelerometer is connected to the charge amplifier (Fig. 5.1(e)), which is powered by the DC power supply shown in Fig. 5.1(f). The output voltage from the charge amplifier is measured in the data acquisition (DAQ) box (Fig. 5.1(i)) and the data are collected in the measurement computer (Fig. 5.1(j)), which is used to calculate the reference acceleration. The energy harvester is connected in parallel to an external resistor, as it is shown in Fig. 5.1(h), the voltage drop can similarly be measured in the DAQ box and the result is collected in the measurement computer. The output power from the energy harvester can then be calculated as the dissipated power in the external load R,

$$P_{\mathrm{RMS}} = \frac{V_{\mathrm{RMS}}^2}{R}, \tag{5.1}$$

where P_{RMS} and V_{RMS} are the root mean square power and voltage, respectively. Notice that in this case the internal resistance of the DAQ box of 50 MΩ is ignored, since it is more than 2 orders of magnitude larger than the load normally used as the external resistor. For the same reason the voltage measured without the external resistor is considered open circuit voltage.

5.1.1 The acceleration measurement

The measurement scheme of the acceleration is shown in Fig. 5.2. The actual reference accelerometer is represented by a charge source q connected in parallel with a capacitor C_{a}. The electric cable has its own internal capacitance C_{c} and resistance R_{c}. The charge amplifier consists of an operational amplifier supplied by +10V on one side and -10V on the other, a range capacitor C_{r} and a time constant resistor R_{t}.

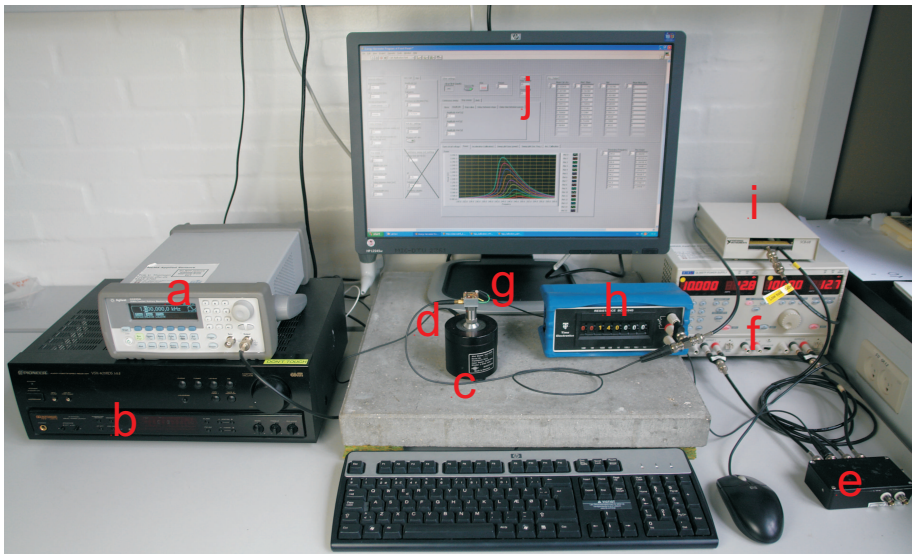

FIGURE 5.1: A photograph of the shaker measurement setup. The setup consists of a) Agilent 33220A 20kHz Arbitrary Waveform Generator, b) Pioneer VSX-405RDS Mk II audio amplifier, c) Brüel & Kjær type 4810 mini-shaker, d) Brüel & Kjær standard piezoelectric reference accelerometer type 8305, e) Charge amplifier with "TL081CP" operation amplifier, f) DC power supply for the operation amplifier in the charge amplifier, g) energy harvester, h) Time Electronics decade resistor 1040, i) National Instruments data acquisition box, j)The measurement computer running LabVIEW.

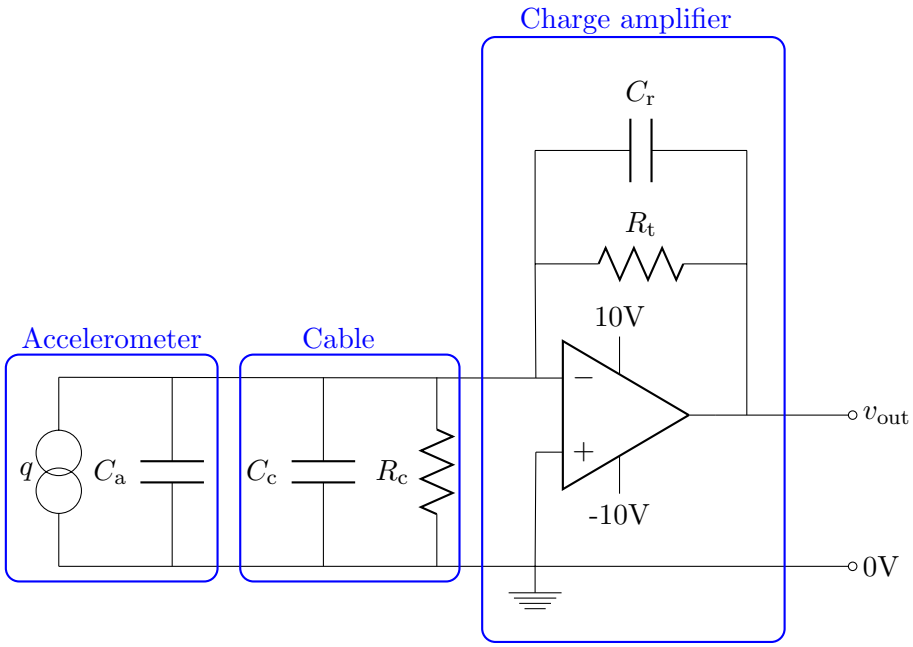

FIGURE 5.2: A sketch of the circuit diagram for the reference acceleration measurement scheme, which include the reference accelerometer, cables and the charge amplifier.

Using the theory of the operation amplifier, the output voltage is given by

$$V_{\text{out}} = I_{\text{in}} Z \tag{5.2}$$

where I_{in} is the input current between plus and minus in the operational amplifier and Z is the impedance in the feedback loop. By ignoring the effect of the cable, the input current becomes

$$q = C_{\text{a}} V_{\text{in}} \tag{5.3}$$

$$I_{\text{in}} = \dot{q} = C_{\text{a}} \dot{V}_{\text{in}} \tag{5.4}$$

where is q is the charge signal from the accelerometer and V_{in} is the corresponding open circuit voltage. C_{a} is the internal crystal capacitance. Using the generalized impedance concept in frequency domain, V_{out} is found to be

$$V_{\text{out}} = j\omega C_{\text{a}} V_{\text{in}} \left(\frac{R_{\text{t}}}{1 + j\omega C_{\text{r}} R_{\text{t}}} \right) \tag{5.5}$$

$$= \frac{j\omega C_{\text{a}} R_{\text{t}}}{1 + j\omega C_{\text{r}} R_{\text{t}}} V_{\text{in}} \tag{5.6}$$

where $\omega = 2\pi f$ is the angular frequency. If $\omega C_{\text{r}} R_{\text{t}}$ term in the denominator is sufficiently larger than 1, Eq. 5.5 can be rewritten to

$$V_{\text{out}} = \frac{C_{\text{a}}}{C_{\text{r}}} V_{\text{in}}. \tag{5.7}$$

By combining it with Eq.5.3 and the fact that the accelerometer sensitivity S_{a} is given as

$$S_{\text{a}} = \frac{q}{a}, \tag{5.8}$$

a resulting acceleration a is found to be

$$a = \frac{C_{\text{r}}}{S_{\text{a}}} V_{\text{out}}. \tag{5.9}$$

The accelerometer sensitivity is $S_{\text{a}} = 0.92$ pC/g and a 180 pF range capacitor is used. Furthermore, the output voltage from the charge amplifier V_{out} is measured as a RMS value, thus the calculated acceleration is also given in RMS

$$a_{\text{RMS}} = 196 \frac{g}{\text{V}} \times V_{\text{out,RMS}}. \tag{5.10}$$

The measured accelerations are reported in fractions of the gravitational acceleration g (9.81 m/s^2).

The cut-off frequency of the system is determined by condition that

$$1 = \omega C_{\mathrm{r}} R_{\mathrm{t}} \Leftrightarrow \tag{5.11}$$

$$f = \frac{1}{2\pi C_{\mathrm{r}} R_{\mathrm{t}}} = 68\mathrm{Hz}, \tag{5.12}$$

where a time constant resistor $R_{\mathrm{t}} = 13\mathrm{M}\Omega$ is used. A cut-off frequency of 68 Hz will suffice since the lowest resonant frequency measured on the energy harvesters are around 160 Hz.

5.2 Softening effect

The PZT softening effect is almost always observed when high voltage or large deflection are involved [35–38]. This material softening effect is also observed when measuring the harvesters in the shaker setup. The effect has several characteristics, such as

- the peak power frequency reduces as the acceleration increases
- an asymmetric peak shape
- the peak shape is dependent on the frequency sweep direction.

The effect of the frequency sweep direction is shown in Fig. 5.3, where voltage is measured at 3 different RMS accelerations, 0.2 g, 0.6 g and 1.0 g. The sweep direction is noted as up for going from lower frequencies to higher frequencies and down, which is from higher frequencies to lower frequencies. Notice that the up sweep directions give a smaller bandwidth compared their down sweep counterparts. The effect also seems to be more severe at higher acceleration level. The rest time between each frequency change is set to 50 ms, by increase of the rest time one might suspect the effect of down and up sweep would be reduced. This was not the case however, no significant changes were observed by increase of the rest time to 500 ms, 1000 ms or even 1500 ms, as it is shown in Table 5.1. Therefore the standard 50 ms rest time is still used.

Another interesting phenomenon is the bad reproducibility when doing the frequency up sweep as it is shown in Fig. 5.4, where three repeating up sweep measurements and three down sweep measurements are conducted. Notice that the down sweep measurements are pretty much on top of each other as expected, whereas the up sweep measurements differs near the peak power frequency. This is believed to be caused by the sensitivity to the starting condition due to the softening effect, which is a non linear effect. Since the down sweep seems to be less sensitive to small deviations in the starting condition, therefore the down sweep measurement is used as standard.

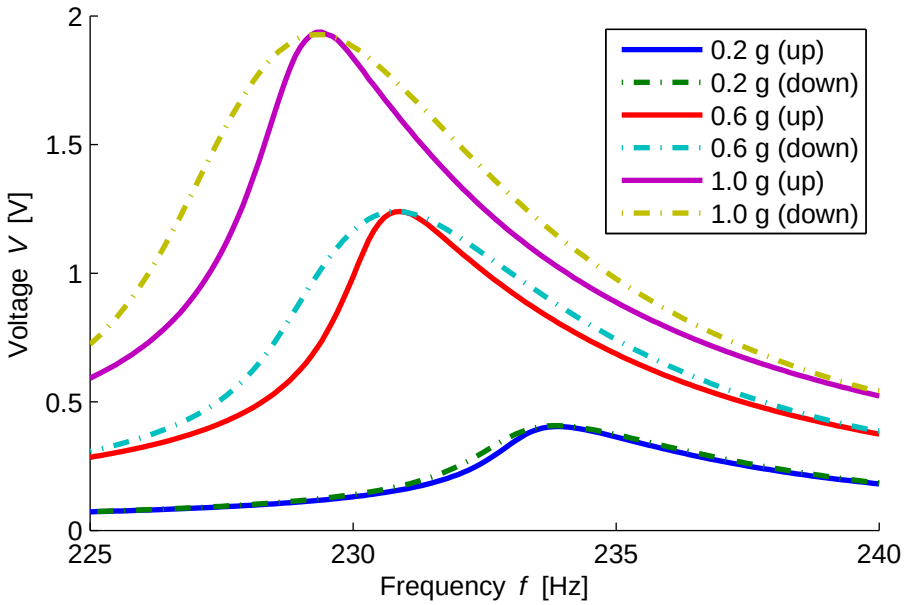

FIGURE 5.3: The effect of frequency sweep direction of an unimorph energy harvester is shown in this plot. The open circuit voltage is measured as a function of different accelerations and frequency sweep directions.

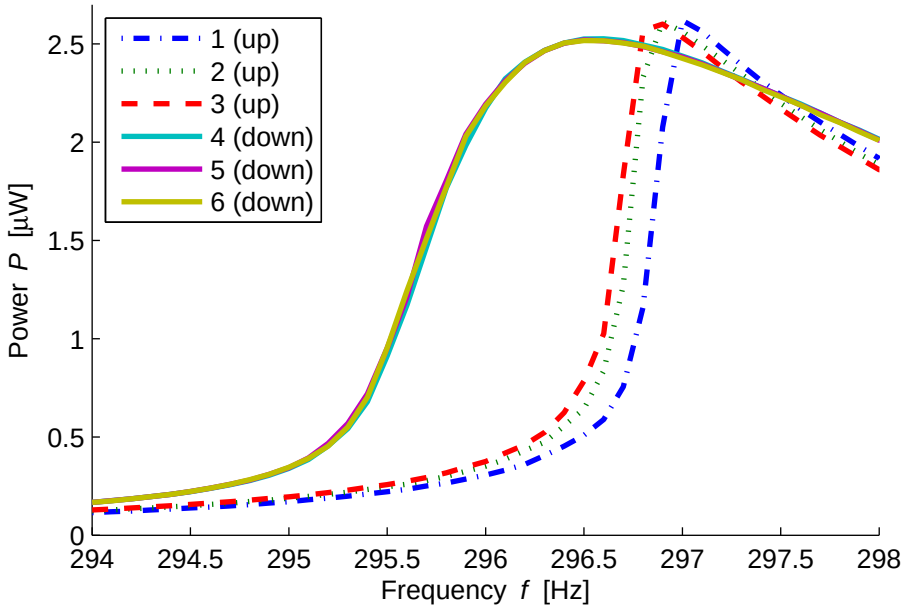

FIGURE 5.4: The power as a function of the frequency is plotted, with three up sweep measurements and three down sweep measurements.

TABLE 5.1: The bandwidth BW of a harvester is measured with different rest times between each frequency steps. The bandwidth BW is defined here as full width at half maximum of the power output peak.

Rest time [ms]	Up sweep BW [Hz]	Down sweep BW [Hz]
50	3.0	3.8
200	3.0	3.6
350	3.0	3.6
500	3.0	3.6
1000	3.0	3.8
1500	3.2	3.6

To further understand the non linearity of the softening effect a simple model is postulated, where the effective spring constant k_{eff} is defined as

$$k_{\text{eff}} = k_0 + k_2 w^2, \tag{5.13}$$

where k_0 is the linear spring constant, which is dominant at low cantilever deflection w and k_2 the non linear term. Since it is a softening effect k_2 should be less than zero in order to reduce the effective spring constant. Integrating the effective spring constant into the harmonic oscillator yields the Duffing equation

$$m\ddot{w} + b\dot{w} + k_0 w + k_2 w^3 = F_{\text{ext}} \sin(2\pi f t) \tag{5.14}$$

where w is the cantilever deflection, m is the proof mass, b is the damping, F_{ext} is the external force, f is the input frequency and t is time. To investigate the systems frequency response to confirm the observed results, a Matlab calculation is made. The idea of this Matlab calculation is to introduce a linear chirp on the input frequency in Duffing oscillator, *i.e*

$$\ddot{w} + \frac{\omega_0}{Q}\dot{\omega} + \omega^2 w + \frac{k_2}{m} w^3 = a_{\text{ext}} \sin(2\pi(f_0 + \frac{r}{2}t)t) \tag{5.15}$$

where r is the chirp rate and f_0 is the starting frequency. Notice that Eq. 5.15 has been rewritten for easier calculation, so the damping is represented by the quality factor and the linear spring constant k_0 is part of the mechanical angular resonant frequency ω_0. To demonstrate the effect of the softening effect the quality factor is set to $Q = 100$ and the angular resonant frequency $\omega_0 = 2\pi \cdot 250\text{Hz}$, $k_2 = -10^7 \frac{\text{N}}{\text{m}^3}$ and proof mass $m = 25\text{g}$. The initial conditions are set to be

$$w(t = 0) = 0 \tag{5.16}$$

$$\dot{w}(t = 0) = 0. \tag{5.17}$$

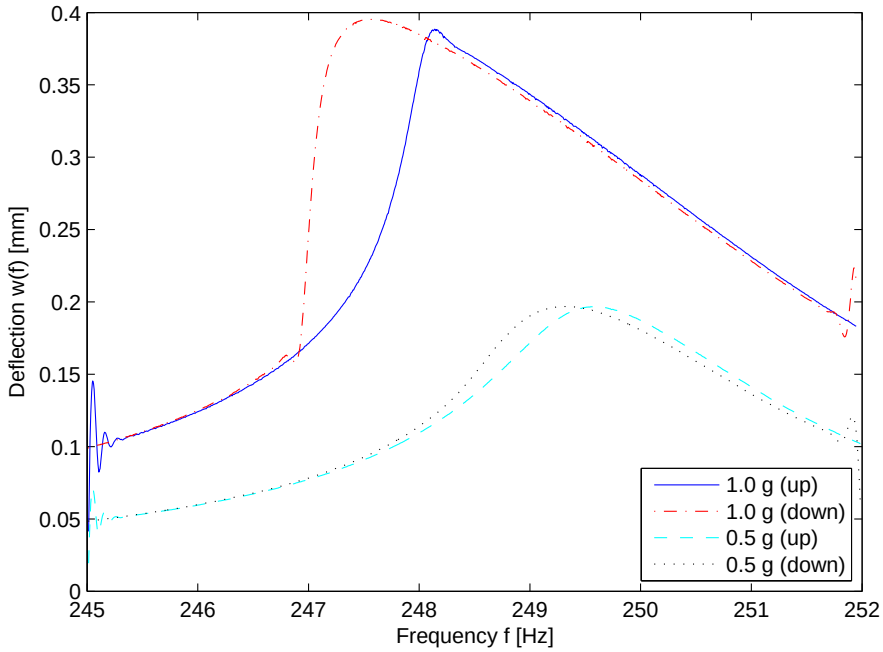

FIGURE 5.5: The solution to the chirped duffing oscillator with up and down sweeps.

The chirp rate is set to $r = \frac{1}{2}\mathrm{s}^{-2}$ and the dependent of whether it is up or down sweep the chirp rate can be either positive or negative. The resulting calculations are shown in Fig. 5.5, the up sweep starts at 245 Hz and ends at 252 Hz and the down sweep starts at 252 Hz and ends at 245 Hz. The fluctuations at 245 Hz for up sweep and 252 Hz for down sweep is caused by the transient of the initial conditions. Notice that all three of the aforementioned softening characteristics are present in this simulation. The asymmetry of the deflection peak is present and is more significant at 1.0 g acceleration than 0.5 g. The difference of the frequency sweep direction is clearly shown in Fig. 5.5. The decrease in the peak frequency as a consequence of the increased acceleration is also shown.

Furthermore, to confirm that the effect is truly a mechanical effect the beam deflection is also measured using a Micro-Epsilon laser sensor ILD1401-5 with a sampling rate of 1 kHz. In this measurement the laser sensor is mechanically fixed. The laser spot hits the harvester proof mass and the reflection is detected in an build-in CCD camera, thus the position of the proof mass can be determined. Notice that since the laser sensor is not mounted on the shaker, there is a small error of a few microns caused by the movement of the shaker. However, the error is comparable to the laser sensors resolution of 3 μm and is considered insignificant. The measurement is first done where the electrodes are short circuited, doing so only the mechanical properties are measured. The frequency is swept first upwards then later downwards. The registered maximum deflection where the cantilever is at its most upward position, *i.e.* closest to the detector is noted to be

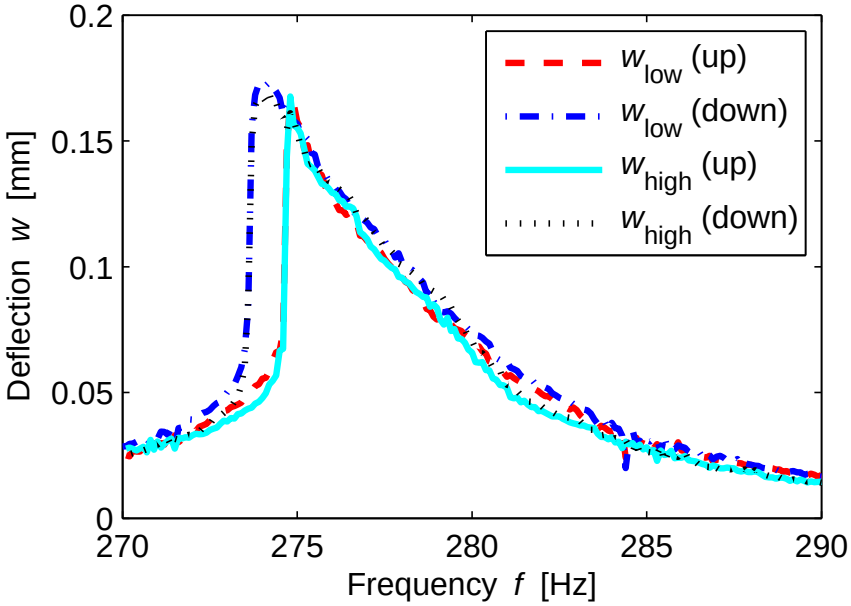

FIGURE 5.6: The proof mass deflection w is measured at 0.5 g input acceleration near the resonant frequency, and the electrodes are short circuited. The frequency is swept downwards. w_{low} is the maximum deflection when the beam is bending upwards and w_{high} is the maximum deflection when the beam is bending downwards.

w_{low}. Similarly, the registered maximum deflection where the cantilever is at its most downward position, *i.e.* furtherest away from the detector is noted to be w_{high}. The resulting deflection measurement at 0.5 g input acceleration is shown in Fig. 5.6. If the electrodes are kept in open circuit, the open circuit voltage V_{oc} can be measured along with the deflections, and the results are shown in Fig. 5.7 and 5.8. These figures clearly shows that the earlier observed softening effect indeed is a mechanical effect which manifested into an electrical effect though piezoelectric coupling, since there is almost a one to one correlation between the deflection and the open circuit voltage.

5.3 Bimorph energy harvesters

In this section results from some types of the bimorph energy harvesters will be presented. Some of the interesting observations are discussed.

5.3.1 Non pressure treated PZT thick film

Few energy harvesters are fabricated with non pressure treated PZT thick film bimorph cantilever beam, this is due to the development of the KOH etch process, which removes the advantage of not pressure treating the PZT thick film. However, some of the data will be presented for later comparison with the high pressure treated PZT energy harvesters.

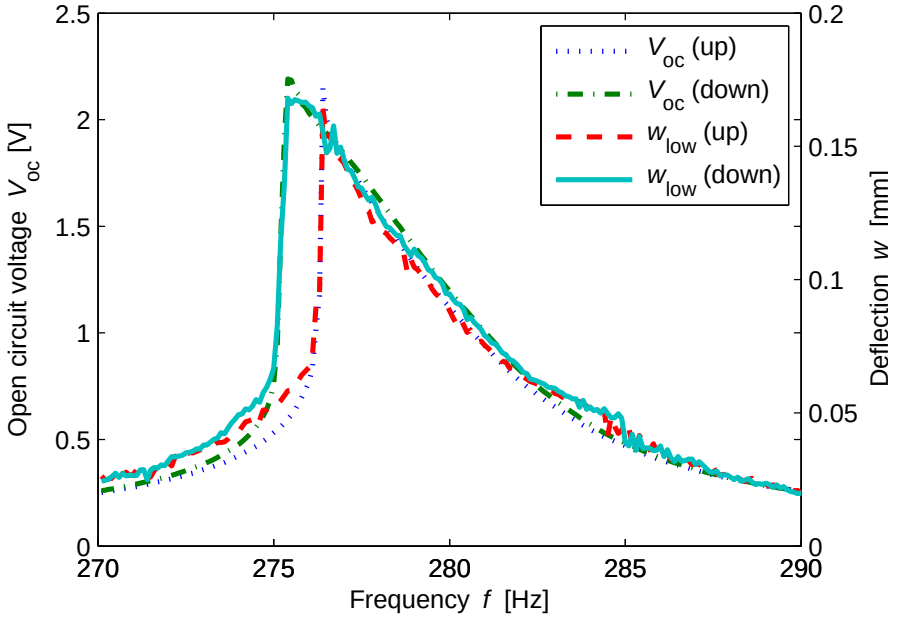

FIGURE 5.7: The proof mass deflection w is measured at 0.5 g RMS input acceleration near the resonant frequency, the open circuit voltage is measured simultaneously. The frequency swept first upwards then later downwards. w_{low} is the maximum deflection when the beam is bending upwards.

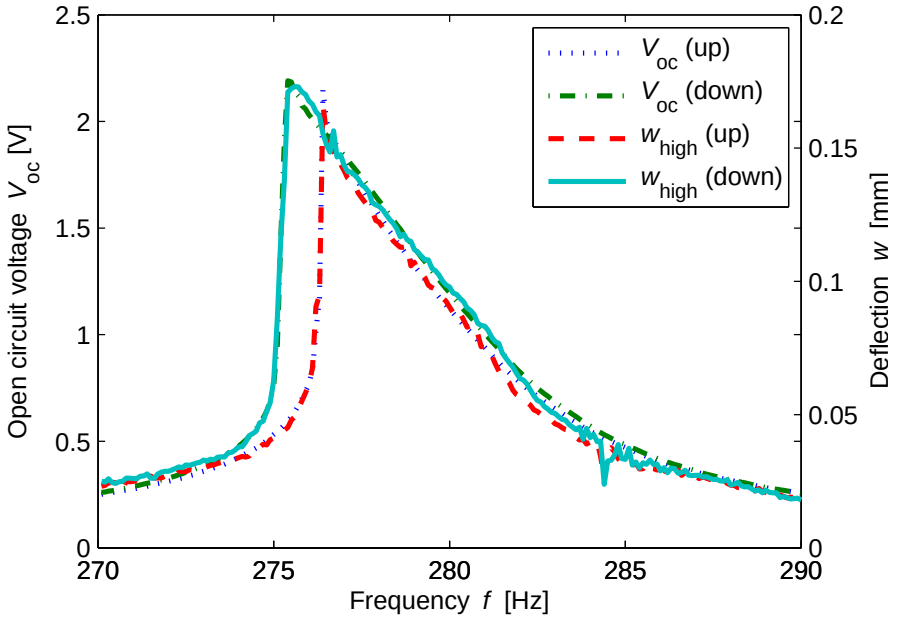

FIGURE 5.8: The proof mass deflection w is measured at 0.5 g RMS input acceleration near the resonant frequency, the open circuit voltage is measured simultaneously. The frequency swept first upwards then later downwards. w_{high} is the maximum deflection when the beam is bending downwards.

Some of the work done regarding the non pressure treated PZT thick film bimorph harvesters were presented in [19, 28].

The chip type presented here has a total PZT thick film thickness of 60 μm, *i.e.* each PZT layer is approximately 30 μm thick. The mass to total length ratio is $\alpha = 70\%$. The results from the impedance measurements are shown in Fig. 5.9, 5.10 and 5.11. The effect of both layers are measured in Fig. 5.9, where the two probes from the impedance analyzer are in contact with the bottom and top electrodes, respectively. The effect of the bottom PZT layer is measured in Fig. 5.10, where the probes are in contact with the bottom and middle electrodes, leaving the top electrode in open circuit. The effect of the top PZT layer is measured in Fig. 5.11, where the probes are in contact with the top and middle electrodes, leaving the bottom electrode in open circuit. The electrical behavior of the PZT layer are similar for a capacitor when the frequency is away from resonance, since the contribution from the mechanical part is negligible. Near resonance the signal is dominated by the mechanical effects, where there are two characteristic peaks, the resonance peak and the anti-resonance peak. At the resonance peak the impedance is at its lowest, this is due to the fact that the mechanical inductance (the proof mass) and the mechanical capacitance (the reciprocal spring constant) cancel out each other, only leaving the mechanical damping as explained in chapter 3. The anti-resonant peak is when the impedance is at its highest near resonance, this is caused by the effect of the capacitance acting as an additional mechanical spring due to the piezoelectric coupling. From the resonance and the anti-resonance peak the effective couplings coefficient can be calculated [14],

$$K_{\text{eff}} = \sqrt{\frac{f_{\text{a}}^2 - f_0^2}{f_0^2}} \tag{5.18}$$

where f_{r} is the resonance frequency and f_{a} is the anti-resonance frequency.

The effective piezoelectric coupling coefficient is measured to be 0.127, as it is shown in Table 5.2. The theoretical value $k_{31} = \sqrt{\frac{d_{31}^2}{s_{11}\varepsilon_{33}}}$ can be calculated by using the value given in Table 2.2 in Chapter 2, and the value is 0.20. Though it is expected that the effective coupling coefficient would be smaller that k_{31}, the difference also can be caused by other various reasons, such as overestimation of the material parameters and so on. However, there seems to be no difference between the measured piezoelectric coupling coefficient on both layers, bottom layers or top layers. It is believed that if the other layer is short circuited instead of been kept in open circuit there should be a difference.

Table 5.2 also shows the optimal resistive load and the measured capacitance. Note that the optimal resistive load R_{opt} is the load where the highest power is achieved, and is optimized in the shaker measurement at $a = 0.5$ g where frequency sweeps are done for

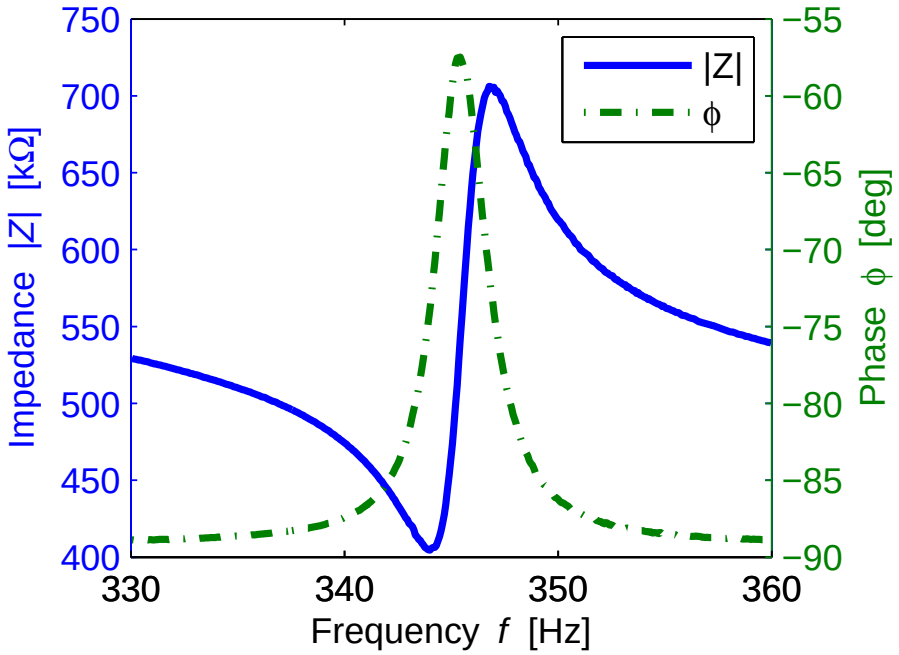

FIGURE 5.9: A typical impedance measurement on a bimorph energy harvester with non pressure treated PZT thick films. In this case the two probes from the impedance analyzer are contacting the bottom and top electrode, respectively. This way the effect from both layers are measured.

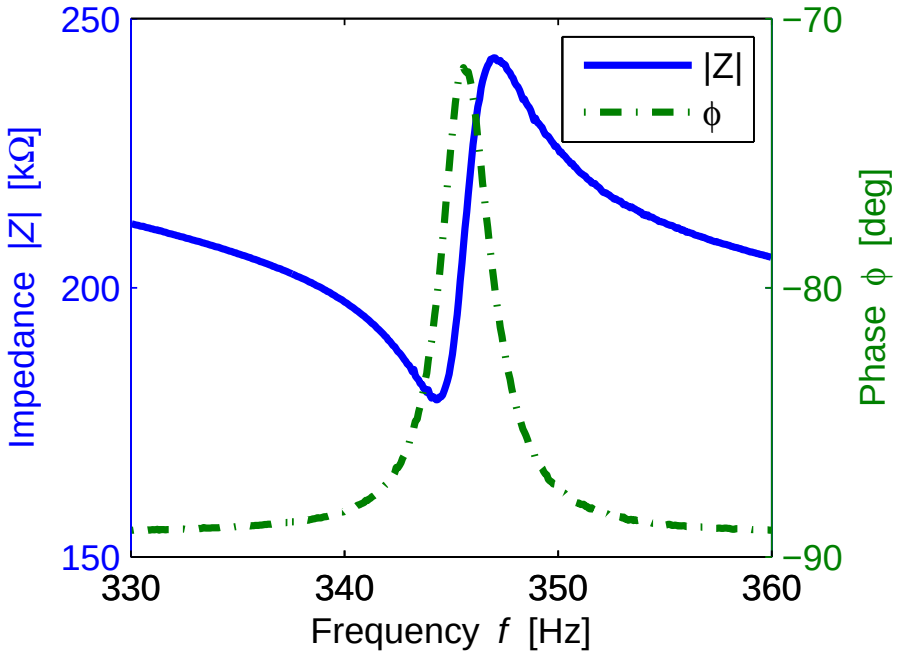

FIGURE 5.10: A typical impedance measurement on a bimorph energy harvester with non pressure treated PZT thick films. In this case the two probes from the impedance analyzer are contacting the bottom and middle electrode, respectively. This way the effect of the bottom PZT layer is measured.

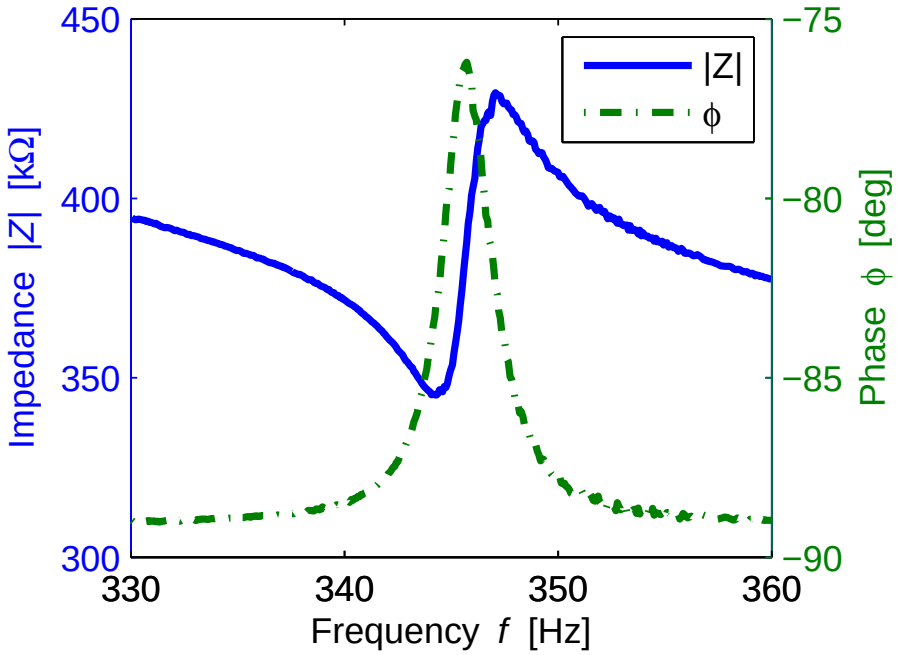

FIGURE 5.11: A typical impedance measurement on a bimorph energy harvester with non pressure treated PZT thick films. In this case the two probes from the impedance analyzer are contacting the top and middle electrode, respectively. This way the effect of the top PZT layer is measured.

increasing loads with a step value of 10 kΩ. The capacitance is measure using a simple multimeter. The difference in the optimal resistive load and the capacitance between the top and the bottom layer is indeed interesting. This means that there is a difference between the two PZT thick film layers. Using the plate capacitor approximation the expected capacitance should be around 3 nF, which is between the measured value of the two capacitors. It might be caused by the second sintering process done to the bottom PZT layer causing the film to shrink further thus reducing the film thickness. This is somewhat confirmed by a SEM cross sectional image shown in Fig. 5.12 where the bottom PZT layer does seem to be thinner than the top layer. The difference can also partially be explained by the parasitic capacitance of the middle electrode contact pad. Note that since the bottom electrode is used as a diffusion barrier, it covers all the areas below the PZT layers. When measuring the capacitance using the bottom electrode, there will be a parasitic capacitance from the other electrode contact pad, this will contribute to an increase in the capacitance and thus a decrease in the optimal resistive load. The capacitance of the top PZT layer is measured between the middle and top electrodes. Since their electrode contact pads are not directly on top of each other the only parasitic capacitance will be the fringing fields, which can be ignored in this case.

The result of the shaker measurement for both PZT layers is shown in Fig. 5.13. In this measurement the advantage of the series bimorph structure is used, since the PZT

TABLE 5.2: The summarized results of bimorph energy harvester with 30 μm PZT bottom layer and 30 μm PZT top layer. The mass to cantilever length is $\alpha = 70\%$.

Parameters	Both layers	Bottom layer	Top layer
K_{eff}	0.127	0.125	0.127
R_{opt} [kΩ]	400	180	350
C [nF]	1.45	3.33	2.24
f_{r} [Hz]	344.0	344.3	344.3
f_{a} [Hz]	346.8	347.0	347.1

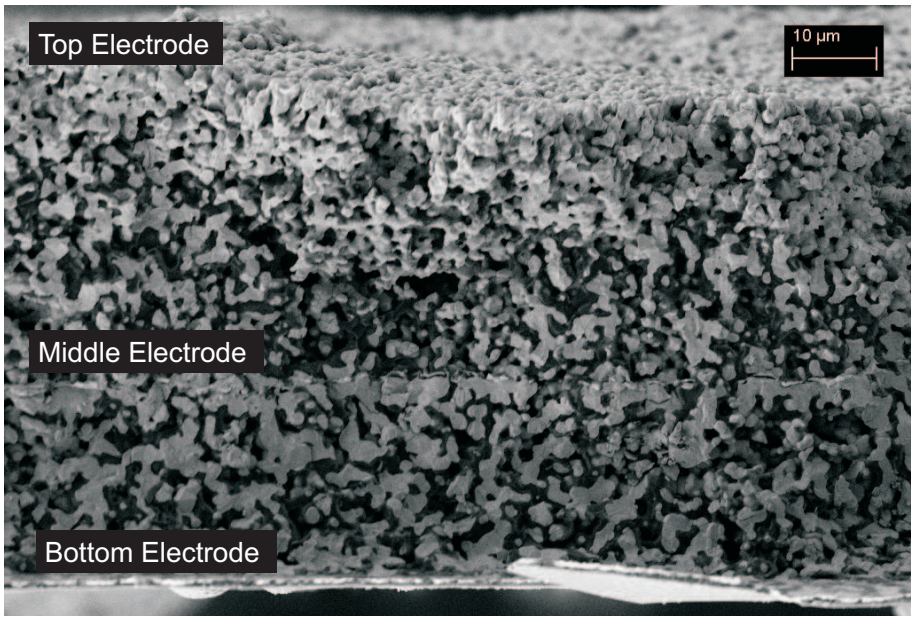

FIGURE 5.12: A cross sectional SEM image of the non pressure treated PZT bimorph cantilever.

layers are oppositely polarized, just by contacting to the top and bottom electrodes the power generated in both layers is collected. The optimal resistive load used in this case is the one that was measured in the impedance analyzer, *i.e.* 400 kΩ, since no significant increase in power was observed by change the load. The harvested power at $a = 1$ g is at 7.4 μW. This value is within the expectation for the bimorph energy harvester with PZT thick film that has not been high pressure treated, since the earlier versions of non pressure treated unimorph energy harvesters have output powers around 1-3 μW [26]. By only contacting the bottom and middle electrodes and leaving the top electrode in open circuit the output power of the bottom PZT layer can be measured and the result is shown in Fig. 5.14, with a resistive load of 180 kΩ. Similarly, the top PZT layer is measured by contacting to the top and middle electrodes and leaving the bottom electrode in open circuit, see Fig. 5.15. A resistive load of 350 kΩ is used here. The results are somewhat interesting, the bottom PZT layer actually performed better than the top PZT layer. The harvested power at $a = 1$ g is 5.4 μW for the bottom layer and only 3.6 μW for the top layer. This suggests that the second sintering of the bottom

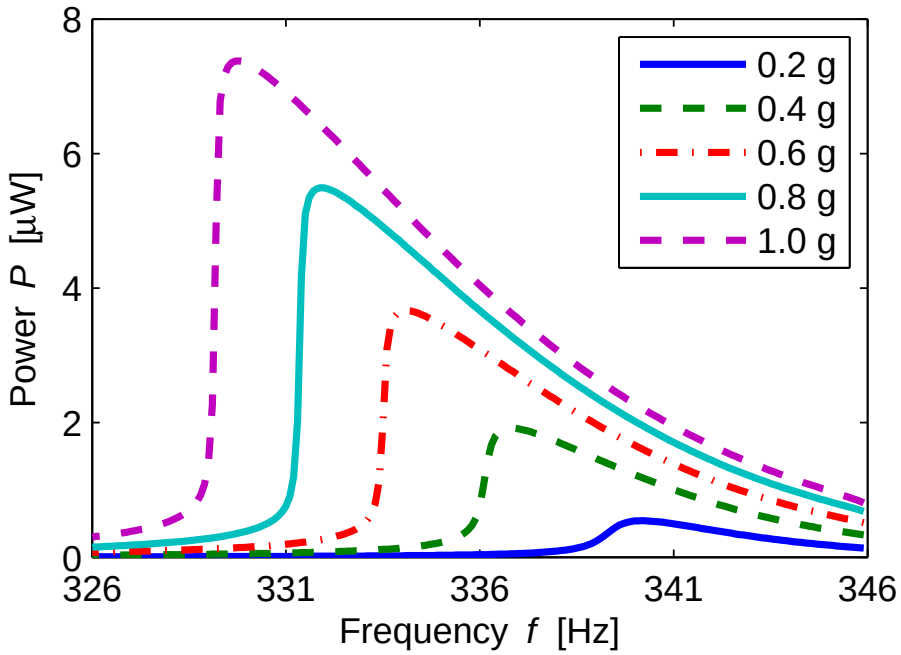

FIGURE 5.13: Power output of both PZT layers as a function of the excitation frequency for different accelerations. The top electrode was connected to the bottom electrode through a resistive load of 400 kΩ.

layer might actually improve its performance. Notice that the power output measured on both layers is less than the sum of the top and bottom layer measured separately, the difference is due to the difference in the used optimal resistive load and the increased system coupling coefficient. The maximum power output can be collected from the Fig. 5.13, 5.14 and 5.15 and plotted as a function of the input acceleration, as it is shown in Fig. 5.16. It is noted from Fig. 5.16 that the advantage of the bimorph structure is not observed at low input acceleration, a possible explanation will be discussed later.

One of the spring softening effects is seen in Fig. 5.13, 5.14 and 5.15, where the peak power frequency decreased with increasing acceleration. These data are collected and plotted in Fig. 5.17. Note that the difference in the peak power frequencies for the measurements on the different layers seems to be small as expected, the changes in the frequencies due to the input accelerations are clearly dominant. The change in the peak power frequency is around 3.0% from 0.2-1.0 g. Note that though the peak power frequency is expected to be between the resonant frequency and the anti-resonant frequency as it is discussed in chapter 3, it is however not the case. This is believed to be caused by the aforementioned softening effect.

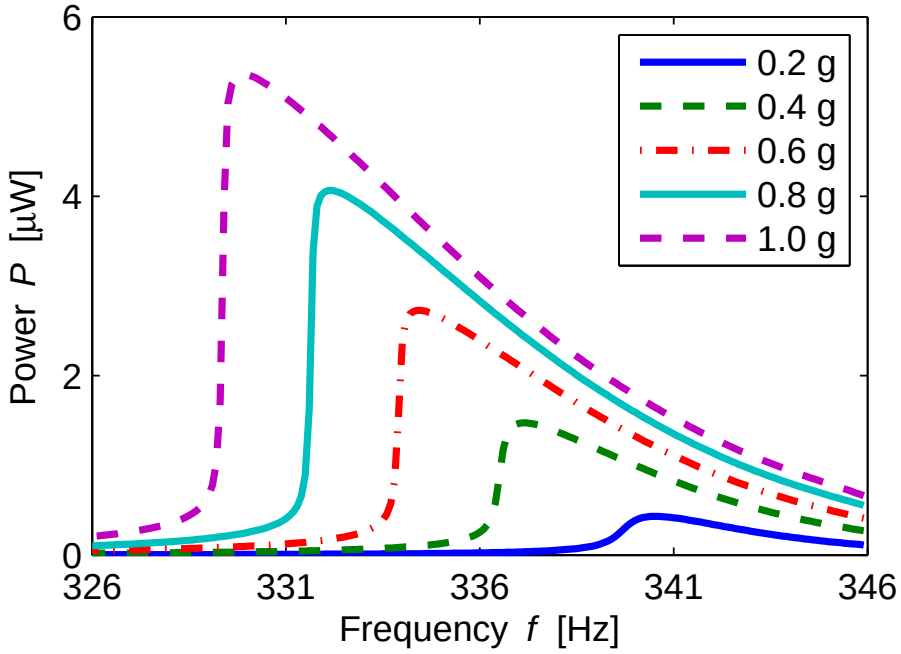

FIGURE 5.14: Power output of the bottom PZT layer as a function of the excitation frequency for different accelerations. The middle electrode was connected to the bottom electrode through a resistive load of 180 kΩ, the top electrode is kept in open circuit.

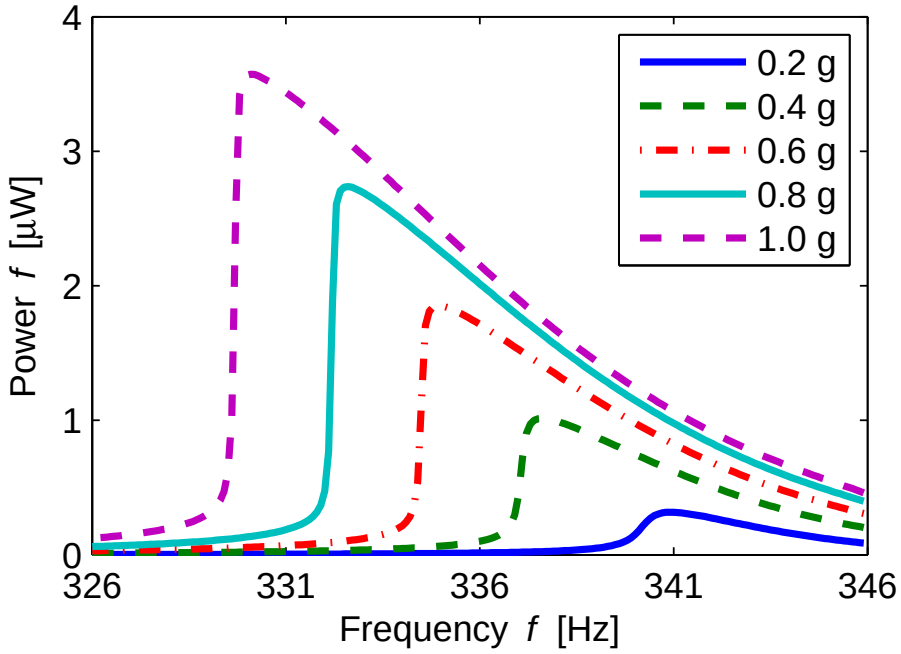

FIGURE 5.15: Power output of the top PZT layer as a function of the excitation frequency for different accelerations. The top electrode was connected to the middle electrode through a resistive load of 350 kΩ, the bottom electrode is kept in open circuit.

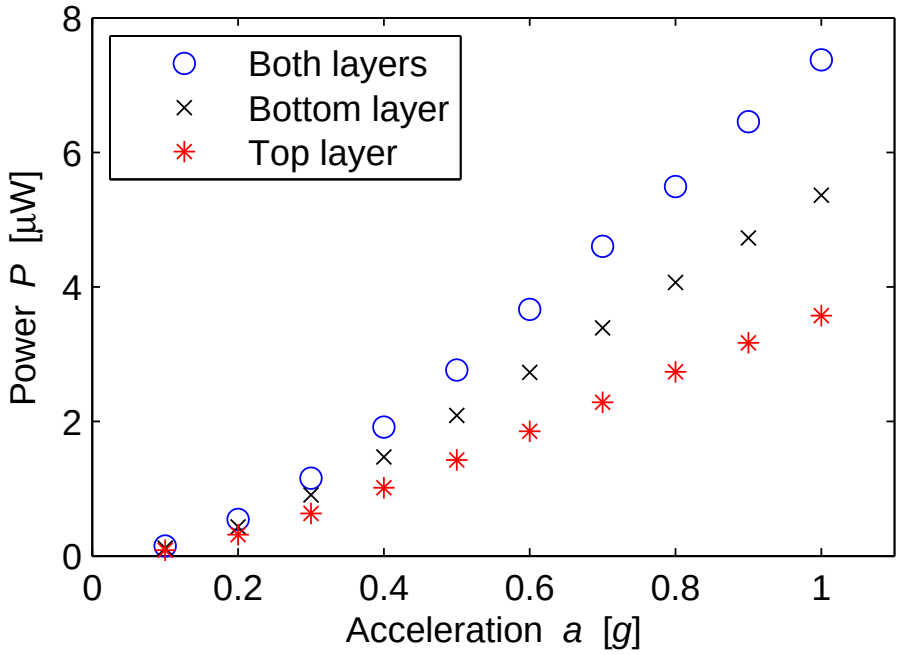

FIGURE 5.16: The power output at resonance is plotted as a function of the input acceleration for measurements on the top layer, bottom layer and both layers.

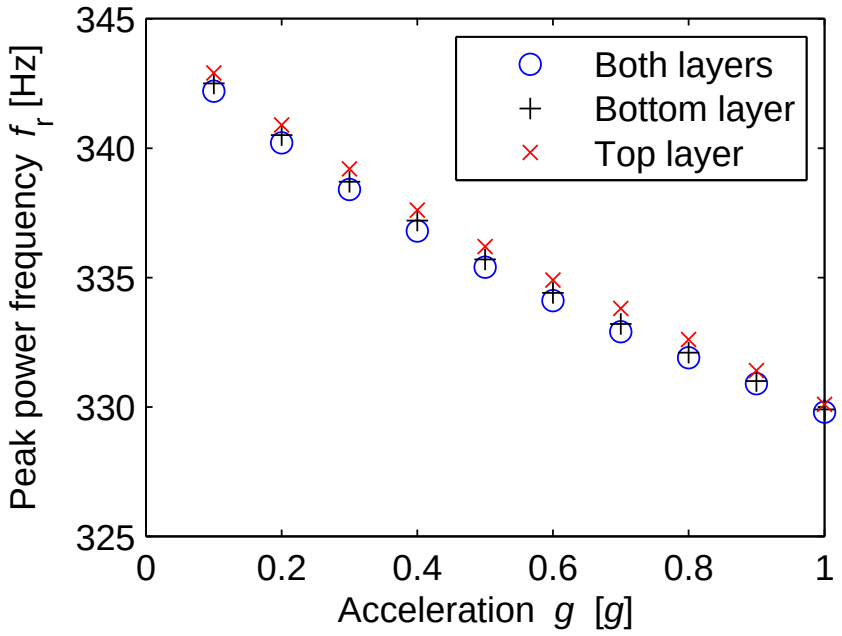

FIGURE 5.17: The peak power frequencies are shown as a function of the input acceleration for measurements on the top layer, bottom layer and both layers.

5.3.2 High pressure treated PZT thick film

In this section the high pressure treated PZT thick film energy harvester will be presented. Some of the works done regarding the high pressure treated PZT thick film bimorph harvesters were presented in [17, 19]. Furthermore, the effect of different mass to length ratio $\alpha = 50\%$ and $\alpha = 70\%$ will be discussed here. First, two chips with cantilever thickness of 40 μm will be presented in detail, where one (harvester 1) has $\alpha = 70\%$ and the other (harvester 2) has $\alpha = 50\%$. The effect of the cantilever beam thickness will also be shown, where the results from three different wafers with different PZT thickness will be shown and discussed.

The data collected are shown in Table 5.3 and 5.4. The piezoelectric coupling coefficient should be 0.28 for the high pressure treated thick film, the measured value is 0.216 for $\alpha = 70\%$ and 0.186 for $\alpha = 50\%$ when measuring on both layers. When measuring on single layer a decrease in the coupling coefficient is indeed observed here.

TABLE 5.3: The summarized results of high pressure treated bimorph energy harvester with 20 μm PZT bottom layer and 20 μm PZT top layer. The mass to cantilever length is $\alpha = 70\%$.

$\alpha = 70\%$	Both layers	Bottom layer	Top layer
K_{eff}	0.216	0.174	0.174
R_{opt} [kΩ]	250	150	180
C [nF]	2.05	5.12	2.81
f_{r} [Hz]	253.9	255.1	255.2
f_{a} [Hz]	260.0	259.1	259.2

TABLE 5.4: The summarized results of the high pressure bimorph energy harvester with 20 μm PZT bottom layer and 20 μm PZT top layer. The mass to cantilever length is $\alpha = 50\%$.

$\alpha = 50\%$	Both layers	Bottom layer	Top layer
K_{eff}	0.186	0.140	0.146
R_{opt} [kΩ]	200	90	130
C [nF]	2.73	7.08	4.16
f_{r} [Hz]	244.3	245.9	245.7
f_{a} [Hz]	248.5	248.3	248.3

The shaker measurement of harvester 1 is shown in Fig. 5.18, where the performance of both layers of the harvester is presented. The achieved power output at 1 g is 37 μW which is significantly higher than its non high pressure treated counterpart. Furthermore, the asymmetry caused by the softening effect is also less prominent compared Fig. 5.13. The decrease in the peak power frequency with increasing acceleration is also less than for the non pressure treated harvester as it is shown in Fig. 5.20. The change

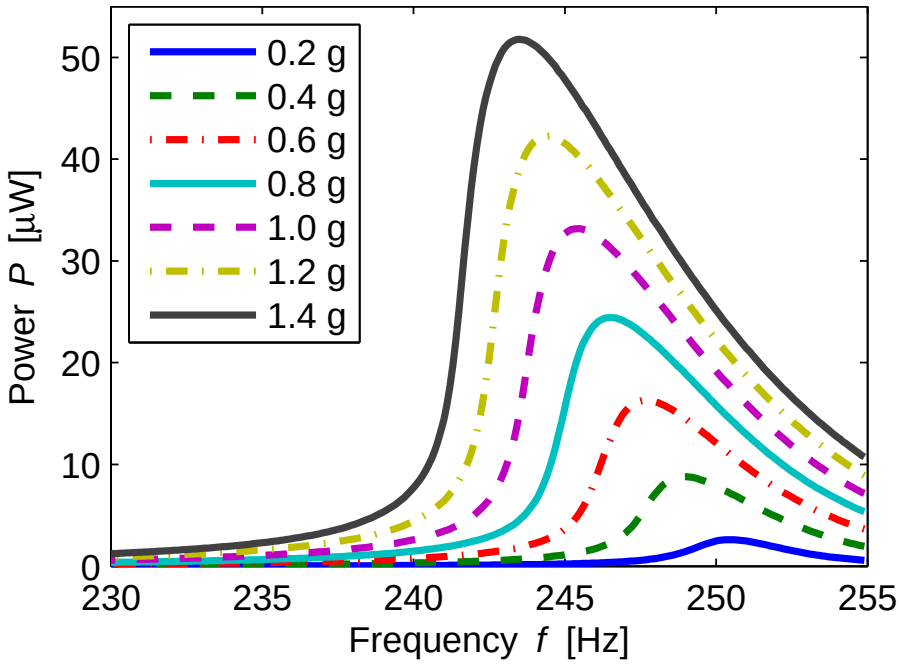

FIGURE 5.18: Power output of both PZT layers as a function of the excitation frequency for different accelerations. The top electrode was connected to the bottom electrode through a resistive load of 250 kΩ.

in the peak power frequency is only 1.6% (from 0.2-1.0 g) only half the value of the non pressure treated harvester.

The output power of harvester 1 for both layer, bottom layer and the top layer is summarized in Fig. 5.19. Note that even though the capacitance and the optimal resistive load of the two PZT layer are still different, their power outputs are much more similar. The similarity of the PZT layers is further consolidated by the cross section SEM image of the bimorph beam shown in Fig. 5.21, where the PZT layers are similar in appearance and thickness. The difference in the capacitance can be explained by the fact that when measuring the capacitance of the bottom PZT layer, the parasitic capacitance of the middle electrode contact pad is included, since the bottom electrode covers the whole chip. Whereas the capacitance of the top PZT layer is measured without the parasitic capacitance since the contact pads for the middle and top electrodes are not on top of each other. Note that effects from fringing fields are ignored here.

The key results from harvester 2 are shown in Fig. 5.22 and summarized results from all the PZT layers in Fig. 5.23 and Fig. 5.24. Key elements observed from harvester 1 are also seen in harvester 2, such as the softening effect. However, notice that even though harvester 1 have the mass to length ratio $\alpha = 70\%$ and seemingly higher piezoelectric couplings coefficient it does not harvest more energy than the harvester with $\alpha = 50\%$, as the theory suggests. This is due to the fact that the variation in the power output due to large variation in the quality factor and/or variation in the piezoelectric coefficient is

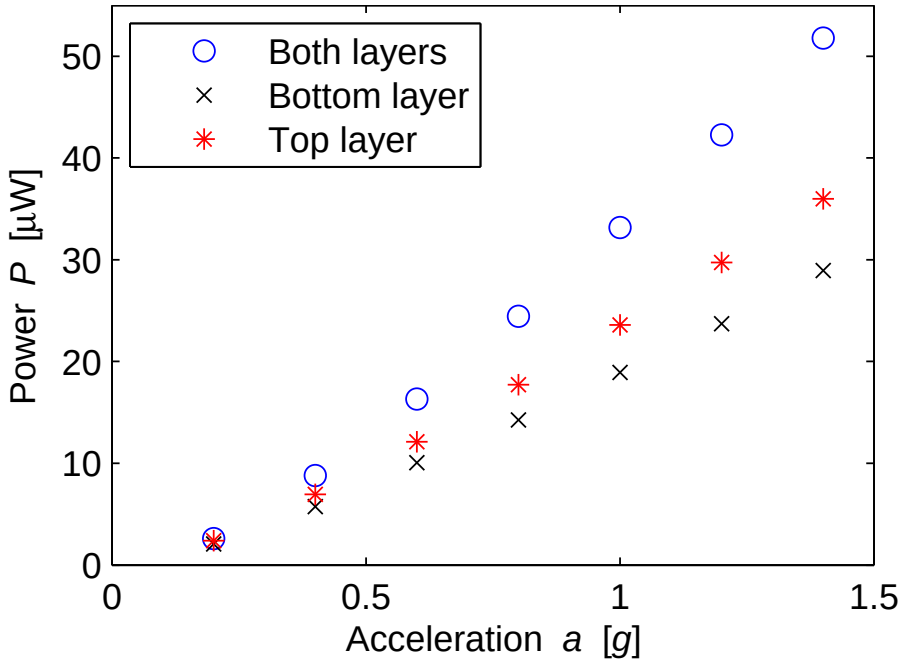

FIGURE 5.19: The power output at resonance is plotted as a function of the input acceleration for measurements on the top layer, bottom layer and both layers.

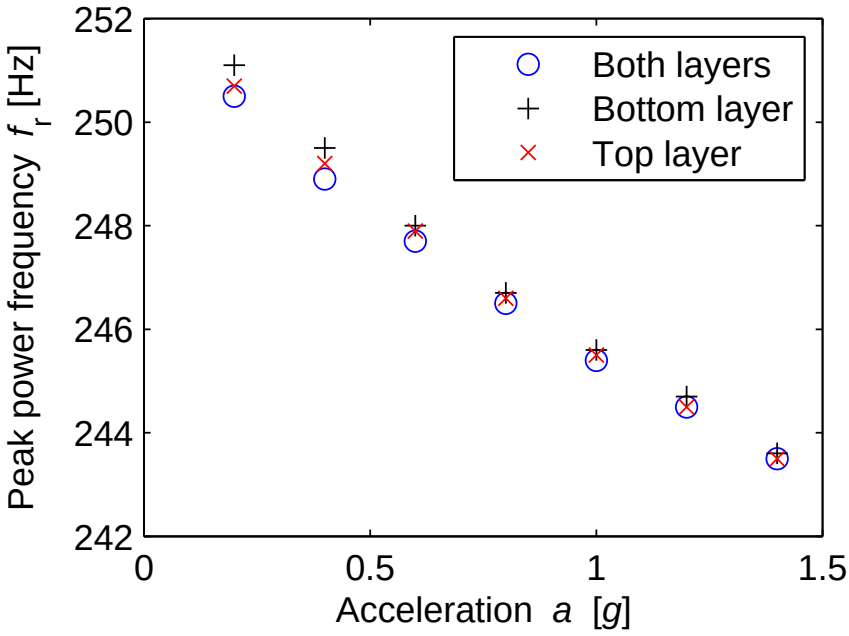

FIGURE 5.20: The peak power frequencies are shown as a function of the input acceleration for measurements on the top layer, bottom layer and both layers.

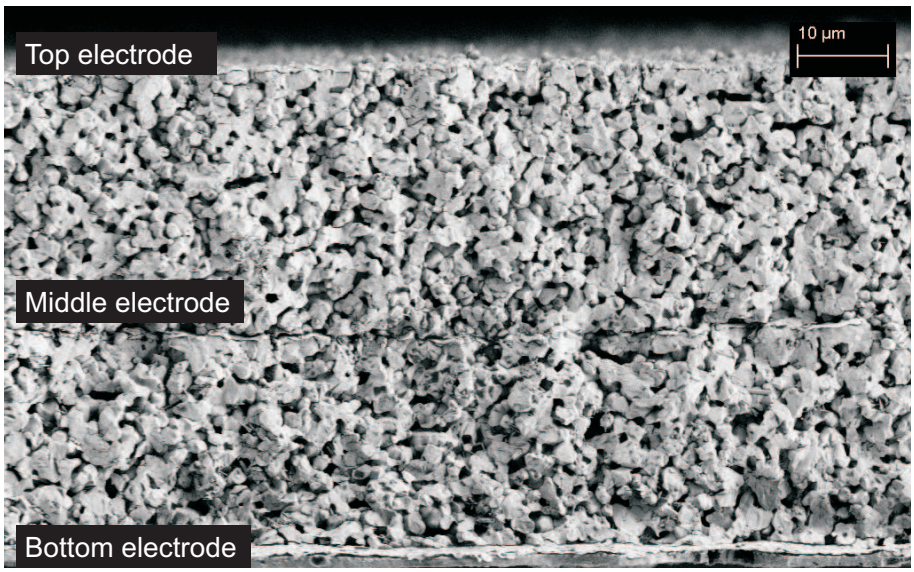

FIGURE 5.21: A cross sectional SEM image of the high pressure treated PZT bimorph cantilever.

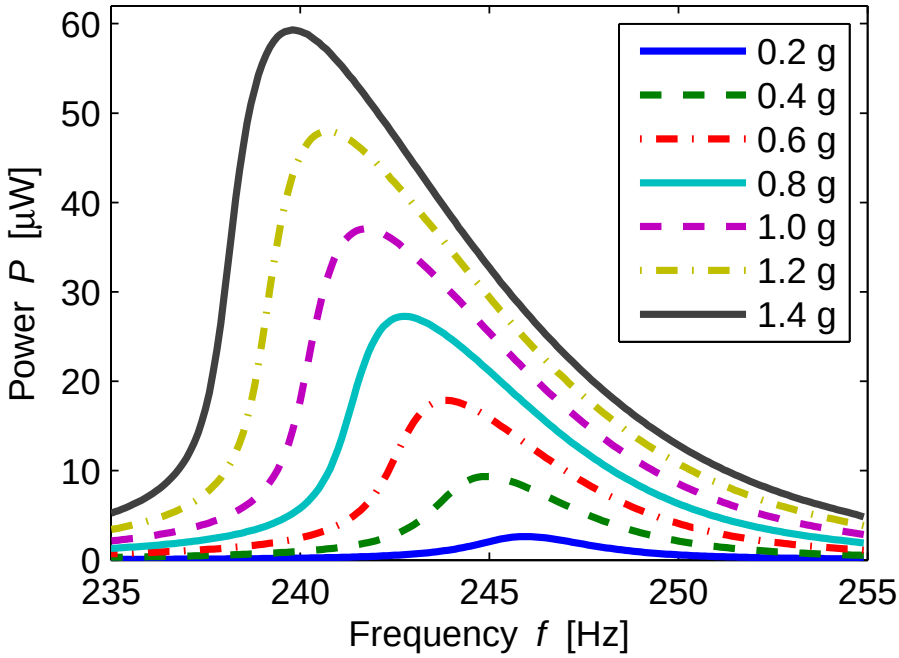

FIGURE 5.22: Power output of both PZT layers as a function of the excitation frequency for different accelerations. The top electrode was connected to the bottom electrode through a resistive load of 200 kΩ.

dominant, thus less determined by the small amount of gain from the increased proof mass, as it is discussed in section 5.4.

A common theme for all of the bimorph harvesters is the fact that they do not harvest more energy at low accelerations compared to if only one layer PZT layer is used. This is believed to be caused by the change in the optimal resistive load as it is predicted by theory developed in chapter 3. The bandwidth BW, which is defined as the full width

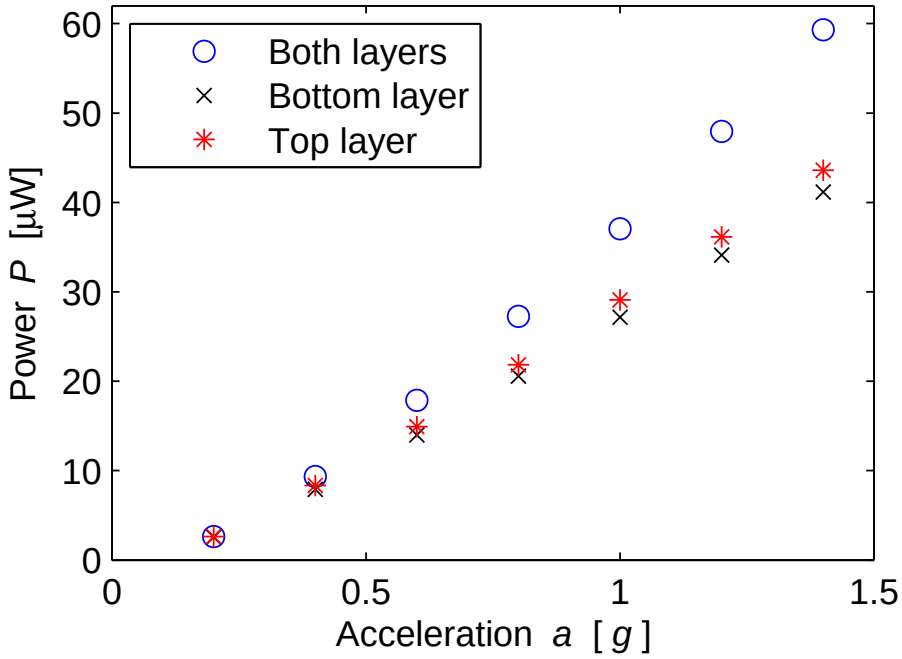

FIGURE 5.23: The power output at resonance is plotted as a function of the input acceleration for measurements on the top layer, bottom layer and both layers.

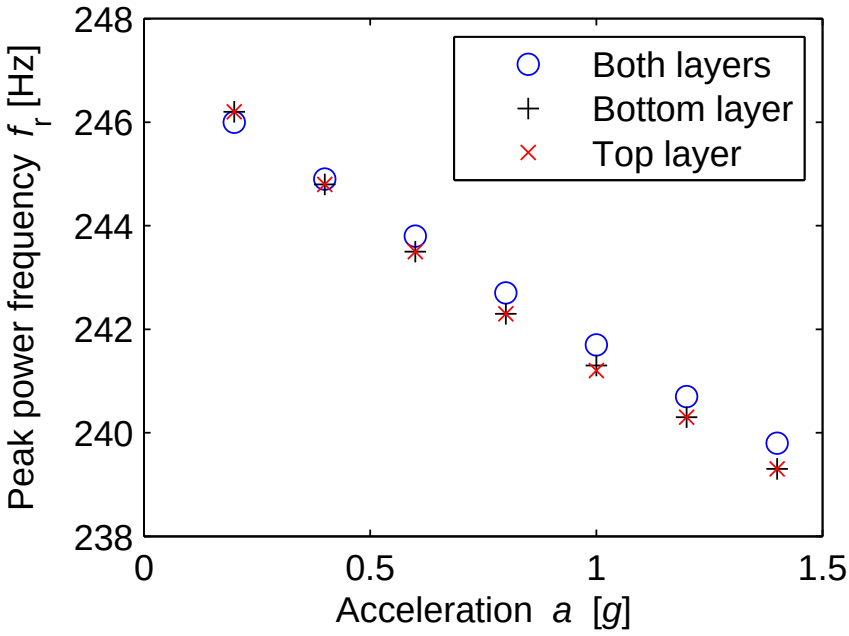

FIGURE 5.24: The peak power frequencies are shown as a function of the input acceleration for measurements on the top layer, bottom layer and both layers.

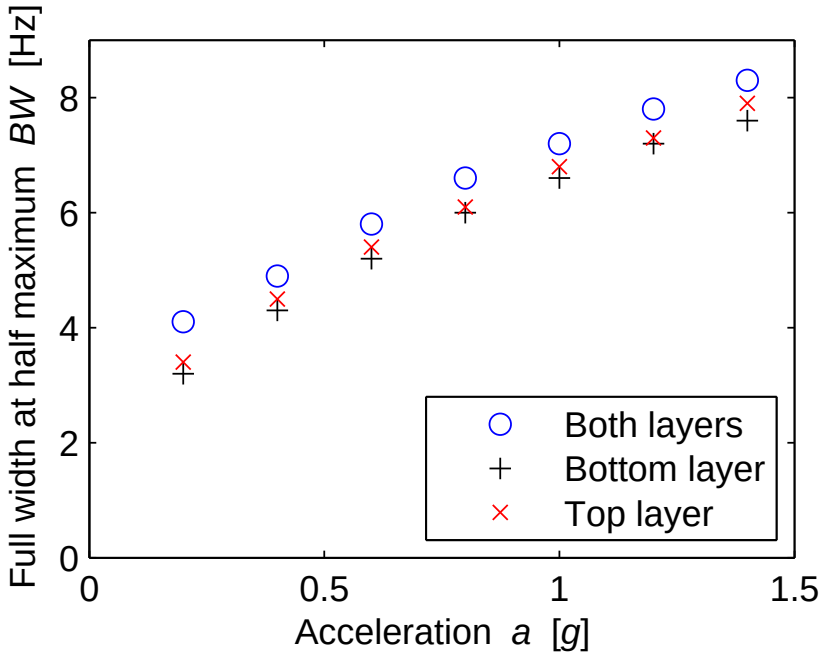

FIGURE 5.25: The bandwidth BW is shown as a function of the input acceleration for measurements on the top layer, bottom layer and both layers.

at half maximum of the power peak in the frequency plot, is shown in Fig. 5.25 for harvester 1. The bandwidth is larger from the results for measuring on both layers than for measuring on single layer, relative difference is 19% at 0.2 g and 7% at 1.4 g. So the loss in the power output for measuring on both layers at low acceleration is compensated by increased bandwidth, *i.e.* the bimorph structure is more damped at low frequency.

Two more wafers were characterized, one with the total PZT cantilever thickness of 34 μm (2 $\times$ 17 μm) and the other with the 46 μm thick cantilever (2 $\times$ 23 μm). The resonant frequencies for $\alpha = 50\%$ and $\alpha = 70\%$ harvesters are measured in the impedance analyzer and plotted as a function of the total PZT cantilever thickness as it is shown in Fig. 5.26. As expected the resonant frequency increases with increasing cantilever thickness. Furthermore, the difference in between $\alpha = 50\%$ and $\alpha = 70\%$ is also observed and as expected the $\alpha = 50\%$ harvesters do have lower resonant frequency.

The power outputs are measured on the wafers at 0.5 g acceleration and the results shown in Fig. 5.27. The expected result is that the power should increase as the PZT cantilever thickness decreases, since with thinner cantilever the stress in the beam is increased. However, the power output for the harvesters with 34 μm thick cantilever actually harvests significant less than the harvesters with 40 μm thick cantilever, this is believed to be caused by the decreased quality with thinner PZT layers. As it was mentioned before the dielectric constant is a good figure of merit for the PZT quality, Fig. 5.28 shows the dielectric constant for the TF2100 thick film as a function of the film

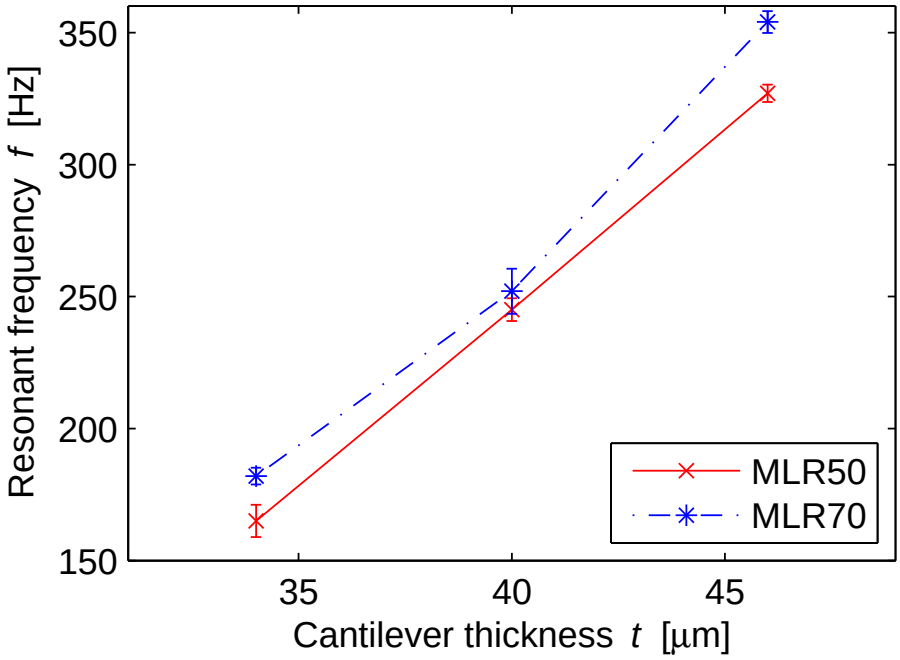

FIGURE 5.26: The resonant frequencies for $\alpha = 50\%$ and $\alpha = 70\%$ harvesters are measured in the impedance analyzer and plotted as a function of the total PZT cantilever thickness.

thickness, notice that as the film thickness is reduced the dielectric constant decreases. Therefore, though the stress in the beam is increased, the quality of the PZT thick films is decreased thus the overall power output is reduced. This result means that there is a optimal PZT thickness that should be screen printed to achieve maximum power output.

5.3.2.1 FIB-SEM investigation

To further investigate the difference between the standard and the high pressure treated PZT film focused ion beam (FIB) milling is used in conjunction with standard SEM imaging. The FIB is used to mill away the PZT ceramic in depth. With each appropriate depth milled, a 2D SEM image is taken. These images can then be used to construct a 3D image of the ceramic using appropriate image visualization program.

QUANTA 200 3D is a Dual Beam machine combining a high-resolution FIB equipped with a Ga+ Source and an SEM equipped with a tungsten filament electron source. The advantage of having a Dual Beam system is that the FIB is only used for milling and not imaging. The imaging is done by SEM. The limited ion beam bombardment on the sample reduces erosion and ion implantation. Quanta 200 3D's inner chamber is shown in Fig. 5.29. The electron beam is generated by an electron gun fitted with a tungsten hairpin filament cathode. Tungsten is used in thermionic electron guns because it has

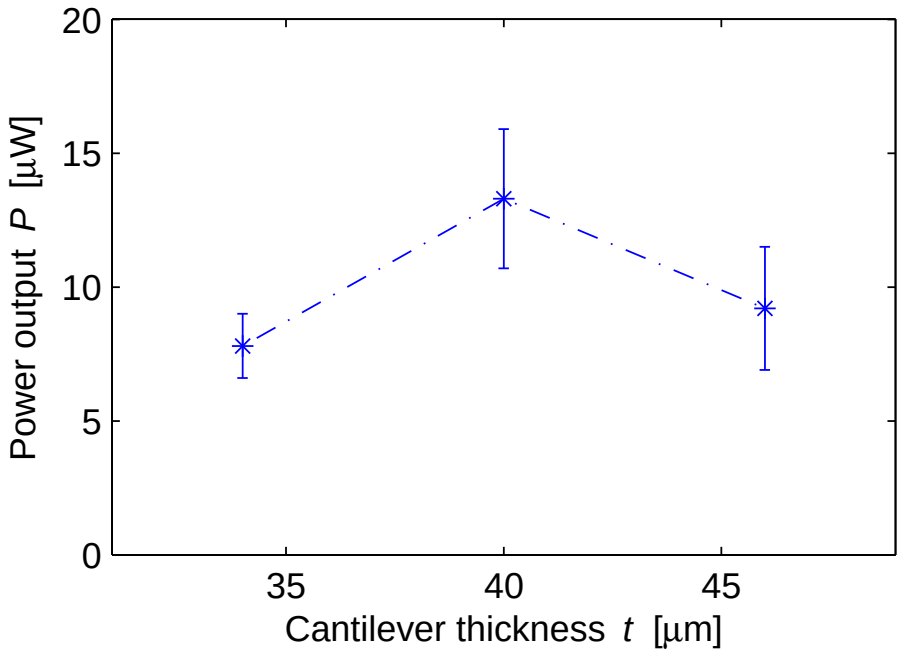

FIGURE 5.27: The measured power output at 0.5 g for harvesters from 3 wafers with different total cantilever thickness.

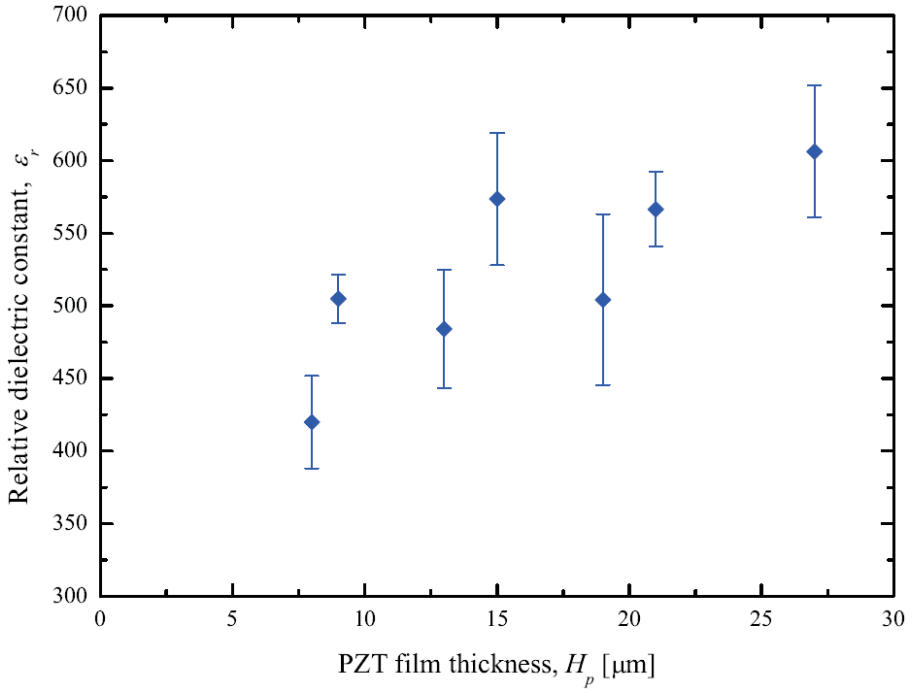

FIGURE 5.28: The dielectric constant is measured as a function of the PZT thickness [33].

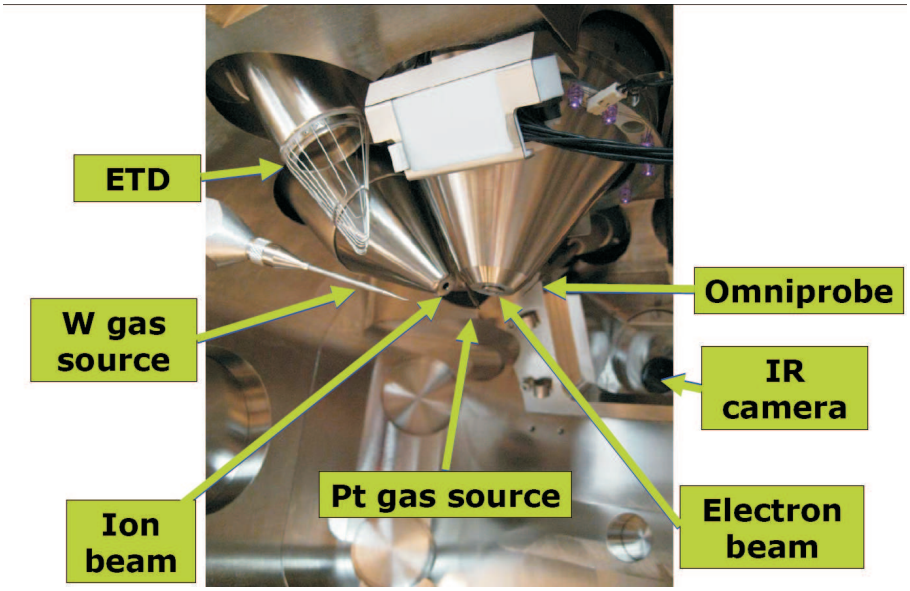

FIGURE 5.29: A picture of the Quanta 200 3D's inner chamber.

the highest melting point and lowest vapor pressure of all metals, thereby allowing it to be heated for electron emission. The ion beam source is a Ga liquid metal ion source (LMIS). The advantage of having such a source is that it can focus into a sub-micrometer beam size, still with a high current (hundreds of pA). The idea of the Ga LMIS is that liquid Ga flows from its reservoir onto a needle tip which faces the extraction electrode. The high voltage between the extraction electrode and the needle tip generate the high electric field. At the needle tip, where the field is strongest, the liquid Ga gets pulled and creating an even sharper tip. This cone shapes tip is called Taylor cone. The sharpness of the cone is determined by electrostatic force and surface tension. As the cone gets sharper, the stronger becomes the electrical field at its apex, when the field is strong enough to ionize Ga in the apex, the emission of Ga+ occurs. However time is needed to have Ga liquid to replenish the lost Ga atoms at the apex. At a certain sharpness of the cone equilibrium is reached, where the emission rate and the replenish rate is equal. Ga LMIS is ideal since Ga has low melting temperature and high surface tension, which means that there will be a high replenish rate. An Everhart-Thornley detector (ETD) is used to detect the secondary electrons, generated either by the ion or electron beams.

The examined samples are screen printed PZT (standard or high pressure treated) on a silicon chips with deposited platinum diffusion barrier. The screen printed PZT thickness is around 20 μm. The chips were diced so the cross section is easily accessible. The diced cross sectional surface is rough, but after just 1.5 μm of FIB milling the undamaged smooth cross section is reached. Since the PZT ceramic is not conducting charging became a major issue. Normally with SEM only a serious charging issue presents a

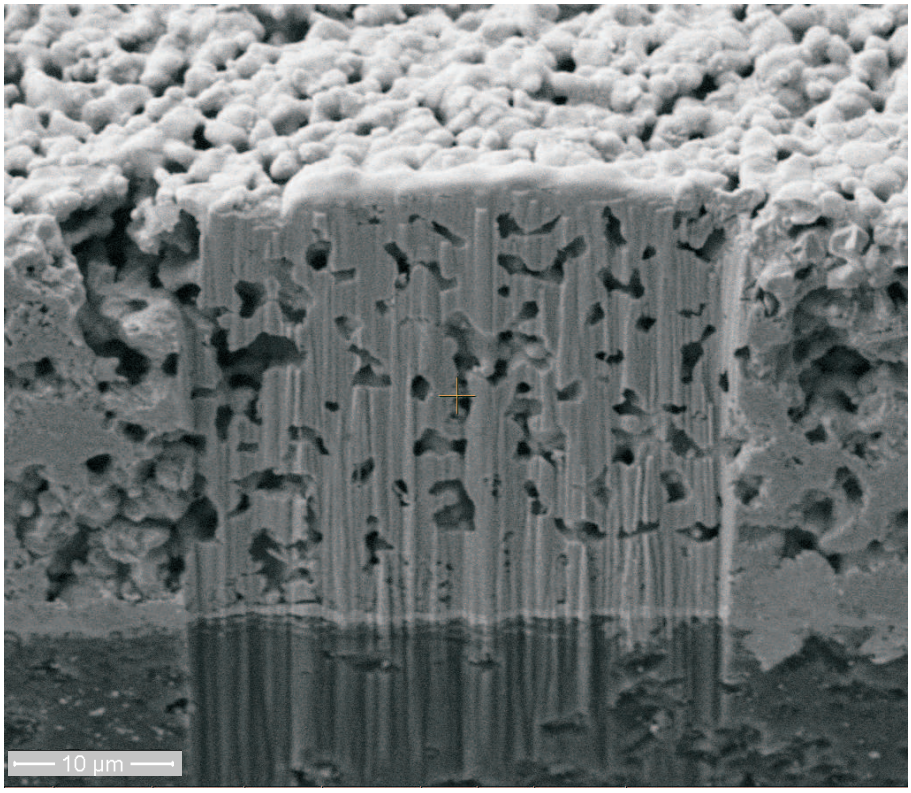

FIGURE 5.30: A SEM image showing the curtain effect caused by beam shift due to sample charging.

problem, where the sample becomes so bright that it is no longer visible, and it will get worse as long as the electron beam is focused at the area. The PZT ceramic, however only has small amount of charging, and do not disturb the imaging too much. However when using FIB for milling, charging will cause beam shift and thus reduce the accuracy of milling. Severe beam beam shift will cause the so called curtaining effect as it is shown in Fig. 5.30. To reduce the effect of charging a thin layer of carbon, about 15 nm, is sputtered on the sample's top, using a carbon coater.

The sample is then placed into the inner chamber. Before the milling can begin, Pt should be deposited on part of the carbon layer, where one wishes to mill. This is done by ion beam-induced deposition (IBID), which is similar to the more commonly known electron beam-induced deposition (EBID). The main difference is the mass. Ga+ ions are much heavier than electrons, thus will generated more secondary electrons with the same current, but in the same time causes more damage to the surface. Since surface damage is not an issue here, IBID is preferred. Furthermore, the EBID Pt will be carbon rich, and is less conducting, which will be less attractive in this case. The idea of IBID is that a precursor gas, containing the material one wish to deposit *i.e.* Pt, is injected into the chamber through an orifice a few hundred micrometers from the sample. The ion beam hits the area one wish to deposit Pt on and generates secondary electrons.

Just as the secondary electrons are leaving the sample, they hit the precursor gas and decomposing it, leaving Pt on the sample. The main purpose of depositing Pt is to form a protective layer. The ion beam intensity is approximately Gaussian, with a high current the beam size will be around 1 μm. Without the Pt layer, the low intensity part of the beam, the beam tail, will begin to mill part of the wall before the main beam has reached the depth. This will result in an angled cut, where the newly milled surface and the top layer will have an angle that is much larger than 90°. Pt is a dense material with low sputter rate. By having a layer of Pt on top, only the high intensity part of the beam will penetrate it, thus having an effective smaller ion beam size for the milling. This will result in a more accurate milling, and the angle between the milled surface and the top will be closer to 90°. If the sample has a low etch rate and high mill depth, the beam tail will eventually mill through Pt, and begin to mill the sample, but 1.5 μm of Pt was found to be sufficient. Another reason to deposit Pt is to avoid redeposition of the milled material from the top to fall down on the newly milled surface.

During milling the ion beam will be perpendicularly to the sample surface. The electron beam from SEM is used to discharge the positive Ga+ ions reducing the charge effects and generating images. An example of the sample cross section is shown in Fig. 5.31. After milling 1.5 μm of the PZT ceramics away a smooth surface is reached, see Fig. 5.32. Thereafter a new image is taken each time 250 nm PZT is milled. Note that if more than 250 nm milling steps are used, the continuous nature of the pores will not be observable, as it is seen in Fig. 5.33 and 5.34. Where the pore patterns are in Fig. 5.33 is still recognizable compared to Fig. 5.32 after 250 nm's milling, which is not the case in Fig. 5.34 where 4 μm is milled away. From these images a 3D pores structure of the PZT ceramics can be constructed. From these data the estimated porosity of the material can be calculated. The resulting porosity for the standard PZT thick film is found to be around 31%, whereas 21% porosity is observed for the high pressure treated thick film. This is in fine agreement with the increase in the density and dielectric constant for the high pressure treated thick film as it is shown in Table 2.2.

5.3.3 Screen printed middle electrode

Bimorph energy harvesters with screen printed middle electrodes were also measured. The bottom and the top PZT thick film is around 25 μm and the Au middle electrode is 5 μm thick, as expected a high resonant frequency of around 520 Hz is observed. The power output at 1 g is found to be around 30 μW thus not higher than that of the standard bimorph energy harvesters. However the high resonant frequency make it an undesirable solution, at least until the screen printed extra proof mass technique is developed so the frequency can be lowered.

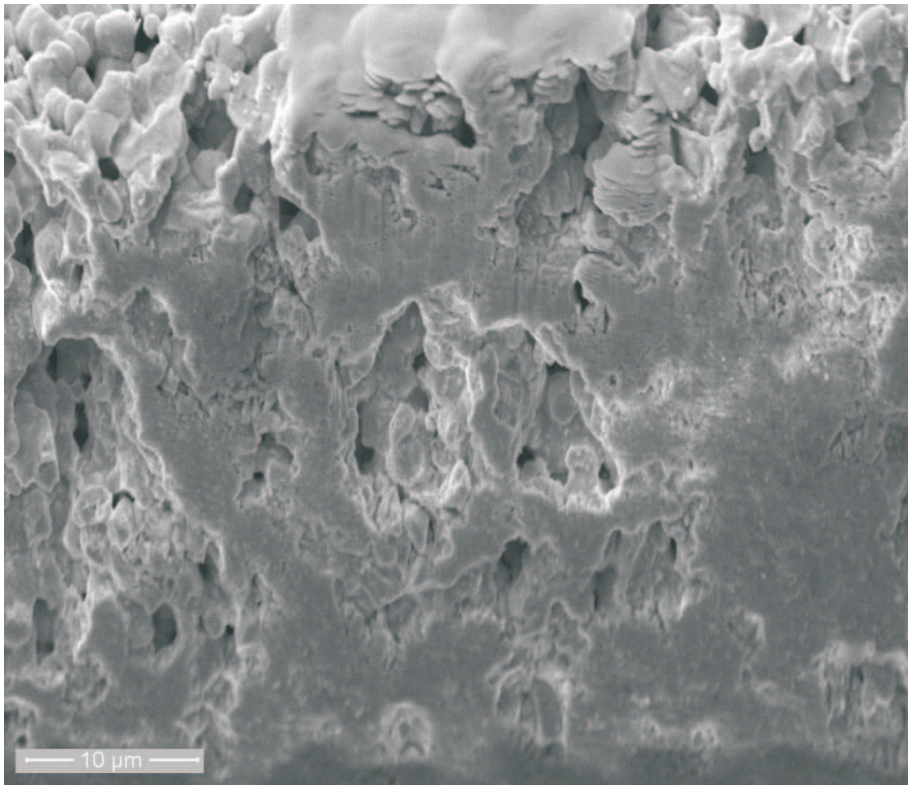

FIGURE 5.31: A SEM image of a PZT diced cross section before FIB milling.

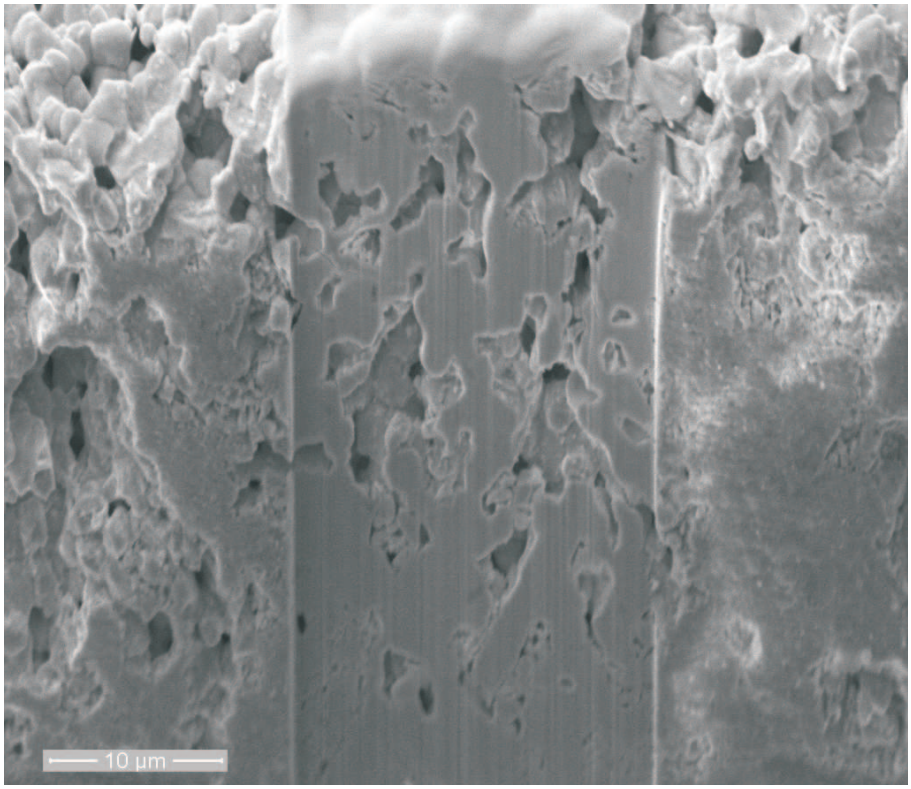

FIGURE 5.32: A SEM image of a PZT diced cross section after 1.5 μm FIB milling of a selected area.

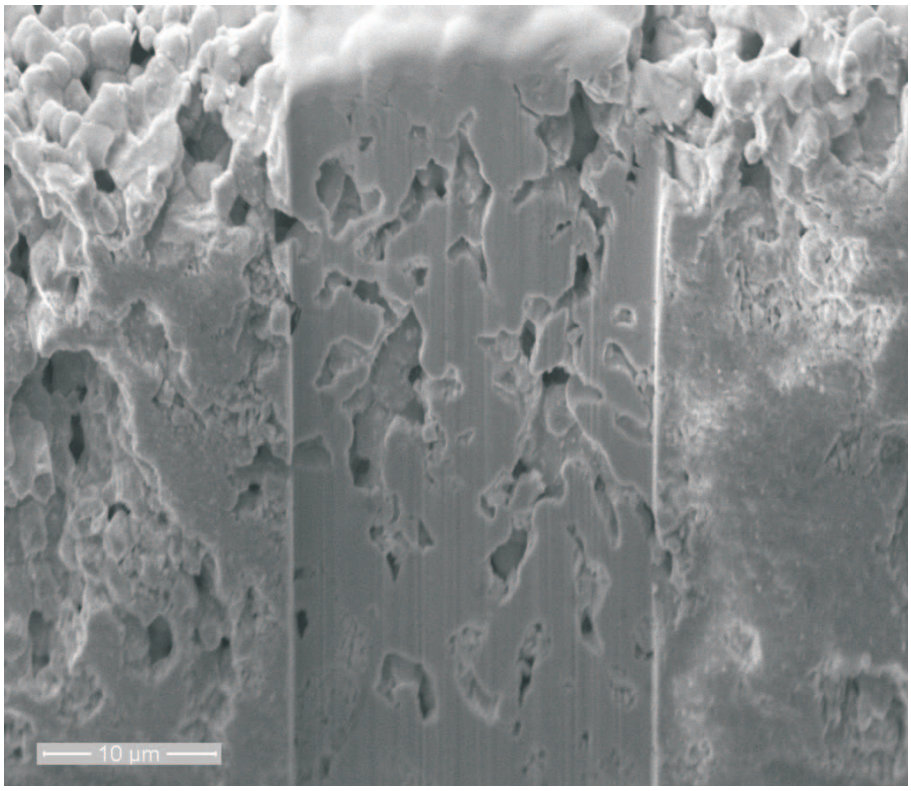

FIGURE 5.33: A SEM image of a PZT diced cross section after 1.75 μm FIB milling of a selected area.

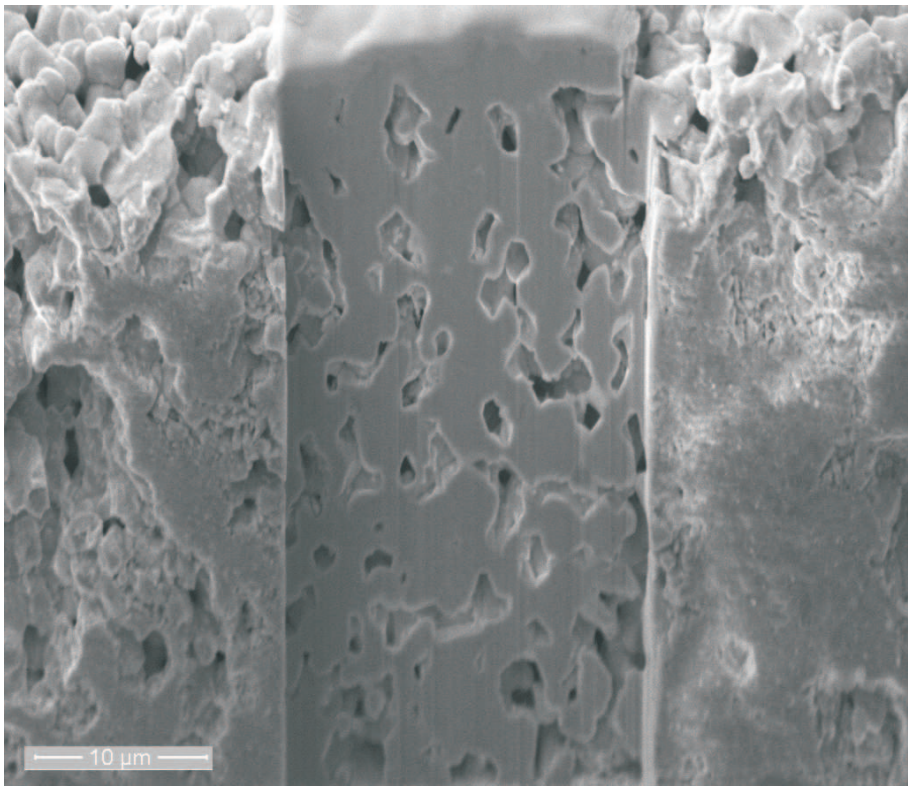

FIGURE 5.34: A SEM image of a PZT diced cross section after 4 μm FIB milling of a selected area.

5.4 Unimorph energy harvesters

In this section the unimorph energy harvesters will be discussed. The non pressure treated unimorph energy harvester will not be presented since obsolete, but some results may be read in [26]. The works done regarding the pressure treated unimorph energy harvesters are presented in [16, 39]. Some of the main results will be summarized. A full wafer (41 energy harvesters) characterization is done on a wafer with only $\alpha = 50\%$ unimorph harvesters and a PZT thickness of 27 μm. The measured avarage capacitance is 5.638 nF with a standard deviation of 0.246 nF, a variation caused by the variations in the film thickness and film quality. Nevertheless, assuming the screen printed PZT thickness is exactly 27 μm the PZT dielectric constant becomes 842 using plate capacitor approximation. This is in fine agreement with the dielectric contant of high pressure treated TF2100 PZT thick film shown in Table 2.2. The average peak power frequency at 0.5 g in open circuit is found to be 333.3 Hz with a standard devation of 9.9 Hz. The average open circuit voltage V_{oc} at 0.5 g is found to be 1.6 V with a standard deviation of 0.52 V. The relative standard deviation of the peak power frequency and the capacitance are 3.0% and 4.4% respectively, which are within the expected uniformity. However, the high relative standard deviation of the open circuit voltage of 33% are unexpected. By rewriting Eq.řefeqn:VocAntiRes in chapter 3 with the relevant material parameters it can be shown that

$$V_{oc} \propto \frac{d_{31} Q a}{s_{11} \omega_0^2 \varepsilon_{33} (1 - k_{31}^2)}. \tag{5.19}$$

Since the variations in the capacitance is relatively small it is safe to assume the large variation in the open circuit voltage is not caused by ε_{33}. The variations in the ω_0 and the mechanical compliance s_{11} are not the source either, due to the low deviation in the peak power frequency. The piezoelectric couplings coefficient k_{31} is generally low and will not cause significant change to the voltage. The input acceleration a is well calibrated in the aforementioned shaker setup. Therefore the large variation in the open circuit voltage is believed to be caused by the either variations in the quality factor Q and/or the piezoelectric coefficient d_{31}. These measurements were done before the acquisition of the Micro-Epsilon laser sensor ILD1401-5, the laser sensor can be used in this case to determine the variation in the quality factor by measuring the displacement. The large variation in the open circuit voltage leads to a large variation in the power output, where seemingly identical harvesters can have an output power between 2.9 - 12.5 μW at 0.5 g. This greatly undermines the optimization of the proof mass length to cantilever length.

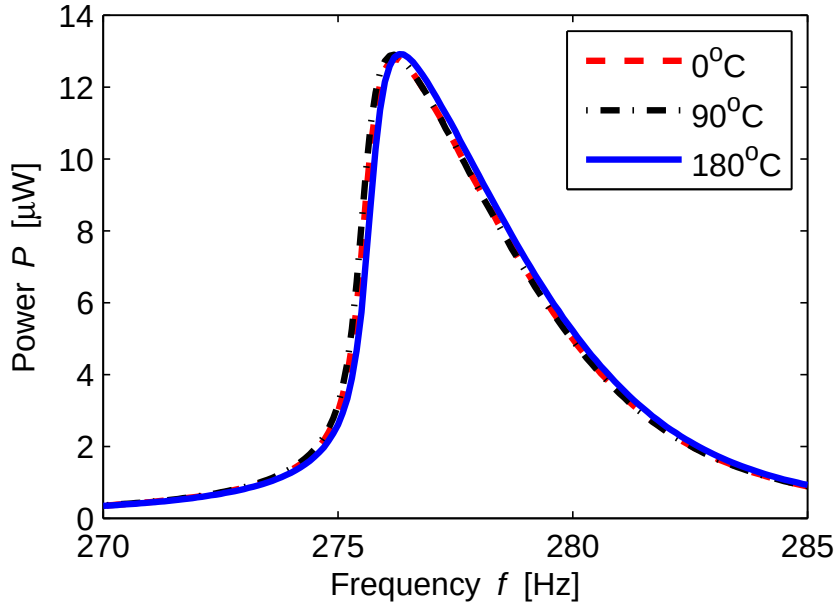

FIGURE 5.35: The power output of an energy harvester as a function of the frequency at positions 0°, 90° and 180°.

5.5 The effect of gravity

Normally, during the shaker measurements the proof mass of the energy harvester moves vertically with electrodes facing upward *i.e.* the gravitational force is acting on the proof mass besides the AC acceleration provided by the shaker. To investigate the effect of gravitational force the shaker is rotated so the shaker and the proof mass movement becomes horizontal, in this case the effects of the gravitational force should be at its minimum. This position will later be referred to as 90°. Furthermore, the energy harvester is also flipped so the proof mass movement again becomes vertical but now the electrodes are facing downwards. This position is denoted 180° and the original position is then 0°. The resulting power output at 0.5 g as a function of the frequency is show in Fig. 5.35. These results show that the difference in power output in between the three positions is less than 1% and the difference in peak power frequency is less than 0.1%. The differences can be considered small, however repeated measurements show the same trends. In the case of output power P, $P_{180^\circ} > P_{90^\circ} P_{0^\circ}$. In the case of resoant frequency f, $f_{180^\circ} > f_{0^\circ} > f_{90^\circ}$. Though the reason for these trends is not clear.

5.6 Discussion of the measured results

Here, some of the main results from this chapter are summarized and discussed.

The softening effect is observed throughout the measurements. To ensure good consistency downward frequency sweep is mainly used.

High pressure treated energy harvesters are better than the harvesters without pressure treatment, with higher power output, less softening, and generally more identical top and bottom layers for the bimorph harvesters.

For the bimorph harvester a general trend of higher capacitance and lower optimal resistive load for the bottom layer than the top layer is observed, it is believed to be caused by the parasitic capacitance between the middle and bottom electrode.

The resonant frequency of the $\alpha = 50\%$ harvesters is indeed lower than the $\alpha = 70\%$ harvesters as theory suggested. However, the $\alpha = 70\%$ harvesters do not harvest more power than the $\alpha = 50\%$ harvesters. This is due to large variation in the measured output power which is overshadowing the advantage of having $\alpha = 70\%$. The variation is believed to be caused by varying quality factor and/or the piezoelectric coefficient.

There seems to be an optimal PZT thickness where the PZT thick film quality and cantilever thickness should be balanced. At current stage of the development process the optimal thickness for etch PZT layer is believed to be 20 μm for each PZT layers in the bimorph harvester and similar thickness for the unimorph harvester.

Chapter 6

Packaging

6.1 Packaging goals

Packaging of the fabricated energy harvesters is a major subject, in particular due to the fragility of the harvesters. Even though no final packaging solution is fabricated, significant progresses were made in the field. The criteria of success for the packaging solution are:

1. Encapsulation of the harvester. This is will prevent physical objects, such as screwdrivers or fingers to strike the fragile cantilever beam.
2. Increase the robustness of the harvester. This will increase the likelihood for the harvester to survive, when subjected to a sudden high acceleration, such as a drop.
3. Easily accessible electric connections. This will require contacts to the bottom, middle and top electrodes to be outside the package solution.
4. The harvester should be hermetically sealed in vacuum. This will increase the quality factor of the harvester, thus improve the power output.

6.2 Anodic bonding packaging

The first package solution introduced is anodic bond, where two 500 μm Pyrex® wafers are bonded on each side of the harvester wafer, the basic idea is shown in Fig. 6.1. Cavities in the Pyrex® wafers are etched in 40% HF acid to accommodate the bending cantilevers of the harvesters, the targeted cavity height is 400 μm. The advantage of this solution are numerous, such as it is a wafer level process, it has a low bonding

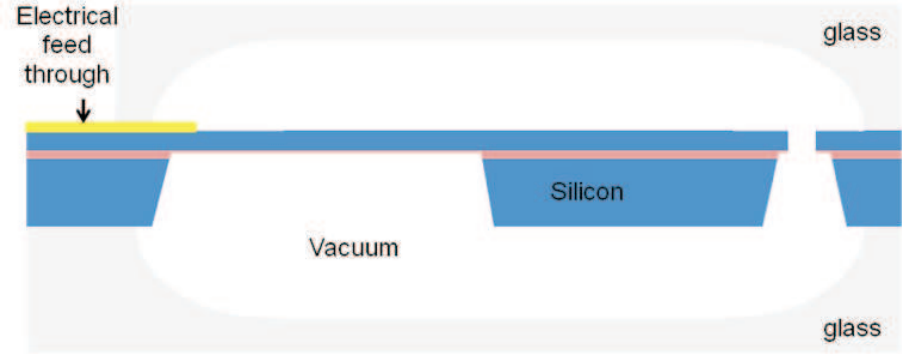

FIGURE 6.1: Sketch of the anodic bonding packaging method.

temperature and it is a well know industrial fabrication method. The wafer level package is a huge advantage since the energy harvester will be encapsulated and protected right after the release etch process, and before the dicing process. Furthermore, it protects the energy harvesters, after they are diced out, from any harsh handling. However, to make such a package solution some details need to be investigated. First, how this triple stack bonding with Pyrex®/Silicon/Pyrex® should be done. Second, how to have electrical feedthroughs without compromising the hermeticity of the bonding. These investigations are presented in the following sections.

6.2.1 Triple stack bonding

The triple stack bonding with a ordinary silicon wafer in the middle and Pyrex® glass wafers on both sides is achieved in [40] only using two electrodes. The idea of the triple stack bonding using two electrodes bonders is to divide the process into two steps. first, bond the silicon and one of the Pyrex® glass wafers together like any ordinary anodic bonding. Then, flip the bonded wafers, treating it like a silicon wafer and bond another Pyrex® glass wafer onto it. The similar technique is implemented using the EVG NIL bond aligner, see Fig. 6.2, at Danchip. Some problems that are observed using this technique is that the applied voltage during the second bonding is oppositely bias compared to the first bonding, the bonding oxygen atoms might be pulled back thus weakening the bonding. The areas where the bonding is so weakened that the silicon and the Pyrex® glass is no longer in contact, are called voids. Another issue is the sodium atoms in the first Pyrex® glass wafer diffuse back to the bonding interface and introduce crack or reforming Na_2O with the oxygen atoms [40]. These areas where sodium atoms are clustered together will later be referred to as cluster areas. Therefore the key of the bonding process is to balance the temperature, voltage and the process time so the void and cluster areas are kept to a minimum. Even though the polarization process of the PZT thick films can be done after the bonding process the temperature still should

not be too high, therefore the temperature used in the anodic bonding processes is set to 320°C. Thus issues such as adhesion or degeneration of the screen printed mass will kept to a minimum. The anodic bonding equipment is similar to the equipment used in [40]. To achieve good bonding each bonding process consist of a low voltage step and a high voltage step. 5 wafer stacks were made where both the front and the back side of the stacks are investigated for void and cluster areas, see Table 6.1 and 6.2. The void and cluster areas are identified and analyzed in photographs, such as the one shown in Fig. 6.3, where the white areas are believed to be void cavities and the brown areas are sodium clusters. Notice that the investigation of the cluster and void areas is done after the triple stack is already bonded for both the 1st bonding and the 2nd bonding. From the results presented in Table 6.1 and 6.2, it is clear that the best bonding is achieved using an initial voltage of 200 V for 5 min and then 400 V for 10 min. The triple stack bonding is thus considered a success with good bondings both in the first and the second bond where the "bad area" is less than 0.3% of the total wafer area.

TABLE 6.1: The bonding parameters used in the 1st bonding of the 5 test wafers are shown in the table. The resulting sodium cluster area and void area after the 2nd bonding on the 1st bonding side are estimated and shown.

Wafer	Bonding parameters	Cluster area [%]	Void area [%]
1	200V (5 min), 400V (10 min)	0.06	0.01
2	200V (5 min), 400V (10 min)	0.18	0.09
3	100V (5 min), 200V (10 min)	1.66	0.44
4	200V (5 min), 250V (10 min)	0.7	0.07
5	200V (5 min), 400V (10 min)	0.05	0.07

TABLE 6.2: The bonding parameters used in the 2nd bonding of the 5 test wafers are shown in the table. The resulting sodium cluster area and void area on the 2nd bonding side are estimated and shown.

Wafer	Bonding parameters	Cluster area [%]	Void area [%]
1	200V (5 min), 400V (10 min)	0	0.22
2	200V (5 min), 400V (10 min)	0.01	0.07
3	200V (2 min), 300 V (5 min), 400V (10 min), 500V (10 min)	0	2.59
4	200V (5 min), 400V (10 min)	0	0.28
5	200V (5 min), 400V (10 min)	0.01	0.07

6.2.2 Electrical feedthroughs

In order to have electrical contact to the bottom, middle and top electrodes outside the packaging solution electrical feedthroughs must be made through the bonding cross

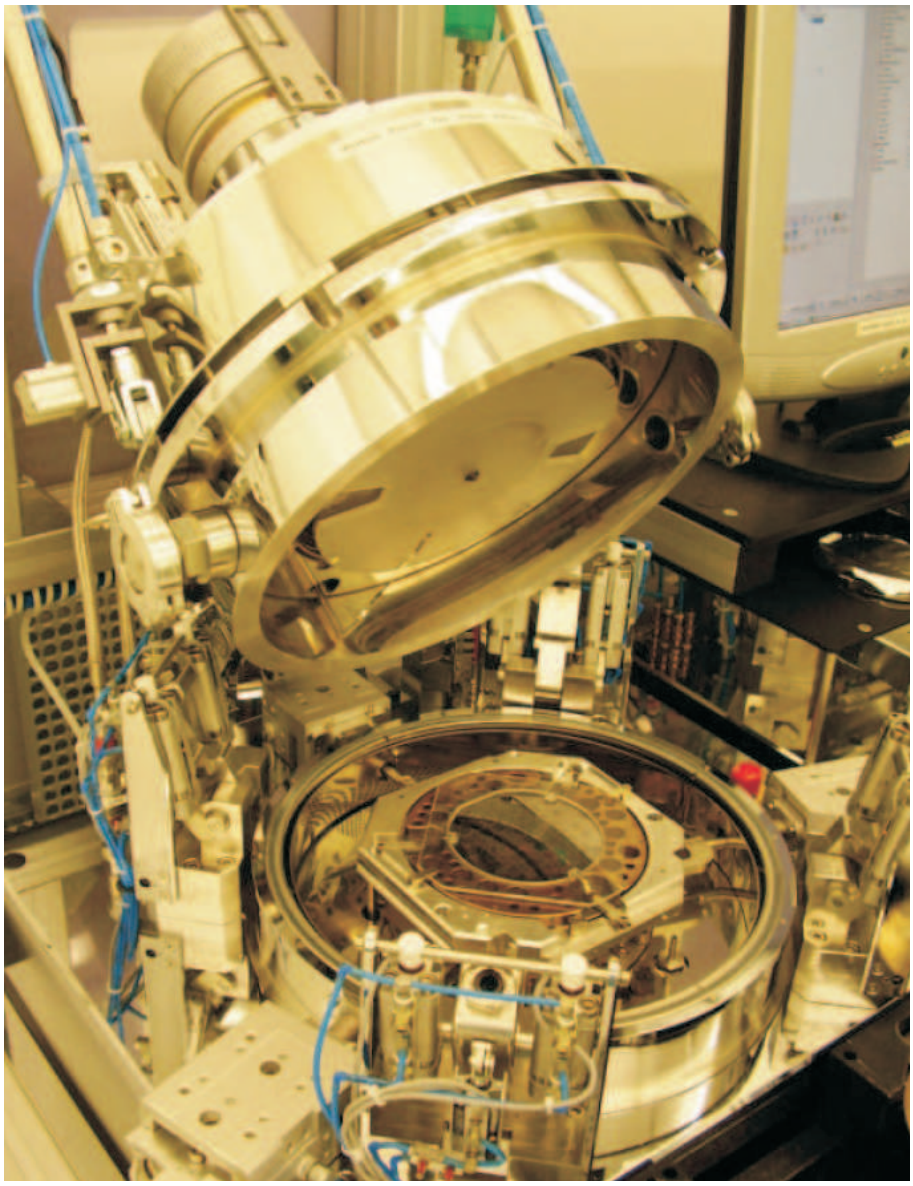

FIGURE 6.2: A photograph of the EVG NIL bond aligner used in the anodic bonding processes.

section. Aluminum is often used as electrical feedthroughs [41], since it bonds to the Pyrex® glass and is relatively easy to deposit. Tests have been done where aluminum wires of different thickness (100 nm, 200 nm and 500 nm) were deposited on to several silicon wafers, which were anodic bonded onto the Pyrex® wafers. The idea is to look at the cross section of the silicon Pyrex® interface where the Al wire is, from which one can evaluate the hermeticity. However, it was found to be difficult, as it is seen in Fig. 6.4, where cross sectional view of the interface is ruined by the dicing process. However, it is noted that the spray water used in the dicing process did penetrate into the Pyrex® cavities, when the wires is more than 500 nm thick. From that one can conclude that wire should be thinner that 500 nm. The hermeticity of the used 100 nm and 200 nm Al

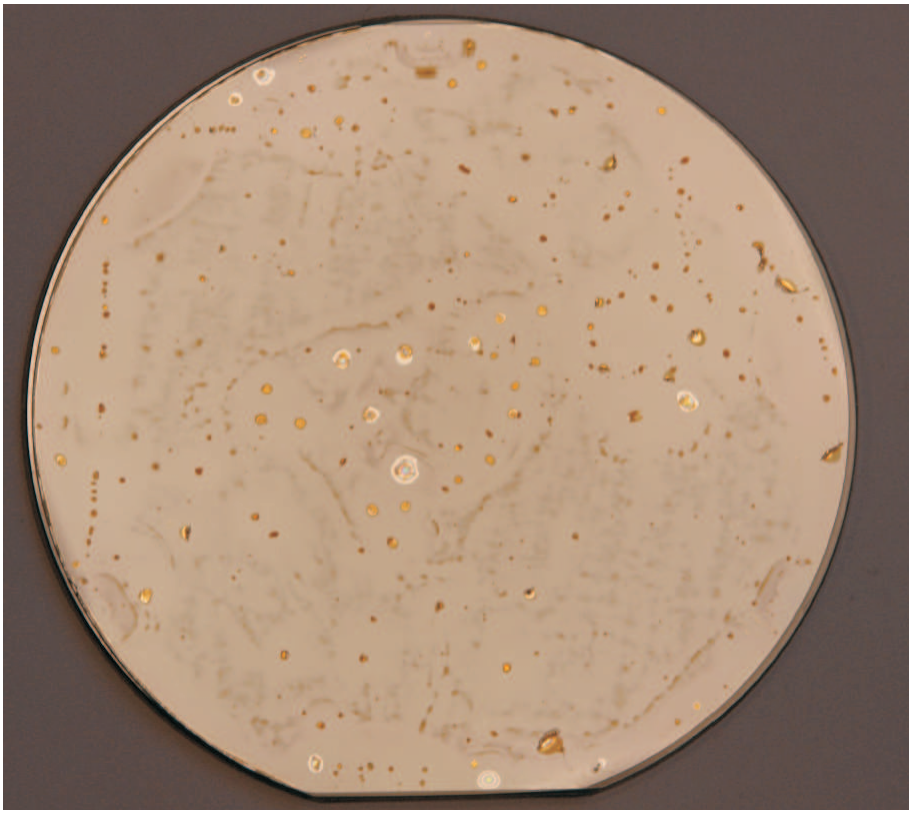

FIGURE 6.3: A photograph of a anodic bonded wafer, the white areas are believed to be void cavities and the brown areas are sodium cluster.

wire still need to be investigated. There are two suggestions regarding the hermeticity test. One, is the common leak test, where a tracer gas like Helium or fluorocarbon is used. To perform the leak test first any trapped gas in the system is removed. Next, soak the system in the tracer gas. Finally, measure the tracer gas leakage under vacuum. The second proposed method is to make a small resonator with the silicon wafer and bond it to the Pyrex® wafers with cavities, and monitor the quality factor of the resonator inside and outside a vacuum chamber. These tests are to be performed in the future.

If the aluminum wire solution is found to be insufficient, then doping part of the silicon surface to make it conducting should considered, however it is deemed too inconvenient at current stage and also have a few drawbacks, such as increased series resistance.

Furthermore, the one of the aforementioned diffusion barrier test, where an opening in the bottom electrode layer is made to investigate the severity of the inter diffusion, is also part of the feedthrough investigation. To use the Al feedthroughs the top and bottom electrodes must be brought down to the silicon level, *i.e.* not on top of PZT which is 20-30 μm thick. To prevent short circuiting with the bottom electrode layer, which is essentially everywhere, the idea is to separate the bottom electrodes layer to different areas where one will be in contact with the top electrode layer, effectively becomes a

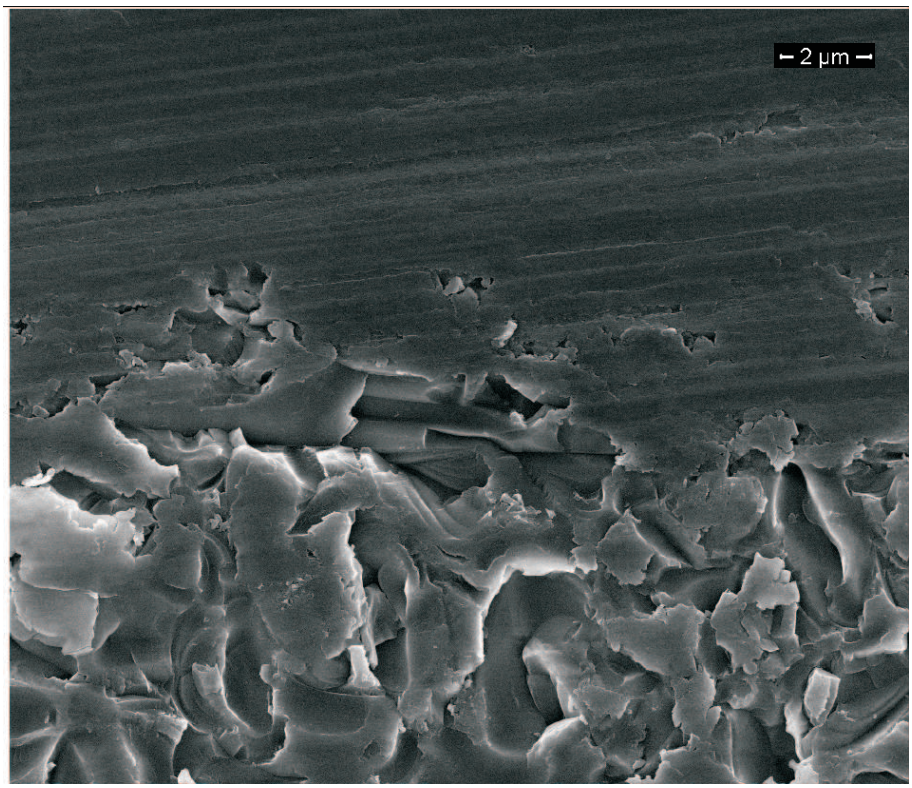

FIGURE 6.4: A SEM image of the cross sectional view of the silicon Pyrex® interface.

top electrode pad and another will be in contact with the middle electrode (if it is a bimorph harvester) effectively becomes a middle electrode pad.

6.2.3 Voltage pull-in

In the previous tests the silicon wafers are not machined. In the real bonding there will of course be a cantilever inside the cavity. When a large bonding voltage is applied charges will be induced in the cantilever. This will result in an electrostatic force that is enhanced as the gap between the proof mass and the bonding electrode on the Pyrex® wafer is getting closer. If the cantilever becomes in contact with the Pyrex® wafer there is a risk that it will bond to it thus ruin the cantilever. The anodic bonding system with the energy harvester can be described as a parallel plate capacitor with one of the plate is suspended by a spring. Using energy conservation the stored potential energy W can be described as the sum of the energy of the capacitor $\frac{1}{2}CV^2$, the applied electrical potential $\frac{1}{2}CV^2$ and the energy in the spring $\frac{1}{2}kx^2$

$$W = \frac{1}{2}CV^2 - CV^2 + \frac{1}{2}kx^2 = -\frac{1}{2}CV^2 + \frac{1}{2}kx^2 \tag{6.1}$$

$$C = \varepsilon_0 \frac{A}{g+x}, \tag{6.2}$$

where the C is the capacitance, V is the applied voltage, k is the spring constant, x is the deflection of the proof mass and g is the cavity height of the Pyrex®. There is an equilibrium position where the electrostatic force is canceled by the spring force, so the total force $F = \frac{dW}{dx}$ is zero.

$$F = \frac{dW}{dx} = \frac{1}{2}\frac{\varepsilon_0 A V^2}{(g + x_{\text{eq}})^2 + k x_{\text{eq}}^2} \Leftrightarrow \tag{6.3}$$

$$V^2 = -\frac{2k}{\varepsilon_0 A} x_{\text{eq}} (g + x_{\text{eq}})^2 \tag{6.4}$$

In the case where the voltage so high that it can pull the system out of the equilibrium system, the $V(x_{\text{eq}})$ will have a unstable maximum. This maximum can be found by $\frac{dV}{dx_{\text{eq}}} = 0$. Since V is not zero the same result can be achieve by differentiate V^2

$$\frac{dV^2}{dx_{\text{eq}}} = 0 \Leftrightarrow \tag{6.5}$$

$$x_{\text{eq}} = -\frac{g}{3} \vee x_{\text{eq}} = -g. \tag{6.6}$$

$x_{\text{eq}} = -g$ is of course not the wanted solution since by then the cantilever is already stuck on the Pyrex®. Insert the solution $x_{\text{eq}} = -\frac{g}{3}$ into Eq. 6.4 yields

$$V_{\text{pull-in}}^2 = V^2(-\frac{g}{3}) = \frac{8}{27}\frac{kg^3}{\varepsilon_0 A} \tag{6.7}$$

$$= \frac{8}{27}\frac{m(2\pi f)^2 g^3}{\varepsilon_0 A} \tag{6.8}$$

where the spring constant is rewritten as $k = m(2\pi f)^2$, inserting the known values, $V = 400V$, $A = 5.5mm \times 3.25mm$ and the lowest resonant frequency of the energy harvesters ($f = 160$ Hz) the needed gap can be calculated and is found to be 150 μm. The aim of the cavity height as mentioned before is around 400 μm, which is significantly larger than the gap needed to prevent pull-in.

From this analysis the idea of anodic bonding packaging method is considered feasible to achieve but still there are numerous tests and investigations needed for a final product. Therefore a more low-tech technique is also investigated.

6.3 Low temperature co-fired ceramic packaging

The low temperature co-fired ceramic (LTCC) is often used in MEMS related products due to its multilayered technology than enables the creation of a semi 3D structures, *e.g.* in the case for the energy harvester packaging to create cavities for the cantilever movements. The LTCC multilayer consists of several ceramic sheets (green sheets).

These sheets can be patterned in various ways, such as punching, micromilling, screen printed with wires, laminated together and finally be co-fired to form the multilayer structure. Co-fire in this case means that the sheets and the screen printed wires are sintered at the same time. One of the advantages of LTCC is that highly conducting thick film wires such as silver or gold can be used, since the sintering is done at the low temperature of around 850°C, whereas high temperature co-fired ceramics (HTCC) sintering temperature is as hight as 1600°C [42].

Since the LTCC packaging solution was introduced late in the project, no practical investigations are make regarding the packaging scheme, therefore only the general packaging concept will be presented. The conceptual design of the packaging solution is made in SolidWorks. The packaging solution consists of two LTCC multilayers structures, one can be considered the lid and the other can be considered base as it is shown in Fig. 6.5. Fig. 6.6 shows the lid from the top, where the screen printed silver wires are visible. In this case only the wires are drawn but more components can be integrated on this side of course. The inner side of the lid is shown in Fig. 6.7, the cavity here is made to accommodate the cantilever of the harvester in the upward deflection position. The harvester should be soldered to the feedthroughs on the inner side of the lid or just glued using conductive glue. Inner side of the base is shown in Fig. 6.8, where the cavity here is larger than the cavity made in the lid since this cavity is going to house the harvester. Furthermore, corners of the cavity have been modified to avoid misfits due to the fact that the harvester edges are probably sharper than the cavity corners. So to encapsulate the package, the base is placed on a hot plate and heated to the solder temperature of of the applied solder material and the lid is moved down, bring the two solder pads in contact, then the package is remove from the hot plate. In theory this packaging solution can be done in vacuum though difficult, however it is found that the advantage of having the system in vacuum is not as essential as originally anticipated.

6.4 Atmospheric package

The need of vacuum in the packaging solution is investigated in this section. There are essentially two questions that need to be answered here

1. what is the effect of running the harvester in vacuum?
2. what is the effect on the harvester if an atmospheric packaging solution is used?

To answer the first question a series of shaker measurements were conducted, where an energy harvester is placed into a vacuum chamber along with the reference accelerometer

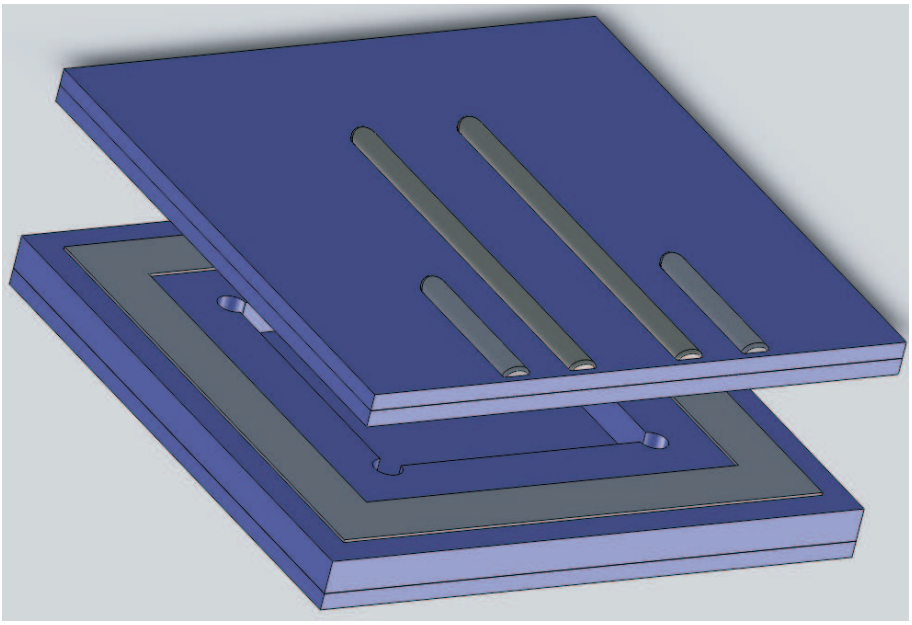

FIGURE 6.5: The LTCC packaging solution where the lid and th base part are shown.

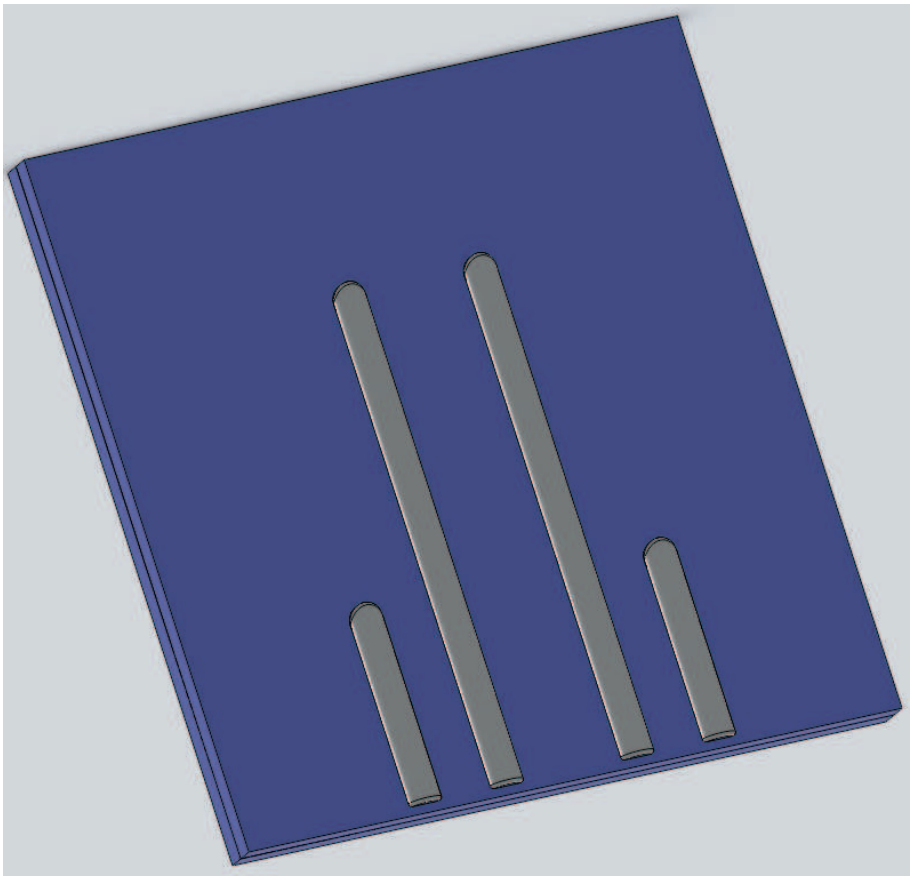

FIGURE 6.6: The top side of the LTCC lid is shown, the silver thick film wires are shown.

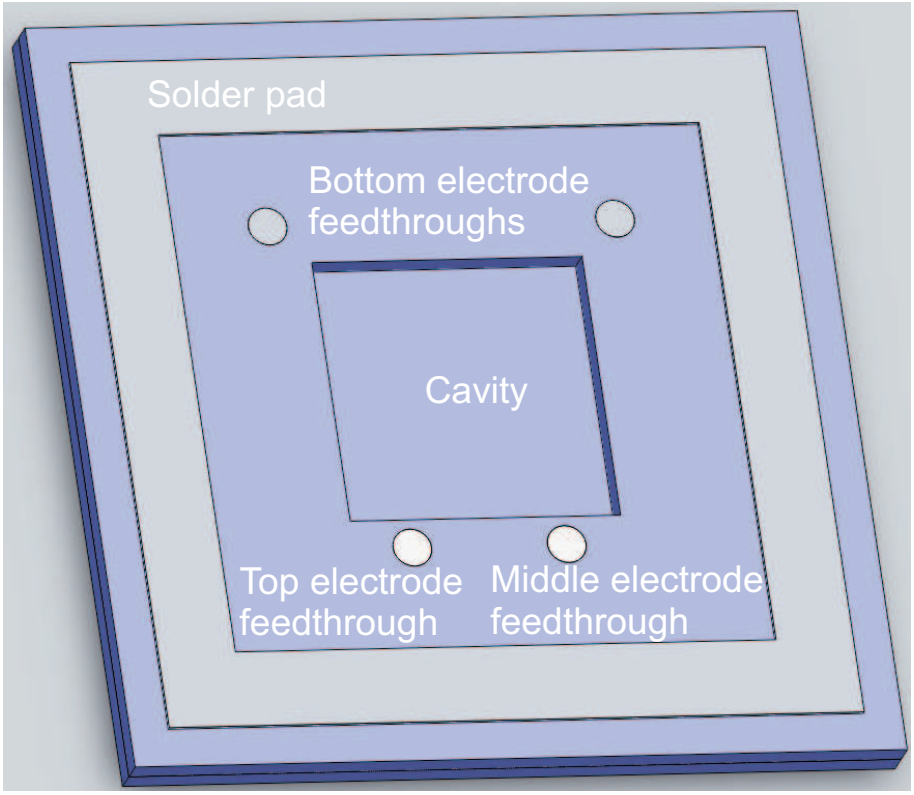

FIGURE 6.7: The inner side of the LTCC lid is shown, the feedthroughs are shown. The cavity is used to accommodate the cantilever deflection, when the cantilever is at an upward position.

and the shaker, and is accelerated with 0.5 g RMS acceleration. The measured peak power output is shown in Fig. 6.9 as a function of the chamber pressure. The result shows that as expected the output power is increased as the pressure decreased. The power output is increased by 9% with the harvester in vacuum. This is related to the decreased air damping in the system, as it can be observed in the change in the bandwidth BW, see Fig. 6.10. The decreased damping is also observed in the frequency shift, as it is shown in Fig. 6.11. So there is indeed an positive effect on the power output by having the harvester running in vacuum, though modest.

The second question revolves around the issue of whether or not a atmospheric packaging solution will reduce the power output even further compared to the unpackaged harvester. This is a bit more difficult to answer since no actually packaging solution has been fabricated, therefore the direct effect can not be measured. However, the AlN energy harvesters presented in [9] shows that the atmospheric packaging greatly decreases the power output as it is shown in Table. 6.3. The AlN energy harvester relied on high quality factor to harvest energy, therefore it is more sensitive to the change in the environment. The total quality factor of the system changed from 810 in vacuum to 430 unpackaged, a change of 47%. This can be compared to the previous result where the quality factor Q can be calculated from the bandwidth BW and the resonant frequency

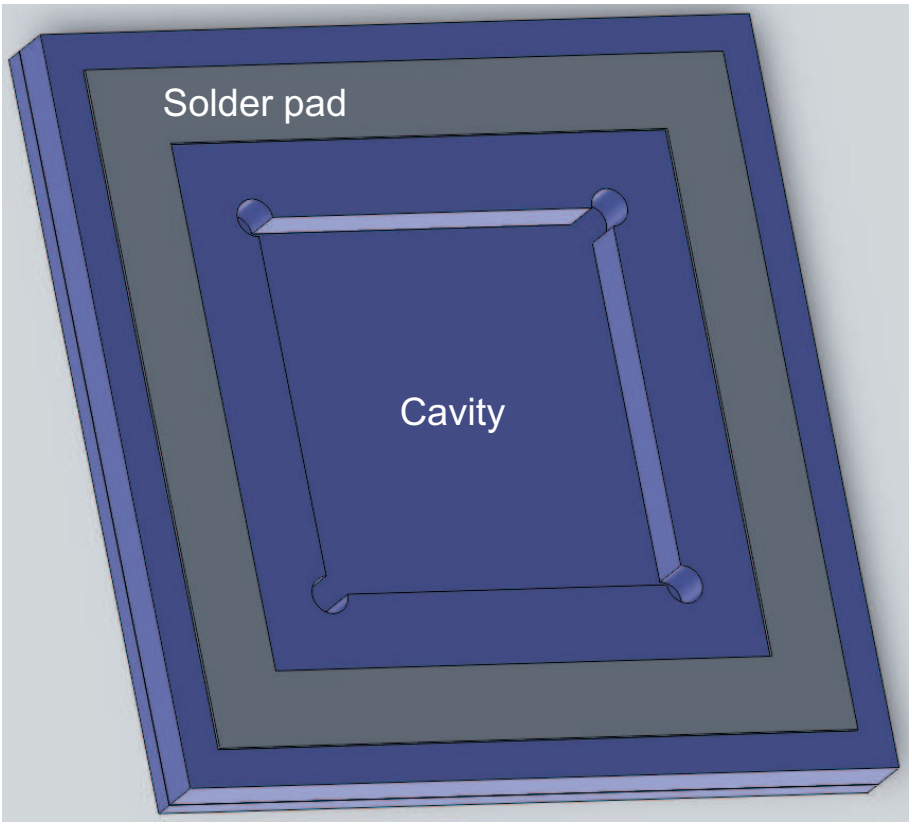

FIGURE 6.8: The inner side of the LTCC base is shown. This cavity is made primarily to house the energy harvester.

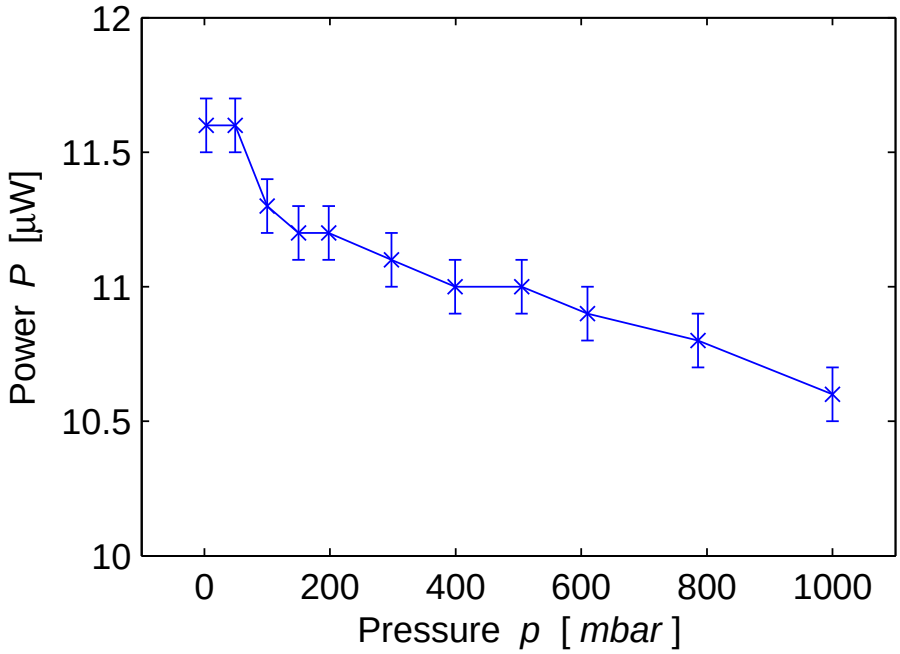

FIGURE 6.9: The output power of an unimorph energy harvester with 0.5 g input acceleration is shown as a function of the pressure it operates in.

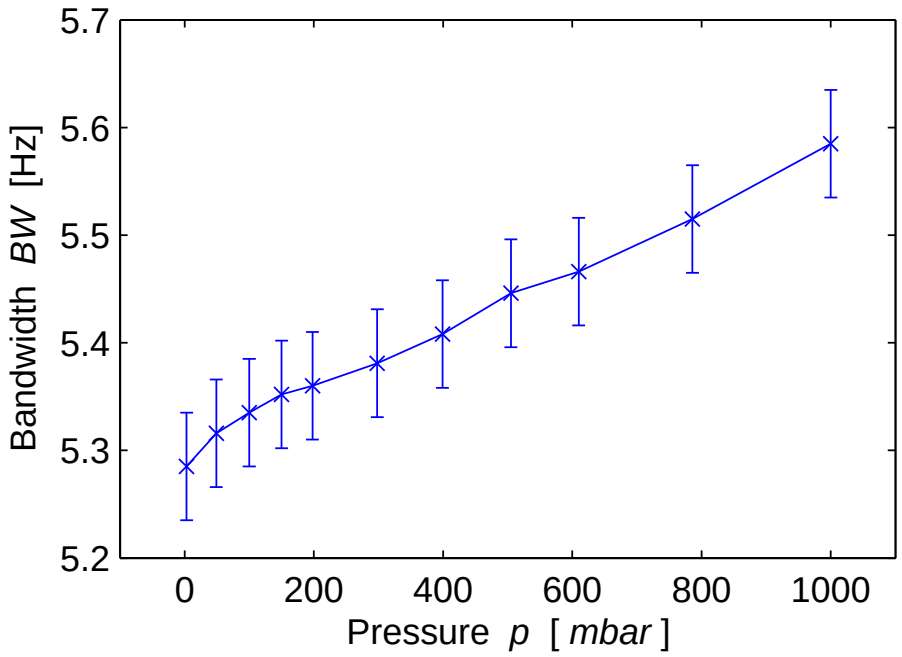

FIGURE 6.10: The bandwidth of an unimorph energy harvester with 0.5 g input acceleration is shown as a function of the pressure it operates in.

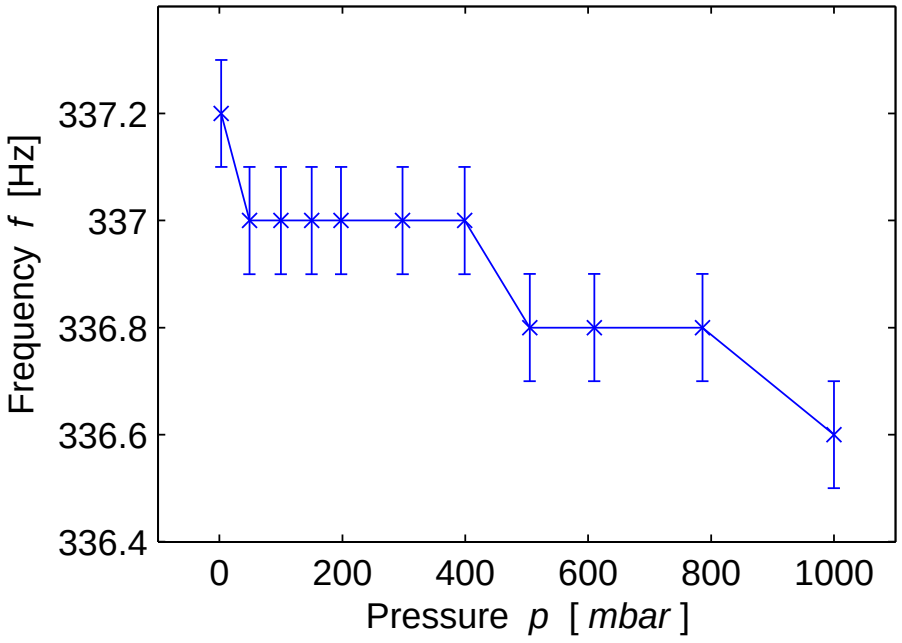

FIGURE 6.11: The resonant frequency of an unimorph energy harvester with 0.5 g input acceleration is shown as a function of the pressure it operates in.

f, where $Q = \frac{f}{BW}$. The change is here is only 0.6% significantly less then the 47% from [9]. Therefore it is believed that when packaged in atmospheric enviroment the power output for the fabricated PZT harvesters should not decrease drastically either. This is somewhat confirmed in [10] where unimorph energy harvester of roughly same size as the ones that are presented in this work is packaged in atmospheric enviroment and still harvest significant amount of energy. Therefore the recommendation regarding the packaging solution is that if the vacuum packaging is proven to be inconvient, an atmospheric package solution should be used.

TABLE 6.3: The effect of the packaging solutions on the AlN energy harvesters from [9].

	Output power [μW]	Total quality factor
Atmospheric package	0.27	80
Unpackaged	10.2	430
Vacuum package	32.0	810

Chapter 7

Additional topics

In all of the previous chapters the focus has been on resonating energy harvesters, however in recent years non-resonating energy harvesters have received significant attention [43–47]. The advantage of a non-resonating energy harvester is that it is no longer bounded to one frequency and will function in different systems with different available frequencies. However, this flexibility is not for free, it will in general result in lower power output. A non-resonate energy harvester relies on the ability to excite the harvester by a pulse, this pulse can either be a mechanical impact force or a change from one cantilever stable state to another. Notice that these methods rely on exciting a resonating harvester to operate outside resonance. This means that a good resonating energy harvester is still needed, the difference is just that it is now included in to a system with extra components. Inspired by these ideas two methods of non-resonating systems were developed while still using the fabricated energy harvesters.

7.1 Impact force system

The first idea relies on harvesting rotational energy, where a solid metal ball is encapsulated inside a tube, see Fig. 7.1, where the diameter of the ball is 14.8 mm. The fabricated energy harvesters are attached to the ends of the tube. The rotation of the tube will cause the metal ball to move inside the tube, each time the ball hits the end where the harvester is attached, the impact energy will be transmitted to the harvester and excites resonance. However, the the tube and the ball seems to be over dimensioned, which made the harvesters unable to survive the impact. Therefore an older version of the harvester is used where cantilever thickness is significantly higher and the resonant frequency is a few kilo hertz. The result is shown in Fig. 7.2. The harvester does seems to respond to the impact, however due to the harvester's high resonant frequency the

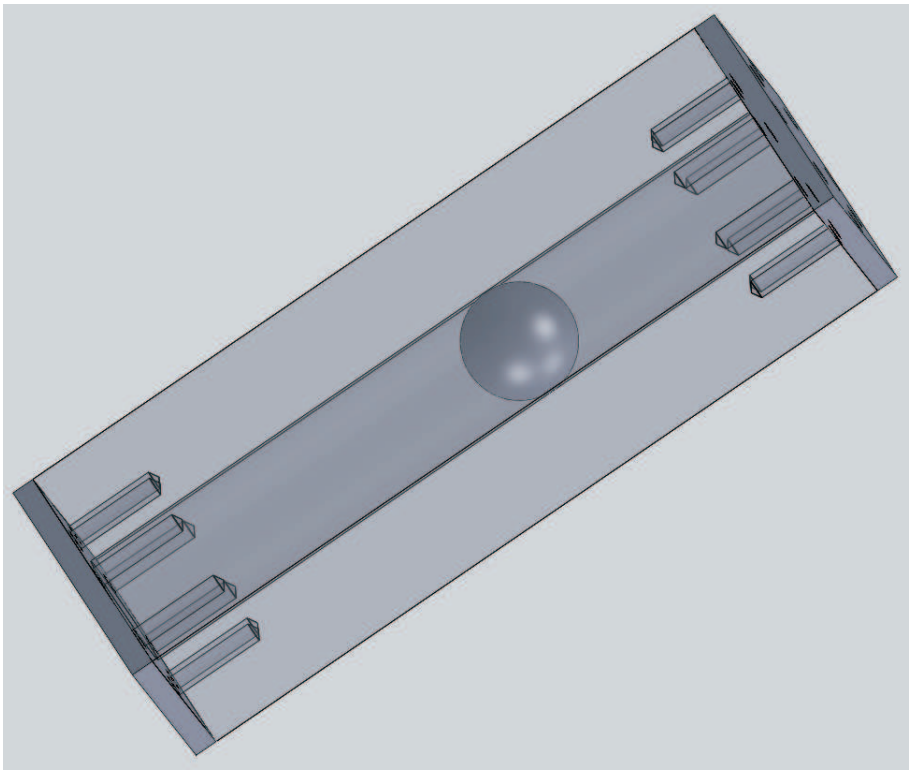

FIGURE 7.1: The fabricated aluminum tube for the impact method harvesting, where the metal ball has a diameter of 14.8 mm.

electrical response dies out relatively fast. The later responses are due to the bouncing of the metal ball.

7.2 Magnetic bistable system

The second idea relies on having two equilibrium positions for the cantilever instead of one, this is also known as bistable harvester. Each time the cantilever changes its equilibrium position the cantilever will resonate. To achieve this two neodymium magnets are placed near the harvester and a soft magnetic metal sheet, such as iron or nikkel sheet, is glued onto the proof mass, as it is shown in Fig. 7.3. The theoretical calculations of regarding this setup are done in [48]. The measured RMS power output for the bistable system and its corresponding linear system (when the magnets are removed) are shown in Fig. 7.4. Utilizing the bistable nature of the system the harvested power is indeed significantly higher than the linear system at low frequency. The bistability is achieved when the frequency is below 90 Hz, since at higher frequencies the cantilever is moving too fast and does not "feel" the magnets. The power peaked at 70 Hz for the bistable system. This is a optimal frequency for the bistable system, where before the transient vibration from the earlier equilibrium change had died out, it is shaken to

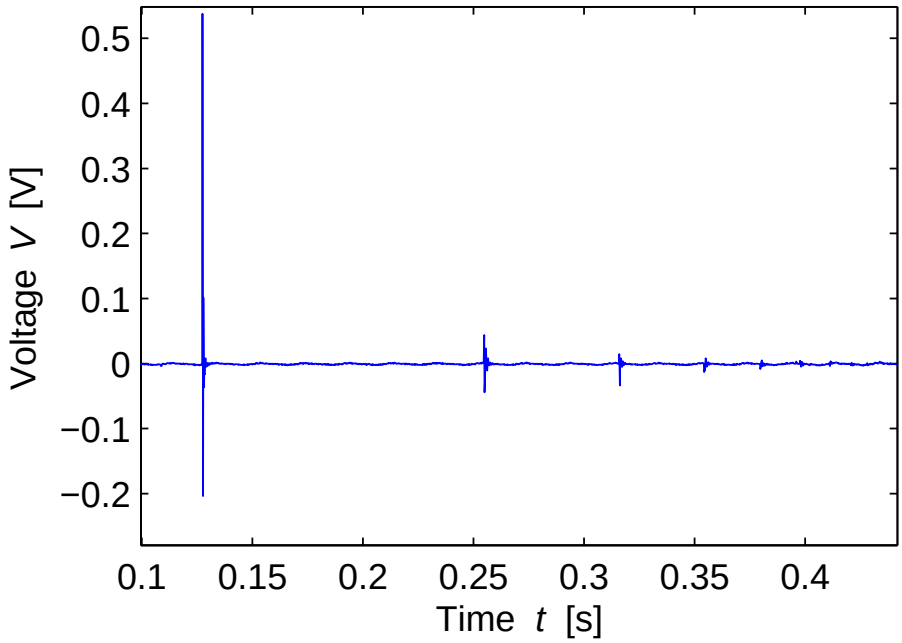

FIGURE 7.2: The measured result of a older version energy harvester from a single impact.

the other equilibrium position. This means the optimal frequency is mostly determined by the quality factor of the system, since a higher quality factor can keep the transient vibration alive longer. At lower frequencies the power again falls since the time between the change of the equilibrium position is longer and longer, this is basically means that the power provided by the shaker is lesser and lesser. Fig. 7.5 shows how the transient voltage slowly decreases before it is increased again by the change in equilibrium position. However, the voltage output for the bistable system is still two orders of magnitude larger than the linear system at a frequency of 50 Hz, as it is shown in Fig. 7.5.

In the aforementioned bistable setup the magnets were not mounted on the shaker. In a real system it can often be difficult to have the harvester be placed on a vibrating source and the magnets are not. Therefore the whole setup was moved onto a larger shaker where both the harvester and the magnets were shaken. However, the same result can not be reproduced. It seems that it is no longer possible to shake the cantilever from one of the equilibrium position to the other. This is believed to be caused by the fact that the movement of the shaker was helping the cantilever changing the equilibrium position, at 0.5 g the peak to peak displacement of the shaker is about 50 μm, which is comparable to the dimensions of the system [48]. However, it is also possible that a changing magnetic field as a result of the moving magnets would also have an effect on the system.

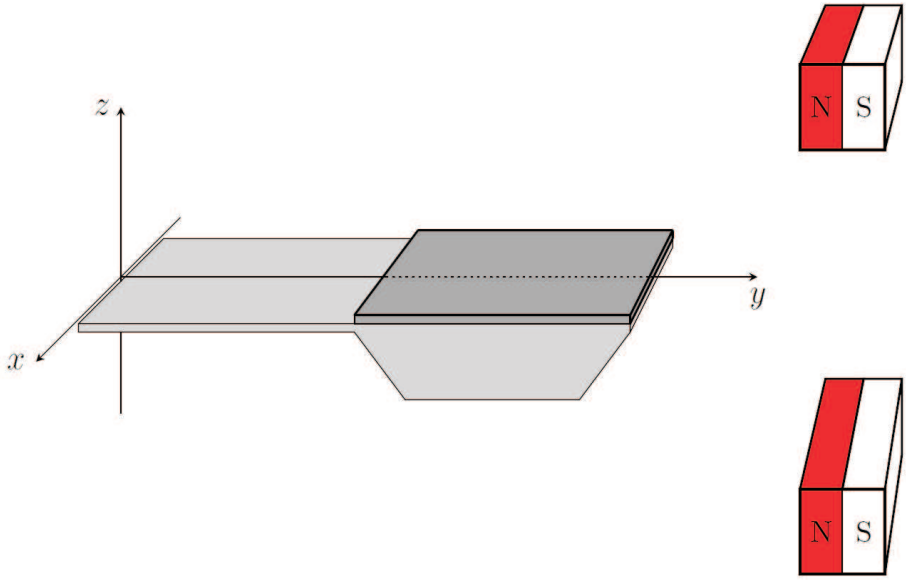

FIGURE 7.3: The bistable harvester setup is shown. Two neodymium magnets are placed near the harvester and a iron sheet of 50 μm thick, is glued onto the proof mass. This figure is taken from [48].

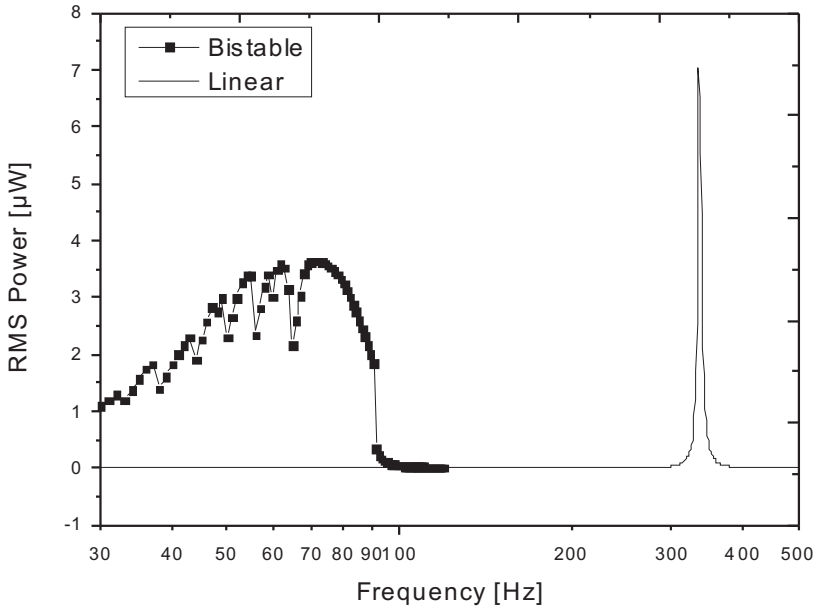

FIGURE 7.4: The RMS power output as a function frequency for bistable and linear system under an input acceleration of 0.5 g is shown. Resistive load of 65 kΩ is used.

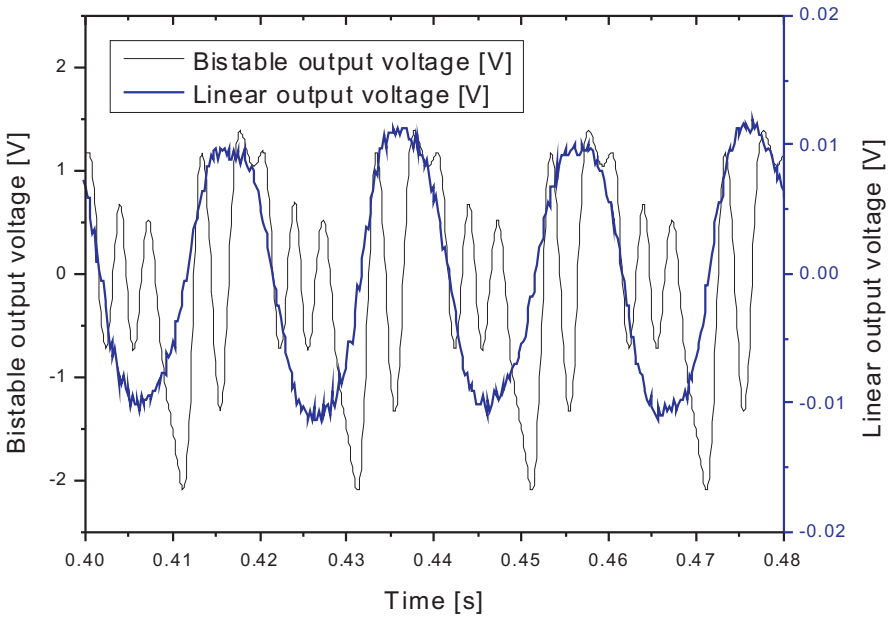

FIGURE 7.5: The voltage output for the bistable system and linear system at a constant frequency of 50 Hz and an input acceleration of 0.5 g.

Chapter 8

Conclusion and outlook

The main objective of the project, to fabricate a working energy harvester for the Elba project which integrates the silicon microtechnology with screen printed piezoelectric thick film, has been achieved. Several harvesters have already been integrated into the Elba demo system completed with rectifier circuits, accelerometer, RF-sender. Various design parameters of different shape cantilevers and different PZT cantilever thickness and PZT treatment were investigated. From these investigations, which consist of both theoretical evaluations and experimental knowledge, the best energy harvesters design have been found. It is also demonstrated that the developed fabrication technique can also be used with other piezoelectric thick film, such as KNN.

The conclusions from the different harvester design parameters will be summarized here. The best result, *i.e.* high power output and robustness, is achieved by an energy harvester having one rectangular cantilever beam. The trapezoidal shaped cantilever harvesters are supposed to have higher power density, which is sounded good in theory, was not measured. Since the reduced volume of the cantilever is not utilized the advantage is further minimized. From the fabrication point of view, it is also clear that the yield is lesser for the trapezoidal shaped cantilever harvester compared to the rectangular ones. The theoretical estimations suggests that at the proof mass to total cantilever length (including the mass length) ratio α of around 70% the highest power output should be achieved and at $\alpha = 50\%$ the lowest resonant frequency can be achieved. Therefore energy harvesters with $\alpha = 50\%$ and $\alpha = 70\%$ were fabricated. Though it is found that harvesters with $\alpha = 50\%$ indeed have lower resonant frequency than the corrosponding harvesters with $\alpha = 70\%$, the harvesters with $\alpha = 70\%$ does not outperform the harvesters with $\alpha = 50\%$ power wise. It is possible that the large variation in the power output between harvesters to harvesters overshadows the increase in power output. The large variation in the power output is believed to be caused by a large variation in the

quality factor or the piezoelectric coefficient. With the recent aquirement of the Micro-Epsilon laser sensor ILD1401-5 the mechanical quality factor can be measured, whether or not the variation of the quality factor is the cause of the large variation in output power can be found. Good results have been achieved with both the unimorph energy harvesters and the bimorph energy harvesters. Both kinds of harvesters have achieved an output power over 35 μW at 1 g. Both kinds of harvesters possessed great potentials and should not be abandoned in favour of the other. The relative simpler fabrication of the unimorph harvester is its great advantage. The flexibilty of the bimorph harvesters enables the possiblity of screen print extra proof mass onto the silicon proof mass is also invalueble for the future developement. The biggest improvement on the energy harvesters is to have the ability to high pressure treate the thick film to further condense the TF2100 PZT thick film, so the mechanical and electrical properties of the film can be significantly improved. Though it was possible to do high pressure treatement after the DRIE process, the yield will be greatly reduced due to the harshness of the treatment. The introduction of the KOH etch with the AMMT wet etch holder is a major step towards enabling the high pressure treatement without reducing the yield, and in the end probably increased the total yield, by strengthning the thick film itself. By using KOH etch later in the fabrication process instead of using DRIE early, the screen printing steps will be done on a bulk wafer and not wafer with thin membranes.

A Comparison of this work with other state of the the art MEMS energy harvesters using the parameters such as resonant frequency, bandwidth, input acceleration and the power output is shown in Table 8.1. The size of these energy harvesters are roughly the same, therefore the often used power density is not compared. A good energy harvester should have a low resonant frequency, large bandwidth, and high power output at a low input acceleration. From this comparison it is clear that this work and the bimorph energy harvester in particular is among the top 3 best fabricated MEMS energy harvesters. The other two being the tungsten proof mass energy harvester made by Aktakka *et al.* [10] and the sputtered AlN energy harvester made by Elfrink *et al.* [9]. The good harvester performance achieved by Aktakka *et al.* is due to the usage of bulk PZT, which is indeed better than the screen printed PZT even with the high pressure treatment as it is shown in Table 2.2. The implementation of a tungsten proof mass further improved its performance. The energy harvester presented by Elfrink *et al.* [9] has comparable performance with this work with roughly the same power output and frequency, but with lower bandwidth. The low bandwidth is due to the harvester's reliance on the high quality factor. The other harvesters under performs compared to the aforementioned three, by either not harvest as much power even at high accelerations or having a significantly higher resonant frequency.

TABLE 8.1: A comparison between the recently published energy harvesters, using the parameters resonant frequency, input acceleration, power output and bandwidth.

Reference	Material	Frequency [Hz]	Acceleration [g]	Power [μW]	Bandwidth [Hz]
Aktakka *et al.* [10]	Thinned PZT	154	1.5	205.0	14
Elfrink *et al.* [9]	Sputtered AlN	325	1.75	85.0	3
Shen *et al.* [38]	Sol-gel PZT	461	2	2.2	1.2
Muralt *et al.* [49]	Sol-gel PZT	870	2	1.4	-
Renaud *et al.* [50]	Sol-gel PZT	1800	2.35	40.0	1
Lee *et al.* [51]	Aerosol PZT	256	2.5	2.8	-
This work	Screen printed PZT (unimorph)	328	1.0	39.3	5
This work	Screen printed PZT (bimorph)	240	1.4	59.3	7.6

Two possible packaging solutions for the energy harvesters are suggested and investigated, one is the anodic bonding packaging solution the other is the LTCC packaging solution. Regarding the anodic bonding package it has been showed that the Pyrex®/Silicon/Pyrex® stack can be bonded. The initial experiments show good results regarding the electrical feedthroughs through the Pyrex®/silicon bonding interface. The theoretical calculations show that the pull-in effect during the anodic bonding process should not be an issue. It was later found that the advantage of sealing the harvester in vacuum is limited, therefore the LTCC package solution is recently introduced. The electrical feedthroughs can be manufactured by punching out the LTCC material and screen printing thick film paste into the punched hole. The cavities can either be made by punching using custom made punching tools or micromilling. The package solution is then finalized by the soldering together the parts.

Besides the energy harvesters themselves a possible better diffusion barrier was investigated. However, no better solution than the current used Pt diffusion barrier was found. Various fabrication issues encountered were solved. The cause of the mysterious short circuit issue was found and dealt with. The introduction of the bottom electrode annealing solved most of the adhesion problems, however adhesion problems still occur from time to time. Various adhesion promoters were tested without significant success.

8.1 Outlook for the energy harvester

There are still much ongoing work and future work in the Elba project. Here are some suggestions for some topics that should be worked on. The packaging solutions started in this project should be completed. The next stage of the anodic bonding packaging solution should be the encapsulation of silicon cantilever test structure with two Pyrex® wafers. There are two benefits to such a test. First, the effect of pull-in can be experimentally tested. Second the silicon cantilever test structure can be used as a resonator, so the packaging hermeticity can be evaluated by measure the resonator quality factor. The next stage of the LTCC packaging solution should be to fabricate the drawn structures. Besides the two packaging solutions presented in this project other solutions should not be ruled out. The adhesion issue is closely related to the diffusion barrier, at more comprehensive investigation should be made where both issues are looked upon. A study of the contaminations due to bad diffusion barrier should be investigated in depth using Energy-dispersive X-ray spectroscopy (EDX).

The improvements that could be done to further improve the unimorph energy harvester are somewhat limited. These improvements are most related to the improvements on the screen printed PZT. A further improved high pressure treatment, so the mechanical and electrical material parameter be even closer to the bulk values, would benefit the harvester significantly. Substantial improvement possibilities exist for the bimorph energy harvester. The fabrication part of the bimorph energy harvester had already been partially discussed. In the future development the screen printing of the middle electrode should be combined with the screen printed extra proof mass. This will hopefully result in a robust energy harvester with a low resonant frequency, that also harvesters more energy. As it was mentioned in the theory sections if one wish to further increase the power output of the energy harvester, more or/and heavier proof mass will the most dominate factor. The KNN energy harvester continues to be a good lead-free alternative and should be worked upon in the future.

Further work should also be put into the non-resonant system development, in particular the magnetic bistable system. The Micro-Epsilon laser sensor ILD1401-5 would be an invaluable tool for the understanding of the cantilever behavior, and may be used to find out the reason for the systems inability to achieve bistability when the magnets are mounted on the shaker.

8.2 Outlook for the Elba system

The energy harvester is of course only part of the story. Two key challenges still remain for the Elba project. In the future the fabricated energy harvester should also be optimized towards the real energy source. The current energy harvester is limited by its size and is optimized for low resonant frequency and high power output. In a real energy source the resonant frequency is fixed and the harvester should be made with that particular frequency. It is believed that the screen printed extra mass, that is currently in development, will be a valuable tool for that. The rectifier circuit and the later power management system is also an important area, where the precious harvested power can be wasted if not optimized. Work has already been done on choosing the best diodes for the rectifier circuit.

Bibliography

[1] E. V. Thomsen, E. Ringgaard, and Sascha Gutt. Application concerning advanced technology projects: ELiminating BAtteries energy harvesters for integrated systems (ELBA), 2009.

[2] Patric Salomon. Micro sensors and microsystems world wide markets and economic impact. In *Eurosensors 2009*, 2009.

[3] Nicholas S Hudak and Glenn G Amatucci. Small-scale energy harvesting through thermoelectric, vibration, and radiofrequency power conversion. *Journal of Applied Physics*, 103(10):101301–101301–24, May 2008. ISSN 00218979. doi: doi:10.1063/1.2918987. URL http://jap.aip.org/resource/1/japiau/v103/i10/p101301_s1.

[4] S P Beeby, M J Tudor, and N M White. Energy harvesting vibration sources for microsystems applications. *Measurement Science and Technology*, 17(12):R175–R195, December 2006. ISSN 0957-0233, 1361-6501. doi: 10.1088/0957-0233/17/12/R01. URL http://iopscience.iop.org/0957-0233/17/12/R01.

[5] K A Cook-Chennault, N Thambi, and A M Sastry. Powering MEMS portable devicesa review of non-regenerative and regenerative power supply systems with special emphasis on piezoelectric energy harvesting systems. *Smart Materials and Structures*, 17(4):043001, August 2008. ISSN 0964-1726, 1361-665X. doi: 10.1088/0964-1726/17/4/043001. URL http://iopscience.iop.org/0964-1726/17/4/043001.

[6] Shad Roundy, Paul K. Wright, and Jan Rabaey. A study of low level vibrations as a power source for wireless sensor nodes. *Computer Communications*, 26(11):1131–1144, July 2003. ISSN 0140-3664. doi: 10.1016/S0140-3664(02)00248-7. URL http://www.sciencedirect.com/science/article/pii/S0140366402002487.

[7] Steven R Anton and Henry A Sodano. A review of power harvesting using piezoelectric materials (20032006). *Smart Materials and Structures*, 16(3):R1–R21, June 2007. ISSN 0964-1726, 1361-665X. doi: 10.1088/0964-1726/16/3/R01. URL http://iopscience.iop.org/0964-1726/16/3/R01.

[8] R Elfrink, T M Kamel, M Goedbloed, S Matova, D Hohlfeld, Y van Andel, and R van Schaijk. Vibration energy harvesting with aluminum nitride-based piezoelectric devices. *Journal of Micromechanics and Microengineering*, 19(9):094005, September 2009. ISSN 0960-1317, 1361-6439. doi: 10.1088/0960-1317/19/9/094005. URL http://iopscience.iop.org/0960-1317/19/9/094005.

[9] R Elfrink, M Renaud, T M Kamel, C de Nooijer, M Jambunathan, M Goedbloed, D Hohlfeld, S Matova, V Pop, L Caballero, and R van Schaijk. Vacuum-packaged piezoelectric vibration energy harvesters: damping contributions and autonomy for a wireless sensor system. *Journal of Micromechanics and Microengineering*, 20(10): 104001, October 2010. ISSN 0960-1317, 1361-6439. doi: 10.1088/0960-1317/20/10/104001. URL http://iopscience.iop.org/0960-1317/20/10/104001.

[10] E. E Aktakka, R. L Peterson, and K. Najafi. Thinned-PZT on SOI process and design optimization for piezoelectric inertial energy harvesting. In *Solid-State Sensors, Actuators and Microsystems Conference (TRANSDUCERS), 2011 16th International*, pages 1649–1652. IEEE, June 2011. ISBN 978-1-4577-0157-3. doi: 10.1109/TRANSDUCERS.2011.5969857.

[11] R. G. Ballas. *Piezoelectric multilayer beam bending actuators: static and dynamic behavior and aspects of sensor integration*. Springer, May 2007. ISBN 9783540326410.

[12] Stephen D. Senturia. *Microsystem design*. Springer, 2001. ISBN 9780792372462.

[13] C.G. Hindrichsen, R. Lou-Mller, K. Hansen, and E.V. Thomsen. Advantages of PZT thick film for MEMS sensors. *Sensors and Actuators A: Physical*, 163(1): 9–14, September 2010. ISSN 0924-4247. doi: 10.1016/j.sna.2010.05.004. URL http://www.sciencedirect.com/science/article/pii/S0924424710002177.

[14] Ferroperm. Ferroperm catalogue - ferroperm piezoceramics, May 2003.

[15] S. Roundy, E. S Leland, J. Baker, E. Carleton, E. Reilly, E. Lai, B. Otis, J. M Rabaey, P. K Wright, and V. Sundararajan. Improving power output for vibration-based energy scavengers. *IEEE Pervasive Computing*, 4(1):28– 36, March 2005. ISSN 1536-1268. doi: 10.1109/MPRV.2005.14.

[16] A. Lei, R. Xu, A. Thyssen, A. C Stoot, T. L Christiansen, K. Hansen, R. Lou-Moller, E. V Thomsen, and K. Birkelund. MEMS-based thick film PZT vibrational energy harvester. In *2011 IEEE 24th International Conference on Micro Electro Mechanical Systems (MEMS)*, pages 125–128. IEEE, January 2011. ISBN 978-1-4244-9632-7. doi: 10.1109/MEMSYS.2011.5734377.

[17] R. Xu, A. Lei, C. Dahl-Petersen, K. Hansen, M. Guizzetti, K. Birkelund, E. V. Thomsen, and O. Hansen. MEMS-BASED PZT/PZT BIMORPH THICK FILM VIBRATION ENERGY HARVESTER. In *PowerMEMS 2011*, Seoul, South Korea, 2011.

[18] W. Kern and D. Puotinen. Cleaning solutions based on hydrogen peroxide for use in silicon semiconductor technology, 1970.

[19] R. Xu, A. Lei, C. Dahl-Petersen, K. Hansen, M. Guizzetti, K. Birkelund, E.V. Thomsen, and O. Hansen. Screen printed PZT/PZT thick film bimorph MEMS cantilever device for vibration energy harvesting. *Sensors and Actuators A: Physical*, (0), 2012. ISSN 0924-4247. doi: 10.1016/j.sna.2011.12.035. URL http://www.sciencedirect.com/science/article/pii/S0924424711007497.

[20] P Glynne-Jones, S P Beeby, P Dargie, T Papakostas, and N M White. An investigation into the effect of modified firing profiles on the piezoelectric properties of thick-film PZT layers on silicon. *Measurement Science and Technology*, 11(5): 526–531, May 2000. ISSN 0957-0233, 1361-6501. doi: 10.1088/0957-0233/11/5/312. URL http://iopscience.iop.org/0957-0233/11/5/312.

[21] Franz Laermer and Andrea Schilp. Method of anisotropic etching of silicon, November 2003. URL http://www.freepatentsonline.com/6531068.html.

[22] K. R Williams, K. Gupta, and M. Wasilik. Etch rates for micromachining processing-Part II. *Journal of Microelectromechanical Systems*, 12(6):761– 778, December 2003. ISSN 1057-7157. doi: 10.1109/JMEMS.2003.820936.

[23] H. Seidel, L. Csepregi, A. Heuberger, and H. Baumgartel. Anisotropic etching of crystalline silicon in alkaline solutions. *Journal of The Electrochemical Society*, 137(11):3612–3626, November 1990. doi: 10.1149/1.2086277. URL http://dx.doi.org/10.1149/1.2086277.

[24] Gary S. May and S. M. Sze. *Fundamentals of semiconductor fabrication*. Wiley, 2004. ISBN 9780471452386.

[25] Ruichao Xu. *Microreactor and Nanoparticle Catalysis*. PhD thesis, Technical University of Denmark, 2009.

[26] Johan Nagstrup. *Piezoelectric MEMS Energy Harvester based on PZT Thick Film*. PhD thesis, Technical University of Denmark, 2009.

[27] Erling Ringgaard and Thom Wurlitzer. Lead-free piezoceramics based on alkali niobates. *Journal of the European Ceramic Society*, 25(12):2701–2706,

2005. ISSN 0955-2219. doi: 10.1016/j.jeurceramsoc.2005.03.126. URL http://www.sciencedirect.com/science/article/pii/S095522190500289X.

[28] R. Xu, A. Lei, T. L Christiansen, K. Hansen, M. Guizzetti, K. Birkelund, E. V Thomsen, and O. Hansen. Screen printed PZT/PZT thick film bimorph MEMS cantilever device for vibration energy harvesting. In *Solid-State Sensors, Actuators and Microsystems Conference (TRANSDUCERS), 2011 16th International*, pages 679–682. IEEE, June 2011. ISBN 978-1-4577-0157-3. doi: 10.1109/TRANSDUCERS.2011.5969848.

[29] S P Beeby, A Blackburn, and N M White. Processing of PZT piezoelectric thick films on silicon for microelectromechancial systems. *Journal of Micromechanics and Microengineering*, 9(3):218–229, September 1999. ISSN 0960-1317, 1361-6439. doi: 10.1088/0960-1317/9/3/302. URL http://iopscience.iop.org/0960-1317/9/3/302.

[30] R. Maas, M. Koch, N.R. Harris, N.M. White, and A.G.R. Evans. Thick-film printing of PZT onto silicon. *Materials Letters*, 31(12):109–112, May 1997. ISSN 0167-577X. doi: 10.1016/S0167-577X(96)00249-2. URL http://www.sciencedirect.com/science/article/pii/S0167577X96002492.

[31] R.A. Dorey and R.W. Whatmore. Electroceramic thick film fabrication for MEMS. *Journal of Electroceramics*, 12(1/2):19–32, January 2004. ISSN 1385-3449. doi: 10.1023/B:JECR.0000033999.74149.a3. URL http://www.springerlink.com.globalproxy.cvt.dk/content/w3231x6g93g16702/.

[32] Spearing S.M. Materials issues in microelectromechanical systems (MEMS). *Acta Materialia*, 48(1):179–196, January 2000. ISSN 1359-6454. doi: 10.1016/S1359-6454(99)00294-3. URL http://www.sciencedirect.com/science/article/pii/S1359645499002943.

[33] C.G. Hindrichsen. *Piezoelectric MEMS Accelerometer*. PhD thesis, Technical University of Denmark, 2010.

[34] L. P. H Jeurgens, W. G Sloof, F. D Tichelaar, and E. J Mittemeijer. Growth kinetics and mechanisms of aluminum-oxide films formed by thermal oxidation of aluminum. *Journal of Applied Physics*, 92(3):1649–1656, August 2002. ISSN 00218979. doi: doi:10.1063/1.1491591. URL http://jap.aip.org.globalproxy.cvt.dk/resource/1/japiau/v92/i3/p1649_s1.

[35] ANSI/IEEE. IEEE standard on piezoelectricity std 176, 1987.

[36] Qing-Ming Wang, Qiming Zhang, Baomin Xu, Ruibin Liu, and L. Eric Cross. Nonlinear piezoelectric behavior of ceramic bending mode actuators under strong electric fields. *Journal of Applied Physics*, 86(6):3352–3360, September 1999. ISSN 00218979. doi: doi:10.1063/1.371213. URL http://jap.aip.org.globalproxy.cvt.dk/resource/1/japiau/v86/i6/p3352_s1.

[37] L.Q. Yao, J.G. Zhang, L. Lu, and M.O. Lai. Nonlinear dynamic characteristics of piezoelectric bending actuators under strong applied electric field. *Journal of Microelectromechanical Systems*, 13(4):645–652, August 2004. ISSN 1057-7157. doi: 10.1109/JMEMS.2004.832187. URL http://ieeexplore.ieee.org.globalproxy.cvt.dk/xpls/abs_all.jsp?arnumber=1321102&t

[38] Dongna Shen, Jung-Hyun Park, Jyoti Ajitsaria, Song-Yul Choe, Howard C Wikle, and Dong-Joo Kim. The design, fabrication and evaluation of a MEMS PZT cantilever with an integrated si proof mass for vibration energy harvesting. *Journal of Micromechanics and Microengineering*, 18(5):055017, May 2008. ISSN 0960-1317, 1361-6439. doi: 10.1088/0960-1317/18/5/055017. URL http://iopscience.iop.org/0960-1317/18/5/055017.

[39] A. Lei, R. Xu, C.M. Pedersen, M. Guizzetti, K. Hansen, E. V. Thomsen, and K. Birkelund. HOMOGENEITY ANALYSIS OF HIGH YIELD MANUFACTURING PROCESS OF MEMS-BASED PZT THICK FILM VIBRATIONAL ENERGY HARVESTERS. In *PowerMEMS 2011*, Seoul, South Korea, 2011.

[40] Tingkai Zhang, Honghai Zhang, Jian Xu, Sheng Liu, and Zhiyin Gan. Study on triple-stack anodic bonding using two electrodes. *Sensors and Actuators A: Physical*, 157(1):168–172, January 2010. ISSN 0924-4247. doi: 10.1016/j.sna.2009.07.003. URL http://www.sciencedirect.com/science/article/pii/S0924424709003252.

[41] Schjlberg-Henriksen, E. Poppe, S. Moe, P. Stors, M M V Taklo, D T Wang, and H. Jakobsen. Anodic bonding of glass to aluminium. *Microsystem Technologies*, 12 (5):441–449, 2005. doi: 10.1007/s00542-005-0040-8.

[42] Yoshihiko Imanaka. *Multilayered Low Temperature Cofired Ceramics (LTCC) Technology*. Springer, 1 edition, December 2004. ISBN 0387231307.

[43] Michael Renaud, Paolo Fiorini, and Chris van Hoof. Optimization of a piezoelectric unimorph for shock and impact energy harvesting. *Smart Materials and Structures*, 16(4):1125–1135, August 2007. ISSN 0964-1726, 1361-665X. doi: 10.1088/0964-1726/16/4/022. URL http://iopscience.iop.org/0964-1726/16/4/022.

[44] E Jacquelin, S Adhikari, and M I Friswell. A piezoelectric device for impact energy harvesting. *Smart Materials and Structures*, 20(10):105008, October 2011. ISSN 0964-1726, 1361-665X. doi: 10.1088/0964-1726/20/10/105008. URL http://iopscience.iop.org/0964-1726/20/10/105008.

[45] M. Ferrari, V. Ferrari, M. Guizzetti, B. And, S. Baglio, and C. Trigona. Improved energy harvesting from wideband vibrations by nonlinear piezoelectric converters. *Sensors and Actuators A: Physical*, 162(2):425–431, August 2010. ISSN 0924-4247. doi: 10.1016/j.sna.2010.05.022. URL http://www.sciencedirect.com/science/article/pii/S0924424710002359.

[46] Ji-Tzuoh Lin, Barclay Lee, and Bruce Alphenaar. The magnetic coupling of a piezoelectric cantilever for enhanced energy harvesting efficiency. *Smart Materials and Structures*, 19(4):045012, April 2010. ISSN 0964-1726, 1361-665X. doi: 10.1088/0964-1726/19/4/045012. URL http://iopscience.iop.org/0964-1726/19/4/045012.

[47] Samuel C. Stanton, Clark C. McGehee, and Brian P. Mann. Nonlinear dynamics for broadband energy harvesting: Investigation of a bistable piezoelectric inertial generator. *Physica D: Nonlinear Phenomena*, 239(10):640–653, May 2010. ISSN 0167-2789. doi: 10.1016/j.physd.2010.01.019. URL http://www.sciencedirect.com/science/article/pii/S0167278910000394.

[48] M. W.H. Ley and I. Fugl. *Designing a Bistable Energy Harvester*. PhD thesis, Technical University of Denmark, 2011.

[49] P. Muralt, M. Marzencki, B. Belgacem, F. Calame, and S. Basrour. Vibration energy harvesting with PZT micro device. *Procedia Chemistry*, 1(1):1191–1194, September 2009. ISSN 18766196. doi: 10.1016/j.proche.2009.07.297. URL http://infoscience.epfl.ch/record/158952.

[50] M. Renaud, K. Karakaya, T. Sterken, P. Fiorini, C. Van Hoof, and R. Puers. Fabrication, modelling and characterization of MEMS piezoelectric vibration harvesters. *Sensors and Actuators A: Physical*, 145146(0):380–386, July 2008. ISSN 0924-4247. doi: 10.1016/j.sna.2007.11.005. URL http://www.sciencedirect.com/science/article/pii/S0924424707008412.

[51] B S Lee, S C Lin, W J Wu, X Y Wang, P Z Chang, and C K Lee. Piezoelectric MEMS generators fabricated with an aerosol deposition PZT thin film. *Journal of Micromechanics and Microengineering*, 19(6):065014, June 2009. ISSN 0960-1317, 1361-6439. doi: 10.1088/0960-1317/19/6/065014. URL http://iopscience.iop.org/0960-1317/19/6/065014.

Appendix A

Journal and conference publications

A. Lei, R. Xu, A. Thyssen, A.C. Stoot, T. L. Christiansen, K. Hansen, R. Lou-Moeller, E.V. Thomsen and K. Birkelund, "MEMS-Based Thick Film PZT Vibriational Energy Harvester", Proceeding, IEEE micro electro mechanical systems (IEEE MEMS), 2011, pp. 125-128.

R. Xu, A. Lei, T.L. Christiansen, K. Hansen, M. Guizzetti, K. Birkelund, E.V. Thomsen and O. Hansen, "SCREEN PRINTED PZT/PZT THICK FILM BIMORPH MEMS CANTILEVER DEVICE FOR VIBRATION ENERGY HARVESTING", Proceeding, The 16th international conference on solid-state sensors, actuators and microsystems (Transducers'11), 2011, pp. 679-682.

M. Guizzetti, T. Zawada, K. Hansen, R. Xu, A. Lei, A. C. Stoot, A. Thyssen, O. Hansen, E.V. Thomsen and K. Birkelund, "Design, fabrication and characterization of piezoelectric power harvesters realized with silicon micromachining and screen-printing technologies", Proceeding, PIEZO 2011-Electroceramics for End-Users VI, 2011.

A. Lei, R. Xu, C.M. Pedersen, M. Guizzetti, K. Hansen, E.V. Thomsen and K. Birkelund, "HOMOGENEITY ANALYSIS OF HIGH YIELD MANUFACTURING PROCESS OF MEMS-BASED PZT THICK FILM VIBRATIONAL ENERGY HARVESTERS", Proceeding, The 11th international workshop on micro and nanotechnology for power generation and energy conversion applications (PowerMEMS 2011), 2011, pp. 387-390.

R. Xu, A. Lei, C. Dahl-Petersen, K. Hansen, M. Guizzetti, K. Birkelund, E.V. Thomsen and O. Hansen, "MEMS-BASED PZT/PZT BIMORPH THICK FILM VIBRATION ENERGY HARVESTER", Proceeding, The 11th international workshop on micro and

nanotechnology for power generation and energy conversion applications (PowerMEMS 2011), 2011, pp. 143-146.

R. Xu, A. Lei, C. Dahl-Petersen, K. Hansen, M. Guizzetti, K. Birkelund, E.V. Thomsen and O. Hansen, "Screen printed PZT/PZT thick film bimorph MEMS cantilever device for vibration energy harvesting", Sensors and Actuaters A: Physical, In Press, Corrected Proof, Available online 27 December 2011.

R. Xu, A. Lei, C. Dahl-Petersen, K. Hansen, M. Guizzetti, K. Birkelund, E.V. Thomsen and O. Hansen, "Fabrication and characterization of MEMS-based PZT/PZT bimorph thick film vibration energy harvesters", In peer review process for Journal of Micromechanics and Microengineering.

Appendix B

Mask layout

B.1 Bottom electrode mask

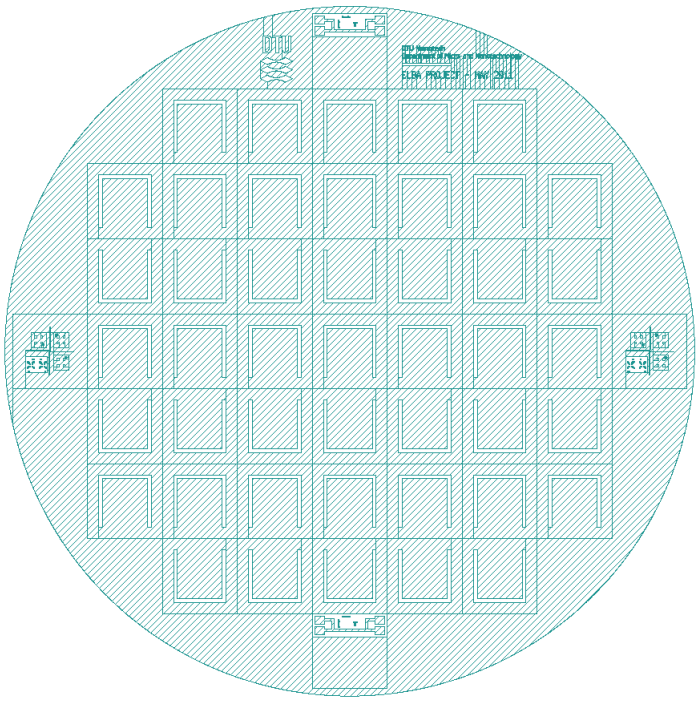

B.1.1 Chip layout: Bottom electrode mask

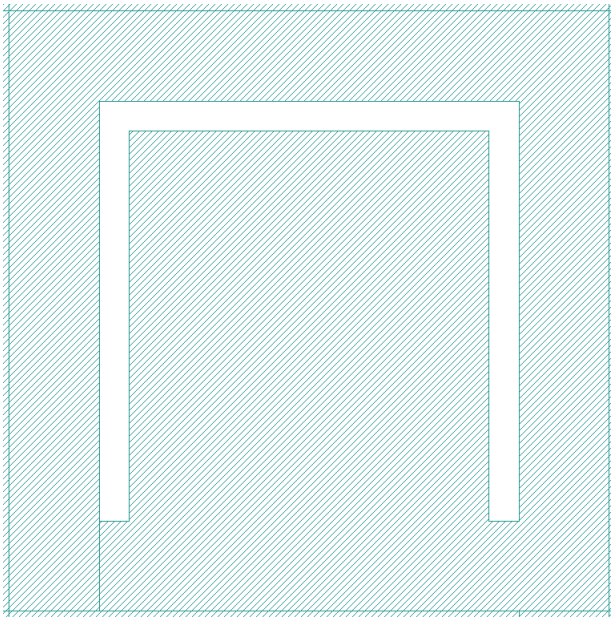

B.2 KOH etch mask

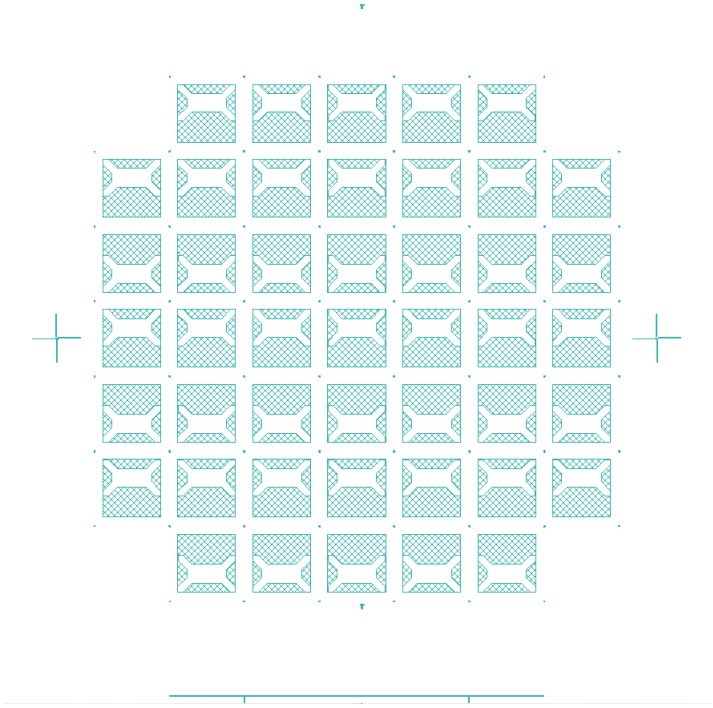

B.2.1 Chip layout: KOH etch mask (Bottom electrode mask is shown as reference)

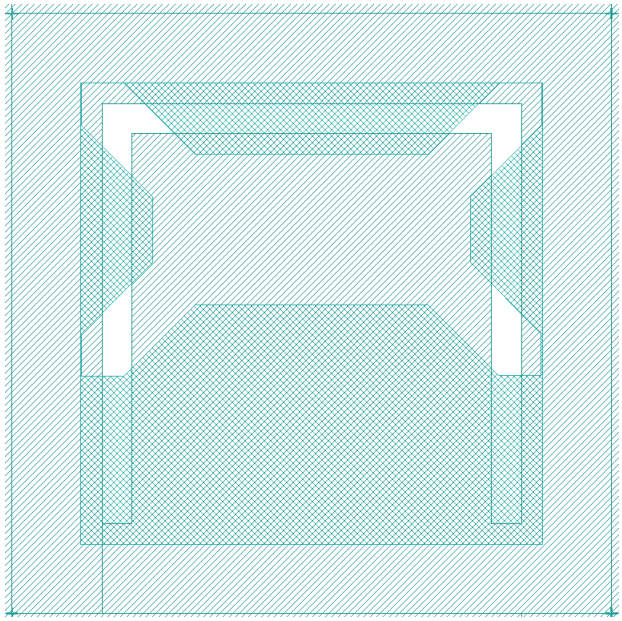

B.3 PZT layer 1 mask

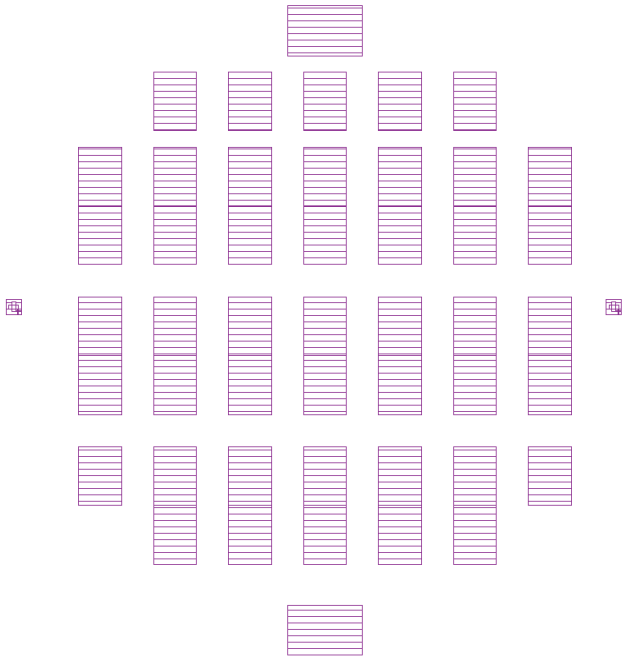

B.3.1 Chip layout: PZT layer 1 mask (Bottom electrode mask is shown as reference)

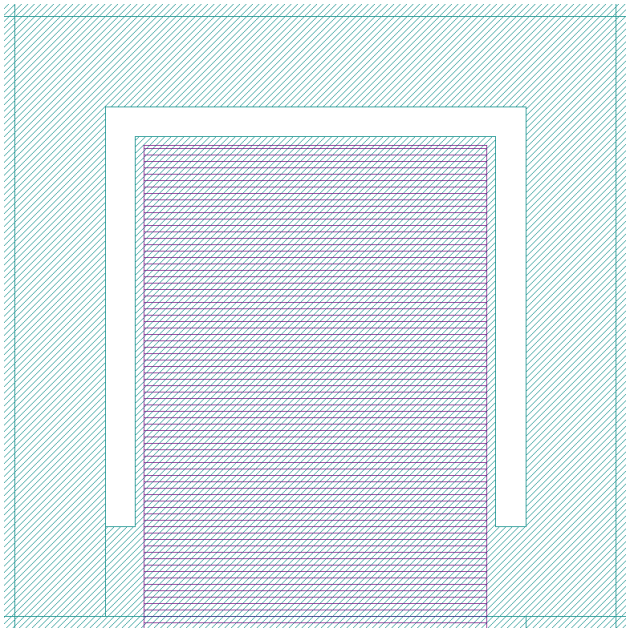

B.4 Middle electrode mask

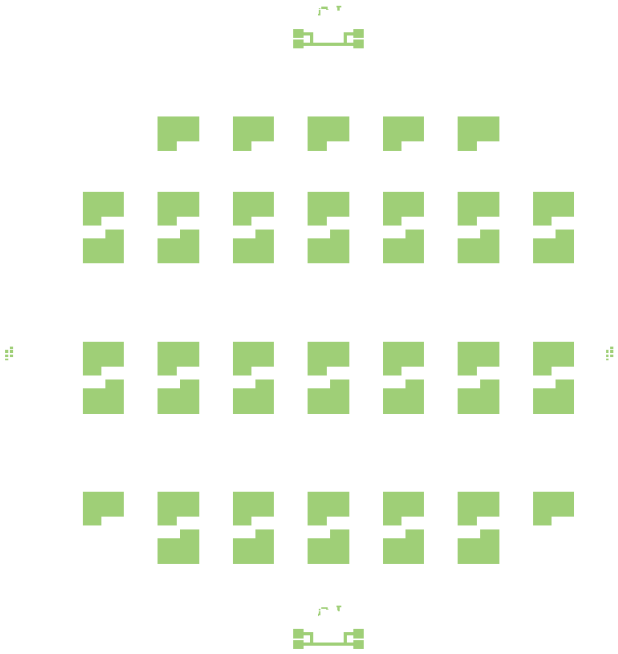

B.4.1 Chip layout: Middle electrode mask (Bottom electrode mask is shown as reference)

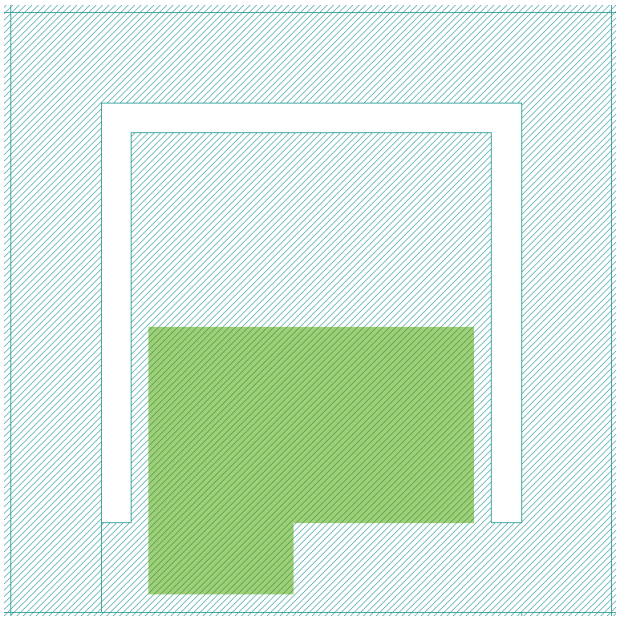

Note: Not used in the fabrication of the unimorph energy harvester.

B.5 PZT layer 2 mask

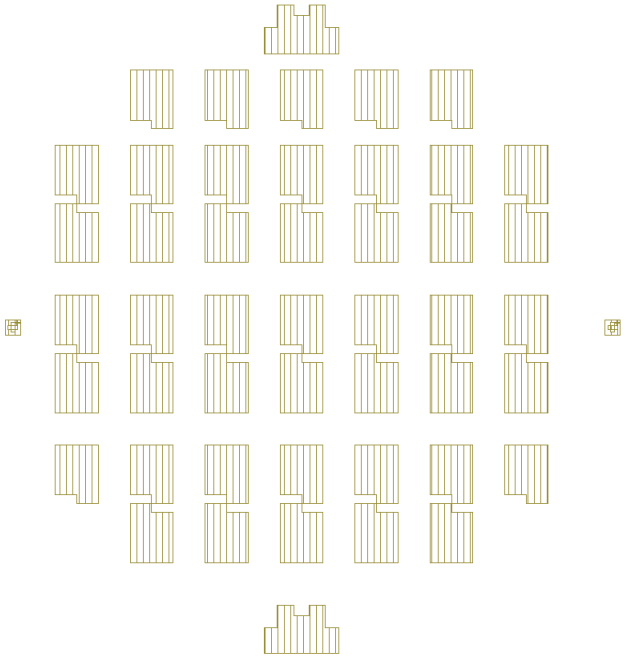

B.5.1 Chip layout: PZT layer 2 mask (Bottom electrode mask is shown as reference)

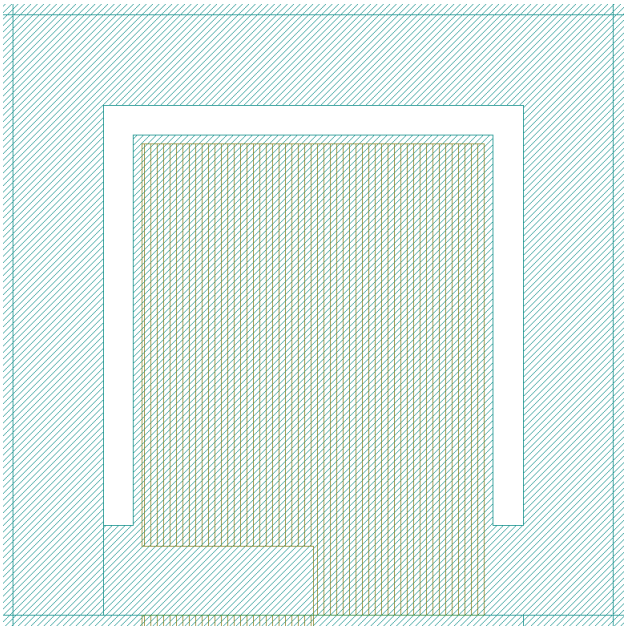

Note: Not used in the fabrication of the unimorph energy harvester.

B.6 Top electrode mask

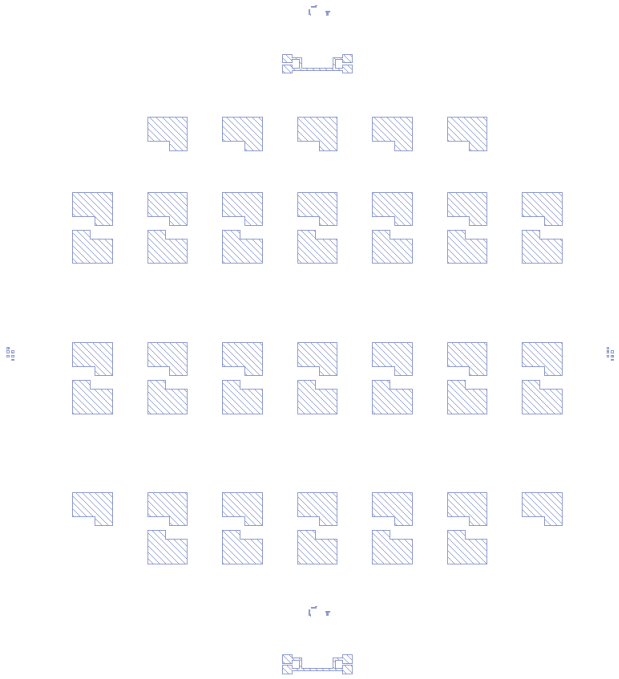

B.6.1 Chip layout: Top electrode mask (Bottom electrode mask is shown as reference)

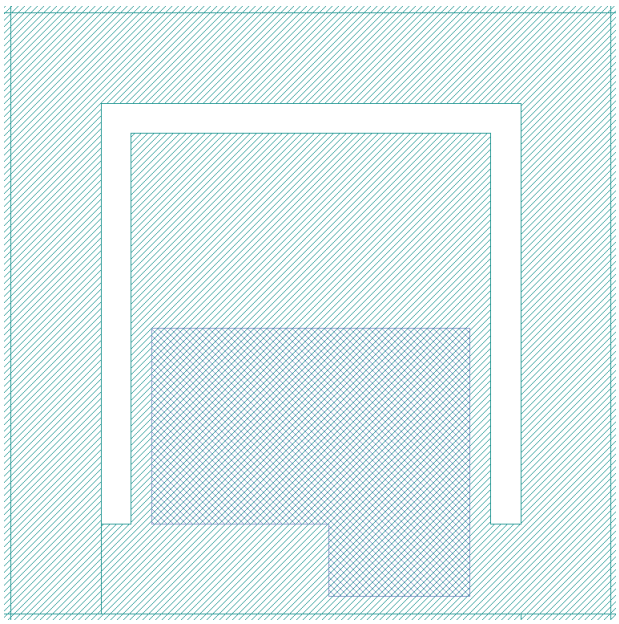

B.7 Screen printed extra mass mask

B.7.1 Chip layout: Screen printed extra mass mask (Bottom electrode mask is shown as reference)

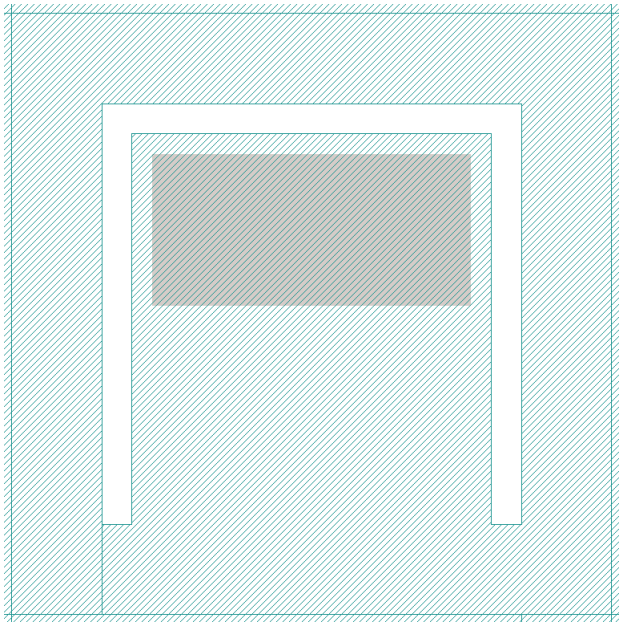

B.8 Trench mask

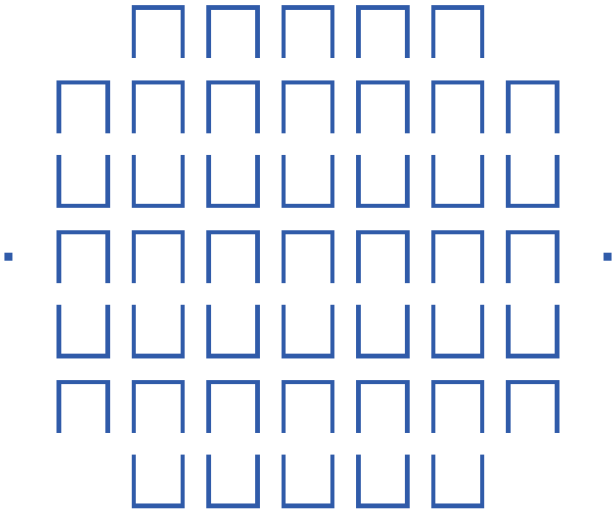

B.8.1 Chip layout: Trench mask (Bottom electrode mask is shown as reference)

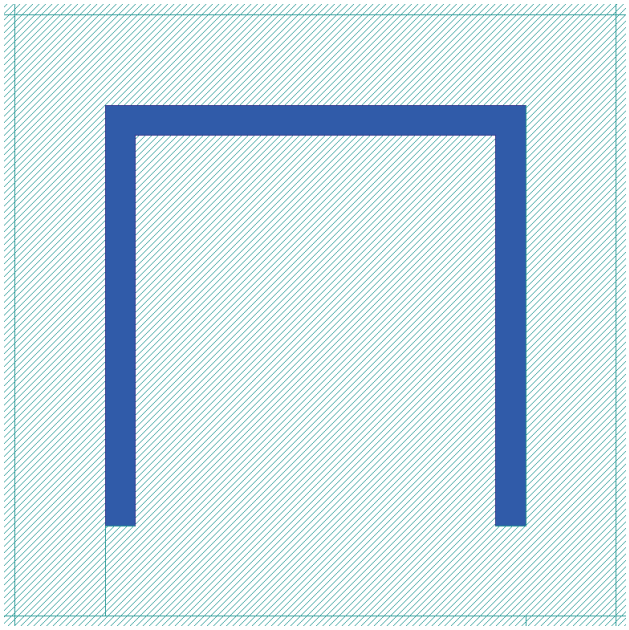

Note: Only used in the fabrication of the unimorph energy harvester.

Appendix C

Relevant documents

PRODUCT DATA

Mini-shaker — Type 4810

USES

- Calibration of accelerometers
- Vibration testing of small objects
- Educational demonstrations
- Mechanical impedance measurements

FEATURES

- Force rating 10 newton (2.25 lbf) sine peak
- Frequency range DC to 18 kHz
- First axial resonance above 18 kHz
- Max. bare table acceleration 550 m/s^2
- Rugged construction
- Optimised to obtain full output force when used with Power Amplifier Type 2718

951138e

Description

Mini-shaker Type 4810 is of the electrodynamic type with a permanent field magnet. It is well-suited as the motive force generator in mechanical impedance measurements where only smaller forces are required. It can also be used in the calibration of vibration transducers, both to determine their sensitivity, by comparison with a standard accelerometer, as well as their frequency response, up to 18 kHz.

The suspension system consists of radial flexure springs that restrict the moving element to almost perfectly rectilinear motion. Laminated flexure springs provide a high degree of damping to minimise distortion due to flexure resonances.

The object to be vibrated is attached to the table by means of a 10–32 UNF screw, the thread size commonly used for mounting accelerometers. Performance limits defined by the maximum displacement (6 mm), maximum force (10 N or 7 N depending on frequency), and the first axial resonance of the moving element (above 18 kHz), are shown in Fig. 1.

Fig. 1
Sine performance curves for Type 4810

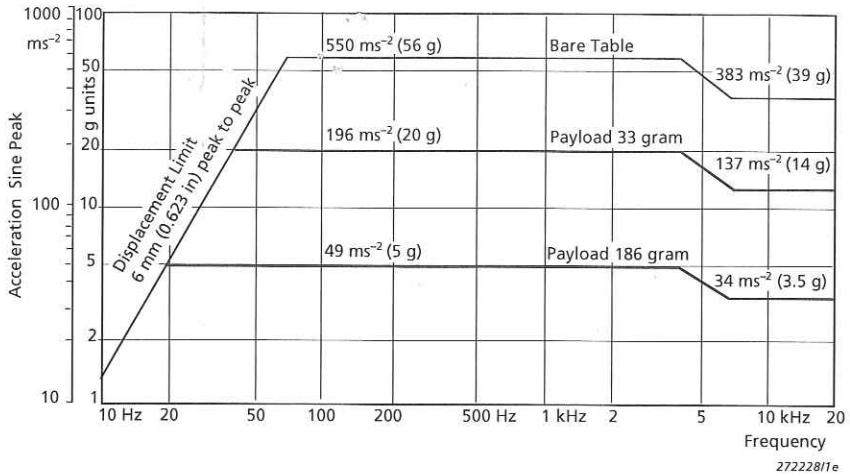

Specifications – Mini-shaker Type 4810

COMPLIANCE WITH STANDARDS
CE compliance with EMC Directive

compliance with EMC Requirements of Australia and New Zealand

Safety, EMC Emission and Immunity: According to relevant standards: EN 61010–1, IEC 61010–1, UL 3111–1, EN 50081–1/2, IEC 61000–6–1/2/3/4, EN 61326–1, CISPR22 Class B limits, FCC Rules Part 15, EN 50082–1/2, EN 61326–1
Temperature: According to IEC 60068–2–1 & IEC 60068–2–2
Operating temperature: +5 to +40°C (41 to 104°F)
Storage temperature: –25 to +70°C (–13 to 158°F)
Humidity: According to IEC 60068–2–3, Damp Heat: 90% RH (non-condensing at 40°C (104°F))
Mechanical: Non-operating according to IEC 60068–2–6, IEC 60068–2–27, IEC 60068–2–29

SPECIFICATIONS
FREQUENCY RANGE: DC to 18 kHz

FIRST MAJOR ARMATURE RESONANCE: Above 18 kHz

FORCE RATING (PEAK):
10 N (2.25 lbf). 65 Hz to 4 kHz
7 N (1.5 lbf). 65 Hz to 18 kHz

MAX. BARE TABLE ACCELERATION (PEAK):
550 m/s^2 (65 Hz to 4 kHz)
383 m/s^2 (6.5 kHz to 18 kHz)
(1 m/s^2 = 0.102 g)

MAX. DISPLACEMENT (PEAK-TO-PEAK): 6 mm (0.236 in)

DYNAMIC FLEXURE STIFFNESS: 2 N/mm (11.5 lb./in)

DYNAMIC WEIGHT OF THE MOVING SYSTEM: 18 grams

MAGNETIC FIELD: Permanent magnet

MAX. INPUT CURRENT: 1.8 A RMS

COIL IMPEDANCE: 3.5 Ω at 500 Hz

CONNECTION: Microsocket 10–32 UNF

TABLE SIZE: 14 mm (0.55 in) diameter

FASTENING THREAD: 10–32 UNF

WEIGHT: 1.1 kg (2.4 lb)

DIMENSIONS
Diameter: 76 mm (3 in)
Height: 75 mm (2.9 in)

Ordering Information

Type 4810	Mini-shaker
Includes the following accessories:	
AO 0069	Cable for connection of Type 4810 to Power Amplifier Type 2718
YQ 2962	Threaded Steel Stud, 0.3 in 10–32 UNF

Optional Accessories

EE 0112	ENDEVCO 2311-1 ISOTRON® Force Transducer
EE 0113	ENDEVCO 2311-10 ISOTRON Force Transducer
EE 0114	ENDEVCO 2311-100 ISOTRON Force Transducer
EE 0115	ENDEVCO 2311-500 ISOTRON Force Transducer
EE 0357	ENDEVCO Model 2312 Force Transducer
Type 8203	Force Transducer/Impact Hammer
UA 0125	Mounting Equipment (includes isolated studs YP 0150 and non-isolated studs YQ 2960)
WA 0429	Trunnion
WZ 0066	Nylon Stinger Kit
EE 5227-002	Bushing Adaptor, ¼–28 UNF to 10–32 UNF
EE 5004	Adaptor, Male 10–32 UNF to Male ¼–28 UNF
JP 0150	Adaptor, 4 mm Socket Pair to BNC Plug for use with old Type 2706

BP 0232–14 01/08

HEADQUARTERS: DK-2850 Nærum · Denmark · Telephone: +4545800500 · Fax: +4545801405 · http://www.bksv.com · e-mail: info@bksv.com
Australia (02)9450-2066 · Austria 0043-1-8657400 · Brazil (011)5182-8166 · Canada (514)695-8225 · China (86) 1068029906
Czech Republic 02-67021100 · Finland (0)9-755 950 · France (01)69907100 · Germany 06103/733 5-0 · Hong Kong 25487486 · Hungary (1)2158305
Ireland (01)803 7600 · Italy 02 57 68061 · Japan 03-3779-8671 · Republic of Korea (02)3473-0605 · Netherlands (31)318 559290 · Norway 66771155
Poland (22)858 9392 · Portugal (1)4711453 · Singapore (65) 377-4512 · Slovak Republic 421 2 5443 0701 · Spain (91)6590820 · Sweden (08)4498600
Switzerland (0)1 880 70 35 · Taiwan (02)7139303 · United Kingdom (0) 1438 739 000 · USA 800 332 2040
Local representatives and service organisations worldwide

Brüel & Kjær

PRODUCT DATA

Piezoelectric Accelerometer
Standard Reference Accelerometer — Type 8305

FEATURES

- Calibration traceable to the National Institute of Standards and Technology
- Laser interferometry calibration of reference sensitivity in accordance with ISO 5347
- Excellent isolation from base strains and low sensitivity to loading

Description

Type 8305 is a piezoelectric accelerometer with side connector. The transducer features two 10–32 UNF receptacles for input/output connection. It can be mounted on the object by means of a 10–32 UNF threaded steel stud. The accelerometer subject to calibration, is mounted on top of Type 8305, also by means of a 10–32 UNF threaded steel stud.

Characteristics

This piezoelectric accelerometer may be treated as a charge source. Its sensitivity is expressed in terms of charge per unit acceleration (pC/g).

In order to ensure a high degree of accuracy for calibration, Type 8305 is based on an inverted, centre-mounted compression design. This construction isolates the active element of the accelerometer from base strains and gives a low transverse sensitivity.

The piezoelectric element used in Type 8305 is the PZ 100 quartz crystal. The housing material is stainless steel.

Calibration

The sensitivity given in the calibration chart has been measured at 160 Hz with an acceleration of 100 ms^{-2}.

For a 99.9% confidence level, the accuracy of the factory calibration is ±2%.

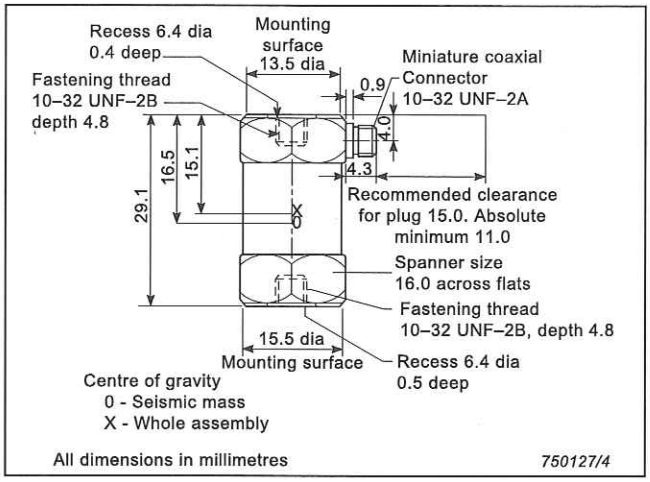

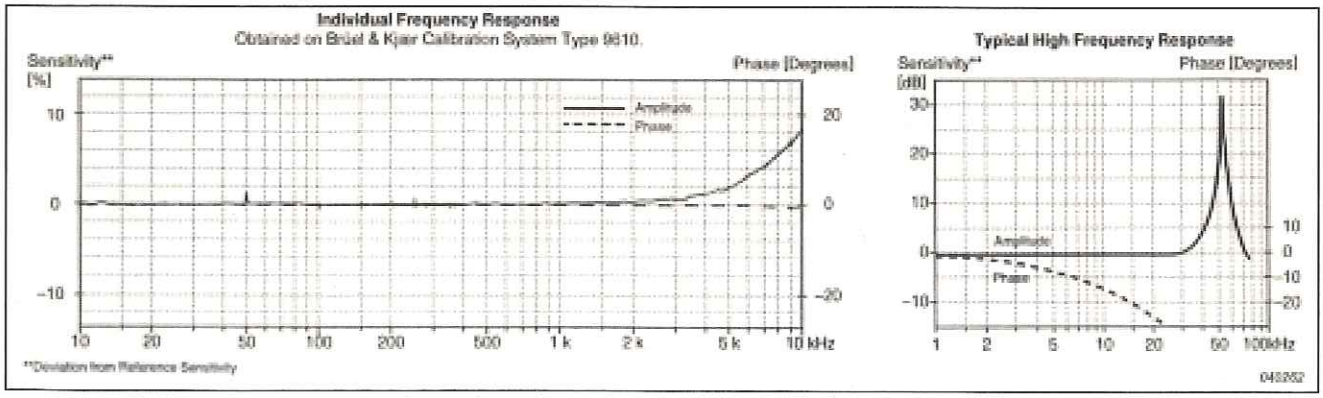

Brüel & Kjær

0,048

Specifications – Standard Reference Accelerometer Type 8305

	Units	8305
Dynamic Characteristics		
Charge Sensitivity (@ 160 Hz)	pC/g	1.25
Frequency Response		See typical amplitude curve
Mounted Resonance Frequency	kHz	38
Amplitude Response [1]: ±2% ±1%	Hz	0.2 to 4400 0.2 to 3100
Transverse Sensitivity	%	<2
Electrical Characteristics		
Min. Leakage Resistance @ 20°C	GΩ	1000
Capacitance	pF	180
Grounding		Signal ground
Environmental Characteristics		
Temperature Range	°C (°F)	–74 to 200 (–101 to 392)
Humidity		Welded, sealed
Max. Operational Sinusoidal Vibration (peak)	g pk	1000
Max. Operational Shock (± peak)	g pk	1000
Base Strain Sensitivity	Equiv. g/μ strain	Top: 0.001 Base: 0.0003
Thermal Transient Sensitivity	Equiv. g/°C (g/°F)	0.05 (0.028)
Magnetic Sensitivity (50 Hz–0.03 Tesla)	g/T	0.1
Physical Characteristics		
Dimensions		See outline drawing
Weight	gram (oz.)	40 (0.58)
Case Material		Stainless steel
Connector		10–32 UNF
Mounting		10–32 UNF threaded hole

[1] Low-end response of the transducer is a function of its associated electronics

Ordering Information

Type 8305 Includes the following accessories:

- AO 0038: 260°C Teflon® low-noise cable, 10–32 UNF, length 1.2 m (4 ft.)
- YQ 2962: 10–32 UNF threaded steel stud. Length 7.62 mm
- YQ 2960: 10–32 UNF threaded steel stud. Length 12.7 mm
- UA 0329 Accessory Box

HEADQUARTERS: DK-2850 Nærum · Denmark · Telephone: +45 4580 0500 · Fax: +45 4580 1405
www.bksv.com · info@bksv.com

Australia (+61) 2 9889-8888 · Austria (+43) 1 865 74 00 · Brazil (+55) 11 5188-8166 · Canada (+1) 514 695-8225
China (+86) 10 680 29906 · Czech Republic (+420) 2 6702 1100 · Finland (+358) 9-521 300 · France (+33) 1 69 90 71 00
Germany (+49) 421 17 87 0 · Hong Kong (+852) 2548 7486 · Hungary (+36) 1 215 83 05 · Ireland (+353) 1 807 4083
Italy (+39) 0257 68061 · Japan (+81) 3 5715 1612 · Korea (+82) 2 3473 0605 · Netherlands (+31) 318 55 9290
Norway (+47) 66 77 11 55 · Poland (+48) 22 816 75 56 · Portugal (+351) 21 47 11 4 53 · Singapore (+65) 6377 4512
Slovak Republic (+421) 25 443 0701 · Spain (+34) 91 659 0820 · Sweden (+46) 8 449 8600
Switzerland (+41) 44 880 7035 · Taiwan (+886) 2 2502 7255 · United Kingdom (+44) 14 38 739 000
USA (+1) 800 332 2040

Local representatives and service organisations worldwide

Brüel & Kjær

BP 2052 – 11 05/06 Rosendahls Bogtrykkeri

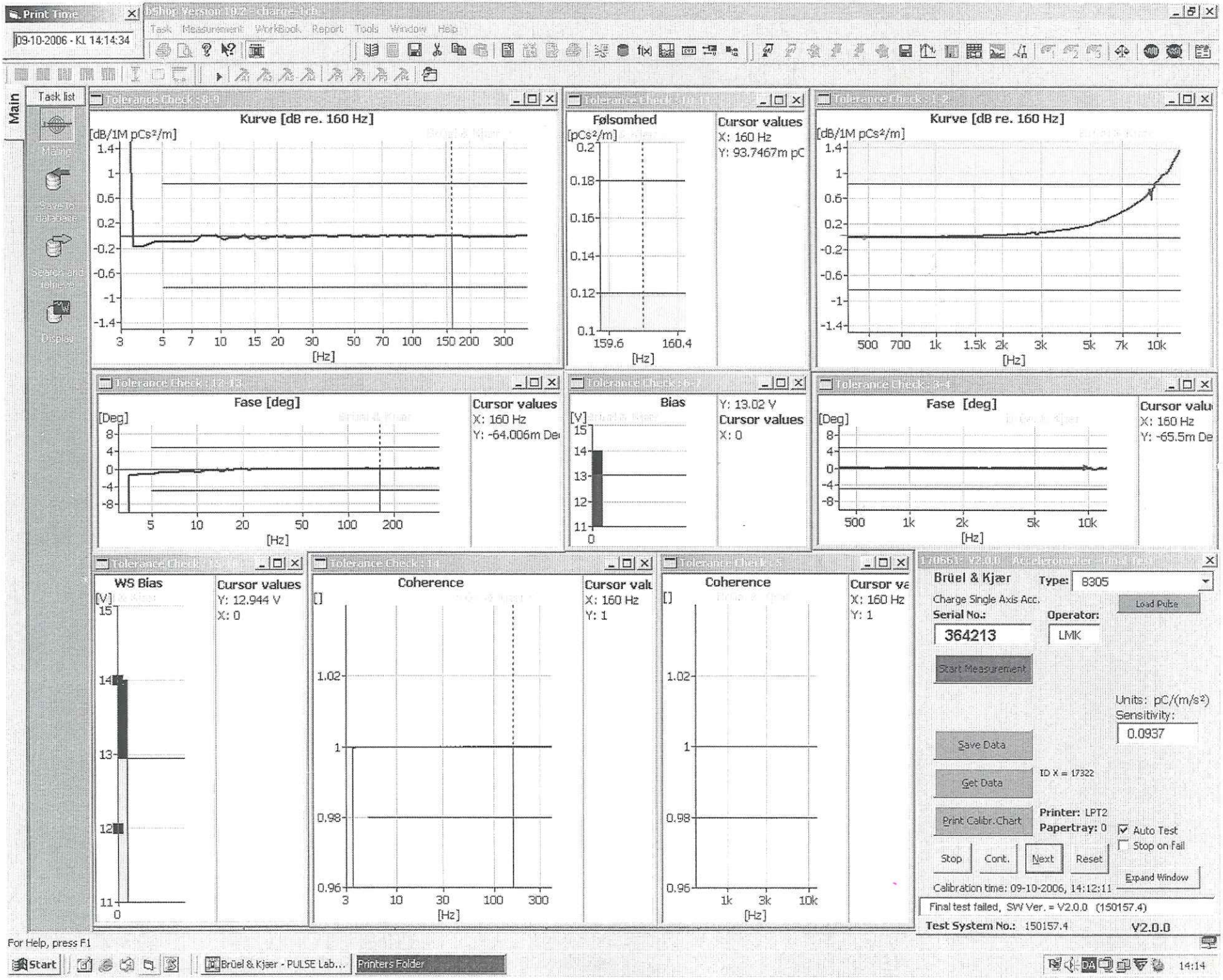
Print Time
09-10-2006 - Kl. 14:14:34
Task Measurement Workbook Report Tools Window Help
Main
Task list
Tolerance Check - ch0
Kurve [dB re. 160 Hz]
[dB/1M pCs²/m]
[Hz]
Tolerance Check - ch1
Følsomhed
[pCs²/m]
Cursor values
X: 160 Hz
Y: 93.7467m pC
[Hz]
Tolerance Check - ch2
Kurve [dB re. 160 Hz]
[dB/1M pCs²/m]
[Hz]
Tolerance Check - ch3
Fase [deg]
[Deg]
Cursor values
X: 160 Hz
Y: -64.006m De
[Hz]
Tolerance Check - ch7
Bias
[V]
Y: 13.02 V
Cursor values
X: 0
Tolerance Check - ch4
Fase [deg]
[Deg]
Cursor valu
X: 160 Hz
Y: -65.5m De
[Hz]
Tolerance Check - ch5
WS Bias
[V]
Cursor values
Y: 12.944 V
X: 0
Tolerance Check - ch6
Coherence
[]
Cursor valu
X: 160 Hz
Y: 1
[Hz]
Coherence
[]
Cursor va
X: 160 Hz
Y: 1
[Hz]
Brüel & Kjær
Type: 8305
Charge Single Axis Acc.
Load Pulse
Serial No.:
364213
Operator:
LMK
Start Measurement
Units: pC/(m/s²)
Sensitivity:
0.0937
Save Data
Get Data
ID X = 17322
Print Calibr.Chart
Printer: LPT2
Papertray: 0
Auto Test
Stop on Fail
Stop
Cont.
Next
Reset
Expand Window
Calibration time: 09-10-2006, 14:12:11
Final test failed, SW Ver. = V2.0.0 (150157.4)
Test System No.: 150157.4
V2.0.0
For Help, press F1
Start
Brüel & Kjær - PULSE Lab...
Printers Folder
14:14

InSensor A/S

TF2100

PZT thick film based on Ferroperm Pz26

Pz26 is an all-round hard PZT material with good coupling factors, high Curie temperature, high mechanical quality factor, low dielectric loss and very good stability over time. Pz26 can be used as a direct replacement for all other Navy I materials. Benefits include strongly improved ageing rates, and extremely stable performance from orders ranging over several years.

The material is compatible with thick film technology and the properties are almost fully conserved in the change from bulk to thick film. The change in properties is mainly attributed to increased porosity in the thick film compared to the bulk material.

Typical applications are:

- High frequency medical imaging
- Miniaturised accelerometers
- Integrated miniaturised phased array ultrasound scanners

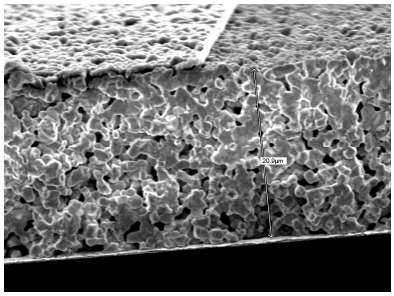

FIG. 1 SEM picture of TF2100

Main characteristics of TF2100

	Symbol	Unit	TF2100
Electrical properties			
Relative dielectric constant at 1 kHz	K_{33}^T		520
Dielectric dissipation factor at 1 kHz	$\tan\delta$	10^{-3}	8
Electromechanical properties			
Coupling coefficients	k_p		29
	k_t		49
Piezoelectric charge coefficients	d_{33}	pC/N	200
	d_{31}	pC/N	-50
Piezoelectric voltage coefficients	g_{33}	10^{-3} Vm/N	50
	g_{31}		-10
Mechanical properties			
Acoustic impedance	Z_a	MRayl	~15
Mechanical Quality Factor	$Q_{m,t}$		100

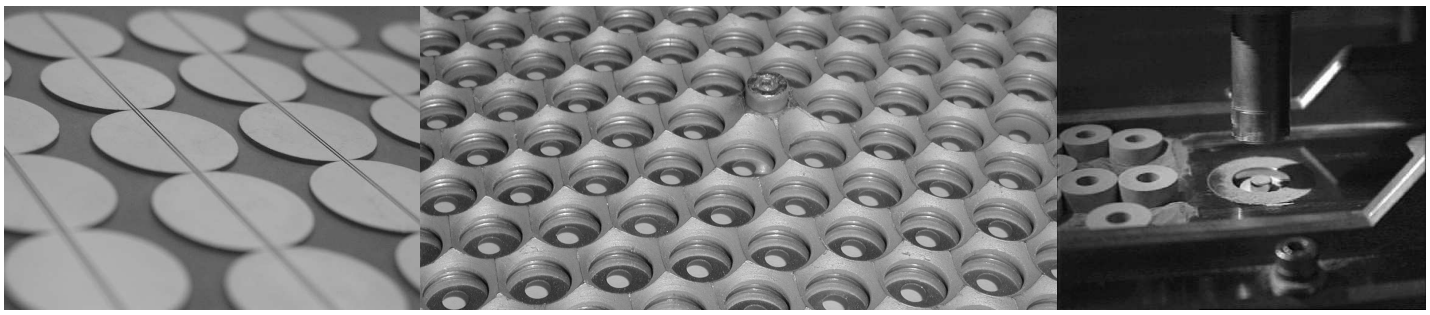

FERROPERM
PIEZOCERAMICS

HIGH QUALITY COMPONENTS AND MATERIALS
FOR THE ELECTRONIC INDUSTRY

Hejreskovvej 18A ∗ DK-3490 Kvistgård ∗ Tel.: (+45) 49 12 71 00 ∗ Fax: (+45) 49 13 81 88
E-mail: pz@ferroperm-piezo.com ∗ Website: www.ferroperm-piezo.com

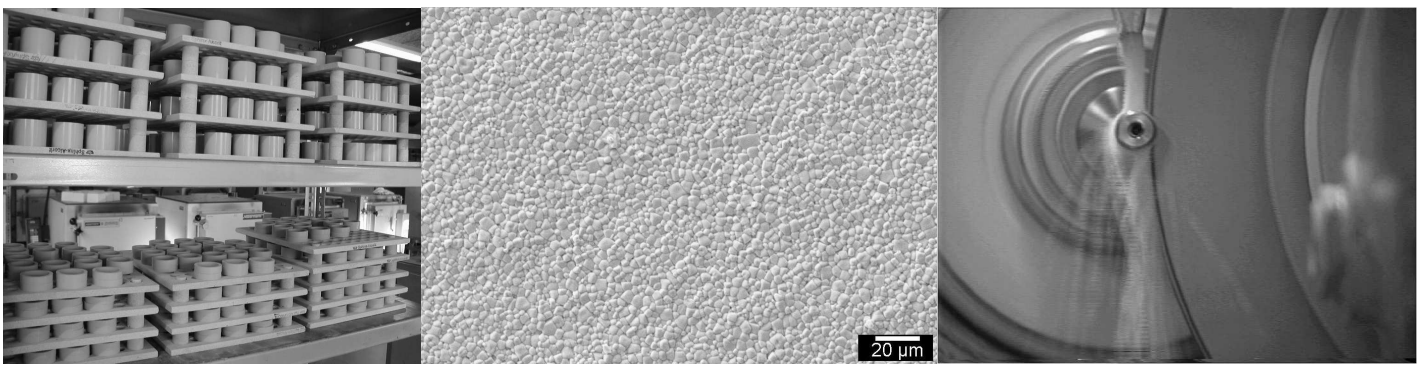

The Company

FERROPERM was registered in Denmark in May 1952 as a personal business to produce iron dust cores, ferrites and ceramic capacitors. In 1955, piezoelectric ceramics based on barium titanate were added to the product range.

The business was transferred to a limited company, ”Industriselskabet Ferroperm A/S” in 1957. This company steadily expanded its activities, and at a time also comprised production of capacitors and optical interference filters.

Since the formation of Ferroperm's Piezoelectric Division in 1958, its turnover has increased by approximately 15 % per year. In 1989 the Piezoelectric Division moved to modern premises to accommodate further expansion, and was turned into a separate limited company in 1998.

After a short period under American ownership in the year 2001, Ferroperm Piezoceramics A/S is now owned by a group of the senior managers in the company in partnership with a strong Danish investment group.

New products have been continuously developed and the Ferroperm product range today includes 6 types of lead zirconate-titanate, PZT, suitable for a variety of applications, a relaxor-based solid solution optimized for medical imaging, bismuth titanate, for use at elevated temperatures, modified lead titanate and lead metaniobate, with high anisotropy, and an electrostrictive material, lead magnesium niobate, PMN.

Finally, for special applications, "HIP Quality" very low porosity ceramics can be obtained in some of the above materials.

Research and Development

Ferroperm has a long standing commitment to R&D and currently spends approximately 20 % of its turnover on R&D projects. There is a close collaboration with leading universities throughout Europe. Ferroperm has continuously been involved in large European projects under Brite/Euram, Eureka, Cost, Esprit, FP5 etc.
Research topics include high-temperature piezo-electric ceramics, high sensitivity materials, lead-free materials, and thick-film technology.

Policy

More than 95 % of the products in Ferroperm Piezoceramics A/S are custom made to meet individual requirements of customers.

Our main focus throughout the entire production process is to provide materials and components with the highest possible reproducibility of properties and parameters, and to obtain the lowest ageing rates in the industry. This enables customers to optimize design and improve performance and production flow, thereby contributing to improved competitiveness on their markets.

May 2003

Table of Contents

Piezoelectric Materials

By definition, a piezoelectric material generates a charge when put under pressure, and will show a change in volume when an electrical field is applied. It can be used as a transducer material for transforming electrical energy into mechanical energy and vice versa. Furthermore, applying an A.C. voltage to the material will cause it to vibrate, and thus generate mechanical waves with the same frequency as the electrical voltage. Similarly, if a mechanical vibration is applied, then a charge of proportional size and same frequency will be generated.

History

Piezoelectric activity was first discovered in single crystals by J. and P. Curie in 1880. However, it was not until 1946 that scientists discovered that $BaTiO_3$ ceramics could be made piezoelectric by application of an electric field. This lead to the discovery of a number of piezoceramics and to the Lead Zirconate Titanate (PZT) family, in 1956. With its increased sensitivity and higher operating temperature, PZT soon replaced $BaTiO_3$ in many existing devices and are still the most widely used piezoceramics today.

The ceramic materials have several advantages over single crystals, including; higher sensitivity (up to several hundred times higher) and ease of fabrication into a variety of shapes and sizes. In contrast, single crystals must be cut along certain crystallographic directions, limiting the possible geometrical shapes.

Applications

Piezoelectric ceramics are used in a broad range of applications due to their excellent properties, such as high sensitivity, ease of manufacture and the possibility of poling the ceramic in any direction. A few applications are listed below:

- Accelerometers.
- Flow meters: Blood, industrial processes, waste water.
- Medical: Imaging, HIFU, IVUS, surgical knives, and cleaning of blood veins.
- Underwater acoustics: echosounders, sonar systems, fish-finders, seabed mapping.
- Industrial sensors based on ultrasound: Level control, detection, and identification.
- Hydrophones: Seismic, biologic, military, underwater communication.
- Inkjet printheads.
- Dental work: Removal of plaque.
- Alarm systems: Movement detectors, broken window sensors.
- NDT: Transducers for Non Destructive Testing.
- Musical instrument pickups.
- Acoustic emission transducers.
- Actuators.
- Micro positioning devices: Optics, scanning tunneling microscopes.
- Surface Acoustic Waves: Personal Computer touch screens, filters.
- Welding and drilling of metals and plastics.

Piezoceramics

Piezoelectric ceramics are, after firing, composed of small grains (crystallites), each containing domains in which the electric dipoles are aligned. These grains and domains are randomly oriented, so the net electric dipole is zero, i.e. the ceramics do not exhibit piezoelectric properties.

The application of a sufficiently strong DC. field will orient the domains in the field direction, as nearly as the orientation of the crystal axes allows. This ability to change the orientation of the domains and achieve a net polarization is called ferroelectricity.

A remanent polarization can be created in ferroelectric ceramics by polarization. After the poling process is complete, a voltage with the same polarity as the poling voltage causes expansion along the poling axis and contraction perpendicular to the poling axis. Compressive or tensile forces applied to the ceramic element will generate a voltage.

Definitions and Terminology

In piezoelectric ceramics, material characteristics depend on the direction of the applied field, displacement, stress and strain. Hence superscripts and subscripts indicating the direction are added to the symbols.

The direction of polarization is generally designated as the z-axis of an orthogonal crystallographic system. The axes x, y and z are respectively represented as 1, 2 and 3 directions and the shear about these axes are represented as 4, 5 and 6. This is shown schematically on page 4. The various piezoelectric material constants are generally expressed with subscripts using this notation. Some examples are shown in the table on next page. In addition to the above, planar modes are sometimes expressed with a subscript ´p´.

The first subscript gives the direction of the electrical field associated with the voltage applied or the charge produced. The second subscript gives the direction of mechanical stress or strain.

Superscripts indicate a constant mechanical or electrical boundary condition. The table below gives a general description of the superscripts.

Parameter	Symbol	Condition
Stress	T	Mechanically free
Field	E	Electrical short circuit
Diel. displacement	D	Electrical open circuit
Strain	S	Mechanically clamped

Curie Temperature

The crystal structure of a material changes at the Curie temperature, T_C, from piezoelectric (non-symmetrical) to a non-piezoelectric (symmetrical) form. This phase change is accompanied by a peak in the dielectric constant and a complete loss of all piezoelectric properties.

Table of Symbols

A	surface area (m^2)
c	stiffness coefficient (N/m^2)
C	capacitance (F)
d	piezoelectric charge coefficient (C/N)
D	diameter (m)
f_1, f_2	-3dB points from the resonance frequency f_r
f_a	anti-resonance frequency (Hz)
f_r	resonance frequency (Hz)
g	piezoelectric voltage coefficient (Vm/N)
k	coupling factor
K	relative dielectric constant
L	length (m)
N	frequency constant (Hz·m)
Q_m	mechanical quality factor
s	elastic compliance (m^2/N)
Th	thickness (m)
T_C	Curie temperature (°C)
W	width (m)
Y	Young's modulus (N/m^2)
Z_m	minimum impedance at f_r (ohm)
tan δ	dielectric dissipation factor
ε_0	permittivity of free space (8.854×10^{-12} F/m)
ε^T	Permittivity at constant stress (F/m)
v	sonic velocity (m/s)
ρ	density (kg/m^3)
σ^E	Poisson's ratio

Symbols And Terminology

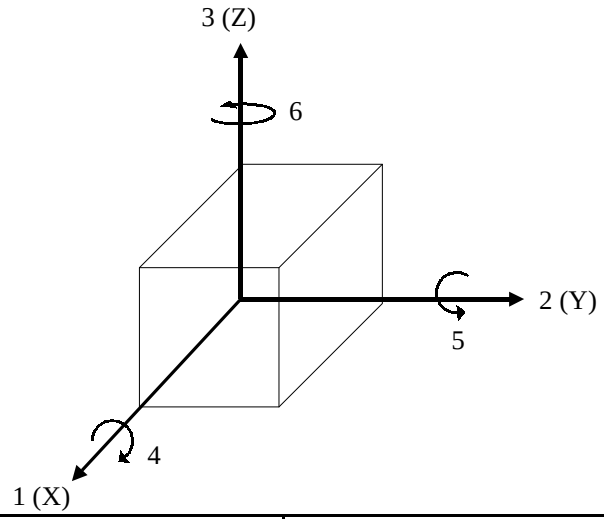

K_3^S
All strains in the material are constant or mechanical deformation is blocked in any direction.
Electrodes are perpendicular to 3 axis.
Relative dielectric constant ($\varepsilon_3^S/\varepsilon_0$).

K_1^T
All stresses on material are constant or no external forces.
Electrodes are perpendicular to 1 axis.
Relative dielectric constant ($\varepsilon_1^T/\varepsilon_0$).

k_p
Stress or strain is equal in all directions perpendicular to 3 axis. Used only for ceramics. Electrodes are perpendicular to 3 axis.
Electromechanical coupling factor.

k_{15}
Stress or strain is in shear form around 2 axis.
Electrodes are perpendicular to 1 axis.
Electromechanical coupling factor.

d_h
Hydrostatic stress or stress is applied equally in all directions. Electrodes are perpendicular to 3 axis (Ceramics).
Piezoelectric charge coefficient.

d_{33}
Applied stress, or piezoelectrically induced strain is in 3 direction.
Electrodes are perpendicular to 3 axis.
Piezoelectric charge coefficient.

g_{15}
Applied stress, or the piezoelectrically induced strain is in shear form around 2 axis.
Electrodes are perpendicular to 1 axis.
Piezoelectric voltage coefficient.

g_{31}
Applied stress, or the piezoelectrically induced strain is in 1 direction.
Electrodes are perpendicular to 3 axis.
Piezoelectric voltage coefficient.

s_{36}^E
Compliance is measured with closed circuit.
Stress or strain is shear around 3 direction.
Strain or stress is in 3 direction.
Elastic compliance.

s_{11}^D
Compliance is measured with open circuit.
Stress or strain is in 1 direction.
Strain or stress is in 1 direction.
Elastic compliance.

Note: All stresses, other than the stress involved in second subscript, are constant except in the case of s where all stresses other than the stress involved in one subscript are constant.

Piezoelectric Modes Of Vibration				
Vibration Mode	Dimensions L - Length W - Width T - Thickness D - Diam eter		Constants To Be Calculated	
			Piezoelectric	Mechanical
Transverse Length Mode	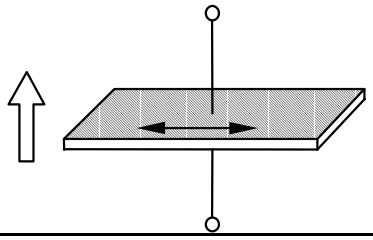	$Th, W < L/5$	$k_{31}, d_{31}, g_{31}, \varepsilon_{33}^{T}$	$s_{11}^{D}, s_{11}^{E}, Q_{31}$
Radial Mode	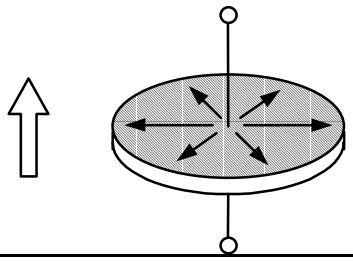	$D > 10Th$	$k_p, \varepsilon_{33}^{S}, \varepsilon_{33}^{T}$	$\sigma^{E}, s_{12}^{E}, Q_p$
Thickness Extension Mode	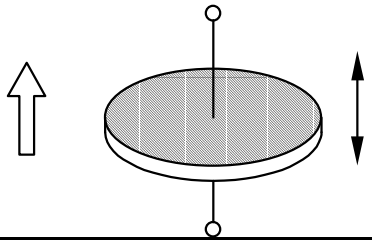	$D > 10Th$	$k_t, \varepsilon_{33}^{S}$	$c_{33}^{D}, c_{33}^{E}, s_{13}^{E}, Q_t$
Longitudinal Length Mode	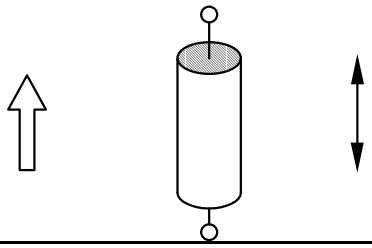	$D < L/2.5$	$k_{33}, d_{33}, g_{33}, \varepsilon_{33}^{T}$	$s_{33}^{D}, s_{33}^{E}, Q_{33}$
Thickness Shear Mode	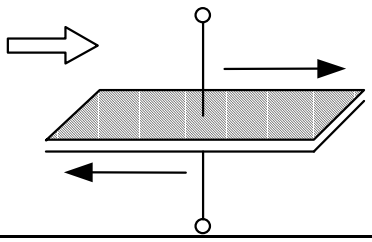	$L > 3.5(Th,W)$	$k_{15}, d_{15}, g_{15}, \varepsilon_{11}^{T}, \varepsilon_{11}^{S}$	$c_{55}^{D}, s_{55}^{D}, s_{55}^{E}, Q_{15}$

Polarisation direction 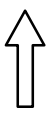

Direction of displacement, 

Dielectric Constant

The relative dielectric constant is defined as the ratio of the permittivity of the material to the permittivity of free space. This is generally measured well below the mechanical resonance. The dielectric constant is derived from the static capacitance measurements at 1 kHz using a standard impedance bridge.

$$K^T = \frac{\varepsilon^T}{\varepsilon_0} = \frac{C^T T}{\varepsilon_0 A}$$

Dielectric Loss Factor

The dielectric loss factor is defined as the tangent of the loss angle (tan δ). The loss factor represents the ratio of conductance to susceptance of a parallel equivalent circuit of the ceramic element. The loss factor can be measured directly using an impedance bridge.

Mechanical Quality Factor

The mechanical quality factor is the ratio of the reactance to the resistance in the series equivalent circuit representing the piezoelectric resonator. The Q_m factor is also related to the sharpness of the resonance frequency.

$$Q_m = \frac{f_a^{\,2}}{2\pi f_r Z_m C^T (f_a^{\,2} - f_r^{\,2})}$$

Alternatively the Q_m factor can also be determined using the equation:

$$Q_m = \frac{f_r}{f_1 - f_2}$$

Frequency Constants

The frequency constant, N, is the product of the resonance frequency and the linear dimension governing the resonance. N is also equal to half the sound velocity in the same direction. The various modes of resonance are shown schematically on page 5.

N_{31}	=	$f_r \cdot L$	Transverse mode, thin bar
N_p	=	$f_r \cdot D$	Radial mode, disc
N_t	=	$f_r \cdot T$	Thickness mode, disc
N_{33}	=	$f_r \cdot L$	Length mode, cylinder
N_{15}	=	$f_r \cdot T$	Shear mode, plate

Piezoelectric Coupling Coefficient

The coupling coefficient (electromechanical coupling coefficient) is defined as the ratio of the mechanical energy accumulated in response to an electrical input or vice versa.

$$k = \sqrt{\frac{\text{Mechanical energy stored}}{\text{Electrical energy applied}}}$$

$$k = \sqrt{\frac{\text{Electrical energy stored}}{\text{Mechanical energy applied}}}$$

The coupling coefficients can be calculated for the various modes of vibration:

$$k_{31} = \sqrt{\frac{\frac{\pi}{2}\frac{f_a}{f_r}}{\frac{\pi}{2}\frac{f_a}{f_r} - \tan\left(\frac{\pi}{2}\frac{f_a}{f_r}\right)}}$$

$$k_p \cong \sqrt{2.51\frac{f_a - f_r}{f_a} - \left(\frac{f_a - f_r}{f_a}\right)^2}$$

$$k_t = \sqrt{\frac{\pi}{2}\frac{f_r}{f_a}\cot\left(\frac{\pi}{2}\frac{f_r}{f_a}\right)}$$

k_{33} and k_{15} can be calculated similar to k_t by using the appropriate resonance frequencies.

Another parameter, k_{eff}, is frequently used to express the effective coupling coefficient of an arbitrary resonator, either at fundamental resonance or at any overtone and is expressed as follows:

$$k_{eff} = \sqrt{\frac{f_a^{\,2} - f_r^{\,2}}{f_r^{\,2}}}$$

Piezoelectric Charge Coefficients

The piezoelectric charge coefficient is the ratio of electric charge generated per unit area to an applied force (C/N or m/V).

$$d = \frac{\text{Strain developed}}{\text{Applied field}} = \frac{\text{Charge density}}{\text{Applied stress}}$$

The *d* constants are calculated from the equation:

$$d = k\sqrt{\varepsilon^T s^E} \text{ (C/N)}$$

$$d_{31} = k_{31}\sqrt{\varepsilon_{33}^T s_{11}^E}$$

$$d_{33} = k_{33}\sqrt{\varepsilon_{33}^T s_{33}^E}$$

$$d_{15} = k_{15}\sqrt{\varepsilon_{11}^T s_{55}^E}$$

Piezoelectric Voltage Coefficient

The piezoelectric voltage coefficient is the ratio of the electric field produced to the mechanical stress applied (V m/N).

$$g = \frac{\text{Strain developed}}{\text{Applied charge density}}$$

$$= \frac{\text{Field developed}}{\text{Applied mechanical stress}}$$

The *g* constants are calculated from the equation:

$$g = \frac{d}{\varepsilon^T} \text{ (V m/N)}$$

$$g_{31} = \frac{d_{31}}{\varepsilon_{33}^T}$$

$$g_{33} = \frac{d_{33}}{\varepsilon_{33}^T}$$

$$g_{15} = \frac{d_{15}}{\varepsilon_{11}^T}$$

Elastic Compliances

Young's modulus describes the mechanical stiffness properties and is expressed as the ratio of stress to strain. In a piezoelectric material, mechanical stress produces an electrical response, which opposes the resultant strain. The value of the Young's modulus depends on the direction of stress and strain and the electrical conditions. The inverse of Young's modulus, *Y*, is the elastic compliance, *s*, which can be calculates as follows (see relevant geometries on page 5):

$$s = \frac{1}{Y} = \frac{\text{Strain}}{\text{Stress}} = \frac{1}{\rho v^2}\left(\frac{\text{m}^2}{\text{N}}\right)$$

$$s_{33}^D = \frac{1}{4\rho f_a^2 L^2}$$

$$s_{33}^E = \frac{s_{33}^D}{1 - k_{33}^2}$$

$$s_{11}^E = \frac{1}{4\rho f_r^2 L^2}$$

$$s_{11}^D = s_{11}^E\left(1 - k_{31}^2\right)$$

$$s_{55}^D = \frac{1}{4\rho f_a^2 Th^2}$$

$$s_{55}^E = \frac{s_{55}^D}{1 - k_{15}^2}$$

Ageing Rate

The ageing rate of a piezoelectric ceramic is an index of the change of certain material parameters with time:

$$\text{Ageing Rate} = \frac{1}{(\log t_2 - \log t_1)}\left(\frac{P_2 - P_1}{P_1}\right)$$

Where
t_1, t_2 are number of days after polarization
P_1, P_2 are measured corresponding values

Standards

- American National Standard on Piezoelectricity. ANSI/IEEE Std. 176, 1987.
- Military Standard. DOD-STD-1376A(SH), 1984. Piezoelectric Ceramic for Sonar Transducers. (Hydrophones and Projectors).
- CENELEC, EN 50324-1, Piezoelectric properties of ceramic materials and components, Part 1: Terms and definitions.
- CENELEC, EN 50324-2, Piezoelectric properties of ceramic materials and components, Part 2: Methods of measurement - Low power.
- CENELEC, EN 50324-3, Piezoelectric properties of ceramic materials and components, Part 3: Methods of measurement - High power.
- International Electrotechnical Commission. IEC Standard 483, 1976. Guide to Dynamic Measurements of Piezoelectric Ceramics With High Electromechanical Coupling.

Recommended literature

For further information regarding theory of piezoelectricity, applications etc., the following literature can be suggested:

- Jaffe, B. et al. ***Piezoelectric Ceramics.*** Academic Press, London, New York, 1971.
- Moulson, A.J., Herbert, J.M. ***Electroceramics.*** Chapman and Hall, 1990. ISBN: 0412294907.
- Setter, N (Ed). ***Piezoelectric Materials in Devices.*** EPFL-LC, 2002. ISBN: 2-9700346-0-3.
- Burfoot, J.C., Taylor, G.W. ***Polar Dielectrics and their Applications.*** University of California Press, 1979.
- Yuhuan Xu. ***Ferroelectric Materials and Their Applications.*** Elsevier Science Publishers B.V., 1991. ISBN: 0 444 88354 1.

References

In order to develop improved and new materials and components Ferroperm invests a large proportion of its turnover on R&D projects. From these research projects a number of publications have been presented (shown in selection):

- Bove, T., Wolny, W.W., Ringgaard, E. & Breboel, K. ***New Type of Piezoelectric Transformer with Very High Power Density.*** Streiffer, S.K., Gibbons, B.J. & Tsurumi, T. (eds.): Proc. of ISAF 2000, 321-324.
- Wolny, W.W. (2000). ***Piezoceramic Thick Films – Technology and Applications. State of the Art in Europe.*** Streiffer, S.K., Gibbons, B.J. & Tsurumi, T. (eds.): Proc. of ISAF 2000, 257-262.
- Ringgaard, E., Nielsen, E.R. & Wolny, W.W. (2000). ***Optimisation of New Liquid-Phase Sintering Aid for PZT.*** Streiffer, S.K., Gibbons, B.J. & Tsurumi, T. (eds.): Proc. of ISAF 2000, 451-454.
- Corker, D.L., Whatmore, R.W., Ringgaard, E. & Wolny, W.W. ***Liquid-Phase Sintering of PZT Ceramics.*** J.Eur.Ceram.Soc., **20** 2039-2045.
- Levassort, F., Tran-Huu-Hue, L.P., Lethiecq, M., Bove, T. & Wolny,W.W. ***New Piezoceramic Films for High-Resolution Medical Imaging Applications.*** Proceedings Of IEEE UFFC, October 2000.
- Bove, T., Wolny, W.W., Ringgaard, E., Pedersen, A. ***New Piezoceramic PZT-PNN Material for Medical Diagnostic Applications.*** Proceedings of Electroceramics 2000.

- Damjanovic, D., Wolny, W.W., Engan, H., Lethiecq, M. & Pardo, L. ***Properties and Applications of Modified Lead Titanate Ceramics.*** Proc. of the 1998 IEEE International Frequency Control Symposium. (IEEE 98CH36165) 770-778.

- Gómez, T.E., Montero de Espinosa, F., Levassort, F., Lethiecq, M., James, A., Ringgaard, E., Millar, C.E. & Hawkins, P. ***Ceramic Powder--Polymer Piezocomposites for Electroacoustic Transduction: Modeling and Design.*** Ultrasonics, 36 907-923.

- Levassort, F., Lethiecq, M., Tran-Huu-Hue, L.P. & Wolny, W.W. ***High Frequency Properties of New Fine-Grained Modified Lead Titanate Ceramics.*** Schneider, S.C., Levy, M. & McAvoy, B.R. (eds.): 1997 IEEE International Ultrasonics Symposium Proc. (IEEE 97CH36118) 947-950.

- Pardo, L., Durán-Martín, P., Mercurio, J.P., Nibou, L. & Jiménez, B. ***Temperature Behaviour of Structural, Dielectric and Piezoelectric Properties of Sol-Gel Processed Ceramics of the System $LiNbO_3$-$NaNbO_3$.*** J.Phys.Chem. Solids, 58 [9] 1335-1339.

- González, A.M. & Alemany, C. ***Determination of the Frequency Dependence of Characteristic Constants in Lossy Piezoelectric Materials.*** J.Phys.D: Appl.Phys., 29, 2476-2482.

- Lethiecq, M., Levassort, F., James, A.S., Wolny, W.W. & Mercurio, J.P. ***High Permittivity Ceramics for Medical Ultrasonic Transducers: a Study on the Optimisation of Processing Parameters.*** Kulwicki, B.M., Amin, A. & Safari, A. (eds.): Proc. 10th IEEE International Symp. on Applications of Ferroelectrics (ISAF '96) . (IEEE 96CH35948) 287-290.

- Levassort, F., Lethiecq, M., Gomez, T., Montero de Espinosa, F., James, A.S., Ringgaard, E., Hawkins, P., Millar, C.E. ***Modeling the Effective Properties of Highly Loaded 0-3 Piezocomposites.*** Levy, M., Schneider, S.C. & McAvoy, B.R (eds.): 1996 IEEE Ultrasonics Symposium Proc. (IEEE) 463-466.

- Pardo, L., Durán-Martín, P., Millar, C.E., Wolny, W.W. & Jiménez, B. ***High Temperature Electromechanical Behaviour of Sodium Substituted Lithium Niobate Ceramics.*** Ferroelectrics, 186 281-285

- Pardo, L., Durán-Martín, P., Wolny, W.W., Mercurio, J.P. & Jiménez, B. ***High Temperature Piezoelectricity of Sodium Substituted Lithium Niobate Ceramics.*** Kulwicki, B.M., Amin, A. & Safari, A. (eds.): Proc. 10th IEEE International Symp. on Applications of Ferroelectrics (ISAF ' 96). (IEEE 96CH35948) 915-918.

- Wolny, W.W., James, A.S., Alemany, C. & Pardo, L. ***Structural Stability of Lead Titanate Based Piezoceramics in Chemically Aggressive Environments.*** Baptista, J.L., Labrincha, J.A. & Vilarinho, P.M. (eds.): Proc. Electroceramics V. 153-156.

- M. R. Cockburn, D. A. Hall, C. E. Millar. ***The Effect of High Temperature Annealing and HIPing on the Dielectric Properties of Modified Lead Titanate Ceramics.*** ISAF ´ 94, Aug. 7-10, 1994, Pennsylvania, USA.

- C. E. Millar, B. Andersen, E. Ringgaard, W.W. Wolny, J. Ricote, L. Pardo. ***Fabrication of High Density, Fine-Grained PZT Ceramics Using a Post Sinter HIP Treatment.*** ISAF ´ 94, Aug. 7-10, 1994, Pennsylvania, USA.

Ferroperm Piezoelectric Materials

Ferroperm manufactures piezoelectric ceramics in 5 material groups, traditional lead zirconate titanate (hard and soft PZT), relaxor-based solid solutions, modified lead titanate, lead metaniobate and bismuth titanate. A brief description of the materials is given below and material data can be found on pages 12 to 16.

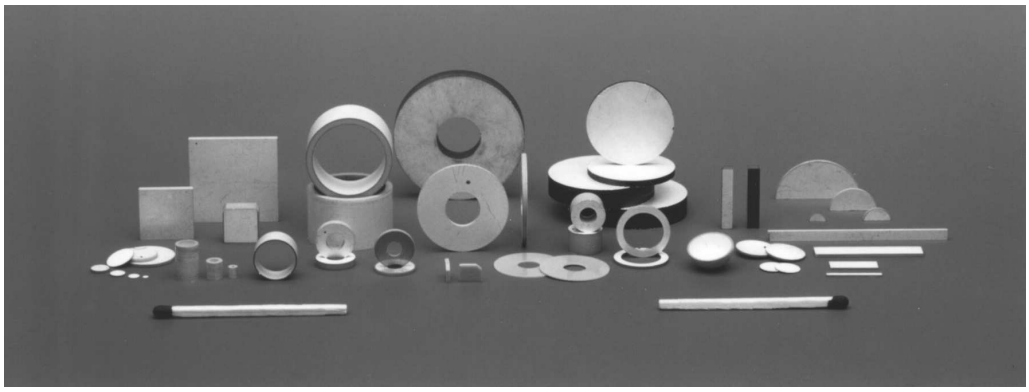

Lead zirconate titanate (Soft).

Type Pz23 and **Pz27**. These materials are characterized by relatively high Curie temperatures (> 350°C), low mechanical Q_M factor and high electrical resistivity at elevated temperatures. **Pz27** has a high dielectric constant, high charge coefficients and high electromechanical coupling coefficients.
Type Pz29 has a lower Curie temperatures, but high dielectric constants, and high coupling coefficients.

Ceramics from these compositions are particularly useful in for a wide spectrum of applications ranging from combined resonant transducers for medical and flow measurements to accelerometers, pressure sensors, and NDT.

Lead zirconate titanate (Hard).

Type Pz24, **Pz26** and **Pz28**. These materials are characterized by high coercive field, high mechanical Q_M factor and low dielectric loss. **Pz24** has a very low dielectric constant. **Pz26** and **Pz28** are both high power and low loss materials.

Typical applications include underwater applications, high voltage generators, high power ultrasonics, e.g. cleaning, welding and drilling devices.

Relaxor-based solid solution

Type Pz21. This material is characterized by a very high dielectric constant, high charge coefficient and high electromechanical coupling coefficients.

Used primarily for medical imaging systems, i.e. phased arrays and composites.

Modified lead titanate. **Type Pz34** has large electromechanical anisotropy, low dielectric constant and properties and have extremely low grain size. It is very stable over time, temperature and frequency.

Recommended for single element high frequency medical transducers and applications where interference from radial modes is a significant problem.

Lead metaniobate. **Type Pz35** is anisotropic, has a low Q_M factor, low acoustic impedance, and low dielectric constant.

Primarily used in NDT systems where low Q_M factor and clean impulse response are required.

Bismuth titanate. **Type Pz46** has a very high Curie temperature (> 600°C) and working temperatures of up to 550°C.

Used in high temperature applications, i.e. accelerometers, flow-meters and pressure sensors.

Material Applications

Application	Material Suggestion									
	Pz21	Pz23	Pz24	Pz26	Pz27	Pz28	Pz29	Pz34	Pz35	Pz46
Underwater										
• Transmitters				●		●				
• Receivers	●			●	●	●	●			
• Hydrophones	●			●	●	●	●			
Transducers/Sensors										
• Level			●	●	●	●	●	●	●	
• Flow			●	●	●	●	●	●	●	
• NDT	●	●	●	●	●	●		●	●	
• Accelerometers	●	●	●	●	●					
• Pressure	●	●			●		●			
• Acoustic Emission	●	●			●		●			
• High Temperature										●
• Shock		●			●					●
Medical										
• Diagnostic	●		●	●	●		●	●		
• Therapeutic			●	●		●				
• Combined / Doppler	●			●	●		●			
Industrial										
• High Voltage				●		●				
• High Power				●		●				
• Automation	●				●		●			
• Actuators	●			●	●		●			
• Motors				●						

Material Data For Standard Test Specimens

Data are measured at 25°C and 24 hours after poling.

	Symbol	Dimension	Pz21	Pz23	Pz24	Pz26	Pz27
Electrical Properties							
Relative dielectric const. at 1 kHz	K_{33}^T	1	3800	1500	400	1300	1800
Diel. dissipation factor at 1 kHz	tan δ	10^{-3}	18	13	2	3	17
Curie temperature	$T_c >$	°C	205	350	330	330	350
Recommended working range	<	°C	130	250	230	230	250
Electromechanical Properties							
Coupling factors	k_p	1	0.60	0.52	0.50	0.57	0.59
	k_t	1	0.47	0.45	0.52	0.47	0.47
	k_{31}	1	0.33	0.29	0.29	0.33	0.33
	k_{33}	1	0.70	0.65	0.67	0.68	0.70
Piezoelectric charge coefficients	$-d_{31}$	10^{-12} C/N	250	130	55	130	170
	d_{33}	10^{-12} C/N	600	330	190	330	425
	d_{15}	10^{-12} C/N	650	335	150	400	500
Piezoelectric voltage coefficients	$-g_{31}$	10^{-3} Vm/N	7	10	16	11	11
	g_{33}	10^{-3} Vm/N	18	25	54	28	27
Frequency constants	N_p	Hz·m	2030	2160	2400	2230	2010
	N_t	Hz·m	1970	2030	2100	2040	1950
	N_{31}	Hz·m	1375	1480	1670	1500	1400
	N_{33}	Hz·m	1325	1600	1600	1800	1500
Mechanical Properties							
Density	ρ	10^3 kg/m^3	7.80	7.70	7.70	7.70	7.70
Elastic compliances	s_{11}^E	10^{-12} m^2/N	18	15	10	13	17
	s_{33}^E	10^{-12} m^2/N	18	19	23	20	23
	s_{11}^D	10^{-12} m^2/N	16	14	10	12	15
	s_{33}^D	10^{-12} m^2/N	9	11	13	11	12
Poisson's ratio	σ^E	1	0.40	0.39	0.29	0.33	0.39
Mechanical quality factor	Q_m	1	65	100	>1000	>1000	80

Standard tolerances:

Electrical Properties	± 10 %
Electromechanical Properties	± 5 %
Mechanical Properties	± 2.5 % (Except for σ^E and Q_m)

Material Data For Standard Test Specimens

Data are measured at 25°C and 24 hours after poling (Pz28 10 days after poling)

	Symbol	Dimension	Pz28	Pz29	Pz34	Pz35	Pz46
Electrical Properties							
Relative dielectric const. at 1 kHz	K_{33}^{T}	1	1000	2900	210	220	120
Diel. dissipation factor at 1 kHz	$\tan\delta$	10^{-3}	4	19	14	6	4
Curie temperature	$T_c >$	°C	330	235	400	500	650
Recommended working range	<	°C	230	150	150	200	550
Electromechanical Properties							
Coupling factors	k_p	1	0.58	0.64	0.07		0.03
	k_t	1	0.47	0.52	0.40	0.34	0.20
	k_{31}	1	0.34	0.37	0.05		0.02
	k_{33}	1	0.69	0.75	0.40		0.09
Piezoelectric charge coefficients	$-d_{31}$	10^{-12} C/N	120	240	5		2
	d_{33}	10^{-12} C/N	320	575	50	100	18
	d_{15}	10^{-12} C/N	375	650	40	50	16
Piezoelectric voltage coefficients	$-g_{31}$	10^{-3} Vm/N	13	10	3		2
	g_{33}	10^{-3} Vm/N	34	23	25	43	17
Frequency constants	N_p	Hz·m	2180	1970	2770		2470
	N_t	Hz·m	2010	1960	2200	1550	2000
	N_{31}	Hz·m		1410			
	N_{33}	Hz·m		1500			
Mechanical Properties							
Density	ρ	10^3 kg/m^3	7.70	7.45	7.55	5.60	6.55
Elastic compliances	s_{11}^{E}	10^{-12} m^2/N	13	17	7		11
	s_{33}^{E}	10^{-12} m^2/N	23	23	7		44
	s_{11}^{D}	10^{-12} m^2/N	11	15	7		11
	s_{33}^{D}	10^{-12} m^2/N	12	10	6		44
Poisson's ratio	σ^E	1	0.31	0.34	0.22		0.21
Mechanical Quality factor	Q_m	1	>1000	90	> 500	15 - 25	> 600

Standard tolerances:

Electrical Properties	± 10 %
Electromechanical Properties	± 5 %
Mechanical Properties	± 2.5 % (Except for σ^E and Q_m)

Relative Dielectric Constant vs. Temperature

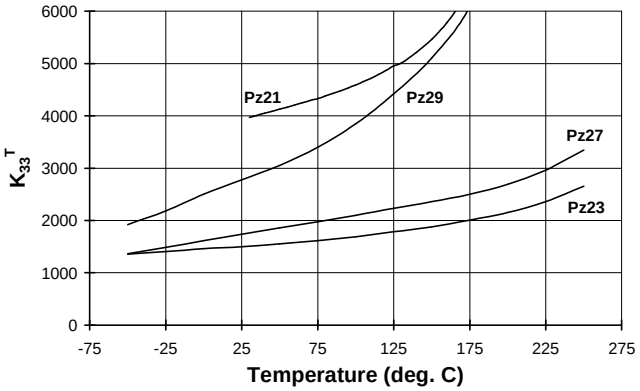

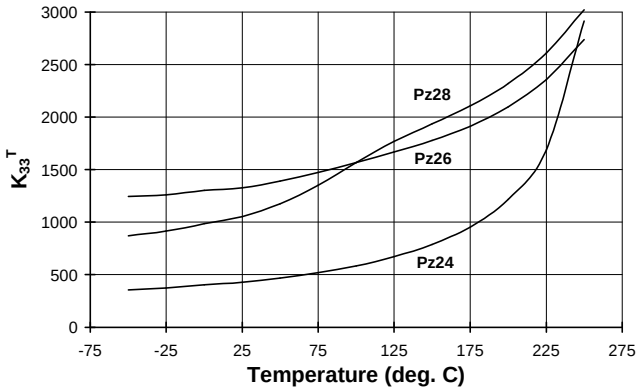

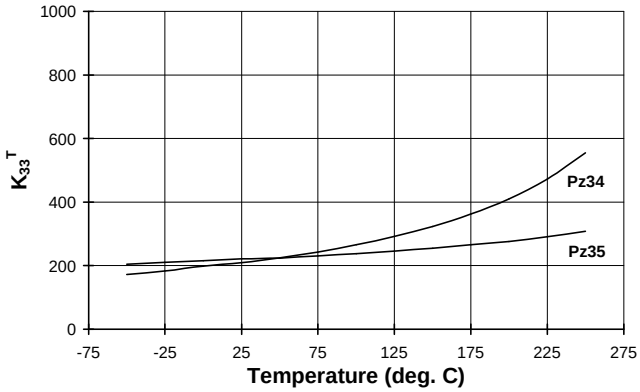

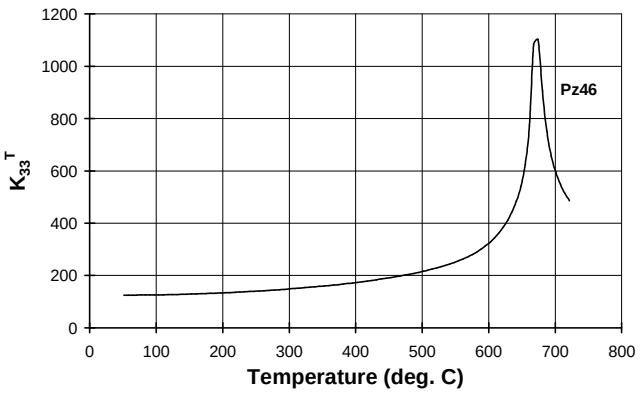

Dielectric Loss vs. Temperature

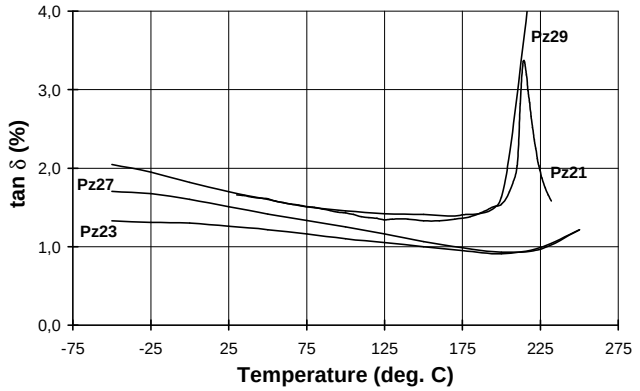

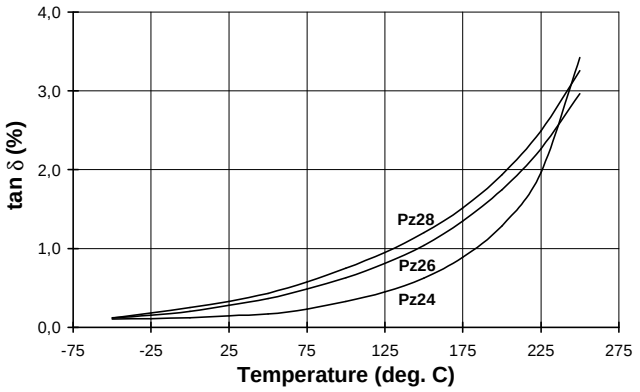

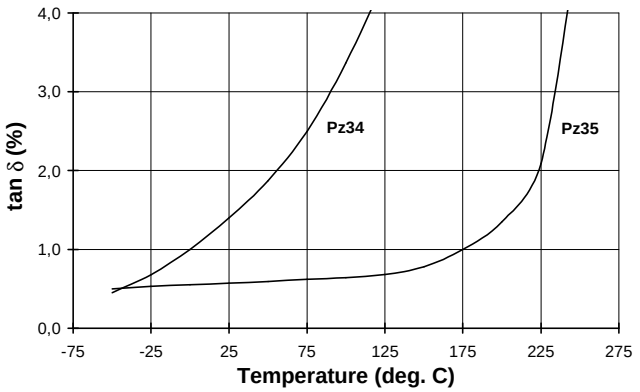

Pz46 measurements were made at "Laboratory of Ceramics, EPFL" Switzerland.

Planar Coupling Factor vs. Temperature

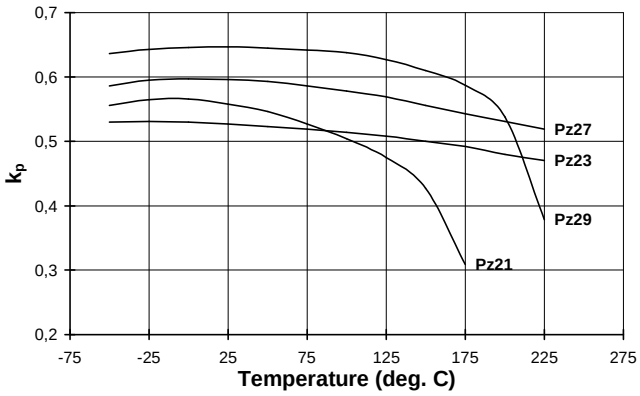

Planar Coupling Factor vs. Temperature

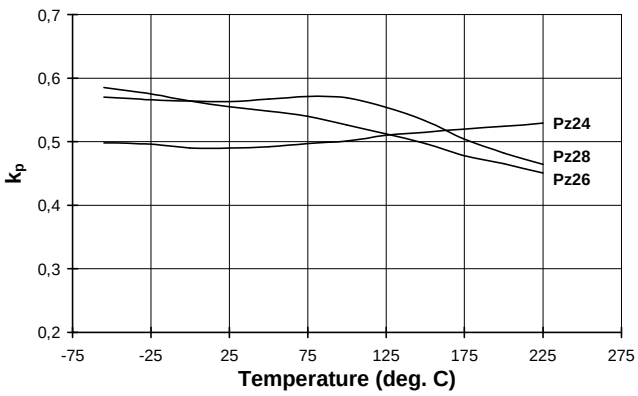

Thickness Coupling Factor vs. Temperature

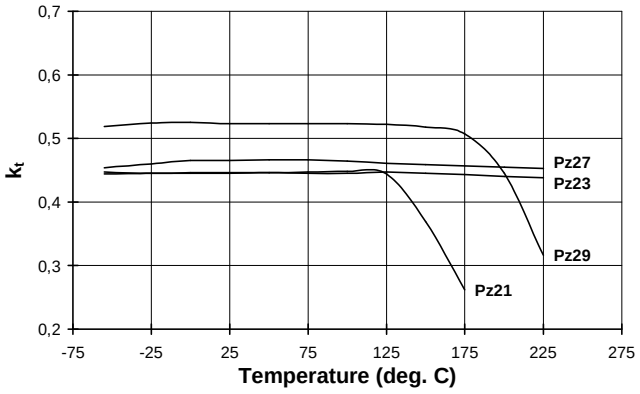

Thickness Coupling Factor vs. Temperature

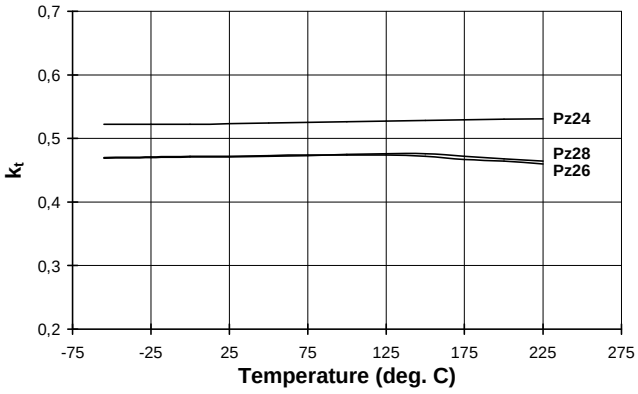

k_{31} Factor vs. Temperature

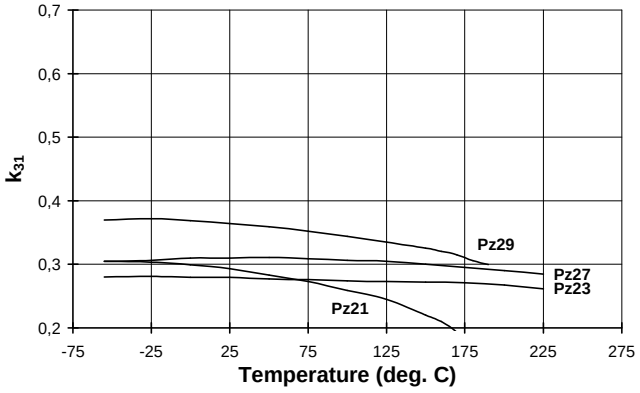

k_{31} Factor vs. Temperature

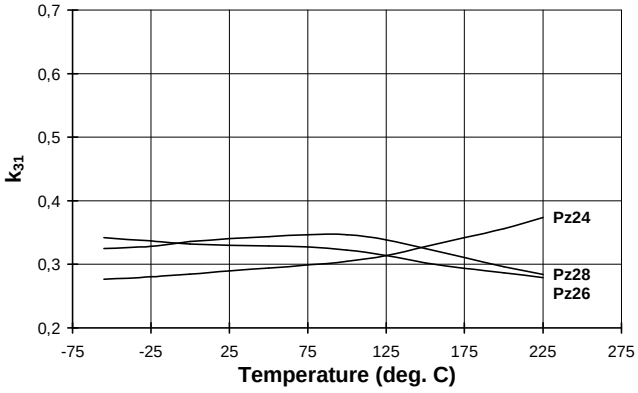

d_{31} Coefficient vs. Temperature

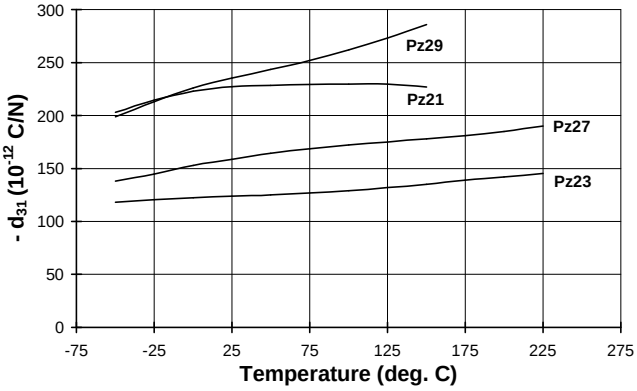

d_{31} Coefficient vs. Temperature

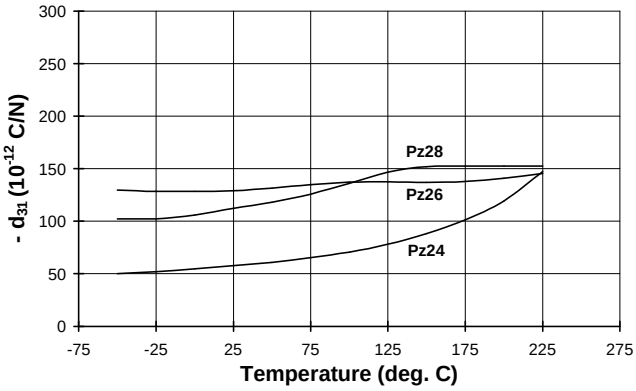

g_{31} Coefficient vs. Temperature

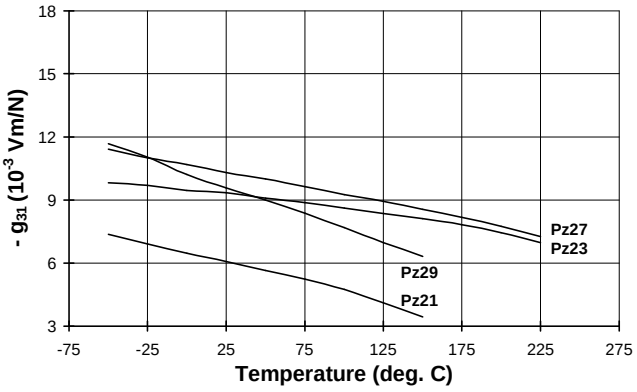

g_{31} Coefficient vs. Temperature

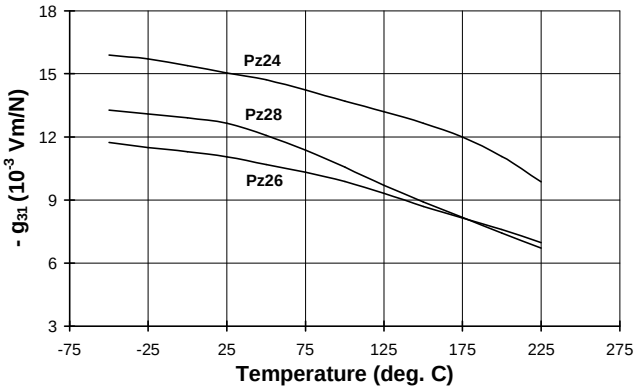

The manufacturing process involves a number of stages shown schematically in figures 1 to 12. The first step is to weigh, dry mix and ball mill [2] the raw materials. The uniform mixture is then heat treated (calcined) [3], during which the components react to form the polycrystalline phase. The calcined powder is ball milled [4] to increase it' s reactivity, and granulated [5], with the addition of a binder, to improve its pressing properties.

After shaping by dry-pressing [6], the binder is burnt out [7] by slowly heating the green ceramics to around 700°C. The parts are transferred to another furnace, where they are sintered [8] between 1200 and 1300°C. The dimensional tolerance of fired parts (± 3 %) is improved by cutting, grinding, lapping etc. [9].

Electrodes are applied either by screen printing or by vacuum deposition [10]. Poling then is carried out by heating in an oil bath at 130-220°C, and applying an electrical field of 2-8 kV/mm to align the domains in the material [11]. The oil bath is used as a heat source and to prevent flash over.

Final inspection [12] is performed 24 hours later, and includes testing of electrode-ceramic bonding as well as measurement of dimensional tolerances, di-electric and piezoelectric properties.

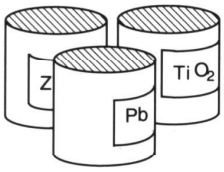

[1] RAW MATERIALS

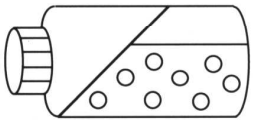
[2] MIXING

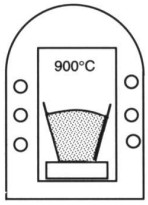

[3] CALCINING

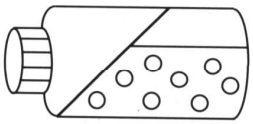
[4] MILLING


[5] GRANULATION

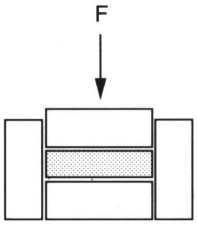

[6] PRESSING

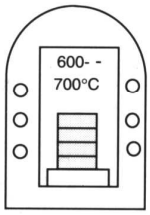

[7] BINDER BURNOUT

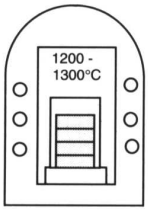

[8] SINTERING

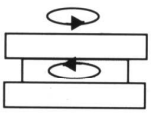
[9] GRINDING/POLISHING

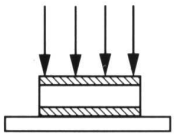
[10] ELECTRODING

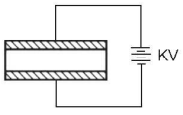

[11] POLING

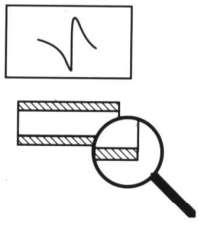
[12] FINAL INSPECTION

Certain commonly requested parts: discs, rings, tubes and square plates in Pz26 and Pz27, are carried in stock for prompt delivery.

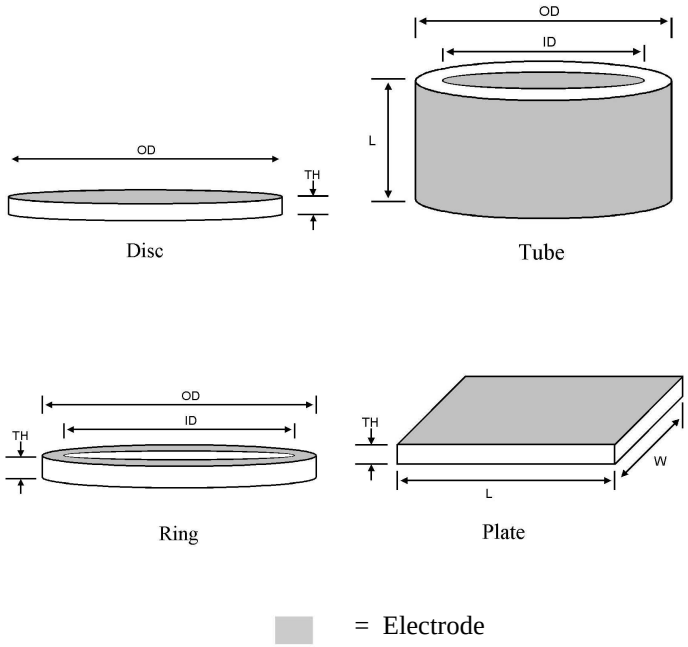

Pz26 And Pz27 Discs
Electrodes on flat surfaces

OD (mm)	*Th* (mm)	Part Number Pz26	Pz27
5.00	0.5	26000	27000
	1.0	26001	27001
	2.0	26002	27002
6.35	0.5	26010	27010
	1.0	26011	27011
	2.0	26022	27012
10.00	0.5	26020	27020
	1.0	26021	27021
	2.0	26022	27022
12.70	0.5	26030	27030
	1.0	26031	27031
	2.0	26032	27032
16.00	0.5	26040	27040
	1.0	26041	27041
	2.0	26042	27042
20.00	0.5	26050	27050
	1.0	26051	27051
	2.0	26052	27052
25.00	0.5	26060	27060
	1.0	26061	27061
	2.0	26062	27062
30.00	0.5	26070	27070
	1.0	26071	27071
	2.0	26072	27072
38.00	0.5	26080	27080
	1.0	26081	27081
	2.0	26082	27082
50.00	0.5	26090	27090
	1.0	26091	27091

Pz26 And Pz27 Tubes
Electrodes on curved surfaces

OD (mm)	*ID* (mm)	*Th* (mm)	Part Number Pz26	Pz27
6.35	5.20	3.20	26201	27201
6.35	5.20	6.35	26202	27202
12.70	11.10	3.20	26203	27203
24.00	20.00	15.00	26204	27204
32.00	28.00	14.00	26205	27205

Pz26 And Pz27 Rings
Electrodes on flat surfaces

OD (mm)	*ID* (mm)	*Th* (mm)	Part Number Pz26	Pz27
5.00	2.30	1.00	26101	27101
5.00	2.30	2.00	26102	27102
6.35	2.40	1.00	26111	27111
6.35	2.40	2.00	26112	27112
10.00	5.00	1.00	26121	27121
10.00	5.00	2.00	26122	27122
20.00	3.80	1.00	26131	27131
20.00	3.80	2.00	26132	27132

Pz26 And Pz27 Plates
Electrodes on flat surfaces

L (mm)	*W* (mm)	*Th* (mm)	Part Number Pz26	Pz27
6.35	6.35	1.00	26301	27301
12.70	12.70	1.00	26302	27302
30.00	30.00	1.00	26303	27303
50.00	50.00	1.00	26304	27304

Materials

In addition to the standard compositions shown in the previous sections, Ferroperm offers a HIP quality (Hot Isostatic Pressed) of most PZT ceramics. The advantage of HIP quality is very low porosity and improved mechanical and piezoelectric properties.

Special formulations and fine-grained materials can be manufactured on request.

Electrodes and special designs

Fired screen-printed silver electrodes are available as standard electrode materials on conventional parts. Other electrode materials include:

- Screen-printed gold-palladium
- Evaporated chromium-silver
- Evaporated chromium-gold
- Evaporated chromium-silver with gold-flash on one side
- Chemically deposited nickel-gold

Polished or fine-grinded surfaces are available on request.

Wrap around electrodes and side connections are made on request, and electrode configurations can be varied to accommodate polarization patterns and acoustic designs.

Custom Products

By far the largest proportion of the production in Ferroperm is made according to customer specification. The ceramics can be produced in many shapes i.e. discs, plates, tubes, rings, hemispheres and focusing bowls. Shear plates, shear tubes and shear rings are available in most compositions. For special requirements, please contact Ferroperm Piezoceramics A/S directly.

Focusing Bowls

Focusing bowls are available in all standard compositions. Special non-standard diameters, resonant frequencies, focal lengths (R_1) and closer tolerances can be made on request.

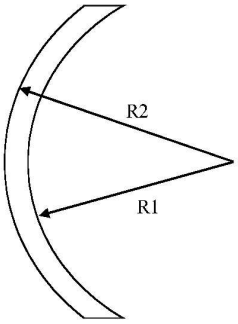

Resonant frequency range available:

- 100 kHz to 10 MHz

Diameter range available:

- 5 mm to 65 mm

Shear plates

Shear plates are offered based on customer specification. Plates can be specified with- our without centre holes.
Electrodes are chemically plated nickel-gold or evaporated silver or gold.

Shear Tubes

Shear tubes are offered based on customer specification. These can be specified with special cuts, slots, or chamfering to aid assembly, and have multiple output signals.
The electrode material is typically chemically plated nickel-gold.

Shear Rings

Shear rings (opposite polarisation/electrode configuration to shear tubes) are offered based on customer specification. These can be specified with special cuts, slots, or chamfering to aid assembly, and have multiple output signals.
Electrodes are chemically plated nickel-gold or evaporated silver or gold.

Soldering Procedure

Clean the area to be soldered thoroughly. Pre-tin the electrode area and the lead. A low melting point Sn/Pb solder containing 2 - 4 % silver is recommended (Multicore LMP, FLUX 362).

Place the lead in the middle of the pre-tinned area, applying a firm pressure, see figure 1 and 2. Heat the lead a little above the ceramic surface. When the solder on the lead melts, move the soldering iron down the lead to ensure the melting of the solder on the silver electrode. Withdraw the soldering iron as soon as the solder has melted (5 - 7 seconds).
Soldering temperature should be approximately 270 - 300°C. Using too low a temperature will increase soldering time. The right temperature is when the solder melts readily. Care should be taken to use a short soldering time as excessive heat could locally depolarise the ceramic, or reduce the piezoelectric properties.

Remove flux according to the recommendations of the solder manufacturer. The electrodes will withstand ordinary ultrasonic cleaning processes.

Tolerances

A set of standard tolerances is used, if nothing else is specified by the customer. This set is separated into several different categories. For most of these categories the customer however have the opportunity to specify other tolerances for the specific parameters, which are most critical for that certain application. Changes in inspection level should however always be discussed with Ferroperm and incorporated into the quotation and ordering as soon as possible in the dialog.

The first step in approval of a new production is the material itself, where a list of tolerances must be fulfilled in order to qualify as one of the 10 materials in the programme. A set of tolerances has therefore been defined. These tolerances are also used to verify any new material batches before it is released for regular production.

Dielectric Properties	
Relative dielectric constant Dielectric loss factor	± 10 %
Electromechanical Properties	
Coupling factors Charge coefficients Voltage coefficients Frequency constants	± 5 %
Mechanical Properties	
Density Elastic compliances	± 2,5 %

Note:
Catalogue values are based on measurements on standard geometries fulfilling recommended geometrical conditions.

For the specific production there will be a list of parameters regarding the size, geometrical parameters and electric behaviour, which have to be fulfilled. The standard tolerances on these are:

	Standard tolerance	Minimum tolerance
Diameter of Rings and Discs		
$OD \leq 10$ mm	± 0,3 mm	0,01 mm
$OD > 10$ mm	± 3 %	0,01 mm
Length and width of Plates	± 0,3 mm	0,01 mm
Thickness of Rings, Discs and Plates		
$Th \leq 1$ mm	± 0,03 mm	0,01 mm
$Th > 1$ mm	± 3 %	0,01 mm
Focussing Bowls		
Radius of curvature (R1 and R2)	± 3 % or ±3 mm whichever is largest	1 mm (dependent on total size)
Diameter	± 3 % or ±3 mm whichever is largest	0,01 mm
Thickness uniformity	Max variation 2,5% or 0,025 mm whichever is largest	0,05 mm (dependent on total size)
Resonance frequency		
Resonance ≤ 4MHz	± 5%	± 0,5%
Resonance > 4MHz	± 10%	± 1%
Capacitance		1 pF

Finally other more subjective parameters will be measured and documented when relevant. Among these parameters are for example, internal cracks, solderability, electrode adherence, surface roughness, and edge resistance in wrap-around electrodes.

Quality Assurance and Standards

The quality system in Ferroperm ensures full traceability for all productions and all operations carried out on an order.

The starting point in the system is that all productions are performed *material-batch-specific* rather than based on generic material data. This means, that before any material is released for regular production, a pilot production has been completed, and all relevant parameters have been measured and approved. The data for a specific batch is saved in a database, which is used by the production manager to optimise the production parameters for each new production.

The material batch number is therefore an important parameter for every new production, and will be clearly marked on both the production- and final inspection sheets.

As shown in previous sections, each production have a number of different processes, which must be performed before a certain part is completed. After each of these operations the responsible operator will record and register the time spent and the quantity of defects generated.

The quality system differentiate between more than 120 different types of defects ranging from simple errors on dimension to more complicated types, such as discrepancies in certain piezoelectric parameters. By operating this highly differential system, a more systematic approach to corrective actions can be taken.

After a completed production, all parts are passed through the final inspection unit. This department is a staff function under the managing director of Ferroperm Piezoceramics. Here qualified and well trained personnel uses modern and periodically calibrated equipment to verify that productions fulfil the internal standards to the materials and the tolerances given by the customer.

Most control operations are based on the statistical sampling described in Military Standard MIL-STD-1050 (ISO 2602-1973). The acceptable quality limit, AQL, is 0.65 - Sample plan 2. By operating this system, it is secured that maximum 0,65% defect parts can be sent to a customer without seeing any problems during inspection.

In some cases customers have one or more critical parameters, where defects cannot be tolerated in spite of an increased cost of the parts. In such cases Ferroperm offer a 100% inspection on these parameters.

Certificates of conformance and/or copies of the final inspection sheets are supplied on request from the customer.

Ordering Information

Submitting the following information when inquiring for quotations will be helpful:

- Type of material
- Geometric shape, dimensions and tolerances
- Electrode material, pattern and polarization
- Quantities required
- Specification of the part if available
- Requested delivery date
- If part-deliveries from stock are required

Packaging and Shipping

Ferroperm uses packaging and shipping methods that ensure safe delivery of products to the customer. These methods are based on our experience in shipping such materials. The shipping method is usually chosen based on the most economical method available. Special packaging and shipping services are available on request.
Shipping damage must be reported to the transport carrier immediately. Returns, if necessary, must be arranged with Ferroperm to obtain return authorisation and re-entry documentation.

Direct Contact and Technical Discussion

Development, design and production of devices and products incorporating piezoelectric elements usually require a high degree of technical knowledge and experience.
As an active partner in this process, Ferroperm Piezoceramics is dedicated to assist at the designing stage with a choice of the best material for the application, guide customers through the definition phase in order to obtain the best quality vs. price ratio, be flexible and supportive at the sample-manufacturing stage, and finally supply consistent high quality reliable products at fair and competitive prices.

Existing or potential customers are therefore always welcome to contact Ferroperm directly in order to discuss problems and possibilities for future orders, and to solve technical and commercial details as quickly and flexible as possible.

Local Distributors

Below you will find a list of Ferroperm's s ales di- tributors in Germany, United Kingdom, France and Brazil.

Main Office and Production Facilities
Ferroperm Piezoceramics A/S Hejreskovvej 18A DK-3490 Kvistgård Tel.: (+45) 49 12 71 00 Fax: (+45) 49 13 81 88 E-mail: pz@ferroperm-piezo.com Website: www.ferroperm-piezo.com

Germany	United Kingdom
Amroh Electronics GmbH Jakob-Kaiser-Straße 2 D-47877 Willich Germany Tel: (+49) 2154 945030 Fax: (+49) 2154 428421 E-mail: amroh@t-online.de, Website: www.amroh.via.t-online.de/piezo.htm	**E.P Electronic Components Ltd.** Unit 22, Station Road Ind. Est. Southwater, West Sussex RH13 7UD United Kingdom Tel: (+44) 1403 733030, Fax: (+44) 1403 733909 E-mail: info@epelectronics.co.uk Website: www.epelectronics.co.uk
France	**Brazil**
Hybrico International ZAE les Glaises 2 bis, Rue Léon Blum F-91120 Palaiseau France Tel: (+33) 1 69 19 13 07 Fax: (+33) 1 69 19 13 09	**Engecer Projetos e Produtos Cerémicos** R.N. Sra. Auxiliedore, 1141 Sta. Felicia - CEP 13560-970 São Carlos - SP Brazil Tel: (+55) 0162 72-6716 Fax: (+55) 0162 72-1125
Poland	
Sonomed ltd. Sliska52, PL00-826 Warszawa, Poland Tel: (+48) 22 65 41 506 Fax: (+48) 22 65 41 507 E-mail: biuro@sonomed.com.pl Website: www.sonomed.com.pl	